



AUTARQUIA ASSOCIADA À UNIVERSIDADE DE SÃO PAULO

**LOW GAIN Nd:YLF LASERS OPERATING IN THE QUASI-THREE LEVEL
TRANSITION AND IN RAMAN LASERS**

Jonas Jakutis Neto

**Tese apresentada como parte
dos requisitos para obtenção do Grau
de Doutor em Ciências na Área
de Tecnologia Nuclear - Materiais**

**Orientador:
Prof. Dr. Niklaus Ursus Wetter
Dr. Helen Pask**

**São Paulo
2012**

INSTITUTO DE PESQUISAS ENERGÉTICAS E NUCLEARES
Autarquia associada à Universidade de São Paulo

**LOW GAIN Nd:YLF LASERS OPERATING IN THE QUASI-THREE LEVEL
TRANSITION AND IN RAMAN LASERS**

JONAS JAKUTIS NETO

Tese apresentada como parte dos requisitos
para a obtenção do grau de Doutor em
Ciências na Área de Tecnologia Nuclear –
Materiais.

Orientador: Dr. Niklaus Ursus Wetter
Co-orientador: Dr. Helen M. Pask

Versão Corrigida
Versão Original se encontra disponível no IPEN

SÃO PAULO
2012

Acknowledgements

I would like to thank Prof. Niklaus Ursus Wetter, my supervisor for nearly 8 years now. Most of what I know today I learned with him. I am glad to be his student all this time, and I hope we will continue this interaction in the future.

I would like to thank Dr. Helen Pask, also my supervisor. We worked together during two and a half years, time that will never be forgotten. She is one of the most special people I have ever met, very kind and always supporting her students either in the lab or in life. She is an inspiration for me.

I thank Dr. Andrew Lee for all lab support, knowledge and the true friendship developed during my stay in Australia.

I thank all my lab friends, Jipeng Lin, Xiaoli Li, Gerald Bonner and Christopher Artlett from Macquarie and Danilo Mariano, Fabíola Camargo, Gustavo Nogueira, Renato Ribamar e Cristine Kores from IPEN-USP. They all have made the lab environment much more pleasant.

I thank my friends from MQPhotonics: Nem Jovanovic, Simon Gross, Eduardo Granados, Tom McGregor, Josh Toomey, Doug Little, Rob Williams, Ben Johnson, Adam Joyce, Martin Ams, Nick Cvetojevic, Geraldine Marien, Ondrej Kitzler, Aaron McKay, Jocelyn, Yuwen Duan, Yiqing Lu, Tim Zhao, Jana Say, Varun, Rajesh, Hua Liu and all the exchange students who stayed there for short periods.

I thank my friends in the Center for lasers and applications in Brazil: Thiago Cordeiro, Renata Costa, Jair, Ivanildo, Horácio, Gerson, Fábio, Fernando, Patricia e Bruno (Campineiro).

I thank all the researchers who supported me in Macquarie University, David Spence, Judith Dawes, Richard Mildren, and others.

I thank Anne Laurence Bibost, a very happy PhD student from the Biology department who for sure made my days happier with her contagious happiness.

I thank my Family, Alcélia Jakutis, Juliano Jakutis e Jade Jakutis for always supporting me on my decisions and everything else.

Finally, I thank everyone who directly or indirectly contributed to this work.

THANK YOU VERY MUCH! MUITO OBRIGADO!

*“The mind that opens to a new idea
never returns to its original size...”*
Albert Einstein

I dedicate this thesis to my family and friends!

This thesis is the result of a joint PhD (cotutelle) realized between Universidade de São Paulo - Brazil and Macquarie University – Australia, with half of the research carried out in Brazil and half in Australia.

Low gain Nd:YLF lasers operating in the quasi-three level transition and in Raman lasers

Jonas Jakutis Neto

Abstract

Lasers operating in the blue and yellow-orange spectral regions are sought after by the applications market either to improve well known technologies or to enable new ones. Blue lasers bring features such as high energy photons and smaller diffraction limited beams, while the yellow-orange range is a hard to reach spectral region where there is a considerable shortage of efficient laser light sources. Applications of the blue lasers are found in high density storage technologies, laser displays, LIDAR systems, optical tweezers and a long range of high precision demanding applications. The yellow-orange lasers also have important applications, with highlights in ophthalmologic laser surgery (photocoagulation), in “true” color displays and as a guide star (exciting sodium lines in the atmosphere).

The investigation of Nd:YLF quasi-three level lasers and Nd:YLF Raman lasers was further studied in this work in order to provide high power and efficient blue and yellow lasers sources. Demonstrations of efficient and multi-Watt operation of a 908 nm laser and its respective second harmonic laser at 454 nm are described. Also, Nd:YLF/BaWO₄ and Nd:YLF/KGW Raman lasers were demonstrated reaching Watt levels in quasi-CW and CW regime with very good beam qualities ($M^2 \leq 2$) at eight different wavelengths: 1147 nm, 1163 nm, 1167 nm, 549 nm, 552 nm, 573 nm, 581 nm and 583 nm. Finally, a blue luminescence originating in some Raman crystals, during Stokes oscillation, has been studied in considerable detail. Its origin and consequences for laser operation (extra loss and heat load) have been identified.

Lasers de Nd:YLF de baixo ganho operando na transição de quase-três níveis e em lasers Raman

Jonas Jakutis Neto

Resumo

Lasers operando nas regiões espectrais do azul e do amarelo-laranja foram recentemente requisitados pelo mercado de aplicações quer para melhorar as tecnologias já conhecidas ou para possibilitar a criação de novas. Isso é devido às propriedades destas regiões espectrais, com o azul trazendo características tais como fótons de alta energia e feixes limitados por difração menores, enquanto a faixa do amarelo-laranja é ainda uma região espectral difícil de se atingir e não foi totalmente acessada ou nem mesmo acessada por fontes de luz laser eficientes. Aplicações dos lasers azuis são encontradas em tecnologias de alta densidade de armazenamento, displays a laser, sistemas LIDAR, pinças ópticas e uma longa série de aplicações que exigem alta precisão. Os lasers amarelo-laranja também têm aplicações importantes, destacando-se aplicações em cirurgia oftalmológica a laser, em displays de cores “reais” e como estrela guia (excitando linhas de sódio na atmosfera).

A investigação de lasers de quase três níveis e laser Raman de Nd:YLF foi realizada neste trabalho. A finalidade é de propor fontes laser de alta potência e eficientes emitindo no azul e no amarelo para suprir as aplicações. Eficiência e potências de saída da ordem de Watt foram demonstradas para um laser de Nd:YLF emitindo em 908 nm assim como no segundo harmônico em 454 nm. Além disso, lasers Raman de Nd:YLF/BaWO₄ e Nd:YLF/KGW foram demonstrados atingindo alguns Watts de potência de saída em regime quasi-CW e CW, com boas qualidades de feixe ($M^2 \leq 2$) e em oito comprimentos de onda diferentes: 1147 nm, 1163 nm, 1167 nm, 549 nm, 552 nm, 573 nm, 581 nm e em 583. Por fim, uma luminescência azul originada em alguns cristais Raman, durante a oscilação Stokes, teve sua origem e seus efeitos colaterais para lasers (perdas e calor adicionais) minuciosamente caracterizados.

Table of Contents

Aknowledgements	1
Abstract	4
Resumo	5
List of Figures	9
List of Tables	13
List of Acronyms	14
1. Introduction	16
1.1. Solid State Lasers	16
1.1.1. Population inversion and optical pumping	19
1.1.2. Neodymium lasers	25
1.2. Nd:YLF	30
1.3. Harmonic generation	37
1.3.1. Considerations on harmonic generation	38
1.3.2. Importance of nonlinear crystal and laser beam parameters.....	42
1.4. Nd quasi-three level lasers	46
1.4.1. Physics	46
1.4.2. Literature review	53
1.5. Raman lasers	54
1.5.1. Physics	54
1.5.2. Literature review	63
1.6. Thesis outline	72
2. General methods	75
2.1. Laser crystals.....	75

2.2.	Raman crystals	76
2.3.	Doubling crystals	76
2.4.	Mirrors.....	77
2.5.	Pump sources and schemes	78
2.6.	Cooling systems	80
2.7.	Resonator design assisted by software	80
2.8.	Characterization methods and equipment	81
2.8.1.	Cary-5E Spectrophotometer	81
2.8.2.	Portable optical spectrometers	81
2.8.3.	Laser Ablation Inductively-Coupled-Plasma Mass-Spectrometry (LA-ICP-MS)	82
2.8.4.	Raman spectrometer	83
2.8.5.	Beamscope	84
2.8.6.	Power meters.....	85
2.8.7.	Photomultiplier tube	85
2.8.8.	Oscilloscope.....	86
2.8.9.	Integrating Sphere.....	87
3.	Nd:YLF quasi-three level laser	90
3.1.	Quasi-CW laser operation at 908 nm and at 454 nm	90
3.2.	CW laser operation at 908 nm and at 454 nm	99
3.3.	Discussion	102
4.	Nd:YLF Raman lasers	108
4.1.	Nd:YLF/BaWO ₄ Raman laser.....	108
4.2.	Nd:YLF/KGW Raman laser.....	113
4.3.	Discussion	119

5. Study of a blue luminescence in solid state Raman lasers.....	125
5.1. Introduction to the problem.....	125
5.2. Spectral characterization	126
5.3. Multi-variate analysis of the blue luminescence (collaboration)	131
5.4. Lifetime characterization	135
5.5. External cavity probing: Q-switch laser probe test	137
5.6. Trace element concentrations – ICP-MS (Inductively coupled plasma mass spectrometry)	139
5.7. Proposed excitation mechanism for blue fluorescence	140
5.8. Measurement of the blue power	141
5.9. Implications of blue emission for Raman laser efficiency	144
5.10. Implications of blue emission for thermal loading of Raman crystals	146
5.11. Chapter summary.....	149
6. Conclusion and Future works.....	152
6.1. Conclusions	152
6.2. Future works.....	155
Appendix A: MathCad worksheets	156
Appendix B: Spectral data of the coatings (mirrors)	165
Appendix C: ICP-MS full data	174
Appendix D: Publications	193
References.....	220

List of Figures

Figure 1. Laser technologies trends in 2009 [12].	18
Figure 2. Population in thermal equilibrium [6].	20
Figure 3. Population inversion condition [6].	21
Figure 4. (a) Longitudinal pump setup and (b) side pump setup.	23
Figure 5. Illustrative energy levels scheme, showing the pump transition.	24
Figure 6. Nd ³⁺ :YAG energy level scheme showing the pump and 1 μ m laser transitions.	25
Figure 7. Nd ³⁺ laser transitions.	26
Figure 8. (a) Absorption and (b) emission spectra of a Nd:YAG crystal [19].	27
Figure 9. Four-level laser energy scheme [6].	28
Figure 10. YLF crystal structure [24].	31
Figure 11. Frequency doubled Nd:YLF laser wavelengths.	33
Figure 12. Nd:YLF energy level scheme at 300 K with the main pump and emission transitions.	33
Figure 13. Nd:YLF polarized (a) absorption cross section and (b) emission cross section [19].	34
Figure 14. Thermal lens dioptric power as a function of incident power for a Nd:YLF crystal [26], for π (squares) and σ (circles) polarizations under lasing (open symbols) and non-lasing (filled symbols) conditions.	36
Figure 15. Phase matching function response.	41
Figure 16. SHG conversion efficiency for different Δn .	42
Figure 17. Refractive index distribution of an uniaxial KDP crystal for two different wavelengths λ_1 -solid black line and λ_2 – red dashed line.	43
Figure 18. Influence of the beam divergence on the SHG conversion.	45
Figure 19. Acceptance bandwidth of a nonlinear crystal.	46
Figure 20. Three level laser scheme.	46
Figure 21. (a) Nd:YAG quasi-four level laser scheme and (b) Nd:YLF quasi-three level laser scheme.	48
Figure 22. Quasi-three level laser scheme used in the modeling.	49
Figure 23. Small signal gain distribution in Nd:YLF, Nd:YAG and Nd:GdVO ₄ crystals for two pump powers (a) 5 W and (b) 15 W (simulations carried out by the author).	52
Figure 24. EM field scattering components.	55
Figure 25. Stokes lines generation.	56

Figure 26. Diatomic system vibration at (a) maximum compression, (b) at equilibrium and (c) at maximum stretch.....	58
Figure 27. (a) Fundamental and Stokes fields beat, and (b) molecular vibration in red at the same frequency of the beat.....	59
Figure 28. (a) Raman Generator and (b) external cavity Raman laser.....	62
Figure 29. Intracavity Raman laser.....	63
Figure 30. (a) Self-Raman laser, (b) Self-Raman SHG laser with an intracavity mirror and (c) SHG Raman laser.....	63
Figure 31. Fiber coupled diode laser longitudinal pumping scheme.....	79
Figure 32. LA-ICP-MS operation scheme [108, 109].....	82
Figure 33. Position of the ablation spots in the crystal sample.....	83
Figure 34. Inside the RENISHAW-INVIA Raman spectrometer [110].....	84
Figure 35. Spectral response of the R446 PMT [111].....	86
Figure 36. Oscilloscope Tektronix TDS 3054 [112].....	86
Figure 37. (a) Integrating sphere and (b) the Spectrafect coating reflectance [7, 8].....	87
Figure 38. Integrating sphere scheme showing the diffuse reflection.....	88
Figure 39. Nd:YLF crystal support.....	91
Figure 40. (a) Absorption spectrum of the Nd:YLF and (b) the overlap of its absorption with the diode emission.....	92
Figure 41. 0.9 μm laser setup.....	93
Figure 42. Cavity with an intracavity Brewster window and a fine angle adjust panel at the back.....	93
Figure 43. Quartz reflectivity as a function of the incidence angle. In red, the actual range of angles tested in the experiment.....	94
Figure 44. Beams reflected by the Brewster window.....	95
Figure 45. Setup used for the 454 nm laser.....	95
Figure 46. 1053 nm output power as a function of absorbed pump power.....	96
Figure 47. High Q cavity 908 nm output power as a function of absorbed peak power.....	97
Figure 48. Output power as a function of reflectivity (transmission of the window).....	97
Figure 49. Output power as a function of absorbed power, for a coupling of 2.5%.....	98
Figure 50. Power scaling of the quasi-CW blue lasers (a) using LBO and (b) using BiBO.....	98
Figure 51. Nd:YLF 0.7 at% Nd^{3+} doped crystal absorption spectrum.....	100
Figure 52. Input-output power curve of the Nd:YLF 908 nm CW laser.....	101
Figure 53. Performance of the Nd:YLF/BiBO (15 mm) 454 nm CW laser.....	101

Figure 54. Simulation of (a) small signal gain and (b) pump intensity as a function of crystal length [17].	104
Figure 55. Simulation of the (a) small signal gain and (b) pump intensity distribution at threshold pump power for the laser demonstrated in this work.	105
Figure 56. Nd:YLF/BaWO ₄ Raman laser setup.	109
Figure 57. Nd:YLF/BaWO ₄ /LBO yellow laser setup.	110
Figure 58. Fundamental laser performance.	111
Figure 59. (a) CW 1167 nm output power as function of absorbed pump power and (b) M ² measurement of the 1 st Stokes laser beam with the beam profiles images in the near field, focus and far field.	111
Figure 60. 583 nm CW laser performance.	112
Figure 61. KGW rotating stage with water cooling.	114
Figure 62. Nd:YLF/KGW 1 st Stokes laser setup.	115
Figure 63. Nd:YLF/KGW/LBO yellow and lime-green laser setup.	116
Figure 64. Raman spectra at the two orientations used in the Nd:YLF/KGW laser.	116
Figure 65. Output power as a function of absorbed pump power for (a) 1163 nm, (b) 581 nm and (c) 552 nm.	118
Figure 66. Output power as a function of absorbed pump power for (a) 1147 nm, (b) 573 nm and (c) 549 nm.	119
Figure 67. Wavelengths generated by the combination of Nd:YLF and KGW.	120
Figure 68. (a) Picture of the blue emission in a KGW crystal and the setup used in the spectral measurements (b) for self-Raman configuration and (c) separated laser and Raman crystals.	127
Figure 69. Blue emission spectra of KGW, Nd:GdVO ₄ , Nd:YVO ₄ and BaWO ₄ crystals.	127
Figure 70. Blue and red emission at 650 nm from a Nd:GdVO ₄ .	128
Figure 71. Comparison between blue emission in a Nd:YVO ₄ self-Raman and (a) Tm:YVO ₄ blue emission and (b) between KGW Raman laser and Tm:KGW [132].	129
Figure 72. Blue fluorescence found in Nd:YLF and Nd:YAG under Raman lasers operation compared to (a) Tm:Yb:Nd:YLF [134] and (b) Tm:YAG [135] found in the literature.	130
Figure 73. Possible path for energy transfer between Tm and Nd ions.	131
Figure 74. Emission spectra of the Nd:GdVO ₄ Raman laser for different diode pump currents.	132
Figure 75. PCR plots for all spectral data. (a) Scores, (b) Loadings.	133
Figure 76. PCR plots of low current data. (a) Scores, (b) Loadings.	134
Figure 77. PCR plots of high current data. (a) Scores, (b) Loadings.	134

Figure 78. Fluorescence lifetime decays for Nd:GdVO ₄ , YVO ₄ , KGW and BaWO ₄ crystals.....	136
Figure 79. Tm:YVO ₄ energy level scheme and the possible paths to populate the blue emitting level.....	137
Figure 80. Setup used for the Q-switch Raman laser probe tests.....	138
Figure 81. Blue upconversion steps.	141
Figure 82. Nd:YLF/KGW laser performance.	142
Figure 83. Laser cavity with the integrating sphere used to measure the blue emission power.	143
Figure 84. Another perspective of the sphere showing the detector field of view.....	143

List of Tables

Table 1. Most relevant physical and optical properties of the Nd-doped YAG, YVO ₄ , GdVO ₄ and YLF crystal hosts [20, 21, 22, 6, 23, 19].	27
Table 2. Parameters used for the simulation shown in Figure 16.	41
Table 3. Summary of the main Raman crystals and their properties.	66
Table 4. Parameters of the multi-wavelength laser [89].	69
Table 5. First-Stokes emissions generated from the fundamental Nd:YLF emissions at 1047 and 1053 nm for four of the most used Raman crystals.	71
Table 6. LBO and BiBO type-I non-linear parameters for 908 nm at 300 K [107].	76
Table 7. LBO type-I non-critical phase matching parameters for all the Raman conversions found in this work [107].	77
Table 8. Summary of the quasi-three level Nd:YLF lasers operating in quasi-CW regime (best results highlighted).	99
Table 9. Summary of the CW results and the quasi-CW obtained for the Nd:YLF quasi-three level laser.	102
Table 10. Summary of the results obtained in the literature and the ones obtained in this work.	103
Table 11. 1 st Stokes, SHG and SFG wavelengths generated by Nd:YLF/KGW system.	114
Table 12. Summary of the Nd:YLF Raman lasers demonstrated in this work.	121
Table 13. Lifetimes obtained in this work and the ones for the corresponding Tm ³⁺ doped hosts.	136
Table 14. ICP-MS Tm ³⁺ concentration measurements.	139
Table 15. Passive losses for the Nd:YLF/KGW resonator.	148

List of Acronyms

SHG – Second harmonic generation

SFG – Sum frequency generation

SRS – Stimulated Raman scattering

HR – High reflectivity

AR – Anti-reflection

ROC – Radius of curvature

CW – Continuous wave

QCW – Quasi-continuous wave

IR – Infrared

DPSSL – Diode pumped solid state laser

LBO – Lithium triborate

BiBO – Bismuth triborate

TEC – Thermoelectric cooler

VECSEL – Vertical external cavity surface emitting laser

PMT – Photomultiplier tube

LA-ICP-MS – Laser Ablation Inductively-Coupled-Plasma Mass-Spectrometry

O.C. – Output coupler

EM – Electromagnetic

ETU – Energy transfer upconversion

N.A. – Numerical aperture

PCA – Principal component analysis

Chapter 1

Introduction

1.1. Solid State Lasers

- 1.1.1. Population inversion and optical pumping
- 1.1.2. Neodymium lasers

1.2. Nd:YLF

1.3. Harmonic generation

- 1.3.1. Considerations on harmonic generation
- 1.3.2. Importance of nonlinear crystal and laser beam parameters

1.4. Nd quasi-three level lasers

- 1.4.1. Physics
- 1.4.2. Literature review

1.5. Raman lasers

- 1.5.1. Physics
- 1.5.2. Literature review

1.6. Thesis outline

1. Introduction

In this introduction chapter an extensive review of the technologies used, their physics and state of art of the lasers developed in this work is done.

First, the solid state lasers systems are introduced and their evolution and principles of operation are described. Then, the neodymium laser media are reviewed in terms of their important characteristics and outcomes, with a particular highlight on Nd:YLF lasers on which this thesis is centred.

Next, the theory of harmonic generation is presented since second harmonic and sum frequency generation are used in this work which enables operation of the lasers in the visible range.

As this thesis focuses on the use Nd:YLF in two low gain laser systems, Nd quasi-three level transition operation and Raman laser systems, these low gain technologies are going to be described and their main achievements reviewed.

Finally, an overview of the work carried out and the structure of the thesis are going to be described in the end of this chapter.

1.1. Solid State Lasers

Lasers can have any atomic system as their active medium. Of course some specific characteristics must be present in this medium to allow laser action. Given that, nowadays it is possible to find lasers made of gaseous active media (eg CO₂ and Argon lasers), liquid active media (eg Dye lasers) and solid active media (eg ruby and neodymium lasers).

The first laser built in 1960 [1] was a solid-state laser, and it used a ruby crystal (sapphire doped with trivalent chromium) as its active medium. This laser was optically pumped by a flashlamp, producing pulsed output at 694 nm. The parallel ends of the crystal were coated with silver, with a small hole at one end to couple out the stimulated radiation.

With the development of Q-switching techniques in 1961 [2], a well behaved laser with high peak output powers became an interesting tool for military applications. The energy could be stored in the laser medium and later released in short pulses, corresponding in time to a few round trips between the resonator mirrors, producing well behaved pulses instead of irregular spikes. The main application found at that time was the

use of the Q-switched ruby lasers as rangefinders, measuring the time of flight of the pulse reflected from a target.

For 10 years the ruby laser dominated the laser market, and was mostly commercialized as rangefinder and as research tool. Other types of applications, such as industrial ones, were still rare because of the properties and cost of the laser source. However, the discovery of the ruby laser triggered the development of other types of lasers, solid, liquid and gaseous.

After the ruby laser, the next solid state laser was built using a uranium-doped calcium fluoride, which lased in late 1960 [3]. Then, in 1961, the first neodymium laser was produced; it used a neodymium doped calcium tungstate crystal [4]. The Nd:YAG (yttrium aluminum garnet –YAG) laser was demonstrated in 1964 [5], and rapidly gained popularity. Nd lasers based on a variety of host crystals (YAG, YVO₄, YLF) have since displaced ruby, dye and gaseous lasers for many applications and remain prominent in the laser market today.

Not only crystals were used as solid state medium for lasers, but also glasses were employed. The first glass laser was demonstrated in 1961 [6], and introduced the possibility of producing active media much bigger in size and with better quality than ruby. Given their high optical gain, Nd:glass lasers were chosen to generate the most powerful lasers in the world (Omega Laser Facility) [7].

Optical fiber amplifiers were first demonstrated in 1963 [8], made of Nd-doped glass fibers. The problem of these amplifiers was the high losses they presented, and they did not attract attention at the time because of it. Only in the 80s, when low-loss fibers could be produced routinely, did these lasers start to attract attention. Nowadays they are well developed and can deliver high optical powers suitable for many industrial applications [9].

Despite their very early demonstration in 1962 [10], it was not until the 1980s that semiconductor lasers became widely available, delivering many benefits in terms of versatility and cost. They have almost all the characteristics desired in an ideal laser, except for the beam quality, which is much poorer than the diffraction limited beams delivered by the crystal and glass based solid state lasers. Semiconductor lasers are still in development, with rising technologies, eg VECSELs (Vertical external cavity surface emitting laser) [11]

that provide better beam qualities and others which expand their operation to the visible and mid-IR wavelength bands. The diode lasers are widely used today for many consumer devices, industrial applications and as solid state laser pump sources. In 2009, Laser Focus World published a market research regarding the trends of the laser technologies, and the diode lasers are responsible for the largest piece of the market, as shown in Figure 1 [12].

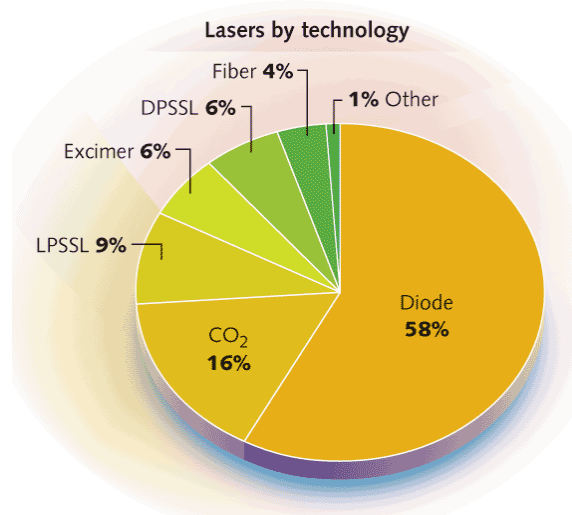


Figure 1. Laser technologies trends in 2009 [12].

In 2009 the diode laser technology held the largest piece of the market, with 58%, with the solid-state lasers (SSL) coming in second. Associating the three SSL technologies displayed, including lamp-pumped SSL (LPSSL), diode-pumped SSL (DPSSL) and fiber lasers, a piece of nearly 20% is occupied by them. This portion should increase, as the DPSSL technology should follow the evolution of the diode lasers and rise together, occupying a larger piece of market.

Finally it is worthwhile to list the main features of the solid state lasers, including their advantages compared to the other laser technologies. Solid state lasers are the most versatile radiation source, being able to deliver a large range of output parameters, including average and peak powers, wavelength and pulse repetition rate. The following topics show the most relevant points one should take in account when choosing solid state technology.

- Wide choice of materials;
- **Average output power:** continuous wave or pulsed operation from mW level up-to hundreds of Watts of output power;
- **Peak Power:** up to terawatts at femtosecond pulse widths can be delivered;
- **Pulse width:** as short as a few femtoseconds to continuous operation. Typically fs-ps for mode-locked operation and ns for Q-switched lasers;
- **Pulse repetition rate:** Q-switched solid state lasers can emit with repetition rates from below 1 Hz to the order of 100 kHz. The mode-locked ones can reach repetition rates between 50 MHz and a few GHz.
- **Linewidth:** from few GHz (rare earth doped crystals) to tens of THz (Ti:Sapphire – 128 THz);
- **Spectral range:** ultraviolet to mid infrared at discrete wavelengths;
- **Beam quality:** diffraction limited beams or multimode as requested;
- Flexibility on choosing the size and shape of the active medium;
- Amplification stages can be added easily;
- Compatible with nonlinear optical processes for frequency conversion.

In the following sub-sections the main physics concepts of solid state lasers are going to be exposed and discussed, and it should provide the necessary knowledge to the reader of this thesis to follow the original research developed in here.

1.1.1. Population inversion and optical pumping

Any atom in an atomic system has a probability to be in a specific energy state intrinsic to the atomic system it belongs to. If one considers a collection of atoms in thermal equilibrium at temperature T, then the relative populations of any two energy levels (E_1 and E_2) is given by the Boltzmann distribution, which can be expressed as follows,

$$\frac{N_2}{N_1} = e^{-\left(\frac{E_2-E_1}{kT}\right)} \quad (1)$$

where N_2 is the population of the upper energy level, N_1 the population of the lower energy level and k is the Boltzmann constant. In the case of thermal equilibrium and an energy separation corresponding to visible wavelength, the majority of the atoms are going to be in

the lower level, with very few atoms found in the higher-lying level. Figure 2 shows an example of such a distribution in thermal equilibrium.

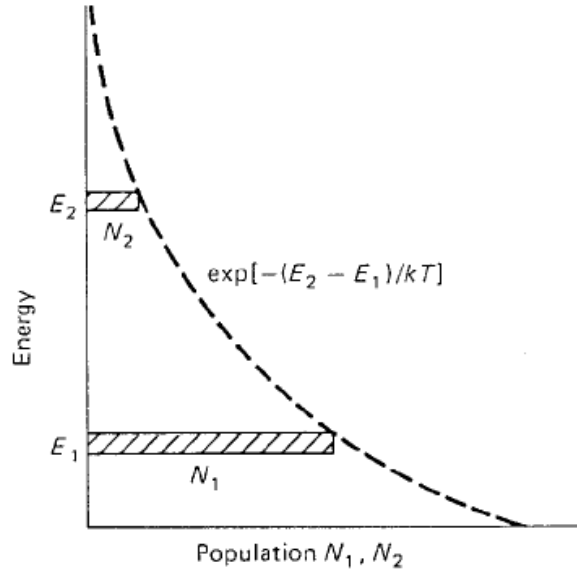


Figure 2. Population in thermal equilibrium [6].

Suppose that it is possible to have more atoms in the upper energy level than in the lower level, even if it is only temporary. This is referred to as a population inversion.

Given that, one can force this inversion to happen and have any photon with energy $E_2 - E_1$ passing through the atomic system stimulating the decay of the excited ions in a cascade process thus emitting photons, in a process called stimulated emission. Therefore, when inversion is achieved, it is possible to amplify a light signal that propagates through this medium. The two essential conditions for the inversion are $N_2 > N_1$ and $E_2 > E_1$. Figure 3 shows the population inversion compared to the thermal equilibrium distribution (dashed line).

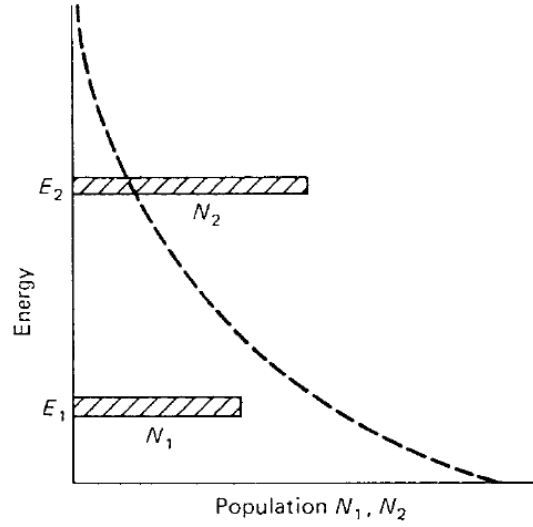


Figure 3. Population inversion condition [6].

It is possible to find three different population situations in an atomic medium. The first one is the thermal equilibrium, in which the lower energy level has more population than the higher energy level, characterizing an absorptive behavior for light passing through the medium. The second one takes place when the populations of the upper and lower levels are the same, causing the medium to be transparent to the light passing through it. The third is the population inversion, which amplifies the light passing through the medium. For a laser, the inversion is a required condition to achieve laser action.

In order to produce an inversion, a source of energy providing an amount of energy of $E_2 - E_1$ to the ions is required to populate the upper level. One last important point is that the pump rate has to overcome the stimulated and spontaneous emission rates, which are always leading the atoms to thermal equilibrium.

The process of raising an atom from any lower energy level to any higher energy level is called pumping. It can be done providing the right amount of energy to the atomic system, which would happen through electrical, thermal or optical excitation in most of the cases.

Only optical pumping will be discussed here as it is the most-widely used nowadays, and is the one used in this work. Even the semiconductors which are normally electrically pumped are starting to be optically pumped, such as the VECSELs [11]. There

are two main types of optical pump sources: incoherent ones (eg lamps) and the coherent ones (eg lasers).

Traditionally lamps were used because they were the only optical source available. They are simple, relatively cheap and can deliver high powers. They are generally used to excite solid state or liquid materials, since these two active media have absorption line broadening and a band structure of several absorption bands within the emission spectrum of the lamp. However, the overlap between the wide emission band of a typical lamp pump and the absorption bands is far from complete and constitutes a waste of power. Because of that, lamp pumped lasers have an optical to optical conversion efficiency of about only 3%. Usually lamp pumped lasers are built with elliptical cavities to increase energy transfer from the lamp to the laser medium [6].

The development of semiconductor diode lasers led to widespread use of coherent pumping. It can enable optical to optical conversion efficiencies near to the quantum limit. This is due to the diode laser light properties, such as the monochromaticity, in which a very narrow band is emitted from the laser source, matching very well with the absorption lines of the material. In particular rare earth doped crystals are benefitted by the narrow band pump, since the line broadening effects are reduced due to the organized, crystalline host and the fact that rare earths have the 5s and 5p outer shells shielding the 4f states where the pump and laser transitions happen [6]. Therefore, rare earth doped crystals present very narrow absorption bands, generally 1 to 2 nm broad.

Nowadays, diode lasers are the most common pump source for solid state lasers. They can deliver hundreds of Watts with high electrical to optical conversion efficiency (60-80%) and relatively low cost. To achieve high energy transfer efficiencies, the spatial and spectral properties of the diode laser needs to be carefully matched to the properties of the laser crystal. Generally, diode lasers can be tuned over a range of a few nanometers (~5 nm) by changing their temperature or operating current. Their emission linewidth is often around 2 to 3 nm wide and they are usually polarized. The challenge of the diode laser pump is the relatively poor beam quality which often demands the use of some type of beam shaping, which generally introduces strong output power losses. Nowadays, it is very common to find fiber-coupled diode lasers, which have a beam shaping system integrated to it in order to couple the diode laser beam to a fiber and thus, delivering circular profiled

beams with better beam quality. However, there are some pump schemes that may not need beam shaping, such as some side pumped lasers [13, 14].

Regarding the pump scheme geometries, one could divide them in two main types: longitudinal pumping and side pumping. Longitudinal pumping is characterized by the same direction of the pump beam and laser mode in the optical resonator, as shown in Figure 4(a). The side pumping configuration, generally brings an orthogonal geometry between pump and laser modes, as shown in Figure 4(b). Of course, many other types of geometry have also been used, and there are many variations to the simple approaches shown in Figure 4.

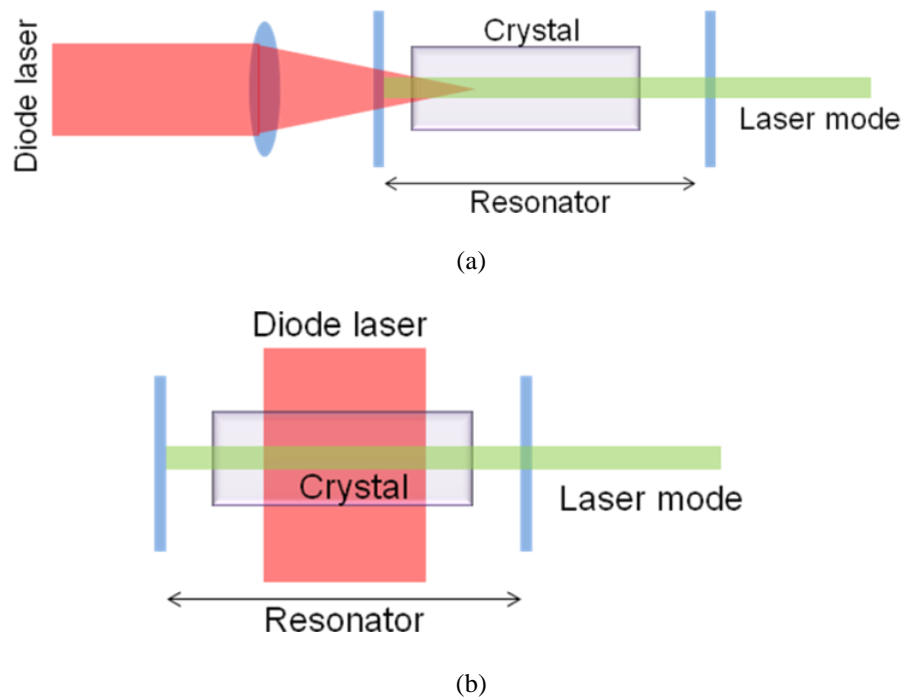


Figure 4. (a) Longitudinal pump setup and (b) side pump setup.

Figure 5 shows a simple energy system where the pump transition is represented by its rate as W_p .

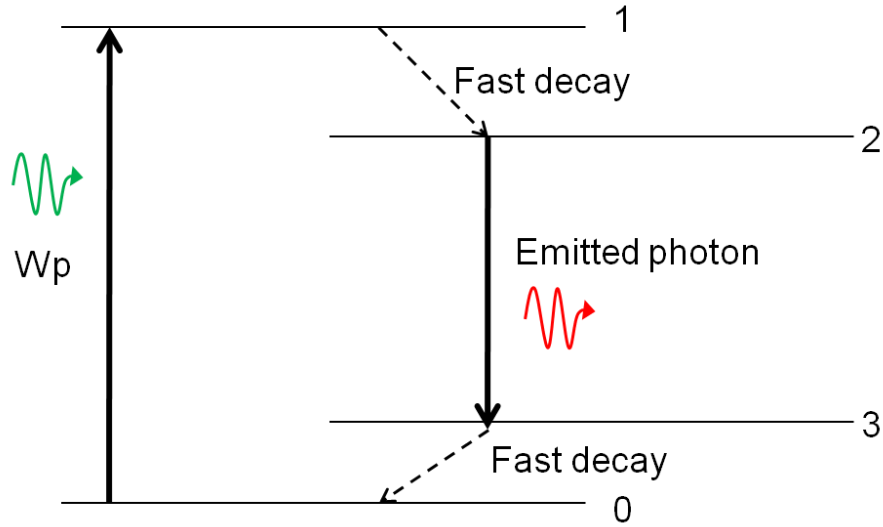


Figure 5. Illustrative energy levels scheme, showing the pump transition.

The energy difference between the level 0 and the level 1 is equal to the photon energy necessary to pump atoms from the state 0 to the state 1. The system shown in Figure 5 is called a “four level” laser system, and is characterized by the involvement of four energy levels in the whole laser process.

Usually, the final pump level (1) has to be above and as close as possible to the upper laser level (2), to avoid any other transition in between that can interfere in the laser performance. Given that, in most cases one will find energy level schemes similar to the one shown in Figure 5, where the atoms in level 1 decay to the upper laser level by non-radiative decay. This non-radiative decay, generally a multi-phonon decay, means that part of the energy deposited by the pump photons is wasted in the form of heat.

Considering the four level laser transition at 1064 nm of Nd^{3+} , shown in Figure 6, it is possible to see two different ways of pumping the laser.

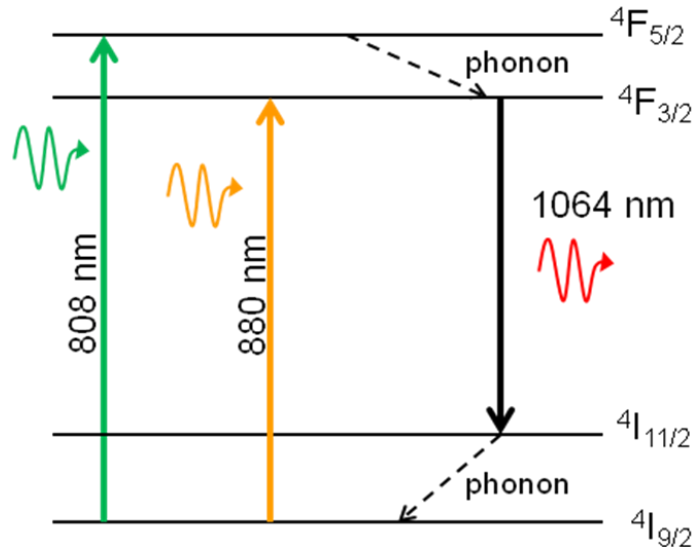


Figure 6. Nd³⁺:YAG energy level scheme showing the pump and 1 μ m laser transitions.

The first one is pumping the fundamental ions from the $4I_{9/2}$ level to the $4F_{5/2}$ level using 808 nm photons. In this case, there is a phonon transition from the $4F_{5/2}$ level to the $4F_{3/2}$ one, which is the upper laser level. After that, the ions will emit a 1 μ m photon to undergo the transition $4F_{3/2} \rightarrow 4I_{11/2}$, which happens by stimulated emission. Finally, the system relaxes again through a multiphonon decay to the ground state, and the cycle starts again. If one considers the energy difference between the pump photon energy and the laser photon energy, it is seen that there is about 24% energy loss on the way.

On the other hand, if the Nd³⁺ ions are pumped directly into the photon emitting level, $4F_{3/2}$, using an 880 nm photon source, the energy loss is reduced to 17%. Thus the efficiency of these lasers can be made higher. This efficient way to pump Nd lasers is called direct pumping, and has been reported in many Nd lasers recently [15, 16, 17], leading to significant improvement in the laser performance.

1.1.2. Neodymium lasers

Amongst the different lasers produced with rare earth ions, the neodymium ones were the first to be demonstrated and are the most popular solid state lasers in the market. The trivalent form of neodymium (Nd³⁺) was incorporated in several hosts, crystals and glasses, which have reached efficient laser action. There are many emitting lines possible in Nd

lasers, among them the strongest ones are, $\sim 0.9 \mu\text{m}$ ($^4F_{3/2} \rightarrow ^4I_{9/2}$), $\sim 1 \mu\text{m}$ ($^4F_{3/2} \rightarrow ^4I_{11/2}$) and $\sim 1.3 \mu\text{m}$ ($^4F_{3/2} \rightarrow ^4I_{13/2}$), as seen in Figure 7.

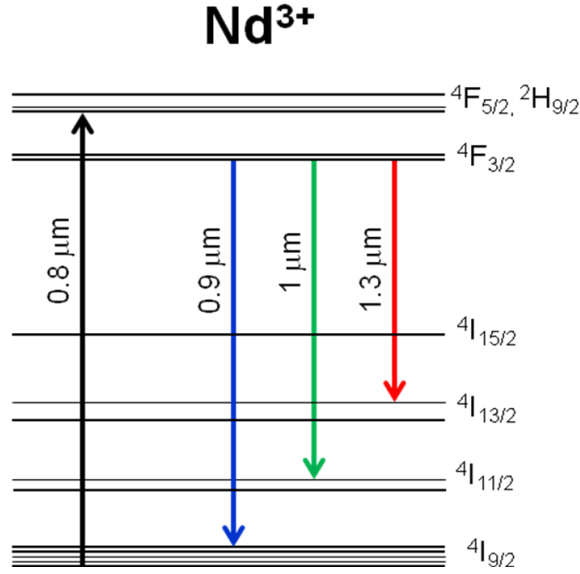


Figure 7. Nd^{3+} laser transitions.

As an example the transition probabilities (based on the branching ratios) of the $^4F_{3/2}$ level in a Nd:YAG crystal are: $\sim 60\%$ for the $1 \mu\text{m}$ transition; $\sim 25\%$ for the $0.9 \mu\text{m}$ transition and $\sim 15\%$ for the $1.3 \mu\text{m}$ transition [18]. Of course these probabilities change a little from host to host. Therefore, one should expect to detect a more intense emission at $1 \mu\text{m}$ when looking at the infrared fluorescence spectrum of a material doped with Nd.

The energy difference between $^4I_{11/2}$ lower level and the ground state is approximately 2000 cm^{-1} which is an order of magnitude higher than the value of kT at room temperature, and therefore the $1 \mu\text{m}$ laser is designated a four level laser. Figure 8 shows the absorption and emission spectra for a Nd:YAG crystal, as an example.

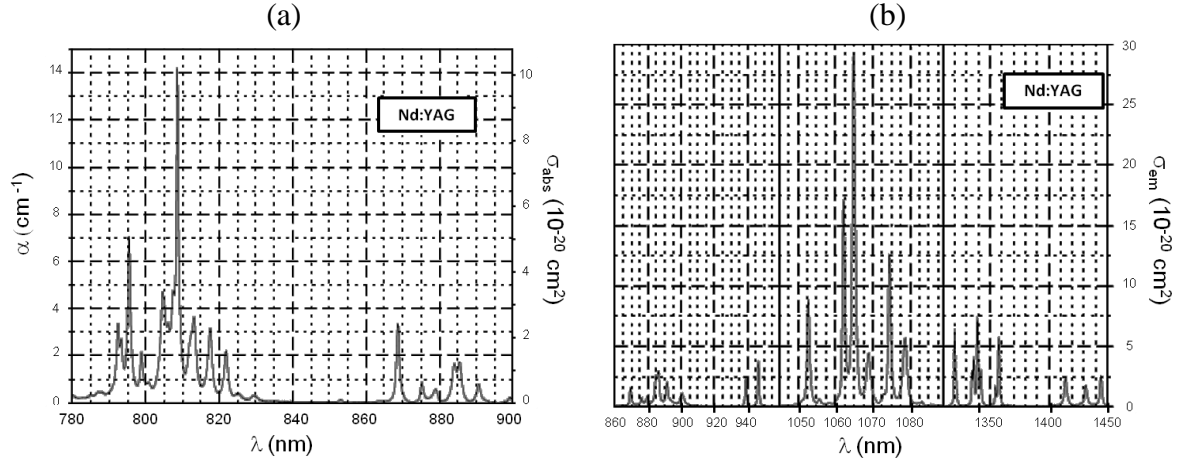


Figure 8. (a) Absorption and (b) emission spectra of a Nd:YAG crystal [19].

By means of nonlinear optics, the infrared emission of the three main transitions can be frequency doubled, thus providing lasers operating in the visible spectral range at red (1.3 μm to 0.65 μm), green (1 μm to 0.5 μm) and blue (0.9 μm to 0.45 μm) wavelengths.

There are several hosts that are able to be doped with neodymium ions and achieve laser action. However, four of them attracted more attention because of their properties and laser performance: Nd:YAG, Nd:YVO₄, Nd:GdVO₄ and Nd:YLF. Table 1Table 1. Most relevant physical and optical properties of the Nd-doped YAG, YVO₄, GdVO₄ and YLF crystal hosts [20, 21, 22, 6, 23, 19]. shows their main physical and optical properties important for their use as a laser active medium.

Table 1. Most relevant physical and optical properties of the Nd-doped YAG, YVO₄, GdVO₄ and YLF crystal hosts [20, 21, 22, 6, 23, 19].

	Nd:YAG	Nd:YVO ₄	Nd:GdVO ₄	Nd:YLF
$^4\text{F}_{3/2} \rightarrow ^4\text{I}_{9/2}$	946 nm	914 nm	912 nm	903 nm (π)
				908 nm (σ)
$^4\text{F}_{3/2} \rightarrow ^4\text{I}_{11/2}$	1064 nm	1064 nm	1063 nm	1047 nm (π)
				1053 nm (σ)
$^4\text{F}_{3/2} \rightarrow ^4\text{I}_{13/2}$	1319 nm	1342 nm	1341 nm	1321 nm (π)
				1314 (σ)
Stimulated emission cross section	2.8	14.1 (π)	2.08 (π)	1.8 (π)

$(\sigma_e) - 1 \mu\text{m transition } (10^{-19} \text{ cm}^2)$		2.95 (σ)	10.3 (σ)	1.3 (σ)
Stimulated emission cross section		0.45 (π)	0.62 (π)	0.12 (π)
$(\sigma_e) - 0.9 \mu\text{m transition } (10^{-19} \text{ cm}^2)$	0.35	0.42 (σ)	0.55 (σ)	0.13 (σ)
$^4F_{3/2}$ lifetime (μs)	230	90	96	500
Thermal conductivity ($\text{W.m}^{-1}.\text{K}^{-1}$)	14	12 (c-axis) 9 (a-axis)	10.4 (c-axis) 8.6 (a-axis)	5.8 (c-axis) 7.2 (a-axis)
Thermal expansion coefficient (10^{-6} K^{-1})	7.5	8.19 (c-axis) 1.69 (a-axis)	7.89 (c-axis) 1.14 (a-axis)	8.3 (c-axis) 13.3 (a-axis)
dn/dT (10^{-6} K^{-1})	7.3	7.9 (c-axis) - (a-axis)	10.1 (c-axis) 13.8 (a-axis)	-4.3 (c-axis) -2 (a-axis)

Looking at the table it is possible to notice that the spectroscopic parameters such as emission wavelengths, emission cross sections and lifetime, as well as the thermal parameters, thermal conductivity, thermal expansion coefficient and refractive index variations with temperature (dn/dT), varies depending on the host. Given that, each crystal has to be studied as a particular case, taking into account their specific advantages and disadvantages.

Next we consider the principles of operation for a Neodymium four-level laser. Figure 9, extracted from [6], shows a more detailed four level Nd laser system scheme with its possible transitions.

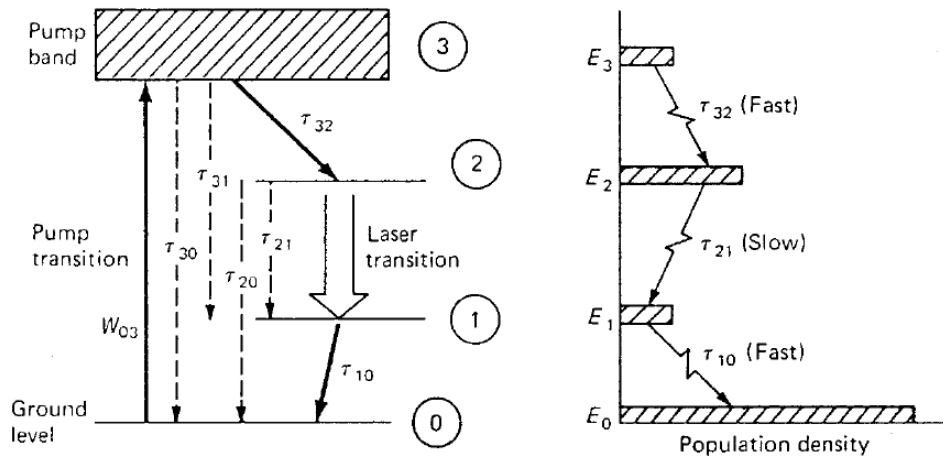


Figure 9. Four-level laser energy scheme [6].

It all starts with a pump transition from the ground state 0 (E_0) to level 3 (E_3). Following the pump transition comes a fast decay to level 2 (E_2), generally by means of a non-radiative decay. Level 2 is the upper laser level and has typically a relatively long lifetime (τ_{21}) in order to accumulate population for a stronger inversion. Thus, the laser transition ($2 \rightarrow 1$) takes place, populating level 1 (E_1), which decays rapidly to the ground state again.

Analyzing the whole process, an important characteristic of the system can be pointed out: level 1 is far from the ground state 0 causing almost all the population to be in the ground state during thermal equilibrium (Boltzmann distribution) as long as the energy gap between level 0 and 1 is large enough to keep the population in level 1 equal to zero. Therefore, inversion will occur with any small number of atoms pumped to level 2. In addition to that, it is important that the relaxation time τ_{10} is much faster than the laser transition lifetime τ_{21} ($\tau_{10} \ll \tau_{21}$). From equation (1) it is possible to observe that if $\Delta E \gg kT$, consequently $N_1/N_0 \ll 1$ and N_1 will be probably empty. In some cases the distance between these two levels is small, thus demanding some kind of cooling of the medium in order to reduce the kT term. In most cases, the calculations based on the population distribution do not take in account levels 3 and 1, since their decays are fast enough to not keep a relevant population stored.

Many lasers can be classified as four-level, including the well-known Nd^{3+} transitions at 1.0 μm and 1.3 μm . The 0.9 μm transition in Nd:YAG can be considered a quasi-four-level transition with very similar characteristics to the four-level system. However, in the majority of other hosts it tends towards a three-level system, being known as quasi-three level laser transition, which will be discussed in a later section of this chapter.

As for the phonon transitions bridging the non-radiative transitions, it is possible to notice that they account for 3% to 25% (depending on the laser transition and on the pump wavelength) of the incident energy converted in Nd lasers (quantum defect). This energy is dissipated in the form of heat, which can be detrimental to laser performance.

The heat load accumulated in the crystals is responsible for the occurrence of cracks, thermal lensing effects, changes to the population distribution and for the vibrations. Thermal lensing is of particular importance to the lasers in this thesis. It is the

result of a combination of mechanical changes due to thermal expansion/compression of the crystal (example end face bulging) and refractive index variation with temperature (dn/dT). Optical resonators can become unstable due to the sudden creation of a lens like element inside it. Further, the lens curvature keeps changing with increase of temperature, which increases with the pump power and also changes depending on the pump beam profile. It would require some kind of dynamic cavity system, which must change its stability conditions according to the pump power applied, enabling the laser to operate in a wide range of pump powers. Another consequence of the thermal lens is the deterioration of the laser beam quality, as the lens may enable higher order modes to resonate stably or cause non-spherical wavefronts due to its irregular geometry.

Because of that, it is important to include a cooling system to dissipate the heat generated in the Neodymium doped crystals, whose worst case scenario is found for the four-level laser systems $\sim 25\%$. Crystal properties such as thermal conductivity, thermal expansion and dn/dT become very relevant to the maintenance of good laser performances and to prevent damages like cracks in the crystals during laser operation. Table 1 brings these three main properties for the most commonly used Neodymium-doped crystals.

There are other sources of heat which can be relevant in some specific cases, such as the relatively strong upconversion encountered in Nd:YLF lasers, which will be further discussed in the next section.

1.2. Nd:YLF

Nd:LiYF₄ (Nd:YLF) is one of the most widely studied laser crystals in the literature, together with Nd:YAG and Nd:YVO₄. It is a crystal that brings some interesting attributes to solid state lasers, such as weak thermal lensing and different laser wavelengths.

The LiYF₄ crystal is a scheelite type crystal, which belongs to the tetragonal spatial group and can have the yttrium ions replaced by other rare earth ions. Figure 10 shows the crystal structure of a YLF crystal [24].

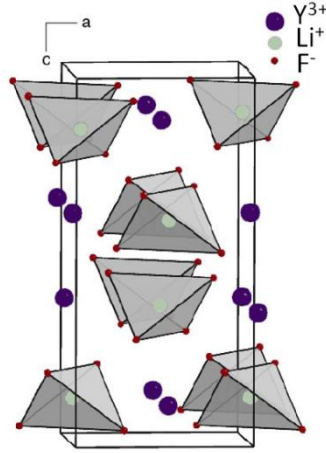


Figure 10. YLF crystal structure [24].

An interesting property of YLF is related to the thermal lensing effect. Looking at the thermal properties of YLF in Table 1, such as the thermal expansion coefficient and the dn/dT (refractive index change as a function of temperature), one can see that the first one is positive and the second one negative. The negative variation of the refractive index creates a diverging lens inside the crystal, while the positive thermal expansion creates a converging lens by means of the crystal end face bulging. Consequently, there is a compensation of lenses resulting in a weak overall lens. Of course the resultant thermal lens depends on the pump geometry and beam profile. Generally the worst case scenario is found in the longitudinally pumped lasers, where the pump beam can be focused to very tight beam waists, thus creating a strong temperature gradient and consequently very strong thermal lensing.

Based on the fact that YLF crystal introduces only a weak thermal lens, the optical resonators built with it should operate more stably even under high pump power, maintaining a good beam quality. However, YLF has a poor thermal conductivity which limits the pump power scalability and exhibits a lower fracture limit than other laser crystals (YAG, YVO₄ and GdVO₄).

The other two interesting characteristics the YLF crystal introduces, are related to its Nd doped form. A Nd:YLF crystal has a radiative lifetime of the $^4F_{3/2}$ upper laser level of 500 μs , which is quite long compared to the 90 μs of the Nd:YVO₄ or even the 230 μs of the Nd:YAG. It brings to Nd:YLF a better energy storage capacity, as it can keep the

pumped ions for an average time of 500 μs before they start to decay. Q-switch lasers benefit from this longer energy storage, since a larger population inversion can be obtained and therefore a higher small signal gain, before the modulation is turned off. As a consequence, higher output peak powers should be obtained from Nd:YLF lasers. However, this is not always the situation, because in some cases a strong upconversion takes place and quenches the upper laser level before the 500 μs lifetime. This causes the shortening of the fluorescence lifetime, thus reducing the energy storage capacity [25, 26]. An approach to avoid upconversion is to use lower Nd^{3+} concentrations, since most of the upconversion is based on energy transfer processes.

YLF is a naturally birefringent crystal which overwhelms any thermally-induced birefringence, guarantying a polarized laser emission. The emission cross section of Nd:YLF is about two times lower than the one for Nd:YAG, although it is not a problem to concern much, since resonator designing can in many cases compensate it.

Finally, a different range of wavelengths can be obtained using Nd:YLF compared to other hosts. For the ${}^4\text{F}_{3/2} \rightarrow {}^4\text{I}_{11/2}$ transition, 1047 nm for π polarization and 1053 nm for the σ polarization are the lasing wavelengths, while for the Nd:YAG, Nd:YVO₄ and Nd:GdVO₄ crystals, the usual lasing wavelengths are at 1063 nm or 1064 nm. For the ${}^4\text{F}_{3/2} \rightarrow {}^4\text{I}_{13/2}$ transition, 1321 nm for π polarization and 1314 nm for the σ polarization are the lasing wavelengths. The transition of the ${}^4\text{F}_{3/2}$ level to the ground state delivers laser emissions at 903 nm for π polarization and 908 nm for the σ polarization.

By simply doubling the frequency of the fundamental wavelengths provided by the Nd:YLF crystal, it is possible to obtain the following range of visible emissions, Figure 11.

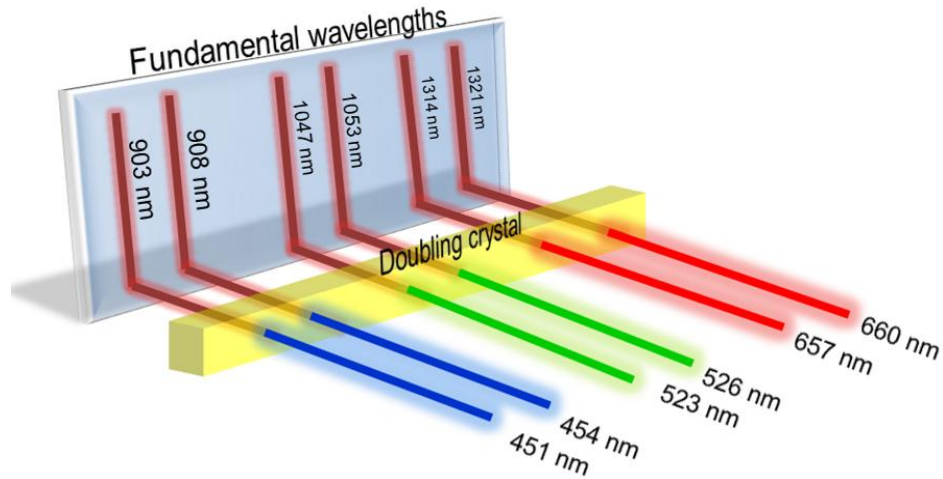


Figure 11. Frequency doubled Nd:YLF laser wavelengths.

Figure 12 shows the energy level scheme of a Nd:YLF crystal at 300 K with its main pump and laser transitions.

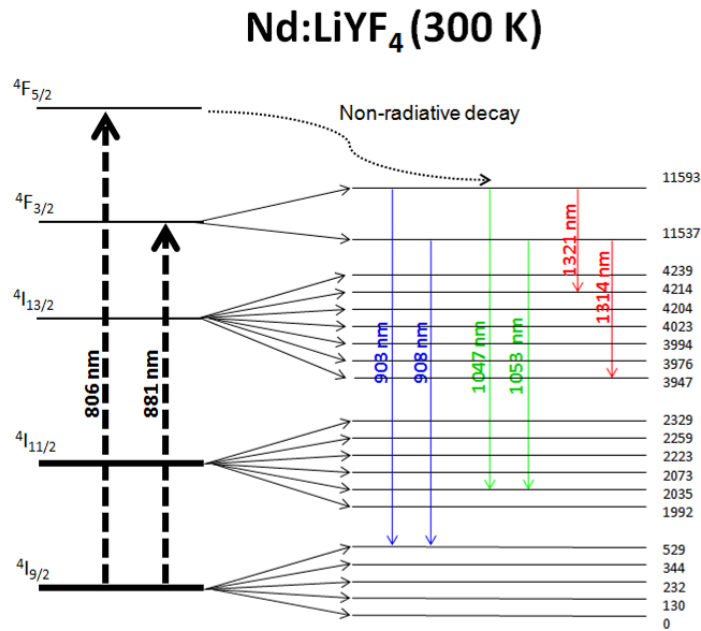


Figure 12. Nd:YLF energy level scheme at 300 K with the main pump and emission transitions.

Nd:YLF is normally pumped to the $^4F_{5/2}$ band, at 792 nm, 797 nm or 806 nm, because of availability of cheap, high-power pump diodes. It can also be pumped directly to the upper laser level $^4F_{3/2}$ reducing the heat load as discussed before, mainly at 869 nm (higher absorption cross section) or 881 nm (more common due to availability of high

power diode lasers). Figure 13(a) shows the absorption cross section spectra (π and σ) and (b) the polarized emission cross section for the Nd:YLF.

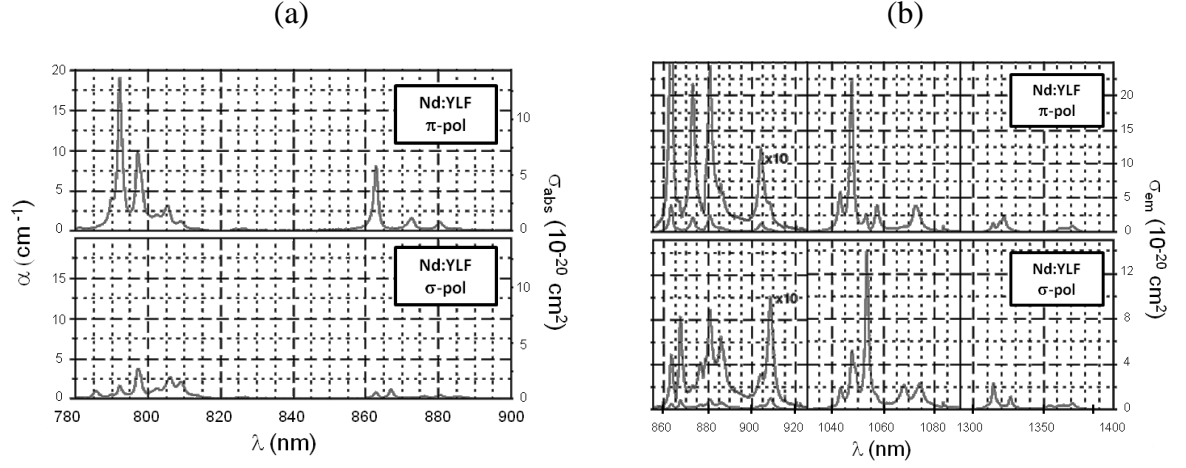


Figure 13. Nd:YLF polarized (a) absorption cross section and (b) emission cross section [19].

Several publications have reported diverse laser cavity setups using Nd:YLF reaching relatively high powers, high efficiency and with very good beam quality. A side-pumped Nd:YLF laser delivering 16.7 W of output peak power at 1053 nm in quasi-CW regime, corresponding to an slope efficiency of 61% has been reported in [27]. The transverse mode of this laser was characterized as a TEM₀₀ mode. In end-pump configurations, output powers as high as 60 W at 1047 nm were reported for CW operation by Bollig *et al.*[28], with corresponding slope efficiency of 52% with respect to the absorbed pump power. The beam quality is not reported but is believed to be very close to TEM₀₀ by visual inspection of the beam profile. Another interesting work was reported in 2005 by Peng *et al* [29], in which an output power of 28 W (CW) at 1053 nm was achieved, using a dual-pump configuration with 60 W total power. The work presents a detailed treatment of upconversion and thermal lens influencing laser efficiency, as a result a 0.4% Nd-doped, 30 mm long crystal was used and a pump beam diameter of about 2.5 mm. Also, in the same work a Q-switched version was described, which delivered more than 52 W of average power for repetition rates from 5 to 30 kHz. The maximum pulse energy demonstrated for this laser was 10 mJ at 5 kHz. A work by Lu *et al.* [16] demonstrated the highest slope efficiency of a Nd:YLF laser reported so far, reaching

76.3%. This laser featured an upper laser level direct pumping scheme, as described earlier in this chapter, pumping the crystal at 880 nm using a 2 W Ti:Sapphire laser, with the laser oscillating at 1047 nm.

For lasers operating on the quasi-three level transition ($^4F_{3/2} \rightarrow ^4I_{9/2}$), two recent reports deserve to be highlighted, Liang *et al.* [17], demonstrating 4.7 W of output power at 908 nm in CW regime, and Lu *et al.* [30], which demonstrated a blue laser at 454 nm with output powers as high as 4.33 W in CW regime. Both lasers used direct pumping schemes at 880 nm with the infrared laser emission reaching a slope efficiency of 43.3% and the visible converted emission achieving an optical conversion efficiency of 13.2% with respect to the incident power. Our group has also achieved good results in the quasi-CW regime at 908 nm and at 454 nm, which are fully described in this thesis and in [31].

The 1.3 μm transition and its second harmonic conversion into the red range have also been demonstrated [32, 33, 34, 35, 36]. Of particular importance are works by Louyer *et al.* [32], Lu *et al.* [35] and Zondy *et al.* [36]. The first author has demonstrated 3.6 W at 1312 nm and 4.8 W at 1322.6 nm in CW operation for a maximum pump power of 16 W. The second author reports a directly pumped Nd:YLF laser operating at 1321 nm resulting in 3.6 W of CW output power for an absorbed pump power of 7.3 W, corresponding to a slope efficiency of 52%. The last author demonstrated an output power of 1.4 W in the red region which is the maximum CW power demonstrated for a red Nd:YLF laser so far [36].

Other relevant works in the field are related to the properties of Nd:YLF which interfere with laser performance, such as thermal lensing [26], thermal fracture limits [22] and upconversion effects responsible for extra heat [26] and upper laser level lifetime quenching [25]. It is well known that Nd:YLF has lower thermal fracture limit than other commonly used laser crystals, and this is due to its small tensile strength [22], which limits the average pump power that the crystal can manage before it cracks.

Regarding to upconversion, Nd:YLF also suffers more than other crystals, eg in comparison with YAG [23], since it presents a longer lifetime of the upper laser level ($\sim 500 \mu\text{s}$), therefore storing more excited ions which can then interact with a neighboring ion (energy transfer upconversion – ETU) or absorb another photon (excited state absorption – ESA) within a lifetime period. In [26], ETU was considered the predominant upconversion process, and a profound experimental and theoretical analyses was made,

demonstrating the influence of the extra heat on the strength of the thermal lens. Figure 14, reproduced from [26], plots the dioptric power (inverse of the effective focal length) of the thermal lens as a function of incident pump power (up to 12 W) in four different conditions; σ -polarization (circles) and π -polarization (squares) under lasing (open symbols) and non-lasing conditions (filled symbols).

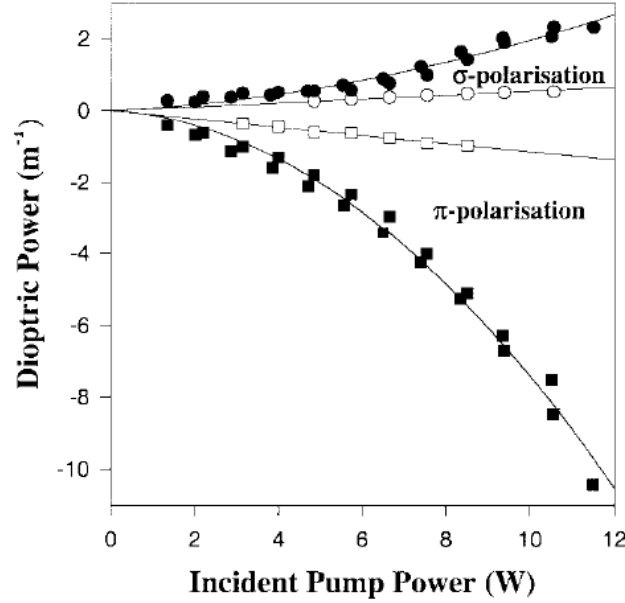


Figure 14. Thermal lens dioptric power as a function of incident power for a Nd:YLF crystal [26], for π (squares) and σ (circles) polarizations under lasing (open symbols) and non-lasing (filled symbols) conditions.

As we can see, the dioptric power increases faster (focal length decreases) for higher pump powers under non-lasing conditions for both σ and π polarizations, with the difference that σ -polarized light experiences a converging lens, while π -polarised light experiences a diverging lens. Under lasing conditions however, these lenses get much weaker, once the laser transition predominates over the upconversion in the competition to quench the upper laser level population, thus drastically reducing the extra heat and therefore the thermal lens caused by the upconversion.

The other consequence of the upconversion is the detrimental lifetime quenching of the upper laser level, which consequently degrades Q-switched laser performance. A good characterization of this effect is described in Pollnau *et al.* [25], which shows a shortening of lifetime from $\sim 500 \mu s$ to $\sim 150 \mu s$, with the increase of the pump intensity.

Up to this point the discussion was on how to achieve inversion, thus gain, in the active medium, particularly Neodymium doped crystals. Next section will introduce the concepts of the harmonic generation, responsible for the conversion of the infrared photons into visible photons.

1.3. Harmonic generation

When intense radiation interacts with matter, both linear and nonlinear responses are observed. These responses come from the light beam electric field perturbation induced in the atoms of a dielectric material. When a light wave propagates through the material, changes in the spatial and temporal distribution of electrical charges take place, which is due to the reaction of the electrons and atoms to the electromagnetic wave.

The strongest atomic system reaction is manifested as a displacement of the valence electrons from their usual orbits, thus originating electric dipoles. Macroscopically, these dipoles are expressed as a polarization. Considering low intensity fields, the effect produces a linear response while for strong fields, the response comes nonlinearly with the dipole amplitudes not reproducing the amplitude of the electromagnetic field which creates them. The linear interaction will radiate the same wave as the incoming wave in terms of phase, polarization and frequency, while the nonlinear interaction generates a wave with higher order frequency components, phenomenon known as frequency conversion.

Frequency conversion is extensively used to add versatility to high power infrared lasers, extending their output wavelengths to the visible range. Nonlinear optics includes elastic interaction (energy conserving process), such as harmonic generation, and inelastic interaction (energy exchanging processes), like stimulated Raman or Brillouin scattering.

In this thesis three nonlinear effects are employed: stimulated Raman scattering (SRS), second harmonic generation (SHG) and sum frequency generation (SFG). SRS is used in all the Raman lasers described in this work shifting the fundamental wavelengths to longer wavelengths and the SHG and SFG are used to convert the infrared emissions to the visible range.

1.3.1. Considerations on harmonic generation

First, we should physically describe the effect of an electric field propagating through a dielectric medium. This field creates electrical dipoles in the material which are represented by an induced polarization (\mathbf{P}). As introduced before, this polarization has two components, one linear (\mathbf{P}_L) and another nonlinear (\mathbf{P}_{NL}). The equation (2) shows the equation which describes the components of the polarization [37].

$$\mathbf{P}(t) = \mathbf{P}_L + \mathbf{P}_{NL} = \epsilon_0 \chi^{(1)} \mathbf{E}(t) + \epsilon_0 \chi^{(2)} \mathbf{E}^2(t) + \epsilon_0 \chi^{(3)} \mathbf{E}^3(t) + \dots \quad (2)$$

χ is the electrical susceptibility tensor of a material, where $\chi^{(1)}$ refers to the linear susceptibility and $\chi^{(2)}$ and $\chi^{(3)}$ refer to second and third order susceptibility. \mathbf{E} is the electric field and ϵ_0 is the electric permittivity of free space. Thus, there is only one component responsible for the linear polarization of a material. If one looks at the electric field in each of the polarization terms, it is seen that the first one responds linearly with \mathbf{E} , the second and the third respond nonlinearly with \mathbf{E}^2 and \mathbf{E}^3 , respectively. The magnitude of each susceptibility decreases with increasing order, starting with $\chi^{(1)}$, which is of the order of unit and $\chi^{(1)} \gg \chi^{(2)} \gg \chi^{(3)}$. For this reason the nonlinear interactions require high intensity fields as their susceptibilities are very small. This high intensity requirement caused the nonlinear effects to be identified only after the advent of the laser, which provided a high intensity light source. The second order susceptibility is responsible for the second harmonic generation (SHG), sum frequency generation (SFG) and others of the same nature. The third term is responsible for stimulated Raman scattering (SRS), Kerr effect and others.

The wave equation in a nonlinear optical media can be deduced from the Maxwell equations,

$$\nabla \times \nabla \times \mathbf{E} + \frac{1}{c^2} \frac{\partial^2 \mathbf{E}}{\partial t^2} = - \frac{1}{\epsilon_0 c^2} \frac{\partial^2 \mathbf{P}}{\partial t^2} \quad (3)$$

where c is the speed of light in vacuum, \mathbf{E} the electric field and \mathbf{P} the induced polarization. Given the relation $\nabla \times \nabla \times \mathbf{E} = \nabla(\nabla \cdot \mathbf{E}) - \nabla^2 \mathbf{E}$ and $\nabla \cdot \mathbf{E} = 0$, equation (3) can be written as [37]

$$-\nabla^2 \mathbf{E} + \frac{1}{c^2} \frac{\partial^2 \mathbf{E}}{\partial t^2} = -\frac{1}{\epsilon_0 c^2} \frac{\partial^2 \mathbf{P}}{\partial t^2} \quad (4)$$

In order to simplify, we consider that the wave oscillates only with a well defined frequency ω_n and propagates along the z axis only. Its electric field can now be described as

$$\mathbf{E}(z, t) = A(z) \cdot e^{i(kz - \omega t)} \quad (5)$$

where $A(z)$ is the amplitude of the electric field and k is the wave vector. Therefore, the second derivative of the electric field with z is given by,

$$\frac{\partial^2 \mathbf{E}(z, t)}{\partial z^2} = 2ik e^{i(kz - \omega t)} \frac{\partial A(z)}{\partial z} + e^{i(kz - \omega t)} \frac{\partial^2 A(z)}{\partial z^2} - k^2 A(z) e^{i(kz - \omega t)} \quad (6)$$

Using the slowly varying amplitude condition,

$$\frac{dA(z)}{dz} k \gg \frac{d^2 A(z)}{dz^2} \quad (7)$$

and the fact that the derivatives in x and y are zero, since we defined the propagation of the wave along z , the wave equation can be rewritten as

$$\left[-2ik \frac{dA(z)}{dz} + k^2 A(z) - \frac{1}{c^2} \omega^2 A(z) \right] e^{i(kz - \omega t)} = -\frac{1}{\epsilon_0 c^2} \frac{\partial^2 \mathbf{P}}{\partial t^2} \quad (8)$$

The wave vector is defined $k = \omega_n/c$, thus the second and third term in the bracket cancel each other. As a result the electric field amplitude variation is given by (9), showing the dependence of the electric field on the polarization created by the incident wave.

$$\frac{dA(z)}{dz} = \frac{1}{2ik\epsilon_0 c^2} \frac{\partial^2 \mathbf{P}}{\partial t^2} e^{i(kz - \omega t)} \quad (9)$$

Now going back to the definition of the second order polarization term given by [37], we have

$$\mathbf{P}(2\omega) = \epsilon_0 \chi^{(2)} \mathbf{E}(\omega)^2. \quad (10)$$

The tensor $\chi^{(2)}$ is also known as the tensor d, or d coefficient, given by: $d = \chi^{(2)}/2$. This tensor has 27 components although, many of them become null depending on the symmetry of the system. As a result, the summation of the non-zero elements gives the effective nonlinear coefficient (d_{eff}).

Taking the definition of the electric field (5) and introducing it into (10), we obtain

$$\mathbf{P}_{2\omega} = \epsilon_0 \chi^{(2)} A_\omega^2 e^{i(2k_\omega z - 2\omega t)} \quad (11)$$

Using this polarization in equation (9), it is possible to calculate the second harmonic power as follows [6]

$$P_{2\omega} = \frac{2P_\omega^2 \omega^2 d_{\text{eff}}^2 l^2}{\epsilon_0 c^3 n_\omega^2 n_{2\omega} A} \text{sinc}^2(\Delta k l / 2) \quad (12)$$

where ω is the incident wave frequency, l is the nonlinear crystal length, A is the beam cross-sectional area inside the medium, n_ω is the refractive index at the frequency ω , $n_{2\omega}$ the refractive index at the doubled frequency and P_ω is the incident power at the frequency ω . It is interesting to notice that the SHG power increases quadratically with the fundamental power, $P_{2\omega} \propto P_\omega^2$.

The phase mismatch is represented by $\Delta k = k_{2\omega} - 2k_\omega$ and it is the argument of the function sinc defined as

$$\text{sinc}(\Delta k l / 2) = \frac{2 \cdot \sin(\Delta k l / 2)}{\Delta k l} \quad (13)$$

Figure 15 shows the sinc function plotted as a function of the phase mismatch, in which is possible to observe that its maximum value occurs for zero mismatch. At this point Δk must be equal to 0, thus the refractive index at ω and at 2ω must be the same. For either higher or smaller refractive index differences, the conversion efficiency decreases rapidly.

$$k_{2\omega} - 2k_\omega = \frac{2\pi n_{2\omega}}{\lambda_{2\omega}} - 2 \cdot \frac{2\pi n_\omega}{\lambda_\omega} = \frac{4\pi}{\lambda_\omega} (n_{2\omega} - n_\omega) \Leftrightarrow n_{2\omega} - n_\omega = 0 \quad (14)$$

$$\text{with } \lambda_{2\omega} = \lambda_\omega / 2,$$

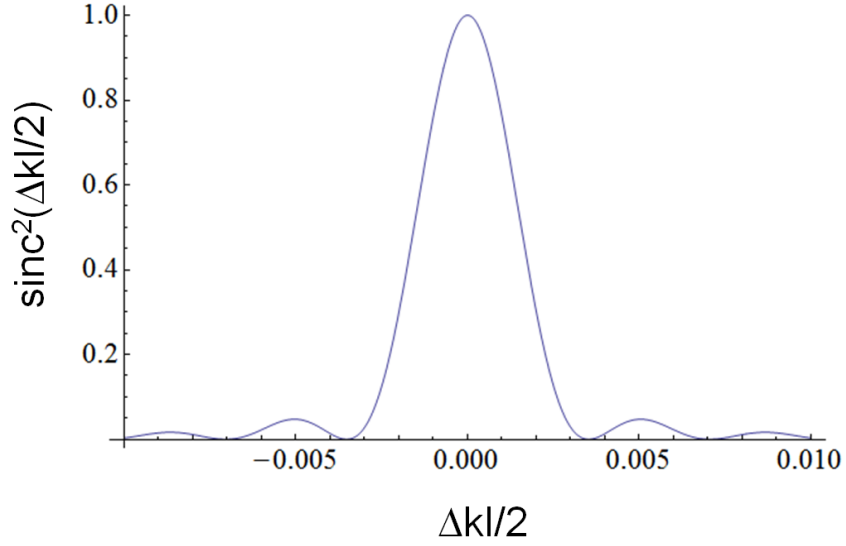


Figure 15. Phase matching function response.

To simulate the conversion efficiency of the second harmonic, as a function of Δk , I have used (12) and considered the ratio $P_{2\omega}/P_{\omega}$. I have then used the equation parameters shown in Table 2. These parameters correspond to the SHG of $\lambda=1064$ nm in a LBO crystal.

$$\frac{P_{2\omega}}{P_{\omega}} = \frac{2P_{\omega}\omega^2 d_{\text{eff}}^2 l^2}{\epsilon_0 c^3 n_{\omega}^2 n_{2\omega} A} \text{sinc}^2(\Delta k/2) \quad (15)$$

Table 2. Parameters used for the simulation shown in Figure 16.

SHG parameters	
ω ($\times 10^6$ GHz)	1.77
d_{eff} (pm/V)	0.83
Crystal length (mm)	5
Beam radius (μm)	200
P_{ω} (W)	200

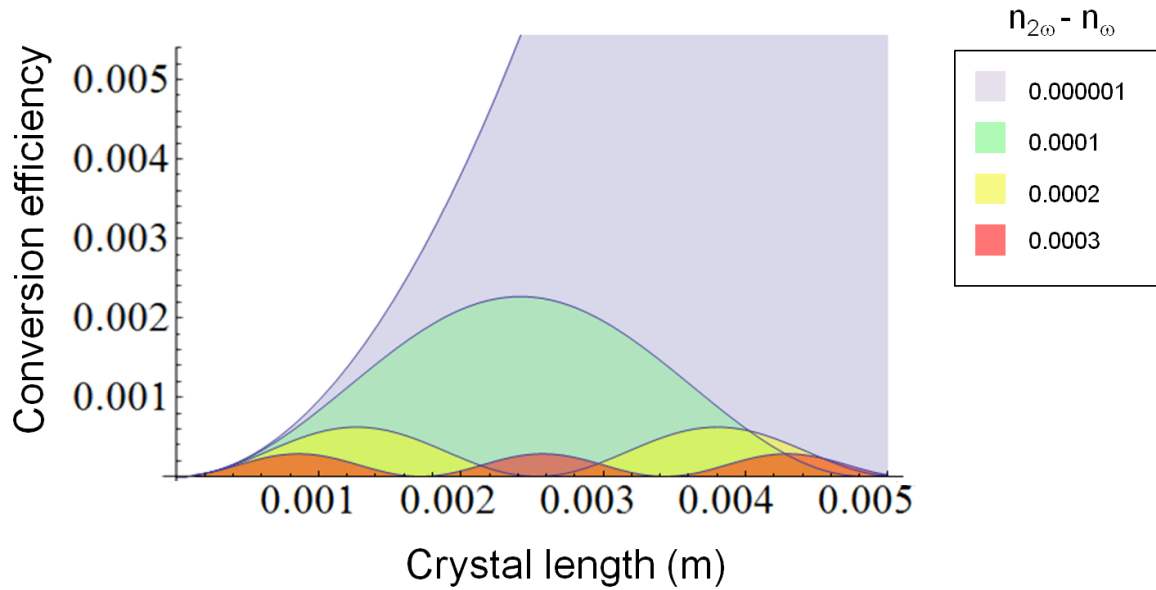


Figure 16. SHG conversion efficiency for different Δn .

In Figure 16, the refractive index difference of 10^{-6} does keep the conversion from 1064 nm to 532 nm to continue throughout the whole crystal length. As this difference increases to 10^{-4} , the conversion goes on up to half of the crystal (green curve) and after that, on the descending part of the curve, the energy is back converted from the SHG to the fundamental, in this case, no SHG photon would come out of the crystal. For higher differences, the energy is converted cyclically, fundamental \rightarrow SHG then SHG \rightarrow fundamental, as for the yellow and red curves.

1.3.2. Importance of nonlinear crystal and laser beam parameters

The nonlinear crystal characteristics and their influence on the SHG process are enumerated below. Typically a nonlinear crystal is selected to suit a particular application or fundamental laser beam, based on these properties.

- **Nonlinear coefficient:** As demonstrated in the previous subsection (1.3.1) the d_{eff} has a quadratic relation with the SHG output power, thus increasing it. This coefficient is an intrinsic property of the material, so choosing the material one can get more or less conversion efficiency.

- Angular phase matching:** In order to obtain efficient SHG, the incident wave must be in phase with the harmonic wave. However, these two waves have different wavelengths and they propagate at different velocities inside a medium with very well defined refractive index, thus are not able to get in phase. The solution comes from birefringent media, which change the refractive index for different wave polarization and angle of incidence. Given that, in many cases it is possible to find an angle in which the harmonic wave experiences the same refractive index of the incident wave, enabling the phase matching, Figure 17.

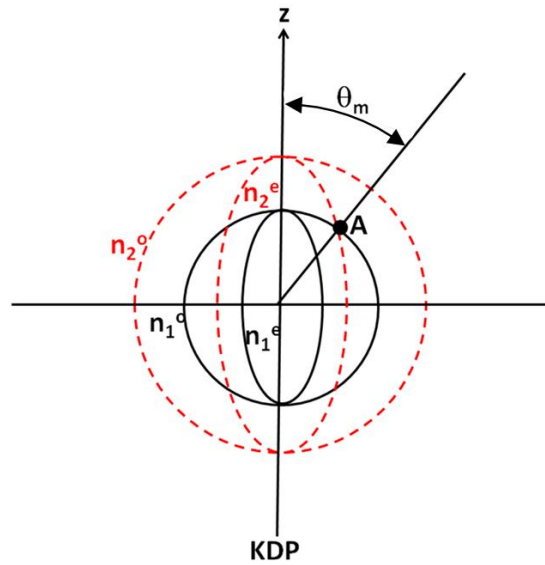


Figure 17. Refractive index distribution of an uniaxial KDP crystal for two different wavelengths λ_1 -solid black line and λ_2 – red dashed line.

In above KDP example, the z axis is representing the optical axis and the solid lines are the representation of the refractive index seen by λ_1 (n_1) and the red dashed lines are the refractive index seen by λ_2 (n_2). The circles correspond to the ordinary polarizations (n^o) while the ellipsoids correspond to the extraordinary polarizations (n^e). As a result, there is an angle θ_m for which the phase matching is possible. At this angle the ordinary beam at λ_1 experiences the same refractive index of an extraordinary beam at λ_2 . This is called critical phase-matching where a critical angle is required to enable SHG.

In addition, there are two types of phase matching which relate to the polarization of the incident and outcome waves: Type I and Type II. The first one requires two photons with the same polarization to generate one second harmonic photon with opposite polarization ($e + e = o$ or $o + o = e$). The second one requires two photons with opposite polarizations to generate one harmonic photon in one of the incident polarizations ($e + o = e$).

- **Temperature phase matching:** In most crystals the refractive indices depend on temperature. In some cases this can be used to reach the birefringent phase matching condition simply by changing the temperature of the medium, i.e. with no angle changes. This is known as noncritical phase matching. For noncritical phase matching schemes, the temperature control has to be very stable, as any temperature change would decrease the SHG conversion efficiency.
- **Walk-off:** The walk-off effect is related to the angular displacement of the energy transport path, given by the Poynting vector (\mathbf{S}), and the \mathbf{k} vector of the incident wave, which happens for angular phase matching (critical). As a consequence, frequency doubled or frequency mixed beams will propagate in a different angle as the fundamental beam, in the extraordinary direction. As a result, the converted beam will be elongated in one of its axes, detrimental for good beam qualities and limits the maximum intensity of the incident beam. This is an effect that happens only for extraordinary beams.
- **Absorption:** The absorption of either fundamental light or SHG light does introduce heat into the nonlinear crystal, thus changing its refractive index. The refractive index inhomogeneity created restricts the volume of the crystal in which the phase matching can be achieved. This kind of issue is generally found in high power continuous wave lasers, whose heat load is very high.
- **Optical quality:** Any refractive index distortions inside the nonlinear medium, such as defects, are going to decrease the maximum conversion efficiency.

Regarding the laser beam, there are some specific characteristics necessary to enable efficient conversion as well. The two most important are:

- **Beam divergence:** As a consequence of angular phase matching, there is an acceptance angle in which the incident beam will be converted, due to the phase matching angle restrictions. In that case the convergence and divergence of the beam has to be inside the acceptance angle, as Figure 18 demonstrates, in order to reach the maximum SHG conversion.

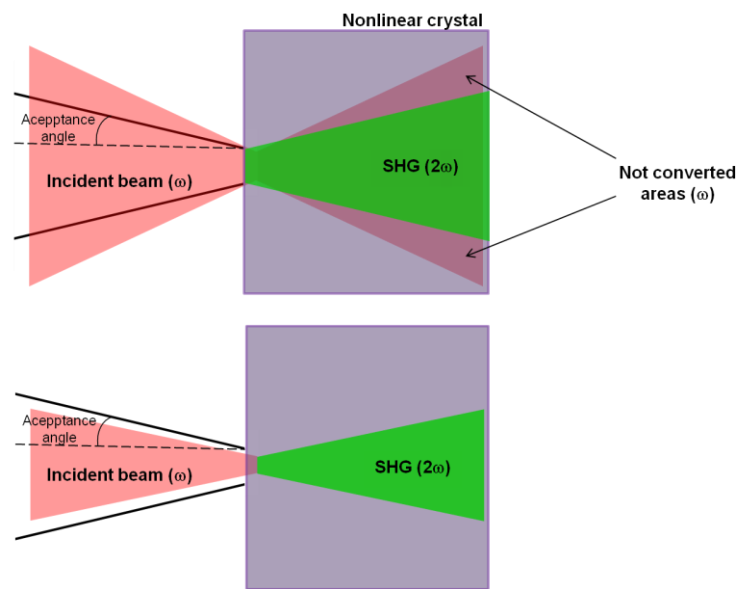


Figure 18. Influence of the beam divergence on the SHG conversion.

- **Spectral bandwidth:** Depending on the bandwidth of the light source to be converted, some of the wavelengths on the edge of the band may not be converted, Figure 19. In fact, each line into the band will experience a different refractive index. This is generally not relevant difference, although for relatively large bandwidth this effect start to be noticed and the condition for phase matching is no longer fulfilled. This is also dependent on material parameters, with some materials having larger acceptance bandwidth than others.

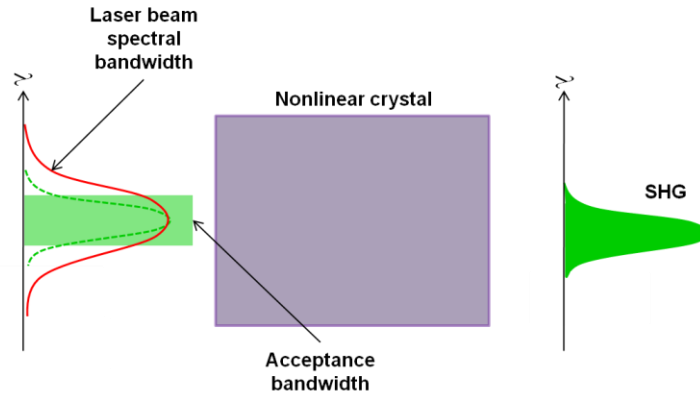


Figure 19. Acceptance bandwidth of a nonlinear crystal.

1.4. Nd quasi-three level lasers

In this section will be described the most relevant physics for the the Nd quasi-three level lasers followed by a review of the key works reported on the field.

1.4.1. Physics

The majority of solid state lasers are based on four level laser systems, in which there are at least four levels involved in the laser process (see Figure 9). However, this is not the only system found in laser materials with possibilities to create laser action. There is another very common laser scheme called three level system, in which only three levels are involved, as represented in Figure 20.

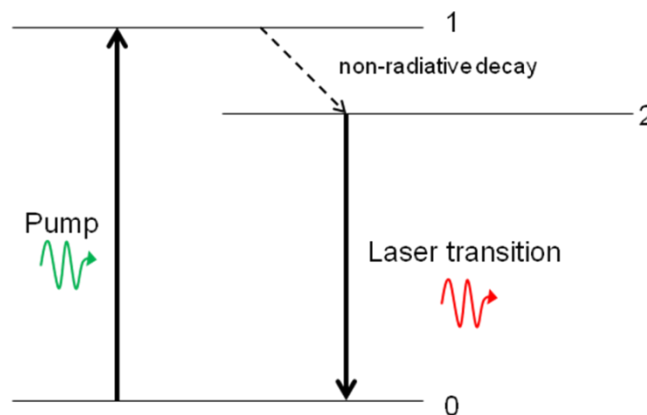


Figure 20. Three level laser scheme.

As seen in Figure 20, the difference between a three level laser and a four level laser starts with the fact that the lower laser level is the ground state in the three level case. If one takes the population distribution at thermal equilibrium given by the Boltzmann law, it will be found that the lower laser level has now a non zero population. In this case, the inversion is harder to reach, since it requires a higher pump power density to put more ions in the excited state than in the ground state as the ground state is already populated. Another important fact is that the laser transition can also be accomplished upwards, characterizing an absorption, due to the natural population in the ground state. Thus, photons generated by spontaneous and stimulated emissions are going to be partly reabsorbed by the system, causing an extra loss.

Fortunately in solid-state lasers the local crystal field causes splitting of the energy levels. Given that, depending on which Stark level of the fundamental multiplet is used as a lower laser level, the amount of reabsorption changes. If the interaction is with the 0 cm^{-1} energy level, the maximum reabsorption takes place (the lower the energy the higher is the population - Boltzmann distribution). For laser transitions terminating on a higher Stark level, reabsorption will lower because the level has lower population. In some cases a Stark level can have extremely low population. Lasers involving less populated ground state Stark levels are generally denominated as quasi-three level lasers or quasi-four level lasers depending on the population of the lower laser level.

A laser system can be called quasi-four level laser when the reabsorption can be almost neglected. An example is the Nd:YAG 946 nm laser, where the lower laser level is the highest ground state Stark level and has only 0.7% of the total population in the whole multiplet, Figure 21(a). The physical treatment of those lasers is basically the same as for a four level laser system.

The quasi-three level laser case is closer to the three level laser systems as the name says. In this case, there is no population number that indicates the limit between a quasi-three level laser and a quasi-four level laser, it depends on other parameters too, such as the stimulated emission cross section. Some examples of quasi-three level lasers are Yb-doped lasers, Nd:YVO₄ (914 nm), Nd:GdVO₄ (912 nm), and Nd:YLF (903/908 nm), as shown in Figure 21(b). In Figure 21 it is possible to see the population difference in the lower laser

level between Nd:YAG and Nd:YLF, with the last one having nearly 5 times more population than the Nd:YAG at room temperature.

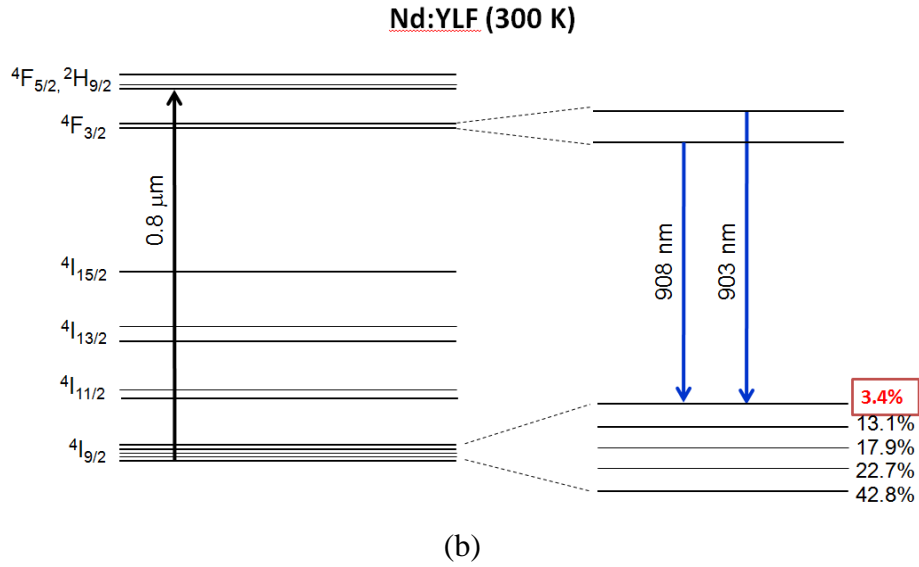
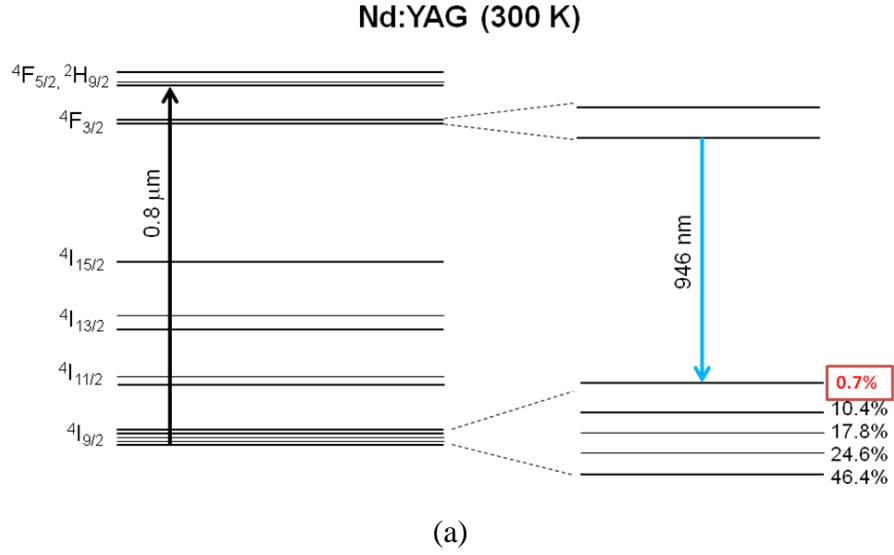


Figure 21. (a) Nd:YAG quasi-four level laser scheme and (b) Nd:YLF quasi-three level laser scheme.

Some mathematical models for the quasi-three level lasers are found in the literature [38, 39, 40]. They describe the population dynamics for the energy levels involved in the laser process in order to predict the gain and even laser performance.

Considering the model described in [40], and the energy level scheme shown in Figure 22, one can have as a starting point the rate equation which describes the population dynamics on the lower laser level N_L that belongs to the N_1 manifold.

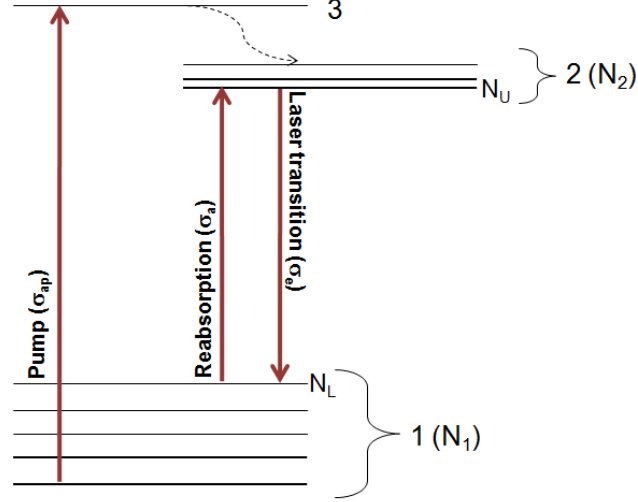


Figure 22. Quasi-three level laser scheme used in the modeling.

Making a simplistic approximation of constant temperature distribution in the whole crystal volume, the emission and absorption cross sections are kept constant as well. Also, considering the transition $3 \rightarrow 2$ a fast transition, we can assume the population in 2 is the only other population than 1. With this approximation, and also neglecting effects like spatial hole burning and assuming the pump beam passes only once through the active medium, the rate equation for the lower manifold can be written as

$$\frac{dN_1}{dt} = AN_2 + \sigma_e IN_2 - \sigma_a IN_1 - \sigma_{ap} I_p N_1 \quad (16)$$

where A is the spontaneous emission rate ($1/\tau_f$), N_2 the upper manifold population, σ_e the stimulated emission cross section for the transition $N_U \rightarrow N_L$, I is the laser mode intensity, I_p the pump intensity, σ_a is the absorption cross section at the laser wavelength (reabsorption), N_1 the lower manifold population and σ_{ap} the absorption cross section at the pump wavelength. The intensities must be given in units of photons per second per centimeter square ($s^{-1} \cdot cm^{-2}$).

Solving (16) in the steady-state regime ($dN_1/dt = 0$), and considering the total population as $N = N_1 + N_2$, we find the expressions for N_1 and N_2 as follows,

$$N_1 = N \frac{A + \sigma_e I}{(\sigma_a + \sigma_e)I + \sigma_{ap}I_p + A} \quad (17)$$

$$N_2 = N \frac{\sigma_{ap}I_p + \sigma_a I}{(\sigma_a + \sigma_e)I + \sigma_{ap}I_p + A} \quad (18)$$

It is possible to obtain the gain coefficient (g) at the laser wavelength by introducing (17) and (18) in,

$$g = \sigma_e N_2 - \sigma_a N_1 \quad (19)$$

As a result the gain coefficient given in cm^{-1} can be calculated by the following equation:

$$g = N \frac{\sigma_e \sigma_{ap} I_p - \sigma_a A}{(\sigma_a + \sigma_e)I + \sigma_{ap}I_p + A} \quad (20)$$

It is also interesting to evaluate the small signal gain coefficient (g_0), which can be used to analyze the laser threshold condition. In this case, we can neglect the laser intensity (I) term, turning (20) into

$$g_0 = N \frac{\sigma_e \sigma_{ap} I_p - \sigma_a A}{\sigma_{ap} I_p + A} \quad (21)$$

At this point, it is easy to notice the degrading influence of the reabsorption losses, represented by the $\sigma_a A$ term, reducing the laser gain.

Now we want to consider the spatial distribution of the beams. Assuming a circular Gaussian distribution for both pump beam and laser mode, and also assuming a TEM_{00} mode oscillation and taking into account the pump beam quality factor M^2 , the expressions describing the radii of pump (w_p) and laser (w_c) beams are given by

$$\omega_p^2(z) = \omega_{p0}^2 + \left(\frac{M^2(z - z_0)\lambda_p}{\pi\omega_{p0}n} \right)^2 \quad (22)$$

$$\omega_c^2(z) = \omega_{c0}^2 + \left(\frac{z\lambda}{\pi\omega_{c0}n} \right)^2 \quad (23)$$

where n is the material index of refraction, λ_p and λ the pump and laser wavelengths respectively, w_{p0} and w_{c0} the pump and laser mode waists respectively and z_0 is the pump waist location along the propagation axis.

Having the spatial distribution of the beams, it is now possible to describe their intensity distribution in the whole crystal using cylindrical coordinate (radius- r ; length- z). For that, the pump absorption coefficient (α_p), the pump power (P_p), the laser intracavity power (P_{int}) and the output coupler transmission (T_{out}) are required.

$$I_p(r, z) = \frac{2P_p}{h\nu_p\pi\omega_p^2(z)} \exp(-\alpha_p z) \exp\left(\frac{-2r^2}{\omega_p^2(z)}\right) \quad (24)$$

$$I(r, z) = (2 - T_{out}) \frac{2P_{int}}{h\nu_{laser}\pi\omega_c^2(z)} \exp\left(\frac{-2r^2}{\omega_c^2(z)}\right) \quad (25)$$

Finally, the net gain (G) per double pass integrated over the whole active medium can be described as

$$G = \left[1 + \int_0^l dz \int_0^{r_c} \frac{4 \cdot g(r, z)}{\omega_c^2(r, z)} \exp\left(\frac{-2r^2}{\omega_c^2(z)}\right) r \cdot dr \right]^2 \quad (26)$$

where l is the crystal active medium length and r_c the crystal radius.

In order to reach laser oscillation the net gain (G) has to be equal to the round-trip losses, determined by the output coupler transmission (T_{out}) and passive losses (L). Assuming low intracavity losses, this condition can be described as

$$G = \frac{1}{1 - T_{out} - L} \quad (27)$$

Taking the quasi-three level laser parameters of the Nd:YLF (908 nm), Nd:YAG (946 nm) and Nd:GdVO₄ (912 nm) crystals, it is possible to calculate their small signal gain distribution in the whole crystal, and with it, the total net gain in each case. To exemplify I have chosen two different pump powers, 5 W and 15 W, and simulated the small signal gain curves at the center of the beams ($r = 0$) using (21), (22) and (24). The same doping concentrations of 0.6 at% and crystal lengths of 10 mm were chosen for the three crystals for the purpose of comparison and the results are shown in Figure 23. The pump beam parameters used in the simulations are typical of those found in fiber coupled diode lasers, a 100 μm core diameter fiber ($M^2 = 40$). The output beam is focused to a 250 μm beam radius on the face of the laser crystal. The pump transition used is the $^4I_{9/2} \rightarrow ^4F_{5/2}$, at 806 nm for Nd:YLF and 808 nm for Nd:YAG and Nd:GdVO₄.

The double pass net gain calculated can be obtained using (26) and is also shown in Figure 23 for each case, giving an idea of which one would oscillate or even support more resonator losses, therefore lower pump threshold.

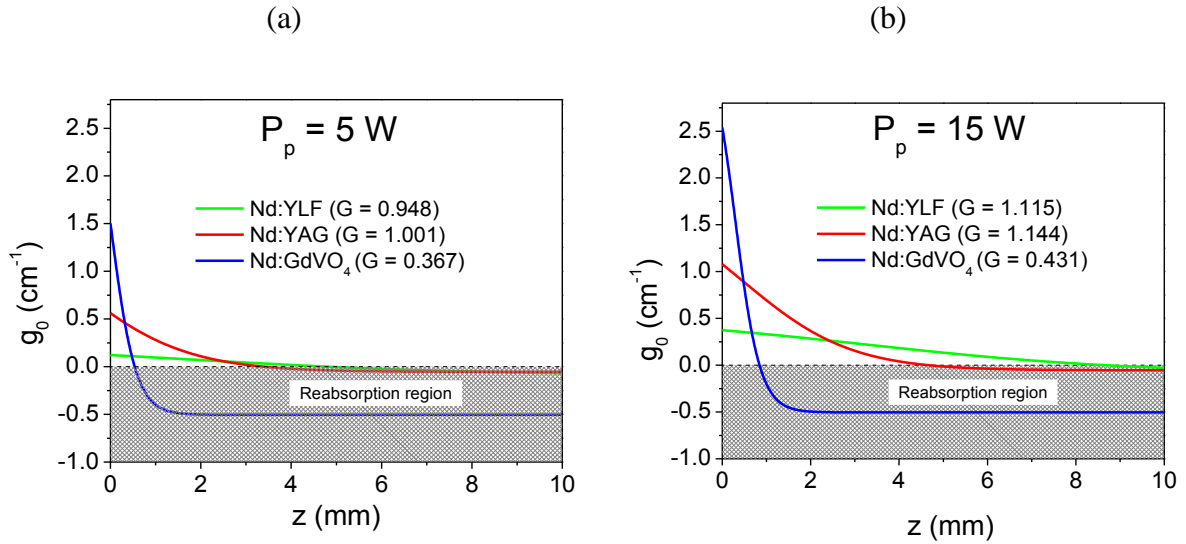


Figure 23. Small signal gain distribution in Nd:YLF, Nd:YAG and Nd:GdVO₄ crystals for two pump powers (a) 5 W and (b) 15 W (simulations carried out by the author).

Analyzing the double pass gains (G) in these six different situations, one will find that only three of them have chances to reach laser action ($G > 1$): Nd:YAG - 15 W ;

Nd:YLF – 15 W and Nd:YAG – 5 W. The last one has tiny chances to keep an oscillation, as its G is only slightly higher than one, which would easily be overwhelmed by a small loss.

To increase the gain on these lasers we can look at the parameters of the equations (20) and (21). Both saturated gain and small signal gain are dependent on the material parameters, such as the absorption and emission cross sections, including the lifetime of the upper laser level ($A=1/\tau_f$). Accordingly, one should choose a material with high emission cross section (σ_e), low reabsorption cross section (σ_a) and long fluorescence lifetime (τ_f). The later would reduce the spontaneous emission rate (A), keeping the upper laser level populated longer enabling stronger inversion and reducing the number of decays that populate spontaneously the lower laser level. For the saturated gain case, there is also the traditional saturating effect caused by the stimulated emission with some contribution of the reabsorption $(\sigma_a+\sigma_e)I$.

The Nd:YLF example in Figure 23 is a case where by increasing the pump power it was possible to overcome the reabsorption losses by having pump absorption in the whole length of the crystal. Accordingly, it is a priority for most quasi-three level lasers to spread the pump absorption through the whole crystal length to get a similar effect, either by reducing the Nd concentration or using a pump wavelength at a lower absorption cross section.

1.4.2. Literature review

The first diode pumped quasi-three level laser was reported by Fan *et al.* [41]. It was a Nd:YAG laser emitting at 946 nm operating at room temperature. Many other works have followed it, applying frequency doubling in order to obtain efficient and high power blue lasers [42, 43, 44].

These lasers were not restricted only to the Nd:YAG crystal, they were also demonstrated based on Nd:YVO₄ [45], Nd:GdVO₄ [46], Nd:YLF [30] and various lesser known crystals [47, 48]. Table 1 (in section 1.1) provides the wavelengths obtained from the $^4F_{3/2} \rightarrow ^4I_{9/2}$ transition, in Nd:YAG and in the other cited crystals.

Multi-Watt operation of these lasers in the infrared was demonstrated with more than 10 W of output power. In 2006 Zhou *et al.* [44], reported a maximum CW output

power of 15.2 W Nd:YAG laser at 946 nm. A more recent work [49], demonstrated high power and high efficiency continuous wave operation of a Nd:GdVO₄ laser at 912 nm. The Nd:GdVO₄ crystal was pumped at 880 nm, which reduced the heat load, allowing the maintenance of a good beam quality ($M^2 \sim 1.5$ at 14 W of absorbed power) with an output power of 8.1 W and a slope efficiency of 68% (optical-to-optical efficiency of 58%). A Nd:YLF 908 nm was also demonstrated using a direct pump scheme, reaching a maximum output power of 4.7 W in CW regime [17] with an optical to optical efficiency of 39.8%.

The best continuous wave results in the blue were obtained in Nd:GdVO₄ and in Nd:YVO₄ lasers. An output power of 14.8 W was demonstrated at 456 nm using the Nd:GdVO₄ as the active medium, reaching a diode-blue conversion efficiency of 37% [50]. Another similar work has demonstrated 13.2 W of output power at 457 nm, which corresponds to a diode-blue conversion efficiency of 34.7%, using a Nd:YVO₄ crystal [51]. Other lasers reported did not achieve such high output powers, but some of them deserve to be highlighted as in the case of Nd:YLF. The Nd:YLF quasi-three level laser enables the deepest blue emission among the cited crystals, 451 nm (π) and 454 nm (σ), and output powers of 4.5 W in CW regime were reported at 454 nm [30].

The success of neodymium lasers operating on this transition, inspired the current search for lasers operating in the more populated degeneracies of the Nd fundamental level, which enables the generation of even deeper blue lasers [52].

1.5. Raman lasers

This section will describe the basic physics of the Raman lasers and also the main works on the field are highlighted and discussed, in the context of the present thesis work.

1.5.1. Physics

Discovered in 1928 by C. V. Raman [53], Raman scattering is an inelastic process where part of the energy of the incident light is transferred to the medium, such that the scattered (Stokes) light has a different frequency.

The interaction between an incident electromagnetic (EM) field and the scattering material has to be observed from the molecule/atoms point of view in order to be

understood. Electrons orbiting the atoms are perturbed periodically at the frequency of the incident wave, creating a cyclic charge separation, known as an induced dipole. This dipole determines the frequency context of the scattered radiation. The majority of the scattered light has the same frequency of the incident field ($\omega_i = 2\pi\nu_i$). Such scattering is termed “elastic” scattering, and the most usual types are Rayleigh and Mie scattering. A small (typically 1 in 10^6) fraction of the scattered light will have different frequency to the incident light, arising from “inelastic” scattering processes. Raman scattering is one of the possible inelastic processes (Brillouin scattering is another), and is the responsible for frequency shifted components, known as Stokes ($\omega_s = 2\pi\nu_s$) and anti-Stokes ($\omega_a = 2\pi\nu_a$). A scheme of these two types is shown in Figure 24.



Figure 24. EM field scattering components.

As this thesis concerns only the Stokes process, the anti-Stokes will not be discussed further.

The molecular vibrational modes are generally the responsible for absorbing the residual energy, $\hbar\omega_v$, in the case of Stokes emission ($\hbar\omega_s = \hbar\omega_i - \hbar\omega_v$). This vibrational energy is very dependent on the material structure, atoms, bonds and so on.

An interesting characteristic of Raman scattering is that it can be cascaded, or in other words, the 1st Stokes photons (ω_{s1}) can be shifted in the same way of the first incident field, generating the 2nd Stokes (ω_{s2}) and so on. Figure 25 shows a representative energy level scheme with the generation of multiple Stokes photons.

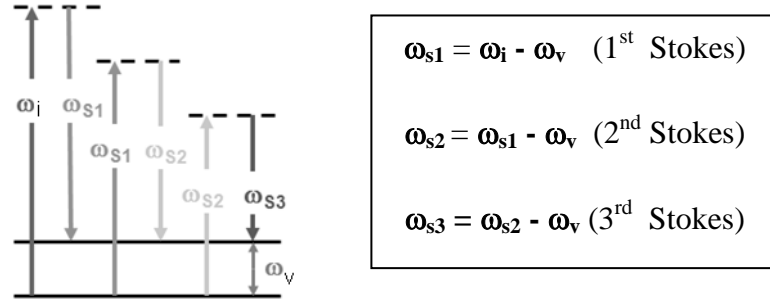


Figure 25. Stokes lines generation.

Theory of spontaneous Raman scattering

As mentioned above, a dipole is induced in the material by the incident EM field; its strength P can be expressed as [54]

$$P = \alpha E \quad (28)$$

where α is the polarizability and E the electric field of the incident wave. The electric field is given by

$$E = E_0 \cos(\omega_i t) \quad (29)$$

with ω_i given in rad/s where $\omega_i = 2\pi c / \lambda_i$ and E_0 is the amplitude of the electric field. Inserting (29) in (28) we can describe the induced dipole moment as a function of the time.

$$P = \alpha E_0 \cos(\omega_i t) \quad (30)$$

The polarizability depends on the particular position of the individual atoms, thus there is a need to describe the instantaneous position of the atoms involved. The atoms actual displacement $q(t)$ around their equilibrium position originated by a specific vibrational mode can be described as

$$q(t) = q_0 \cos(\omega_v t) \quad (31)$$

where ω_v is the frequency of the vibrational mode and q_0 is the maximum displacement around the equilibrium point.

An important assumption about the polarizability (α) must be made, a statement that the polarizability of the atomic system varies with the internuclear separation $q(t)$ according to the equation (32). This is a good approximation for relatively small displacements, such as up to ~10% of the bond length [54].

$$\alpha = \alpha_0 + \frac{\partial \alpha}{\partial q} q(t) \quad (32)$$

The polarizability at the equilibrium position is given by α_0 and the derivative term describes the variation of the polarizability with the displacement. Substituting (31) in (32) we can have

$$\alpha = \alpha_0 + \frac{\partial \alpha}{\partial q} q_0 \cos(\omega_v t) \quad (33)$$

Lastly, we take this polarizability definition and insert into (30) as follows

$$P = \alpha_0 E_0 \cos(\omega_i t) + \frac{\partial \alpha}{\partial q} q_0 E_0 \cos(\omega_i t) \cos(\omega_v t) \quad (34)$$

Using the trigonometric relation, $\cos x \cdot \cos y = \frac{1}{2} [\cos(x - y) + \cos(x + y)]$, it is possible to observe the three frequency components generated, ω_i , $(\omega_i - \omega_v)$ and $(\omega_i + \omega_v)$.

$$P = \alpha_0 E_0 \cos(\omega_i t) + \frac{\partial \alpha}{\partial q} \frac{q_0 E_0}{2} \cos[(\omega_i - \omega_v)t] + \frac{\partial \alpha}{\partial q} \frac{q_0 E_0}{2} \cos[(\omega_i + \omega_v)t] \quad (35)$$

The first term describes an elastic scattering, Rayleigh or Mie, where the frequency of the incident EM field is maintained, and the last two terms are inelastic scatterings composing the Stokes (at lower frequencies) and anti-Stokes (at higher frequencies) emissions, respectively.

Analyzing equation (35) it is clear that the term $\partial\alpha/\partial q$ must not be zero in order to make Raman scattering possible. Therefore, a Raman active material must have at least one vibrational displacement mode of its atoms/molecules that produces a change in polarizability. We can take as an example a simple diatomic system as shown in Figure 26.

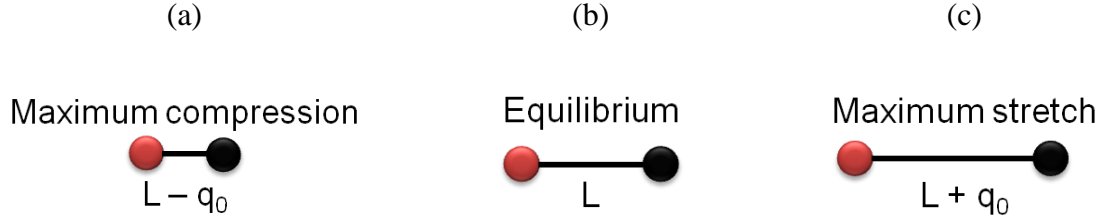


Figure 26. Diatomic system vibration at (a) maximum compression, (b) at equilibrium and (c) at maximum stretch.

When the system is at its maximum compression ($L - q_0$) as in Figure 26(a), the electrons from the red atom are going to have a strong interaction with the black atom nucleus, and vice versa. As a result, they will not be perturbed much by the incident field. On the other hand, as shown in Figure 26(c), when the atoms are far from each other ($L + q_0$), they are going to be more sensitive to the incident field, as they feel less influence from each others nucleus, thus they are more easily perturbed by the field. Finally, in terms of polarizability, when the system is at maximum compression, its polarizability reduces, while if the system is found at maximum expansion, its polarizability increases.

Stimulated Raman scattering (SRS)

Having in mind the nonlinear description of spontaneous Raman scattering, we can now think on how its stimulated version takes place.

Physically speaking, the dynamic modulation of the polarizability creates the frequency sidebands on the laser field. Now if one traps the Stokes band into a resonator, we will have two fields propagating together, ω_i and ω_s . These two fields are going to beat and thus modulate the total intensity as [37]

$$I(t) = I_0 + I_1 \cos(\omega_i - \omega_s)t \quad (36)$$

where I_0 is a time independent intensity term and the second term has I_1 as an intensity amplitude which oscillates at the frequency $\omega_i - \omega_s$. Given that $\omega_i - \omega_s = \omega_v$, we found out that the beat frequency is exactly the molecular vibration frequency. Therefore, the atomic system involved is going to experience a coherent excitation provided by the beat, leading to a stronger molecular vibration. This stronger vibration increases the Stokes field undergoing this region, which in turn leads to an even stronger molecular vibration. As a result of this cyclic process we have a coherent Stokes field amplification, defining the stimulated Raman scattering (SRS). I have considered (simulated) this in the context of a solid-state Raman laser. Figure 27(a) shows the plots of the fundamental and Stokes frequencies found in Nd:GdVO₄ self-Raman laser (author's simulation), 1064 nm ($\nu_i=282$ THz) and 1173 nm ($\nu_s=256$ THz), evidencing the beating pattern created. In Figure 27(b), we show a superposition of these two waves with the molecule vibrational oscillation in red, demonstrating the resonance between the beat generated by the two propagating fields and the molecular oscillation.

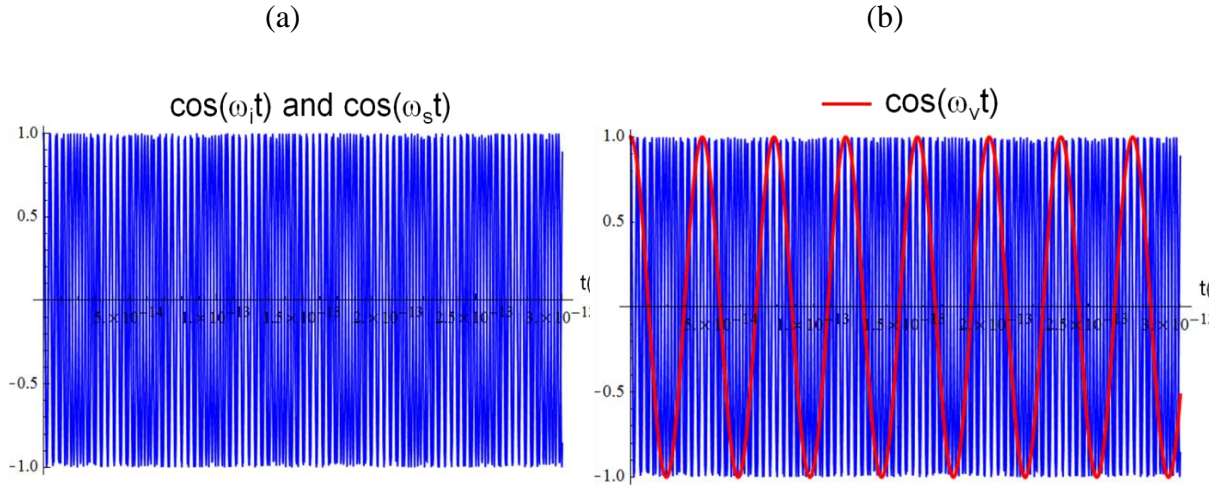


Figure 27. (a) Fundamental and Stokes fields beat, and (b) molecular vibration in red at the same frequency of the beat (simulation by the author).

A further quantitative description of the SRS process can be found in [37]. From here the phenomenological description will be focused on the laser operation as follows in the next section.

Raman lasers

In order to build a Raman laser, it is necessary to introduce in the laser setup a Raman active material, in which the SRS occurs. Generally it is placed inside the resonator where the photon field is very high, required to reach the SRS threshold, as discussed later in this section.

Regarding the Raman laser operation, there are two operation regimes to be considered in the analysis: Steady-state and transient regimes.

The Raman laser is considered to operate in a steady-state regime when the duration of pumping τ_p is much longer than the decay time T_R (this is the decay time for the phonon transition). In this case, the Stokes emission intensity $I_s(z)$ has the following dependence [55]

$$I_s(z) = I_s(0) \cdot e^{(g_R I_p z)} \quad (37)$$

where I_p is the pump intensity, z is the crystal length, and g_R is the Raman gain coefficient described as,

$$g_R = \frac{8\pi c^2 N}{\hbar n_s^2 \omega_s^3 \Gamma} \cdot \frac{\partial \sigma}{\partial \Omega} \quad (38)$$

where the integral Raman scattering cross section is expressed by,

$$\frac{\partial \sigma}{\partial \Omega} = \frac{\omega_s^4 n_s}{c^4 n_L} \cdot \frac{\hbar}{2m\omega_R} \cdot \left(\frac{\partial \alpha}{\partial q} \right)^2 \quad (39)$$

In these equations N is the density number of Raman active molecules, n_s and n_L are the refractive indices for Stokes emission and pump wavelengths, respectively, m is the molecular oscillator reduced mass, Γ is the linewidth for the Raman transition which is equal to the inverse of T_R and c is the light speed in vacuum. The integral cross section and the polarization of the Stokes scattered light depends on the orientation of the crystal with respect to the polarization of incident light. Theory predicts that high Stokes scattering intensity, as well as the gain, occurs when it has a polarization oriented orthogonally to the pumping polarization, although in practice it may be different in some cases. In this

regime, the Raman gain coefficient (g_R) increases as the Raman linewidth and wavelength decrease and the integral scattering cross section increases.

In the absence of a Stokes field, the SRS grows with spontaneous emission integrated over the Raman transition linewidth for a given solid angle ($\Delta\Omega$).

$$I_s(0) = \frac{\omega_s^3 n_s^3}{c^2} \cdot \frac{\hbar}{(2\pi)^3} \cdot \Delta\Omega \quad (40)$$

Since $I_s(0)$ typically presents values around 10^{-15} W/cm² [55], to reach the Raman threshold it is necessary an exponent $g_R I_b z$ with a value above 30. Considering a crystal operating in the steady state regime with gain coefficient of 10 cm/GW (typical of a crystal with high Raman gain) and 30 mm long it would require a pump intensity greater than 1 GW/cm². However, this usually exceeds the damage threshold of many candidates for this purpose.

There is also a transient regime where $\tau_p \ll T_R$, where the Stokes emission grows according to [55]:

$$I_s(z) = I_s(0) \exp(-\tau_p / T_R) \exp[2(\tau_p g_R I_b z / T_R)^{1/2}] \quad (41)$$

In the case of $\Gamma T_R = 1$, the Stokes intensity increase does not depend on the linewidth and the exponential term depends on $z^{1/2}$ instead of z . Consequently, Raman crystals with higher scattering cross section are more interesting for this regime.

It is possible to generate the second, third and higher orders of Stokes emission. This occurs when the first Stokes intensity becomes sufficiently strong to be shifted too, and then starts to generate the second Stokes. The same can happens with the second, third and other Stokes orders, creating a cascade effect. This usually takes place in cavities with a high Q factor, and this effect is used in Raman lasers used for generating multiple wavelengths [56].

Raman laser engineering

Three main types of configuration are used to obtain SRS frequency conversion; these are usually called Raman generators, external cavity Raman lasers and intracavity Raman lasers.

In Raman generators, the simpler configuration among the three cited, the pumping beam with high peak power and pulse duration of the order of 10-100 ps passes through the Raman crystal generating the Raman shifted output in a single step. This conversion mechanism has shown conversion efficiencies as high as 95%. To reach the threshold of SRS, the pump beam is typically focused in the crystal to reach intensities of about 1 GW/cm^2 . Intensities of this magnitude are close or exceed the damage threshold of many crystals and also allow other nonlinear effects such as self-focusing (also related to χ^3) that compete with the SRS. Figure 28(a) shows a schematic drawing of a typical Raman generator. For the case of pulses having duration longer than the travel time of the photon inside the crystal, it is beneficial to use an optical resonator (which allows the amplification of Stokes field through multiple passes), such as the external cavity Raman laser shown in Figure 28(b). The output coupler is a partial reflector mirror at the Stokes emission wavelength, and often this mirror has high reflectivity at the wavelength of the pump making the pump beam pass twice through the crystal thus increasing the conversion efficiency.

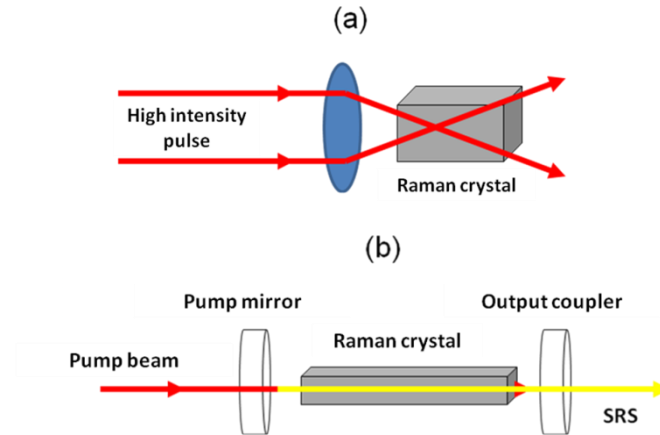


Figure 28. (a) Raman Generator and (b) external cavity Raman laser.

The intracavity Raman laser configuration, shown in Figure 29, is usually used when the output power of a particular laser is not so high. In this case, the Raman medium is set up inside the cavity where it can find a highly intense fundamental field. Above the Raman threshold there are two intracavity fields: fundamental and Stokes.

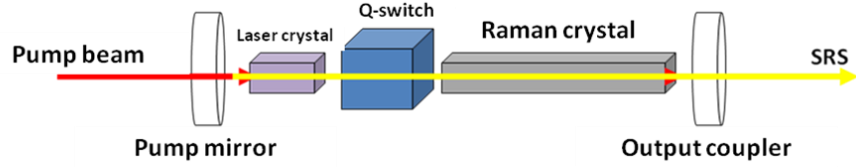


Figure 29. Intracavity Raman laser.

There are many variations of the intracavity configuration. One is called a self-Raman laser and is shown in Figure 30(a). Here the active medium is the same as the Raman medium and performs the two functions of generating the laser fundamental and Raman-shifting, thereby simplifying and shortening the optical resonator. Another approach is using an intracavity mirror, either to separate the fundamental and Raman cavities, the so called coupled cavities, or even to simple redirect the visible beam from the doubling crystal to the output, and not going to the laser crystal, thus adding heat (Figure 30(b)). The visible Raman lasers can be found with active medium and Raman crystal separately, which prevents the two thermal loading processes to be in the same crystal. On the other hand, it adds two more, lossy interfaces, Figure 30(c).

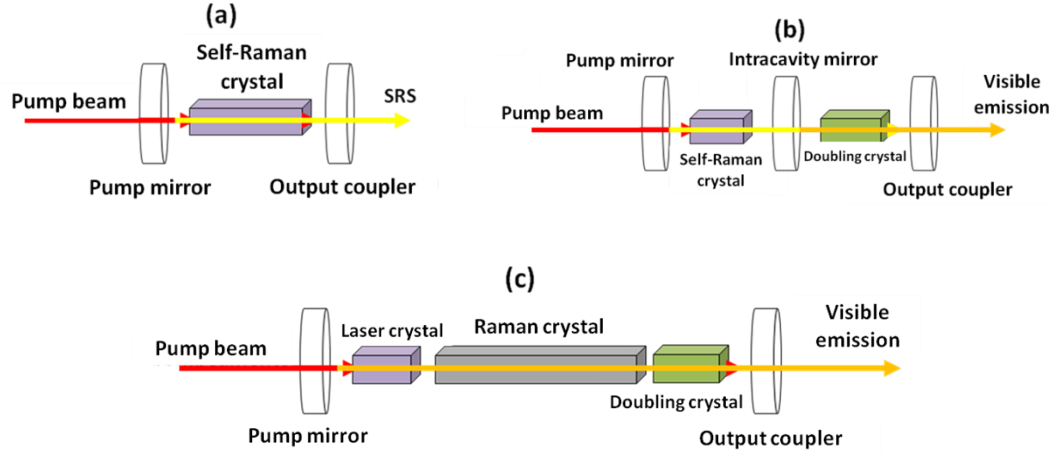


Figure 30. (a) Self-Raman laser, (b) Self-Raman SHG laser with an intracavity mirror and (c) SHG Raman laser.

1.5.2. Literature review

This PhD work has the objective to exploit the unique characteristics of Nd:LiYF₄ (Nd:YLF) crystals in order to achieve developments in Raman lasers. In the long term,

such development might include power scaling (>5 W of output power in the visible), improve the management of the “green-like problem” (yellow problem in this case), which presents itself as an amplitude noise generated by the frequency doubling process, and generation of new wavelengths in the near infrared and visible range are some of the outcomes. Also, this crystal can be useful in pulsed lasers due to its longer upper level lifetime when compared to other crystals. All these advantages as well as the disadvantages will be further described in the last section of the chapter.

The first four sub-sections provide a brief review of the Raman laser field since the discovery of Stimulated Raman Scattering (SRS) until the real laser devices developed until now. Since the present project concerns the development of a Crystalline Raman lasers, the review focus on the results of only this type of Raman laser.

Stimulated Raman Scattering (SRS)

The first notice of the Stimulated Raman Scattering was made by accident in 1962, by Woodbury and Ng, which later became a patent [57]. They were working in a Q-switched ruby laser combined with an intracavity nitrobenzene Kerr cell, when they noticed a decrease of power at 694 nm as it was pumped harder. More detailed studies showed some increasing of power at a red shifted wavelength. Theoretical description of the phenomenon was done in the same year by R.W. Hellwarth [58], where he discussed the dynamic behavior of the shifted laser light based on stimulated Raman scattering using measurable material parameters, such the Raman scattering cross section. After that, the effect was found in many liquids and crystals by Eckhardt *et al* [59], and others.

Later on, in 1966 [60], Eckhardt provided a guide to select Raman materials. Such work focused on the material analyses and light properties in order to help with the prediction of Raman behavior in new materials. One year later, Bloembergen did a huge theoretical and experimental review of all the stimulated Raman scattering outcomes since their discovery [61]. So far, most of the Raman active materials studied were liquids or gases, only few solid state materials were found, like diamond, calcite and α -sulphur.

Through the 70s and 80s other solid state materials were discovered with potential application in stimulated Raman scattering. Nitrate based crystals, such as $\text{Ba}(\text{NO}_3)_2$ [62], showed very high Raman gain at 532 nm (47cm/GW) and 1064 nm (11cm/GW). Also

KGd(WO₄), KGW, a tungstate crystal, was another important discovery at the time, which is still used nowadays. This material does not have a Raman gain as high as barium nitrate, but it is birefringent and depending on the polarization of the optical field, it is possible to access different Raman shifts (901 cm⁻¹ or 768 cm⁻¹). In addition, this crystal can be doped with Nd³⁺ and then generates both, fundamental field and SRS [63].

More recently, the vanadate based crystals were found to be good candidates for efficient Raman shifting as well as they were well explored as efficient crystals for fundamental lasers at 1064 nm when doped with Nd³⁺ [64, 65, 66, 67],. Kaminskii *et al.* [68] were the first to demonstrate the Raman potential in YVO₄ and GdVO₄ crystals in 2001. After that, many Raman lasers started to be build using Nd:YVO₄ and Nd:GdVO₄. In one of the more recent experiments the highest CW intracavity visible self-Raman laser with 5.3W of output power at 559 nm was built [69]. Later, Kaminskii *et al.* reported observation of the non-linear Raman effect in a LuVO₄ crystal [70], in which it was shown to be a promising self-Raman laser material.

Nowadays, two crystals are extensively used in Raman lasers because of their special properties. One of them is the BaWO₄ crystal, which presents one of the highest Raman gains (second to diamond) among all the others studied, combined with good optical properties and chemical stability [71,72]. The last two properties make this crystal more suitable than Ba(NO₃)₂, which has a higher Raman gain, but is hygroscopic and has not such good thermal properties [55]. The very best crystal is an old known material, the diamond, which provides, with no doubts, the best properties among all the solid materials investigated for the Raman shift generation [73] . Although, this was known since the very beginning of the SRS history, it only recently became available with cheaper prices and better optical qualities. Synthetic diamond is now produced artificially, by *Chemical Vapor Deposition* (CVD) [74]. Table 3 presents the main materials used nowadays and their properties.

Table 3. Summary of the main Raman crystals and their properties.

	Raman shift (cm⁻¹)	Gain coeff. at 1064 nm (cm/GW)	Damage Threshold (GW/cm²)	Thermal conductivity (Wm⁻¹K⁻¹)	Ref
				2.6 [100]	
KGW	768/901	4.4/3.5	10	3.8 [010] 3.4 [001]	[75]
BaWO₄	926	8.5	-	3	[75]
YVO₄	892	4.5	1	5.2	[55]
GdVO₄	885	4.5	1	5	[75]
Ba(NO₃)₂	1047	11	0.4	1.17	[55]
Diamond	1332	12	-	2000	[73]

Solid State intracavity Raman lasers

Due to the fast developments in SRS theory and experiments during the 60s, real laser devices were produced in the following period. These new lasers provided access to new wavelengths in the near infrared and visible range showing high efficiency and then, becoming a promising tool. The following review focus on the intracavity design in continuous wave operation and visible lasers.

CW Raman Lasers

The first work showing continuous wave (CW) operation of Raman lasers was an argon-ion-laser-pumped Ba(NO₃)₂ crystal [76], reported by Grabtchikov in 2004. It was pumped at 514 nm and generated 543 nm shifted output laser in an external cavity configuration. Actually, the first intracavity CW Raman laser, which this review concerns, was made in 2005 by Demidovich *et al.* [77], consisting in a Nd:KGW self-Raman laser. It reached a maximum output power of 54 mW at 1181 nm, corresponding to a diode-Stokes efficiency of 2.6%.

A detailed review on CW Raman lasers up to 2007 can be found in [55]. Since then only a few works tried to couple infrared emission to the 1st Stokes. This is because the optimum 1st Stokes output transmission was found to be quite low, around 1% and also

because the frequency doubled version of these lasers was more interesting from the application point of view. Nonlinear coupling (second harmonic/sum frequency generation) has been used to extract the potential of CW intracavity Raman lasers, resulting in yellow-orange lasers.

From 2007 onwards, there were some groups reporting over multi-Watt CW output powers in a variety of systems. Dekker *et al.* have reported 2.04 W at 1173 nm extracted from a Nd:GdVO₄ self-Raman laser [78]. In 2009, one of the highest output powers was reported by Fan *et al.* [79], demonstrating 3.36 W using a Nd:YVO₄ and a BaWO₄ crystal with the 1st Stokes at 1180 nm. During the following years, many others reached output powers up to 3 W in CW Raman lasers [80, 81, 41].

Nowadays, output powers of 5.1 W at 1217 nm and 6.1 W at 1139 nm were achieved by Savitski *et al.* [82]. The 1217 nm laser was based on a commercial Nd:YLF laser module (153 W of diode pump power in side pump configuration), and a diamond crystal as the Raman active medium. The 1139 nm laser has also used the Nd:YLF laser module, but this time combined with a KGW crystal; the power of 6.1 W is the highest CW output power for a crystalline intracavity Raman laser so far. Another interesting fact is found yet in this work, the M^2 of the diamond based Raman laser was of about 1.1, and the one obtained with the KGW crystal was of about 5.5. In fact, this happened because of the excellent thermal properties of the diamond, which has a thermal conductivity of 2000 W/mK [82], 500 times higher than KGW, ~3.8 W/mK, thus resulting in a very weak thermal lens and very weak or no mode degradation. Higher powers from the CW diamond can be expected in future.

Limiting factors for CW operation are also related to the thermal lens. In this case, the lens build up is not only due to the pump loading in the laser crystal, but also to the continuous shifting process (photon fundamental = **phonon** + photon Stokes) that generates the Stokes field. This is the major limitation for CW self-Raman lasers power scaling, which associates both heating effects in one crystal.

The best prominent results in terms of efficiency with CW crystalline Raman lasers were obtained using nonlinear coupling to the visible; their review follows in the next section.

Visible Raman lasers

Defined as an efficient route to couple the intracavity power from Raman lasers, nonlinear conversion (second harmonic and sum frequency generation, SHG/SFG respectively) have been extensively used to generate visible lasers, mainly in the yellow–orange range of the spectrum. The first report, by Ammann in 1979 [83], demonstrated conversion at five different visible wavelengths. These five waves came from SHG or SFG of the intracavity oscillating fields, fundamental, 1st Stokes and 2nd Stokes. In 2008, an exhaustive review [75] was done of visible Raman lasers. Until that moment the best result of visible pulsed Raman laser was 3.14 W of average power using a Nd:YAG/BaWO₄/KTP system emitting at 590 nm [84]. For the CW systems, 704 mW (5% of efficiency) [85] was the maximum output power obtained. However, in this case, when the duty cycle of the pump was changed to 50%, the output power had a significant increase to 1.57 W, corresponding now to an efficiency of 7.9%. It exposed once more the fragility of Raman laser systems under thermal stress.

Post 2008, in the pulsed domain, in 2009 an average power of 5.7 W at 588 nm was reported [86]. The improvement obtained in this work came from the use of a composite Nd:YVO₄/YVO₄ crystal, which provided a better thermal management. The same group optimized their results in the end of the same year, when they reported 7.9W at the same previous wavelength. The use of a double-end diffusion bonded Nd:YVO₄ crystal scaled up the performance of such a laser, showing a diode to yellow conversion efficiency of 30% and a slope efficiency of 43% [87]. This is the highest average power reported until the present moment in pulsed intracavity doubled Raman lasers.

Exploring the CW regime, Lee *et al* reported in 2008 an output power of 2.51 W at 586.5 nm doubling a Nd:GdVO₄ self-Raman laser [88]. Early in 2010, the same group demonstrated 2.9 W using BaWO₄ Raman crystal, which has almost twice the Raman gain coefficient of GdVO₄ [81]. The highest output power and conversion efficiency so far, in CW regime, comes from the sum frequency mixing process done in a Nd:GdVO₄ self-Raman laser. The LBO crystal was temperature tuned to reach the phase matching between 1064 nm and 1176 nm, generating a lime-green emission at 559 nm. It delivered an output power of 5.3 W with 21% of diode-to-visible conversion efficiency [69].

Some of the latest results in the field show the versatility of the visible Raman lasers. By means of the Nd:GdVO₄ self-Raman configuration, which showed the best result up to date, multi-Watt operation was demonstrated for three visible wavelengths [89]. The results follow in the Table 4.

Table 4. Parameters of the multi-wavelength laser [89].

	Conversion type	Max power	Diode-visible conversion	LBO temperature (deg C)
Green: 532 nm	SHG: 1064 nm	4.6 W	16%	155
Lime: 559 nm	SFG: 1064+1176 nm	5.3 W	20%	95
Yellow: 586 nm	SHG: 1176 nm	4.3 W	17%	45.5

Recently, CW 2nd Stokes laser was demonstrated using a Nd:GdVO₄ self-Raman set up [90]. As a result, around 950 mW of output power was extracted at 1308 nm corresponding to a conversion efficiency of 6.8%. Introducing a LBO crystal in the cavity, 1027 mW (4.9% diode-visible conversion efficiency) was obtained in the red, 620 nm, by means of SFG. Such results expand even more the versatility of the visible Raman lasers.

State of the art and future trends

There are many topics in crystalline Raman lasers to be further developed and understood yet. New materials have been constantly introduced to the field, bringing new options and characteristics to the Raman lasers. The diamond itself is not fully explored yet and is the most promising material for Raman, so a major effort is given to its development, particularly in terms of high optical quality production.

Power and efficiency scaling still have plenty of room to evolve. Therefore, there are several works concentrated on how to extract the maximum of the already existing Raman lasers. Direct thermal lens characterization of self-Raman lasers (Nd:GdVO₄) [91], and separated crystal (BaWO₄) configurations were recently reported [92], with the idea to understand better the influence of the composite lens in the resonator. Also, more efficient pump geometries have been explored, such as double polarized end pumping [93], which

improves the spatial overlap between pump and laser mode, and dilutes the thermal load over the whole crystal. Disk laser geometries and the use of crystals with weaker thermal lensing, such as is this work (Nd:YLF), are other approaches to improve the performance of the Raman lasers.

In terms of beam quality, the lasers demonstrated with multi Watt outputs also generally present very poor beam quality. One of the trends to improve the beam quality of these lasers is demonstrated in this thesis, with the use of Nd:YLF as the laser active medium, due to its weak thermal lensing.

Theoretical and experimental analysis of SRS competition with other effects is also under study and would improve the performance or even help forming new ideas. Analysis of the competition between SRS in laser and Raman crystals has been reported, and also between different Raman transitions [94].

There is still room for new wavelengths, coming with new materials or new combinations such as the ones demonstrated here, Nd:YLF/BaWO₄ and Nd:YLF/KGW. This versatility of the Raman lasers must be further explored.

Finally, the losses are one of the biggest issues for such very low gain lasers. The minimization of the losses for the Stokes wavelength in these lasers increased a lot their performance, as shown also by the modeling work published by Spence *et al.* [95]. An interesting approach to reduce the Stokes loss is to use coupled cavities, in which the Stokes mode does not pass through the laser crystal, thus removing the losses from the coating and possible optical defect in that crystal [96]. In this thesis, we have studied another possible loss mechanism present in some Raman lasers. It is a blue fluorescence that emanates from the Raman crystal above SRS threshold. By understanding the mechanism which feeds the blue fluorescence, one can find the way to avoid it, thereby improving the laser performance.

Nd:LiYF₄ lasers and their advantages for a Raman laser

Raman lasers using Nd:LiYF₄ (Nd:YLF) as active medium have been reported few times although this material deserves more attention as it adds some interesting characteristics to the existing crystalline Raman lasers. One of its features is that the radiative transitions occur at shorter wavelength than in other neodymium doped crystals used in Raman

resonators, namely at 903 nm, 908 nm, 1047 nm, 1053 nm, 1313 nm and 1321 nm. This characteristic permits new Raman wavelength at either the near infrared or in the visible spectral range, which is very interesting from the applications point of view. Additionally, this crystal presents two emissions (σ and π) with different energies from the same transition, which can be accessed simply by changing the polarization of the propagating wave, permitting two first-Stokes emissions with differing wavelengths. Moreover, the thermal lensing behavior of Nd:YLF is peculiar, since the refractive index change as a function of temperature is negative which partially compensates the positive lens generated by the bulging of the crystal end facet. For this reason Nd:YLF presents a very weak thermal lens, which favors a good beam quality even with high pump powers and also very good resonator stability [97, 98, 99]. This is in stark contrast to other high gain media whose output power is limited by the onset of resonator instabilities caused by the strong thermal lens. However, there is a drawback to YLF which is its small thermal fracture limit (33MPa) [22] that is 5 times smaller than in Nd:YAG.

A most interesting feature of the Nd:YLF crystal is its long upper state lifetime of 520 μ s. Many Raman lasers work in a Q-switched mode [100, 101, 102, 103, 104, 105], where the longer upper-laser-level lifetime is of great importance and should permit higher conversion efficiencies than other crystals, e.g. Nd:YAG (\sim 230 μ s), Nd:YVO₄ (\sim 100 μ s) and Nd:GdVO₄ (\sim 95 μ s) [106].

Table 5 shows the first-Stokes and second harmonic wavelengths expected when using Nd:YLF as active medium and four different Raman crystals operating on the $^4F_{3/2} \rightarrow ^4I_{11/2}$ transition.

Table 5. First-Stokes emissions generated from the fundamental Nd:YLF emissions at 1047 and 1053 nm for four of the most used Raman crystals.

Laser crystal	Raman crystal/ Raman shift (cm ⁻¹)	Fundamental emission / Energy (cm ⁻¹)	First stokes emission (SRS)	Second harmonic (SHG)
Nd:YLF	YVO ₄ / 892	1047 nm / 9558	1154 nm	577 nm
	GdVO ₄ / 885		1153 nm	576.5 nm
	KGW / 901 and 768		1155 nm e 1137 nm	577.5 nm e 568.5 nm
	BaWO ₄ / 926		1159 nm	579.7 nm

YVO ₄ / 892	1053 nm / 9502	1161 nm	581.7 nm
GdVO ₄ / 885		1160 nm	580.2 nm
KGW / 901 and 768		1162 nm e 1144 nm	581.3 nm e 572.1 nm
BaWO ₄ / 926		1167 nm	583 nm

1.6. Thesis outline

This work is a dedicated research about the use of Nd:YLF within low gain laser systems, specifically quasi-three level Nd lasers with and without frequency doubling, and crystalline Raman lasers with or without frequency doubling. These kind of lasers have as a main issue the need for very low loss resonators, pushing the coating technologies and high optical quality crystal growth to their limits. While these requirements make these lasers very expensive, these lasers provide output at wavelengths that are hard to reach by other means, including the deep blue and the yellow-orange spectral regions.

Two types of low gain laser systems are studied in this research; quasi-three level Nd:YLF lasers operating at 908 nm; and Raman lasers using Nd:YLF as active medium operating at 1.1 μm . Furthermore, these lasers are doubled in frequency to reach the visible range in the blue and yellow-orange spectral region. In addition, a possible source of loss for Raman lasers is also studied, characterized by a blue luminescence originated in the Raman crystals above the Stokes lasing threshold.

Following this introduction, chapter 2 describes the general methods and equipment used to develop this research. Chapters 3, 4 and 5 contain the experimental research with results and discussion on their developments and achievements. Chapter 3 is related to the Nd:YLF quasi-three level laser operating at 908 nm and also its conversion to the blue range. Chapters 4 and 5 are dedicated to the Raman lasers, with the first one showing the performance of two different Raman lasers (Nd:YLF/KGW and Nd:YLF/BaWO₄) and the last one showing the investigation of a blue luminescence originated in many Raman crystals under Stokes oscillation. This blue luminescence had been observed in several Raman lasers but was not characterized in depth so far. Chapter 6 has the conclusions and suggestions for future works.

Finally, there are four appendixes. Appendix A brings the MathCad worksheets used for the calculations in the thesis. Appendix B has the coating data for the mirrors,

Appendix C the full data of the ICP-MS measurements and in the Appendix D the publications generated during the PhD.

Chapter 2

General methods

- 2.1. Laser crystals**
- 2.2. Raman crystals**
- 2.3. Doubling crystals**
- 2.4. Mirrors**
- 2.5. Pump sources and schemes**
- 2.6. Cooling systems**
- 2.7. Resonator design assisted by software**
- 2.8. Characterization methods and equipment**

2. General methods

This chapter describes the general methods and apparatus used throughout this thesis. It starts showing the characteristics of crystals, mirrors, diode lasers, the schemes used for pumping the lasers, mounts, and cooling system, after that it introduces the computer assisted laser cavity simulation software (LASCAD) and finishes describing the equipments and facilities used for characterization.

2.1. Laser crystals

The main laser crystal used in this work was the Nd:YLF and will be the focus of this subsection, although other lasers were built using Nd:GdVO₄ and Nd:YAG for the blue fluorescence experiments. Basically, four different a-cut (cut along the crystalline a-axis) Nd:YLF crystals were used for the different experiments performed.

For the quasi-three level experiments, two crystals were used. The one used for quasi-CW operation has dimensions of $3 \times 3 \times 10 \text{ mm}^3$, with Nd³⁺ doping concentration of 0.7 at%. The other one used for CW regime has dimensions of $3 \times 3 \times 15 \text{ mm}^3$ with the same doping concentration of the previous one. Both crystals have the same coatings on their end faces, characterized by low reflectivity at 903 nm, 908 nm ($R < 0.1\%$), 806 nm ($R < 0.5\%$), 1047 nm/1053 nm ($R < 0.3\%$) and 1313 nm/1321 nm ($R < 4\%$). These crystals and coatings were produced by Crystech Inc. (China).

For the Raman laser experiments, other two variations of Nd:YLF were used. One has dimensions of $4 \times 4 \times 15 \text{ mm}^3$, with Nd³⁺ doping concentration of 1 at%. The other one has the same dimensions and doping concentration, with the difference that one of the end faces is Brewster cut with no coating. The coated faces of both crystals have the following characteristics: Low reflectivity at 1047 nm/1053 nm ($R < 0.2\%$), at 1135-1170 nm ($R < 0.1\%$) and at 881 nm ($R < 5\%$). These crystals were also produced by Crystech Inc. (China).

2.2. Raman crystals

For the Nd:YLF Raman lasers developed in this work two different Raman crystals were used , a BaWO₄ crystal and a KGW crystal.

The BaWO₄ crystal has dimensions of 4×4×25 mm³, and was cut for propagation along the a axis (a-cut). The coatings on its end faces were low reflectivity at 1047-1180 nm (R<0.2%). This crystal was obtained from the collaboration with the State Key Laboratory of Crystal Materials and Institute of Crystal Materials, Shandong University - China, by means of Prof. H. Zhang and Prof. J. Wang.

The KGW crystal has dimensions of 4×4×25 mm³, and was cut for propagation along the N_p refractive index axis. The coatings on its faces had low reflectivity at 1047 nm/1053 nm (R<0.2%) and at 1064-1170 nm (R<0.1%). This crystal was produced by EKSMA Optics (Lithuania).

2.3. Doubling crystals

LBO (LiB₃O₅) and BiBO (BiB₃O₆) were the non-linear crystals used in this work to achieve second harmonic generation and sum frequency mixing.

For the blue laser project, both LBO and BiBO were explored in three different lengths (3×3 mm² - 10, 15 and 20 mm long). They were all cut for type-I critical phase matching. The main parameter of LBO and BiBO crystals for doubling of 908 nm is shown in the Table 6. Their end face coatings are characterized as follow: Low reflectivity at 903 nm/908 nm (R<0.1%), at 1047 nm/1053 nm (R<2%) and at 451 nm/454 nm (R<0.3%). Cstech Inc. was the crystal provider.

Table 6. LBO and BiBO type-I non-linear parameters for 908 nm at 300 K [107].

	LBO	BiBO
Transparency (nm)	160-2600	286-2500
d _{eff} (pm/V)	0.80	3.45
Acceptance angle (mrad·cm)	4.45	1.10
Walk-off angle (mrad)	12.7	45.7
Cut at θ / ϕ (°)	90 / 22.2	159.2 / 90

In the frequency doubled Raman lasers, LBO with dimensions of $4 \times 4 \times 10 \text{ mm}^3$ was used in all the cases. In this case, LBO was cut for type-I non-critical phase matching. The coating of such crystal is as follow: Low reflectivity at 1047 nm/1053 nm ($R < 0.2\%$), at 1150-1180 nm ($R < 0.1\%$) and at 550-590 nm ($R < 1\%$). Table 7 shows the LBO non-linear parameters for the three Stokes wavelengths obtained in this work.

To reach the phase matching condition, the LBO crystal was heated up. For temperatures up to 63°C , a TEC (thermoelectric cooler) was used to control and keep the temperature stable. For higher temperatures, a resistor was the source of the heating. Both the TEC and the resistor were set in direct contact with the copper mount of the crystal.

Table 7. LBO type-I non-critical phase matching parameters for all the Raman conversions found in this work [107].

LBO	SHG (1147 nm)	SHG (1163 nm)	SHG (1167 nm)	SFG (1053+1147 nm)	SFG (1053+1163 nm)
d_{eff} (pm/V)	0.84	0.84	0.84	0.84	0.84
Acceptance angle (mrad·cm)	286.1	150	142.8	290.2	209.3
Walk-off angle (mrad)	-	-	-	-	-
Non-critical phase matching temperature ($^\circ\text{C}$)	63	50	48	109	101

2.4. Mirrors

A variety of resonator mirrors were used in this work. In order to better organize and show the most important ones, they are set out below in a list of topics. They were available in different radii of curvature, from flat to 500 mm concave (diameters of 1", $\frac{1}{2}$ " or $\frac{1}{4}$ "). The spectral data of all the mirrors used in this work can be found in the Appendix B.

- **Mirrors for the 908/454 nm lasers (Layertec GmbH - Germany):**
 - ✓ Pump mirror: High reflectivity at 908 nm ($R \sim 99\%$); Low reflectivity at 806 nm ($T \sim 5\%$), at 1047/1053 nm ($T \sim 2\%$), at 1314/1321 nm ($T \sim 5\%$) and at 454 nm ($T > 98\%$);
 - ✓ Output coupler: same as the pump (the coupling was not made by a mirror in the experiments at 908 nm);
 - ✓ Visible output coupler: same as the pump one, $T > 98\%$ at 454 nm.
- **Mirrors for the Raman lasers (ATFilms - USA):**
 - ✓ Pump mirror: High reflectivity at 1047/1053 nm ($R > 99.99\%$) and at 1150-1180 nm ($R > 99.99\%$); Low reflectivity at 806 nm ($T \sim 98\%$), at 881 nm ($T \sim 96\%$), at 560-579 nm ($T > 75\%$) and at 580-590 nm ($T > 94\%$);
 - ✓ Intracavity mirror: High reflectivity at 530-590 nm ($R > 97\%$); Low reflectivity at 1047/1053 nm ($R < 0.1\%$) and at 1160-1190 nm ($R < 0.1\%$);
 - ✓ Output coupler for 1st Stokes: High reflectivity at 1047/1053 nm ($R > 99.9\%$); Transmissions at 1147 nm ($T \sim 0.1\%$) and at 1160-1170 nm ($T \sim 0.3\%$);
 - ✓ Visible output coupler: same as the pump mirror; Transmission at 560-579 nm ($T > 75\%$) and at 580-590 nm ($T > 94\%$);

2.5. Pump sources and schemes

Fiber-coupled diode lasers were used as the pump sources for the lasers developed in this work. Two diodes with different characteristics were chosen to pump Nd:YLF, one emitting at 806 nm and another emitting at 881 nm for direct pumping.

The 806 nm diode (Apollo Instruments Inc. –USA) has a fiber coupled to it which has a core diameter of 100 μm , and it was able to provide up to 50 W of CW output power. The numerical aperture (NA) of the fiber is of 0.22. It also operates in pulsed mode, using

an internal module for the temporal modulation ($>100\ \mu\text{s}$ pulses / up to 1 kHz). This diode is water cooled, which is done by means of a temperature controlled chiller. It was used to pump the Nd:YLF quasi-three level laser.

The other diode emits at 881 nm (LIMO GmbH - Germany) and was used to pump the Raman lasers. This one is able to deliver CW output powers up to 40 W and was coupled to a fiber with 100 μm of core diameter and 0.22 of NA. It was cooled by a thermoelectric cooler (TEC) which gives more precision and stability to the temperature set.

Various pump optics were needed to focus the beam coming out from the fiber into the crystals. For that, a set of two lenses are used. The first lens is introduced to collimate the beam from the fiber, while the second one focuses the collimated beam in the laser crystal. Those lenses have anti-reflective coatings to reduce the reflection losses and deliver pump powers as close as possible to what comes out of the fiber. This type of pump scheme is mostly used in longitudinally pumped lasers, as shown in Figure 31, where high pump intensities are needed.

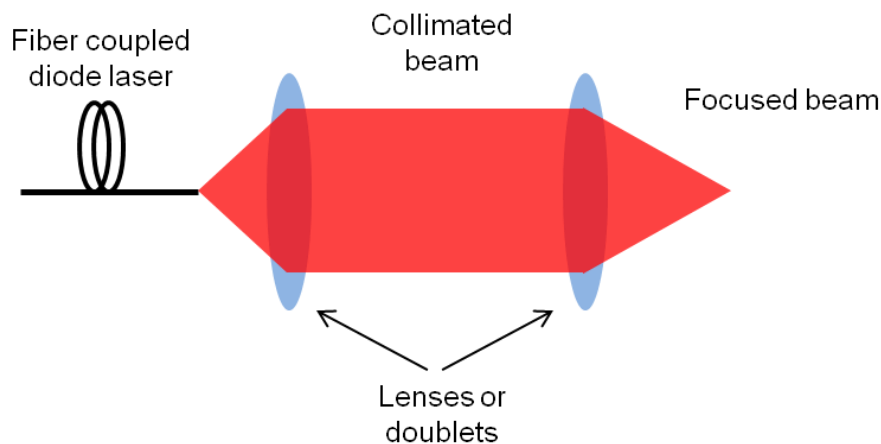


Figure 31. Fiber coupled diode laser longitudinal pumping scheme.

Achromatic doublets were used in the quasi-three level lasers, which reduces chromatic aberration then providing smaller beam waists.

2.6. Cooling systems

As the lasers developed in this work are made to operate under high power conditions, it is essential to have powerful and efficient cooling systems. For that, temperature controlled water was pumped through diode laser and crystal mounts by means of a chiller.

The crystal mounts are made of copper and have internal channels for water flowing. This flow of cool water takes out the heat generated in the crystal due the laser operation. To remove heat from the crystal is of extreme importance, as it helps to keeping the thermal lens as low as possible and to avoiding thermal fracture. In addition, in the case of the quasi-three level lasers, cooling is necessary to decrease the laser medium temperature reducing the population of the upper Stark levels in the lower laser level, thus decreasing the reabsorption loss.

For the laser diodes, the cooling is not only required to avoid damaging them, but it also can be used to temperature tune the diode emission within a short range (± 5 nm). This enables the diode emission to be set exactly on the absorption peak of a specific active medium, consequently increasing absorption efficiency. In this case, both water and TEC cooling systems were used, given that the second one needs some type of low rate heat extraction system coupled to it in order to dissipate the heat transferred to the bottom plate (generally a low pressure water flow through a copper mount coupled to the TEC cooler mount is enough).

2.7. Resonator design assisted by software

To design the resonators we have used the software LASCAD (Las-cad GmbH). This software is able to perform simulation of the transverse mode size formed in the cavity by means of ABCD Gaussian beam propagation. Also, there is a finite element analysis (FEA) package that we used to simulate the thermal lens created by the pump beam in the laser crystal. The simulated thermal lens can then be incorporated into the ABCD resonator model to understand its impact on the resonator stability under different pump conditions.

LASCAD enables the insertion of other intracavity optical elements such as thin lenses and refractive index interfaces. It can also treat the horizontal and vertical transverse

planes separately, allowing simulation of astigmatic beams. The stability point of the cavity is plotted in the stability diagram if desired.

2.8. Characterization methods and equipment

In this sub-section, the main instruments and pieces of equipments used for this research are described.

2.8.1. Cary-5E Spectrophotometer

In order to measure precisely the absorption of the laser crystals, as well as the transmission and reflectance of the crystal coatings and resonator mirrors, a Cary-5E spectrophotometer was used. Such equipment provides a wide spectral range for these measurements, from 175 nm to 3300 nm, with a maximum resolution of 0.01 nm in the ultraviolet-visible range and 0.04 nm in the near infrared.

As in this work we were interested in polarized spectral data, and there was not any internal mechanism in the Cary-5E to enable polarized spectra to be recorded, additional polarizing optics were inserted, such as polarizing prisms. The spectra were generally recorded with resolution of 0.5 nm for measurements over a wide spectral range (>100 nm) and around 0.1 nm when measuring features over narrower spectral range (20-50 nm), eg in the case of absorption of laser crystals.

2.8.2. Portable optical spectrometers

For non-absolute spectral intensity distribution measurements, two types of portable optical spectrometers were used. They were made by Ocean Optics. Inc, and were generally used to monitor the wavelength of the diode lasers and the solid-state laser emissions.

An USB-2000 was used to measure the wavelengths in the range of 200-1100 nm, with a resolution of 0.3 nm. This was used to measure the visible emissions of the frequency doubled lasers, the diode emission around 0.8 μm and the fundamental laser emissions around 1 μm .

Another spectrometer, the HR-4000, was used for measurements in the near infrared range from 1050 nm to 1200 nm, with a high resolution of 0.09 nm. Therefore, it

was mostly employed to measure the spectrum of the Stokes lines, which were around 1.17 μm , although also it was still able to measure some of the fundamental lines, such as 1053 nm (Nd:YLF) and 1064 nm (Nd:GdVO₄ and Nd:YAG). In addition, it could measure the visible lines with very high resolution, using the second diffraction order of the diffraction grating.

2.8.3. Laser Ablation Inductively-Coupled-Plasma Mass-Spectrometry (LA-ICP-MS)

The ICP-MS technique is a very well known method to quantify the elements contained in a specific material. The principle of this method is to ionize the sample with inductively coupled plasma, whose ions will be separated and quantified by a mass spectrometer.

The one used in this work, which belongs to Macquarie University Geochemical Analysis Unit (GAU), has a Laser module coupled to the ICP-MS. Such laser is responsible to ablate solid samples, whose mass goes to the plasma torch of the ICP-MS. Given that, it is possible to characterize the elements of solid materials, such as crystals, with very low detection limits. Figure 32 shows a schematic view of a traditional LA-ICP-MS.

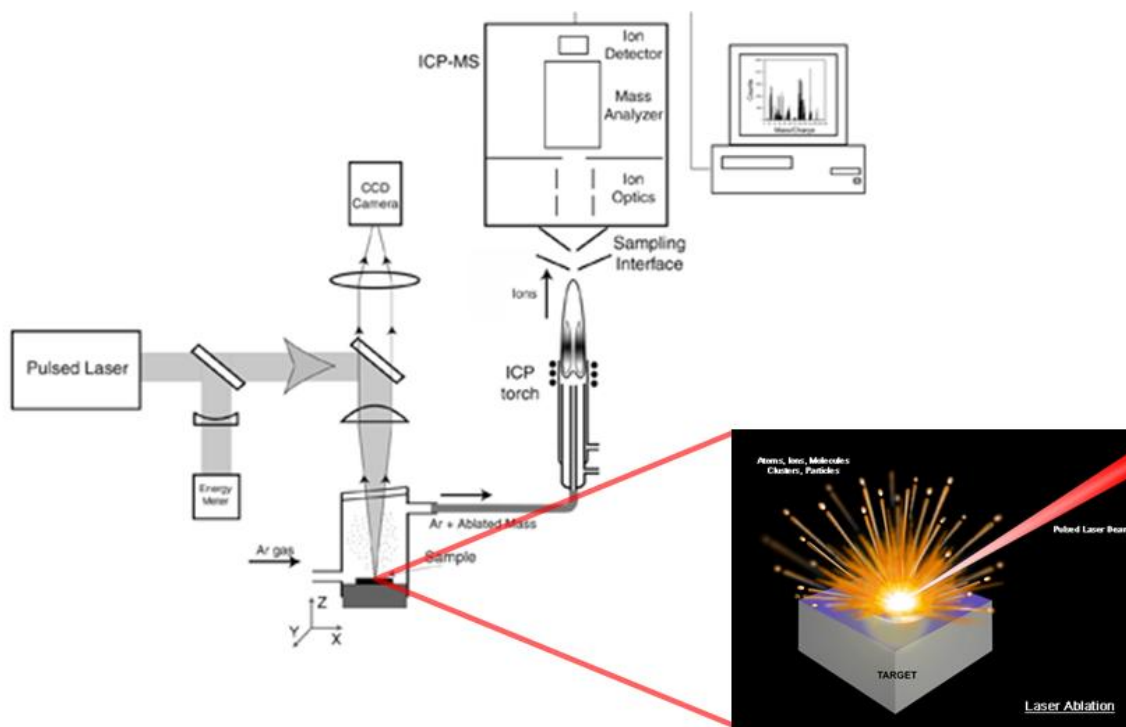


Figure 32. LA-ICP-MS operation scheme [108, 109].

The model used in this work is a 7500 ICPMS (Agilent), and it was used to characterize rare earths concentration in the Raman crystals, mainly Tm^{3+} and Nd^{3+} , in order to find the origin of the blue fluorescence described in Chapter 5. Three different spots were measured in the crystal slabs, two close to the faces and one in the middle, Figure 33. More than one layer must be removed by the ablation process before the data acquisition, since the surfaces of the crystals are very susceptible to having a higher concentration of impurities.

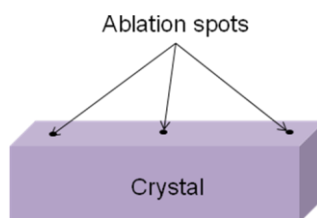


Figure 33. Position of the ablation spots in the crystal sample.

2.8.4. Raman spectrometer

The Raman spectra found in this work were obtained using a RENISHAW-IN VIA Raman spectrometer, located at the University of Sydney. This Raman spectrometer is composed by three main parts: the laser source; the microscope; and the spectrometer.

The laser sources available could deliver five different wavelengths, 488 nm, 514 nm, 633 nm, 785 nm and 830 nm. For the tested samples, the 514 nm line (Argon laser) was chosen, in order to avoid absorption by the materials at shorter wavelengths.

The laser was delivered to the sample using a microscope, which gives very small beam waists, therefore very high excitation intensities, resulting in high Raman scattering signal.

In the spectrometer the scattered light passes through a notch filter, which avoids that the excitation light gets in the detection zone, and then through a diffraction grating which disperses the wavelengths. Each wavelength will be detected in different pixels of a CCD (charge-coupled device) array. The spectral resolution is of 1 cm^{-1} . It is a system fully controlled by computer. Figure 34 shows the light path through the spectrometer from the light source to the detection of the scattered light into the CCD.

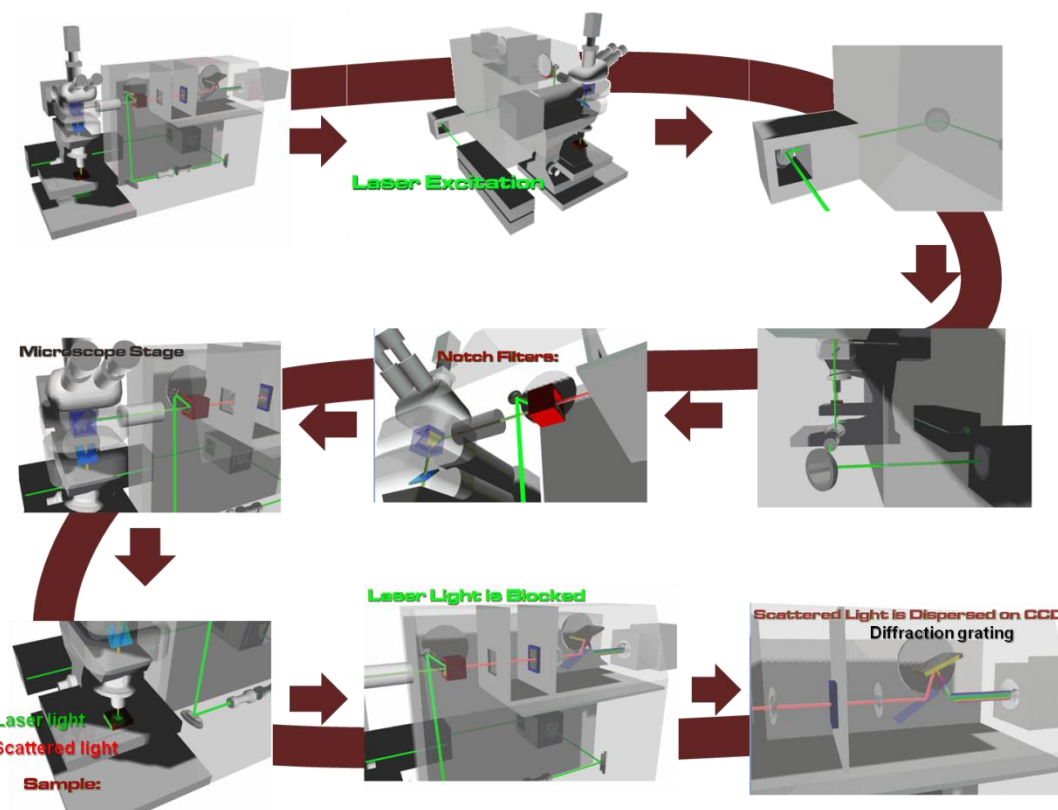


Figure 34. Inside the RENISHAW-INVIA Raman spectrometer [110].

2.8.5. Beamscope

The beam quality of the lasers are an important parameter to be characterized. For this purpose a beamscope (Gentec Beamscope-P7) was used to measure the M^2 of the lasers built. Using two slits that move on the x-y plane of the beam, such beamscope can measure the diameter of the beam in a specific point of the z direction. In this work, the beam scope was associated to an automatic translation stage, which translated the beamscope module on the z axis, providing then a range of beam diameters in the z direction. This data was then analysed and fitted using the data analysis software Origin (OriginLab Corp.), or the beamscope software to determine M^2 .

This specific beamscope can measure beam sizes of 3 μm to 25 mm (interchangeable slits), and the wavelength range depends on the detector, which can be Silicon, Germanium or Indium Arsenide, covering the range of 190-4000 nm. Also, it can measure both CW and pulsed lasers (>5 kHz).

2.8.6. Power meters

The output powers of the lasers were characterized using power meters and different heads, for different range of powers. Two power meters were used for that, one is the PM100A (Thorlabs), whose power range goes from 100 pW to 200 W, limited by the head coupled to it. The other power meter used was a PM100D (Thorlabs), which features a big digital display and operates in the same range as the previous one.

Different heads were used depending on the range of output powers. For diode laser characterization up to 10 W and all the solid-state lasers built, the thermopile head S310C (Thorlabs) was the chosen one, since it operates from 10 mW to 10 W, with a resolution of 200 μ W. For output powers up to 25 W, a MPE-2500 (Spiricon) power meter was used. Another head used was an 818P-150 (Newport) employed for powers up to 150 W (water cooled), generally used to characterize diode lasers with output powers as high as 50 W.

2.8.7. Photomultiplier tube

A photomultiplier tube (PMT) was employed to characterize the lifetime of the blue fluorescence, discussed in Chapter 5. The reason why a PMT was used instead of the traditional fast detectors, is that the intensity of the light measured was too weak, only detectable by a very high sensitivity detector, such as the PMTs.

The one chosen for this purpose was a R446-Hamamatsu photomultiplier tube. Such PMT has a high sensitivity at the blue region, and response time of few ns. As the expected emitting level lifetimes are of the ms order, this PMT was adequate to the measurements. Figure 35 shows the spectral response of the R446 PMT.

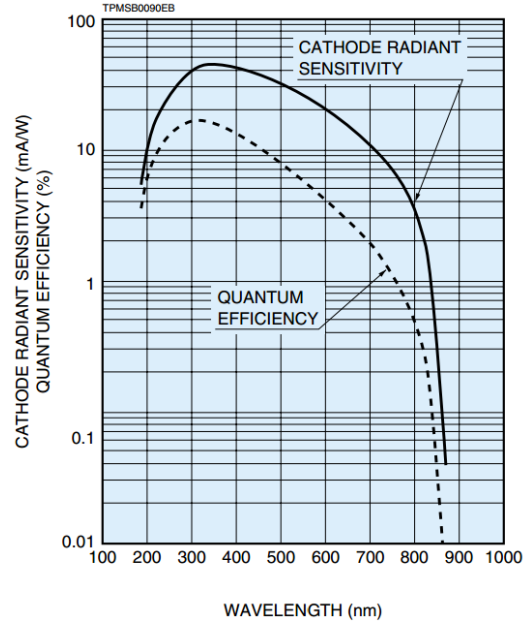


Figure 35. Spectral response of the R446 PMT [111].

2.8.8. Oscilloscope

For temporal analysis, a digital oscilloscope (Tektronix TDS 3054) was used, Figure 36. The lifetime measurements were all observed and recorded by means of this oscilloscope, which can output data by means of a floppy disk. It has a bandwidth of 500 MHz and has a sampling rate of 5 GS/s.



Figure 36. Oscilloscope Tektronix TDS 3054 [112].

2.8.9. Integrating Sphere

In order to estimate the blue fluorescence power originated in the Raman crystals, an integrating sphere was used. The one chosen is produced by Labsphere Inc, and it has a diameter of 9.5 cm, four ports and a Spectrafect coating on the internal wall (Figure 37(a)). The Spectrafect coating is a white coating which presents diffuse reflectivity in a wide range of wavelengths (350-2400 nm), as shown in Figure 37(b).

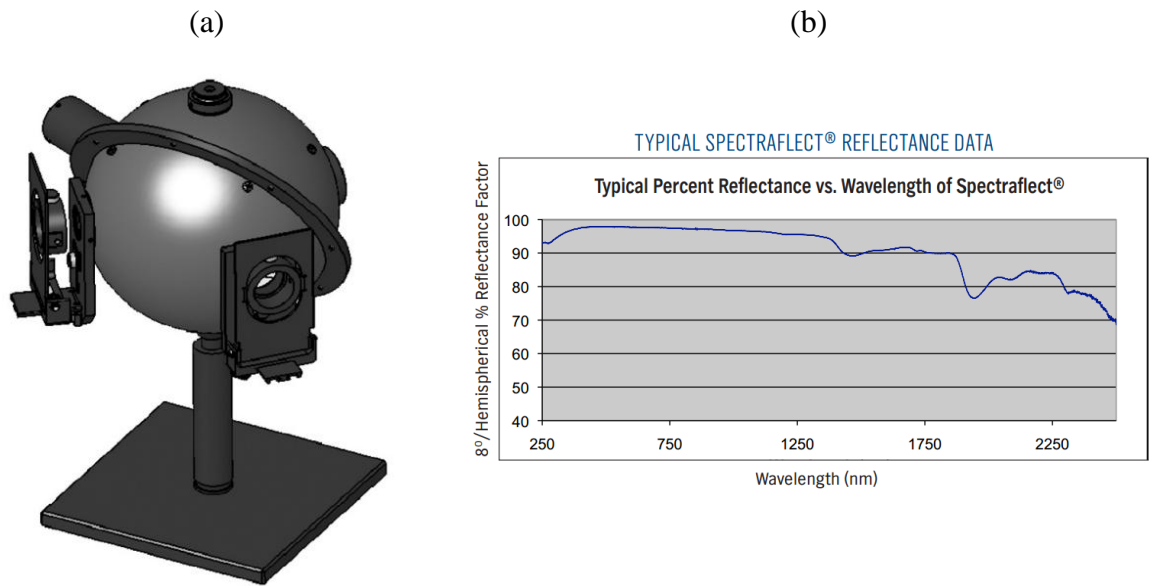


Figure 37. (a) Integrating sphere and (b) the Spectrafect coating reflectance [7, 8].

The principle of the integrating sphere is based on diffuse reflectance. Considering a light source inside the sphere, its light rays incident on any point of the internal surface of the sphere will lose spatial information by means of diffuse reflection, and then after multiple reflections, the intensity is going to be distributed equally in all the points of the sphere (Figure 38). Using ports to couple in or couple out some amount of light, it is possible to estimate precisely the total power produced by the light source.

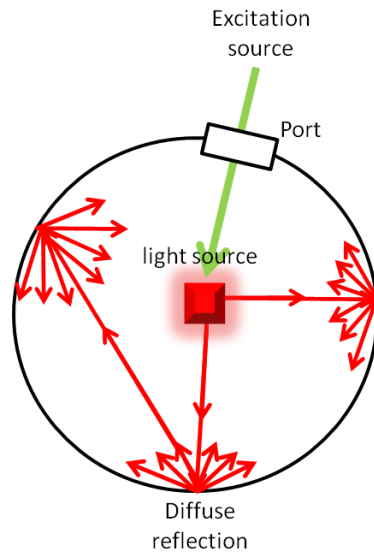


Figure 38. Integrating sphere scheme showing the diffuse reflection.

Chapter 3

Nd:YLF quasi-three level laser

- 3.1. Quasi-CW laser operation at 908 nm and at 454 nm**
- 3.2. CW laser operation at 908 nm and at 454 nm**
- 3.3. Discussion**

3.Nd:YLF quasi-three level laser

In this section the Nd:YLF quasi-three level lasers are described. The experimental setup, operation and the results obtained for the quasi continuous operation (quasi-CW) are shown, followed by the continuous wave operation version of this laser. The last part of the chapter brings a summary and a deep discussion regarding the results obtained in this work, theory and other similar lasers found in the literature.

3.1. Quasi-CW laser operation at 908 nm and at 454 nm

In this section we describe the quasi-three level Nd:YLF laser operating in quasi-CW mode, ending with deep blue laser generation.

The $^4F_{3/2} \rightarrow ^4I_{9/2}$ Nd³⁺ transition in the YLF crystal, which terminates at the upper Stark level of 529 cm⁻¹, emits at 903 nm (π) and at 908 nm (σ). These emission wavelengths are shorter than those found in the most common crystals used for the same purpose such as Nd:YAG (946 nm), Nd:YVO₄ (914 nm) and Nd:GdVO₄ (912 nm), allowing Nd:YLF lasers to reach deeper blue wavelengths by means of SHG. This fact associated to YLF's interesting properties described in the introduction, served as the motivation for this study.

A Nd:YLF crystal with dimensions of 3x3x10 mm³ and Nd³⁺ doping concentration of 0.7 at% was acquired for such purpose. This crystal presents AR coatings at 806 nm (T>90%), 903/908 nm (T>99%), 1047/1053 nm (R<5%) and at 1.3 μ m (T<10%). In fact, the coating becomes complex because of the various distant regions that it has to cover. any parasitic oscillation at other than the 0.9 μ m Neodymium transitions must be avoided. Finally, the crystal is wrapped in an Indium foil and inserted in a cooper mount for cooling purposes, as show in Figure 39.

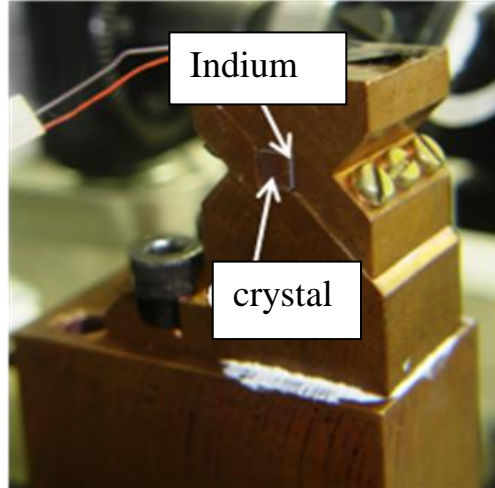


Figure 39. Nd:YLF crystal support.

Water flows inside the mount, and keeps it cooled to about 10°C. This is an especially important step, since the lower laser level is populated at room temperature, and a few degrees cooler crystal temperature can aid reducing this population and thus the reabsorption losses.

The pump system used was composed of a fiber-coupled diode laser (Apollo Instruments-USA) emitting around 808 nm, with a fiber core diameter of 100 μm and a numerical aperture of 0.22. The nearest absorption peak of Nd:YLF to 808 nm is at 806 nm and can be reached by temperature tuning of the diode, as show in Figure 40. A 50.8 mm focal length doublet was used for collimation of the fiber output and a 200 mm focal length doublet was used for focusing the beam inside the crystal. This pump injection scheme delivered 50 W of diode power with a beam waist of 225 μm . This beam size was chosen in order to optimize the gain inside the crystal and at the same time maintain good overlap between the lowest order resonator mode and the pump beam.

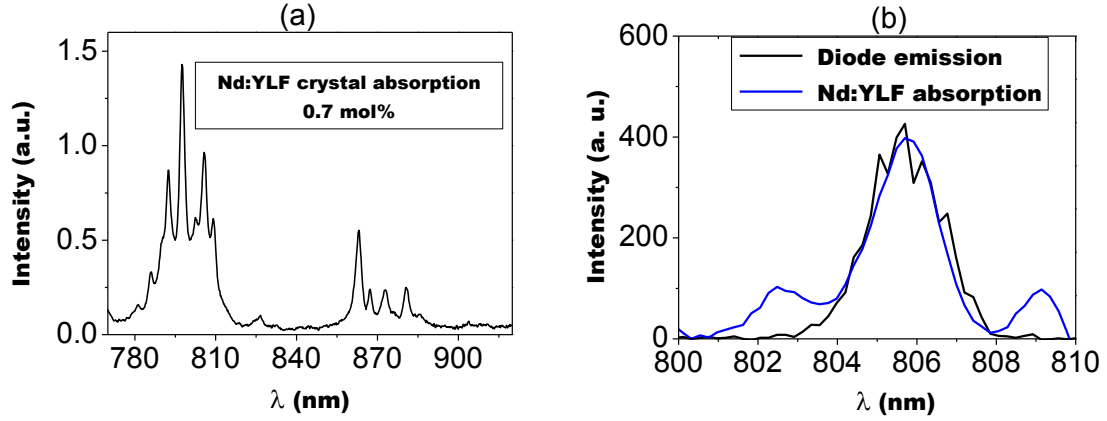


Figure 40. (a) Absorption spectrum of the Nd:YLF and (b) the overlap of its absorption with the diode emission.

Before starting to build the quasi-three level laser, a very simple laser operating at the 1053 nm transition was built in order to investigate the maximum pump power the crystal could support. For this experiment, a very short plane-parallel cavity was built with HR mirrors and the diode laser tuned to reach 806 nm at 11 W of optical power. The absorption at this wavelength is 90%. Next the incident pump power is increased in CW operation until a rollover can be noticed in the curve of output power against absorbed power. At this point the thermal lens is so strong that the cavity becomes unstable and therefore decreases its output power until, eventually, the Nd:YLF crystal breaks. In the case of this particular host crystal, the onset of a rollover as a function of pump power occurs very close to crystal fracture whereas in other, more robust crystals the rollover occurs much before crystal fracture.

The cavity was then modified to resonate the 908 nm or the 903 nm transition. The laser was operated in a quasi-CW regime with a duty cycle of 3% and pulse duration of 2 ms. This way, the thermal load deposited, which is proportional to the average pump power, becomes very low and the crystal can be pumped at much higher peak powers than the maximum it could support during CW regime. Given the low thermal load, it was possible to keep the wavelength the same throughout the whole pump power range.

The diode was tuned to 806 nm (32°C water temperature) and the cavity was mounted using a flat pump mirror, and a curved end-mirror with 100 mm ROC, both AR-coated at 806 nm and 1047/1053 nm and HR-coated at 903/908 nm, Figure 41. The most

efficient cavity length was determined experimentally, which was 9 cm long for this specific configuration.

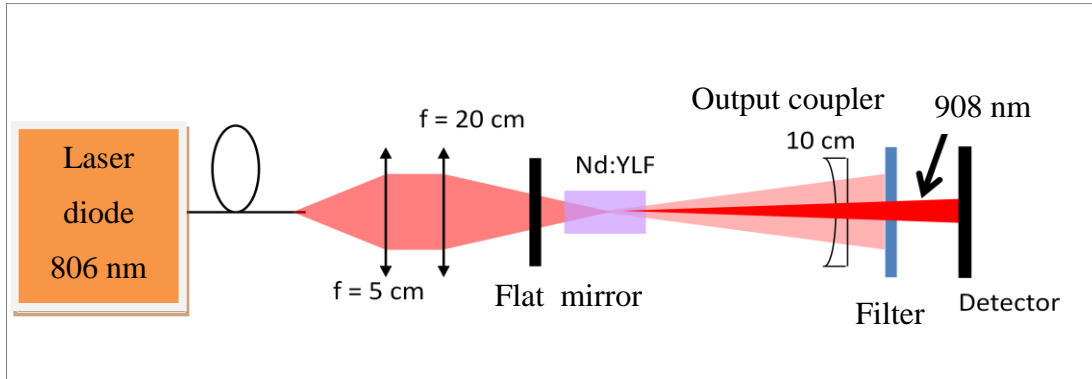


Figure 41. 0.9 μm laser setup.

In order to determine the optimum output coupling, a Brewster window was introduced in the cavity. This window was made of Quartz, whose refractive index is well known (1.46), with very good surface quality to not introduce extra losses to the oscillating field. The window together with the end-mirror acted as an output coupler for the linearly polarized laser. By rotating the window it was possible to tune the reflectivity of the output coupler from 0% at Brewster angle (angle of incidence of 56°) to more than 20%. Figure 42 shows the setup for this experiment.

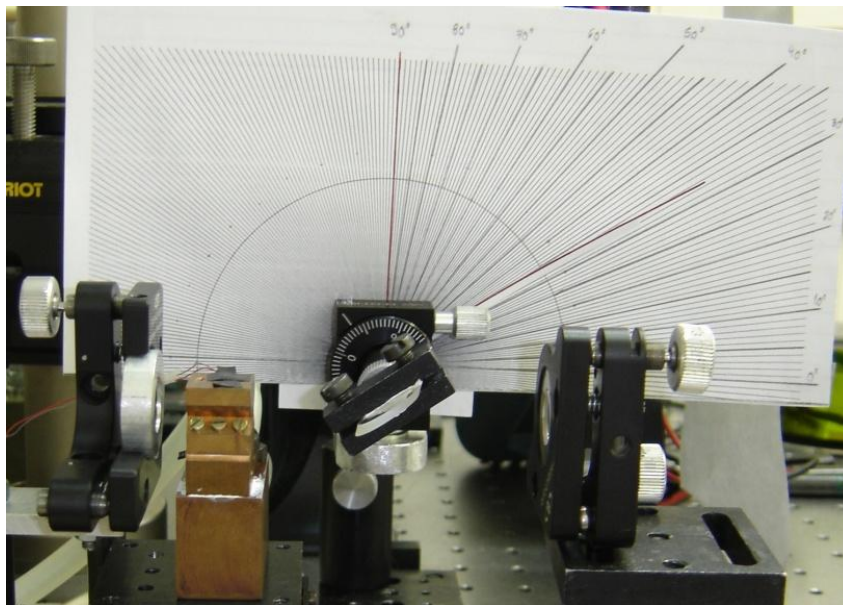


Figure 42. Cavity with an intracavity Brewster window and a fine angle adjust panel at the back.

Figure 43 shows a simulation for a refractive index of 1.46 when the photon polarization is parallel to the incidence plane, and in red the actual region measured in this work.

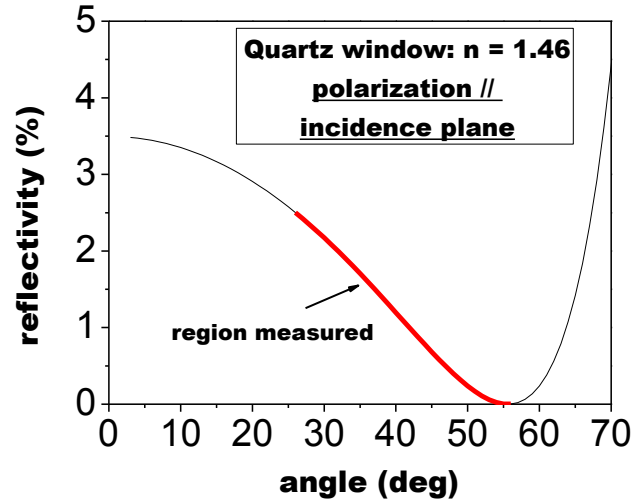


Figure 43. Quartz reflectivity as a function of the incidence angle. In red, the actual range of angles tested in the experiment.

The output power measured was the sum of the front and back reflections of the Brewster window. Figure 44 is a scheme of the set up, where D1 and D2 were deflected to a power meter (Coherent, model-PS19, associated to a Field-Max2) by low loss gold mirrors. Yet, two absorber filters were put in front of the power meter, with each one absorbing 90% at 806 nm and 10% at 908 nm. Finally, the angle of the window varied from 56° to 26°, which is equivalent to total reflectivities of 0 to 10% (four reflections have to be taking in account, air-glass, glass-air, forward and backward, where each of the reflections follows Figure 44), respectively.

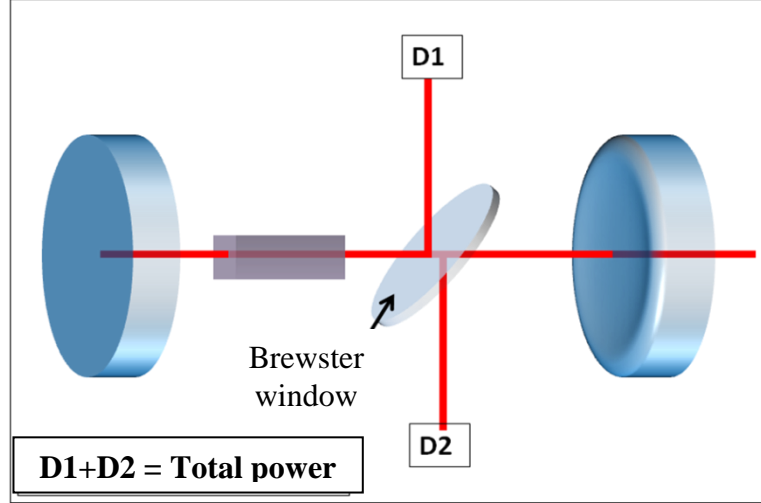


Figure 44. Beams reflected by the Brewster window.

To obtain the blue emission, the Brewster plate was removed and a SHG crystal was inserted. Also, the cavity was changed and the mirrors were inverted, the curved one was used as the pump mirror and the flat one as the output coupler. The setup is shown in Figure 45.

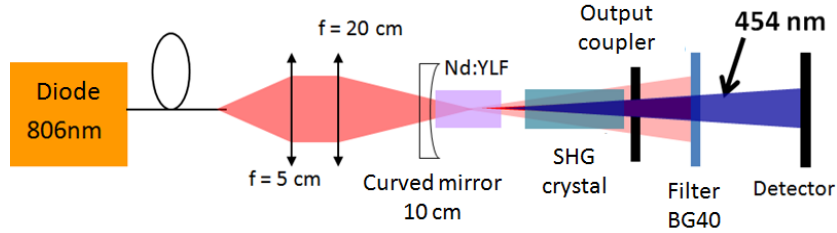


Figure 45. Setup used for the 454 nm laser.

The SHG was studied using two different type-I nonlinear crystals, BiBO and LBO, for critical phase matching, as well as different lengths, 10, 15 and 20 mm. The nonlinear crystal was placed near the flat mirror where the beam waist was smaller, around $125 \mu\text{m}$ for the 4 cm long cavity, in order to obtain a better conversion. Detection was made similarly to that described before, the only difference is that a blue band-gap filter (BG40) is used in front of the head of the power meter, allowing only the 454 nm photons to reach the detection area. Coatings with high transmission at 454 nm and 908 nm ($T > 99\%$) were deposited on the LBO and BiBO crystals faces. The mirrors have the same coating used in

the previous laser, 908 nm, noting that they have high transmission at 454 nm ($T > 95\%$), in order to couple out the blue generated by SHG.

Results

From the first experiment that defined the maximum pump power by means of the rollover in the input- output curve, a maximum allowable absorbed pump power of 13 W (CW) was determined as shown in Figure 46, in which the laser only shows a tendency to decrease the output power at 13 W due to the strong thermal changes. Pump powers above 13 W were not tried in order to prevent crystal damages. The laser emitted at 1053 nm only, certainly favored by the mirror reflectivity.

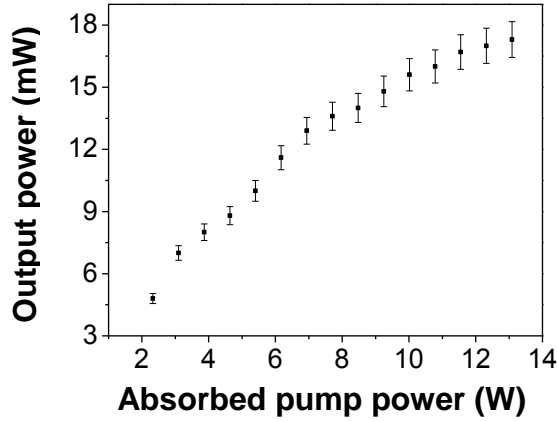


Figure 46. 1053 nm CW output power as a function of absorbed pump power.

The laser emission was purely at 908 nm (σ). This occurs because of the stronger emission cross section of the 908 nm transition when compared to 903 nm, as reported before [113]. The slope efficiency obtained in the high Q cavity was 1.4% with a peak output power of 270 mW, as shown in Figure 47.

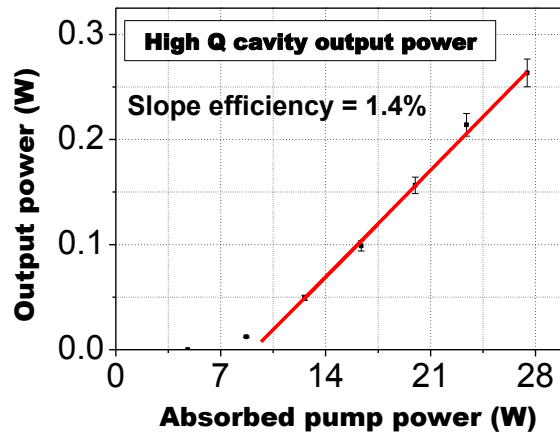


Figure 47. High Q cavity 908 nm qCW output power as a function of absorbed peak power.

Using the Brewster window, it was possible to determine the optimum coupling for the 908 nm intracavity field, which was 2.5% transmission. Figure 48 shows the output power curve as a function of the window reflectivity pumped at 20 W. The red line is just a guide to the eye.

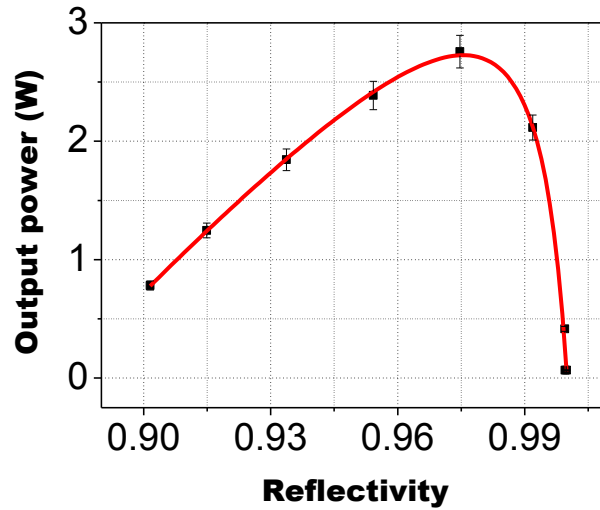


Figure 48. Output power as a function of reflectivity (transmission of the window).

In order to obtain 2.5% of reflectivity in the Brewster window, an incidence angle of 45° is necessary. With the angle fixed for the optimum coupling, a power scaling measurement was performed, Figure 49. An output peak power of 5.5 W was obtained at

908 nm for 27 W of pump power, corresponding to an optical efficiency of 19.8% and a slope efficiency of 33.6%. The threshold pump power was of 4.5 W.

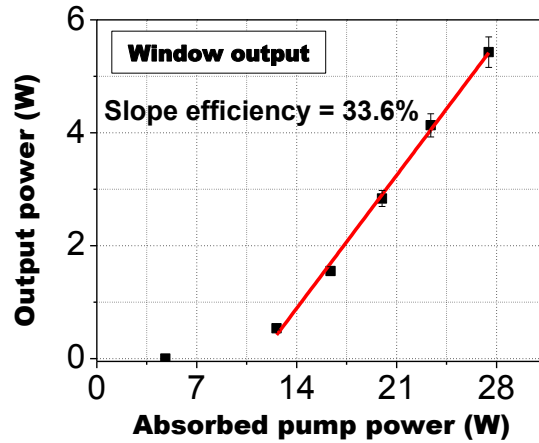


Figure 49. Output power as a function of absorbed power, for a coupling of 2.5%.

The SHG results at 454 nm followed the same order of magnitude of the infrared laser, reaching a maximum peak output power of 3.5 W. Figure 50 shows the power scaling curves for the blue lasers using each one of the doubling crystals.

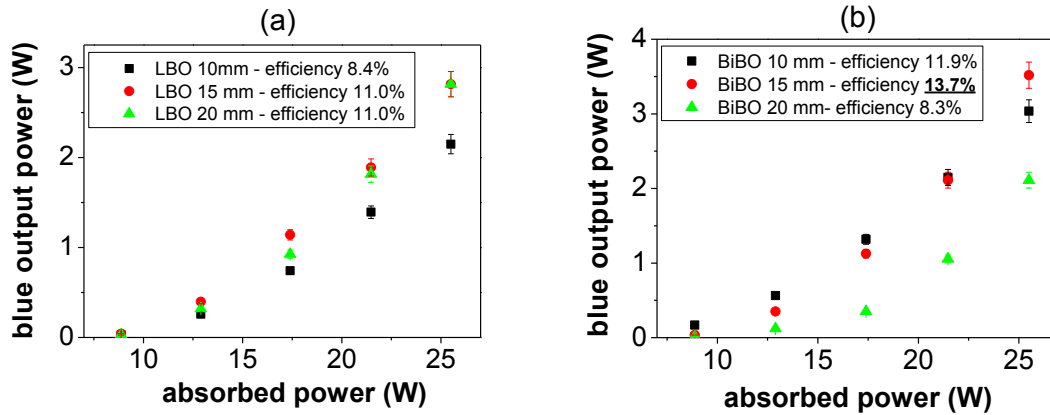


Figure 50. Power scaling of the quasi-CW blue lasers (a) using LBO and (b) using BiBO.

With LBO, the best result was achieved using crystal lengths of 15 mm and 20 mm. In this case the diode to visible conversion efficiency was 11%, with a maximum peak output power of 2.8 W. Using BiBO the best result was using a 15 mm long crystal and the

diode to visible conversion efficiency was of 13.7%, with a maximum output peak power of 3.5 W. Table 8 summarizes all the quasi-CW lasers results described in this section.

Table 8. Summary of the quasi-three level Nd:YLF lasers operating in quasi-CW regime (best results highlighted).

Laser crystal	Doubling crystal	Wavelength (nm)	Peak output power (W)	Conversion efficiency (%)	Lasing threshold (W)
Nd:YLF	-	908	5.5	33.6 (slope)	4.5
	LBO (10 mm)	454	2	8.4	7.5
	LBO (15 mm)		2.8	11	7.5
	LBO (20 mm)		2.8	11	7.5
	BiBO (10 mm)		3.1	11.9	6
	BiBO (15 mm)		3.5	13.7	7.5
	BiBO (20 mm)		2.1	8.3	7.5

3.2. CW laser operation at 908 nm and at 454 nm

The operation of the Nd:YLF 908 nm and 454 nm lasers in CW regime are demonstrated in this section.

The transition from qCW operation to CW operation in three-level lasers is a difficult task. Upon changing the modulation of the diode from pulsed to CW, using the same laser described in the section 3.1., no laser operation could be observed. The explanation for that is related to reabsorption, described in more detail in the first chapter of this thesis. Continuous wave operation offers around 33 times more heat load than the quasi-CW regime (3% duty cycle). More ions will be found in the lower laser level, according to Boltzmann distribution, and achieving population inversion will be a much more difficult task, thus increasing the pump power threshold of the laser.

Knowing the effects of reabsorption effects on the laser gain (chapter 1), changes in the crystal size and pump wavelength were made, trying to reduce these effects. The main idea in this case was to distribute more the absorption all over the crystal, thus improving the heat dissipation. With a better heat distribution comes the lower temperature in the crystal which results in a lower population in the lower laser level and consequently lower

reabsorption loss. In order to get a better distribution of the absorption, either the concentration of Nd^{3+} should be reduced or a smaller absorption coefficient/cross section should be chosen.

We did not have a lower concentration crystal available, but we had a 15 mm long Nd:YLF crystal with 0.7 at% Nd-doping. This crystal was pumped at a wavelength of lower absorption coefficient, distributing thereby the heat and still keeping the overall absorption high due to its length of more than 5 mm.

The wavelength chosen was 802 nm, which has an absorption coefficient of 1.4 cm^{-1} , as shown in Figure 51. With the 15 mm long crystal the total absorption at 802 nm is 88% comparable to the 90% absorption obtained for the 10 mm crystal pumped at 806 nm.

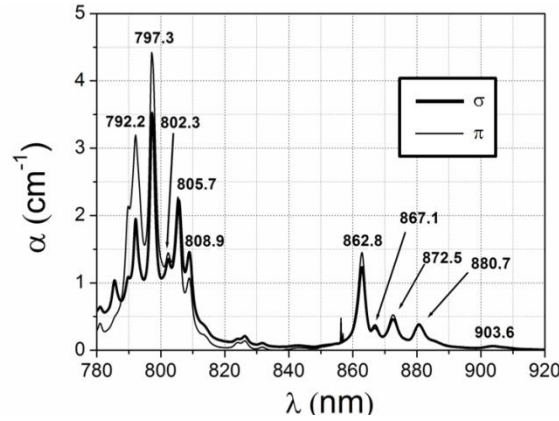


Figure 51. Nd:YLF 0.7 at% Nd^{3+} doped crystal absorption spectrum.

The cavity was the same used for the pulsed operation. To tune the diode to 802 nm, the temperature of the cooling water was reduced to 20°C.

For the blue laser SHG experiment the same cavity as described in section 3.1. was used. In this case, the doubling crystal was the 15 mm long BiBO, since the best SHG conversion efficiency in the quasi-CW regime was demonstrated using this crystal.

Results

The results were not as promising as the ones obtained for pulsed operation. Operating at 908 nm, the maximum output power delivered was of 700 mW, with an optical efficiency of 4.2% and a slope efficiency of 10.2%. The lasing threshold was 9.8 W. Figure 52 shows the power scaling curve for the 908 nm CW laser.

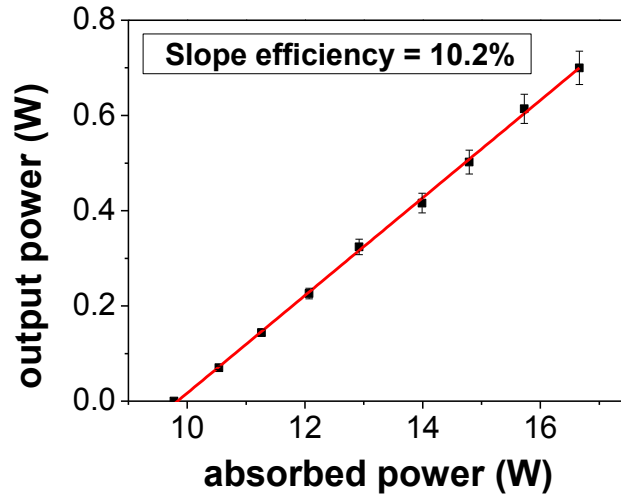


Figure 52. Input-output power curve of the Nd:YLF 908 nm CW laser.

For the 454 nm operation, 200 mW of output power was obtained, as seen in Figure 53. The diode to visible conversion efficiency was of 1.2%.

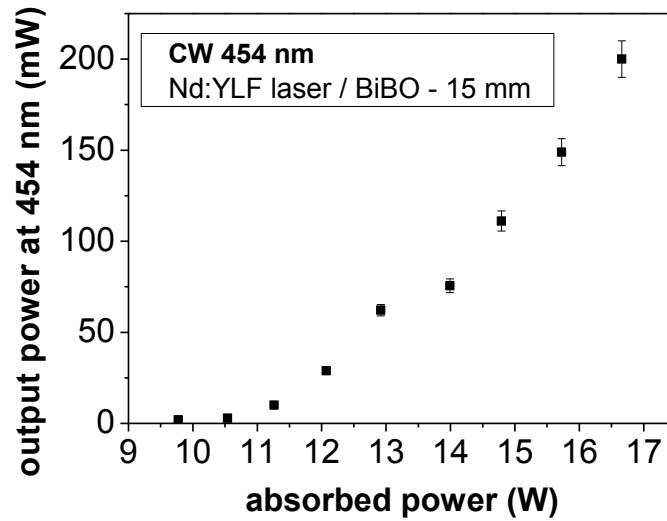


Figure 53. Performance of the Nd:YLF/BiBO (15 mm) 454 nm CW laser.

For comparison, a summary of the CW results together with the quasi-CW results is displayed in the Table 9 below.

Table 9. Summary of the CW results and the quasi-CW obtained for the Nd:YLF quasi-three level laser.

Laser crystal	Regime	Doubling crystal	Wavelength (nm)	Output power (W)	Conversion efficiency (%)	Lasing threshold (W)
Nd:YLF	CW	-	908	0.7	10.2 (slope)	9.8
	q-CW	-	908	5.5 (peak)	33.6 (slope)	4.5
	CW	BiBO (15 mm)	454	0.2	1.2	9.8
	q-CW	BiBO (15 mm)	454	3.5 (peak)	13.7	7.5

3.3. Discussion

The performance obtained from this laser should be compared to other similar experiments from the literature in terms of efficiency and output power.

Few works have been published demonstrating quasi-three level laser operation in Nd:YLF. Spiekermann *et al.* in 2000 [113] demonstrated the operation of a Nd:YLF laser at the π and σ emission lines of 903 nm and 908 nm, respectively. A maximum output power of 1.43 W at 908 nm in quasi-CW mode (duty cycle of 25%) and 1.06 W in CW mode was achieved. The corresponding slope efficiency was of 49% (optical-to-optical efficiency of 28%) in pulsed mode while in CW mode, the slope efficiency was of 32% (optical-to-optical efficiency of 21%). Laser threshold was around 1.5 W (which line σ or π) with an output coupler transmission of 2.7%.

During the time (2012-2011) when these (PhD) experiments were carried out, researchers at other institutions were also working hard towards the same goods. A recent work by Liang *et al.* [17] has so far the record in terms of CW output power for this laser. An output power of 4.7 W at 908 nm was demonstrated, with a slope efficiency of 43.3% (optical-to-optical efficiency of 39.8%). In their case, the threshold was very small, around 1 W of absorbed power at 880 nm (direct pumping scheme) and the same when pumped at 806 nm. The output coupler had a transmission of 3.5% at 908 nm, one percent higher than the one used in this work. Lu *et al.* showed a CW frequency doubled Nd:YLF laser operating at 454 nm with a maximum output power of 4.33 W, corresponding to a diode-blue conversion efficiency of 13.2% [30]. The threshold for this laser was of 8.4 W with a

maximum incident pump power of 32.8 W at 880 nm. The results are summarized in Table 10.

Table 10. Summary of the results obtained in the literature and the ones obtained in this work.

	Wavelength (nm)	Output power (W)	Conversion efficiency (%)	Threshold (W)	Pump scheme	Crystal length (doping concentration)
Spiekermann <i>et al.</i>	908	1.43 (qCW)	49 (slope)	1.5	792 nm (-)	2.4mm, ϕ 3mm (0.6 at%)
Liang <i>et al.</i>	908	4.7 (CW)	43.3 (slope)	0.93	880 nm (ω :200 μ m)	15 mm (1 at%)
This work	908	5.5 (qCW)	33.6 (slope)	4.5	806 nm (ω :225 μ m)	10 mm (0.7 at%)
Lu <i>et al.</i>	454	4.33 (CW)	13.2	8.4	880 nm (ω :200 μ m)	15 mm (1 at%)
This work	454	3.5 (qCW)	13.7	7.5	806 nm (ω :225 μ m)	10 mm (0.7 at%)

Looking at the results obtained in this work, one can see the maximum output power of 5.5 W obtained at 908 nm is higher than the others reported, although the laser operation was in quasi-CW regime. Another good result is the diode-to-blue conversion efficiency, which reached 13.7%, the highest reported. The threshold for the blue laser was also smaller than the one demonstrated in [30], but this is probably because of the lower crystal temperature in the quasi-CW operation and to the fact that they used a four mirror cavity with an intracavity Brewster window, which increases the losses.

Using the data from the literature and the data extracted here, a simulation of the small signal gain (g_0) can be performed using simplified quasi-three level laser theory. These simulations help to gain a better insight of the lasers behavior, e.g. threshold and general performance, and how to improve them.

Simulating the gain for the lasers in Table 10, one can find the small signal gain at 908 nm as a function of crystal length. It was not possible to find all the parameters needed

to simulate the laser in [113], but it is possible to simulate the laser in [17] and the one built in this work.

Inserting the following particular laser parameters given in [17]: Pump - wavelength, beam waist at the crystal and beam quality; Crystal – doping concentration and length; Cavity characteristics – laser mode diameter inside the crystal, passive losses and output transmission; it is possible to vary the pump power until a balance between the effective gain and losses (effective Gain - Losses = 1) is reached, which will be the threshold power. The following behavior of threshold, Figure 54(a), and pump intensity distribution, Figure 54(b), was found.

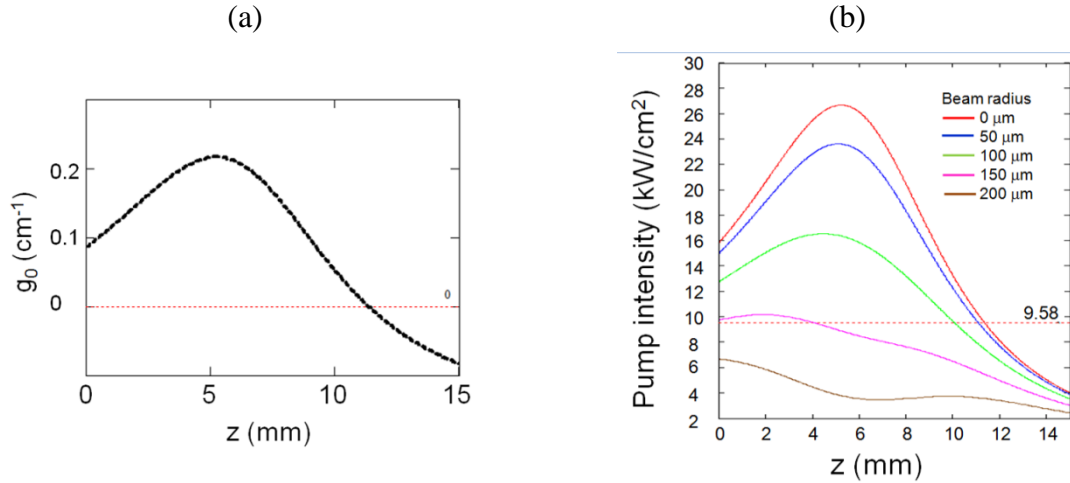


Figure 54. Simulation of (a) small signal gain and (b) pump intensity along the crystal[17].

The zero mark in Figure 54(a) represents the point where the small signal gain is equals to the reabsorption loss. Above the mark, there is more gain than loss and for the points below the mark, the losses are stronger than the gain. In Figure 54(b), the red dotted line represents the transparency intensity which in this case is 9.58 kW/cm^2 .

From Figure 54(b) it follows that the best condition is with the pump beam waist located 6 mm away from the crystal's pump face. The pump threshold power at this condition is 13 W, which is very far from 0.93 W, found in [17]. One way to get such low threshold is by cooling down the Nd:YLF crystal to very low temperatures, reducing the population of the 539 cm^{-1} lower laser level, thus reducing the reabsorption.

In the case of the 908 nm laser described here, the threshold pump power given by the simulation is 4.8 W. Comparing to the experimental quasi-CW threshold of 4.5 W, they are very similar, the experimental one is just slightly lower. This can be explained by the fact that the pump modulation of 3% of duty cycle keeps the crystal at water temperature, 15°C, which is cooler than the room temperature, thus reducing slightly the reabsorption losses. Figure 55 shows the simulation curves obtained for this laser when focusing at the pump facet. The transparency intensity in this case was of 1.82 kW/cm², Figure 55(b).

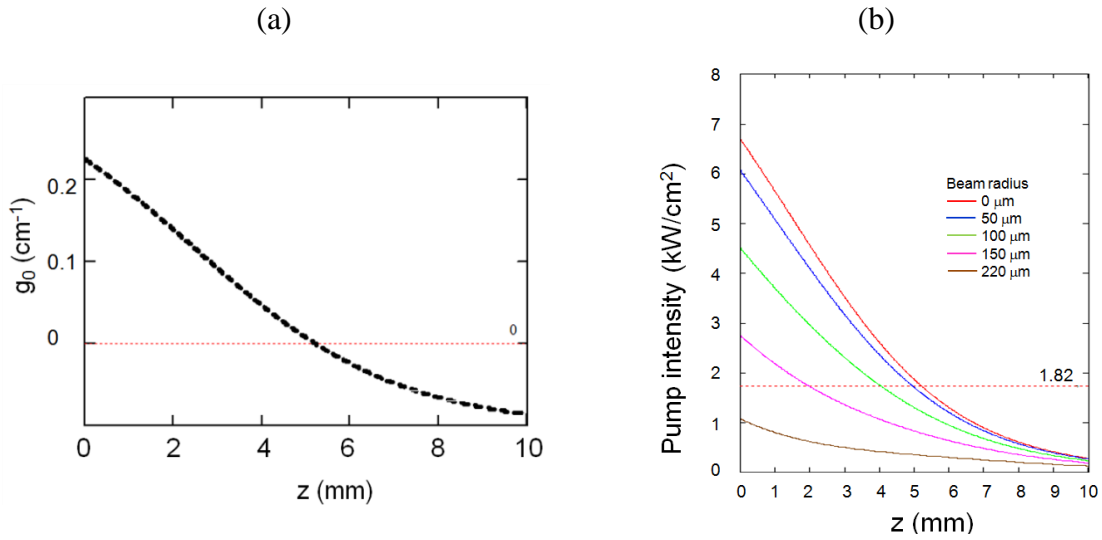


Figure 55. Simulation of the (a) small signal gain and (b) pump intensity distribution at threshold pump power for the laser demonstrated in this work.

For the CW case, a higher threshold was expected, since there is much more heat load. At the beam location the temperature can rise tens of degrees above the temperature of the copper mount (15°C), increasing significantly the population of the lower laser level, and consequently the reabsorption losses. In addition, the crystal used for the CW experiments was 5 mm longer than the one used for quasi-CW, adding an extra reabsorption region.

Regarding the blue lasers, one should be able to obtain similar output powers to that obtained for the 908 nm laser using the optimum coupling transmission [114]. The 454 nm laser demonstrated here did not achieve the 5.5 W the 908 nm laser delivered. This is probably related to the second harmonic conversion efficiency and additional losses the doubling crystal introduces.

The SHG has a strong dependence with intensity, as discussed in the introduction of this thesis. Given that, such lasers should achieve their most efficient operation by increasing the intensity of the laser at the doubling crystal. For that a different cavity configuration should be employed, such as folded cavities or ring cavities, which provide a control of two waists inside the cavity, one for the laser crystal and one for the doubling crystal. This has been shown by Lu *et al.* [30], who used a “Z” type cavity to obtain the 454 nm laser. The output power obtained (4.33 W) was very similar to the one reported for the 908 nm laser (4.7 W) in [17].

Joining the research developed here and the research carried out in [17, 30], there is an apparent pathway to developing efficient lasers at 908 nm and at 454 nm. It was found out that the reduction of the reabsorption is necessary for a good performance of these lasers. It can be reached either by a combination of Nd³⁺ doping concentration and crystal length or by saturating such absorption using high pump powers and very high intracavity fields. In addition the temperature is another factor which influences a lot on the reabsorption, thus it must be kept at temperatures as low as possible.

Chapter 4

Nd:YLF Raman lasers

4.1. Nd:YLF/BaWO₄ Raman laser

4.2. Nd:YLF/KGW Raman laser

4.3. Discussion

4. Nd:YLF Raman lasers

In this section the Raman lasers will be described. Two different lasers were studied, both using Nd:YLF as the laser active medium. Two Raman crystals were employed in order to build up the Stokes field, a BaWO₄, whose laser project and results are detailed in section 4.1. and a KGW, whose details are found in 4.2. Discussions over the performance of the lasers built in this section are done in 4.3.

4.1. Nd:YLF/BaWO₄ Raman laser

All the Raman lasers built in this work were pumped with the same pump source, a 60 W fiber coupled diode laser (LIMO) emitting at 880 nm, with a fiber diameter of 100 μm and a numerical aperture (N.A.) of 0.22. A 25 mm focal length lens is used for collimation and a 125 mm lens is used for focusing, delivering a pump spot of 500 μm diameter inside the Nd:YLF laser crystal. The diode output wavelength is temperature-tuned to 881 nm in order to match one of the absorption peaks of the Nd:YLF crystal [16]. Direct pumping has two main benefits: first, a 33% reduction in heat by eliminating the multiphonon decay from the pump level to the upper laser level, and second, as the absorption coefficient at this wavelength is smaller than at conventional pump wavelengths (806 nm), there is a smoother distribution of the absorption over the whole length of the crystal so that the local temperature rise in the crystal is minimized.

The first Raman laser built in this research is a Nd:YLF/BaWO₄ laser. The Nd:YLF crystal chosen was doped with 1.0 at% Nd³⁺, a-cut oriented and had dimensions of 4x4x15 mm³. The 1 at% doping concentration was chosen in order to have a reasonable absorption at 881 nm without increasing too much the energy transfer upconversion (ETU) rate [26]. The fraction of pump power absorbed in the 15 mm long crystal is 43%, and this is something that could be optimized in the future, for example by double-passing the pump. The crystal faces were coated for high transmission ($T > 95\%$) at 881 nm, with antireflection coating (AR) for fundamental 1047/1053 nm ($R < 0.2\%$) and for first Stokes wavelengths 1135-1170 nm ($R < 0.1\%$). This crystal oscillated at 1053 nm, favored by the mirrors and crystal coatings. The 1053 nm field undergoes a weaker thermal lens than that experienced by the 1047 nm, providing better stability and good beam quality for the laser

even under high pump powers. Amongst several Raman active materials, the BaWO₄ crystal was chosen because of its high Raman gain of ~8.5 cm/GW compared to KGW (~4.4 cm/GW), GdVO₄ (>4.5 cm/GW) and YVO₄ (>4.5 cm/GW) [55]. This crystal was a-cut with dimensions of 4×4×25 mm³. Such a long crystal was chosen due to the fact that in the steady-state regime the Stokes field increases exponentially with the interaction path along the crystal. The Raman shift provided by the BaWO₄ is of 926 cm⁻¹, thus the 1053 nm field is shifted to 1167 nm.

The optical resonator was designed for high Q oscillation of the fundamental 1053 nm and output coupling of the Stokes wavelength at 1167 nm. A flat mirror with high reflectivity (HR) at 1053 nm and 1167 nm (R>99.99%) and high transmission at 880 nm (T>95%) was used as the pump mirror. The output coupler (O.C.) had the same HR coating of the pump mirror at 1053 nm but with a transmission of 0.4% at 1167 nm, and a radius of curvature (ROC) of 250 mm. The cavity was 240 mm long, as shown in Figure 56, and the radii of the resonator modes were estimated using LASCAD software to be 150 μm and 165 μm in the laser and Raman crystals, respectively. We have also measured the performance of the Nd:YLF laser with no Raman crystal and using a 5% transmission mirror as the output coupler. It can give an idea of the limits and fundamental changes that could interfere in the Raman performance.

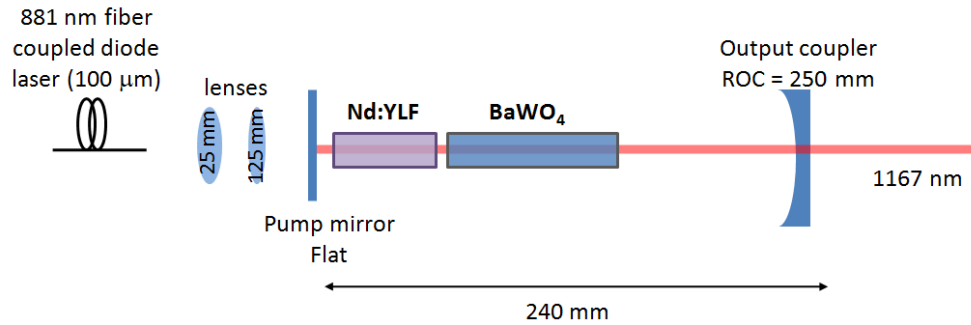


Figure 56. Nd:YLF/BaWO₄ Raman laser setup.

In order to obtain yellow emission from the laser, a lithium triborate crystal (LBO) was added to generate the second harmonic of the 1167 nm Stokes wavelength. This LBO was cut for type-I non-critical phase matching, with dimensions of 4x4x10 mm³. The phase matching temperature was experimentally determined to be 47°C. The cavity has to be modified to no longer couple the 1st Stokes out but, instead, to couple the yellow

wavelength 583 nm out. For that reason, the output mirror had to be changed to one with HR-coating ($R > 99.99\%$) at both fundamental and Stokes wavelengths, with high transmission at 583 nm ($T > 95\%$). Also, the curvature of the mirrors had to be changed, to achieve a small mode size in the doubling crystal but keeping similar beam sizes as before in the laser and Raman crystals. The pump mirror used had a ROC of 400 mm and the output coupler a ROC of 200 mm, and the cavity was 80 mm long, providing TEM_{00} resonator mode radii of 170 μm , 170 μm and 180 μm in the laser, Raman and doubling crystals, respectively. An intracavity mirror, with an antireflection coating (AR) at 1053 nm and 1167 nm ($R < 0.1\%$) and HR at 583 nm ($R > 95\%$), is inserted between the BaWO_4 and the LBO crystal in order to reflect the backward propagating yellow beam into the output of the laser. Figure 57 shows the optical resonator used for the yellow laser.

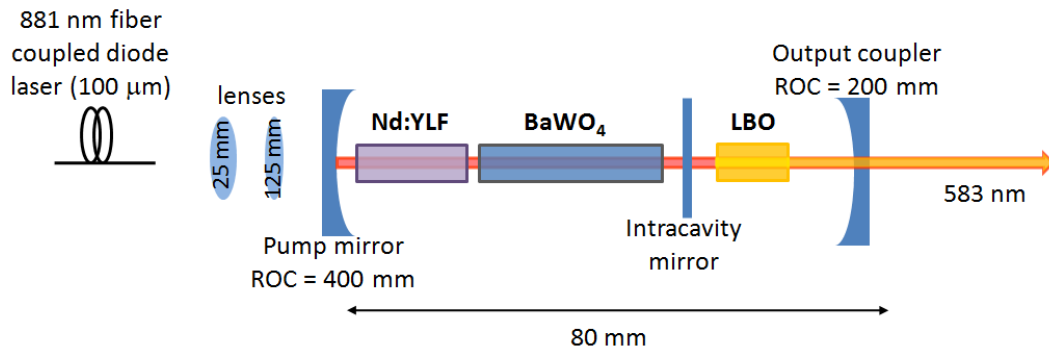


Figure 57. Nd:YLF/BaWO₄/LBO yellow laser setup.

Results

The fundamental laser performance was as expected, maximum output power of 10 W at 1047 nm in CW regime, for a maximum absorbed pump power of 21 W, corresponding to ~50% of optical to optical efficiency. No competition between 1047 nm and 1053 nm was observed. The beam quality was not measured, but by visual inspection it seemed to be a TEM_{00} mode. Figure 58 shows its performance.

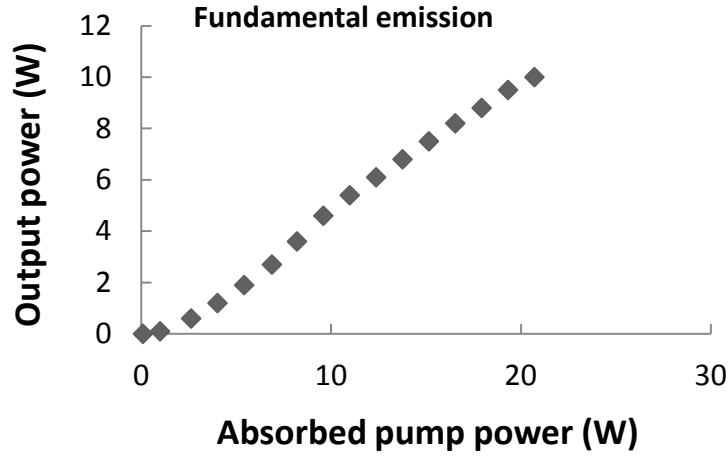


Figure 58. Fundamental laser performance.

Figure 59(a) shows the output power at 1167 nm as a function of absorbed power. The Raman laser provided a maximum output power of 1.5 W when operating in CW regime. The beam quality was measured at a pump power of 15 W using a beam analyzer (Beamscope P8, GENTEC). The measured result is M^2 of 1.43 in the horizontal and 1.51 in the vertical direction, as shown in Figure 59(b). The overall diode to Stokes efficiency was 9%.

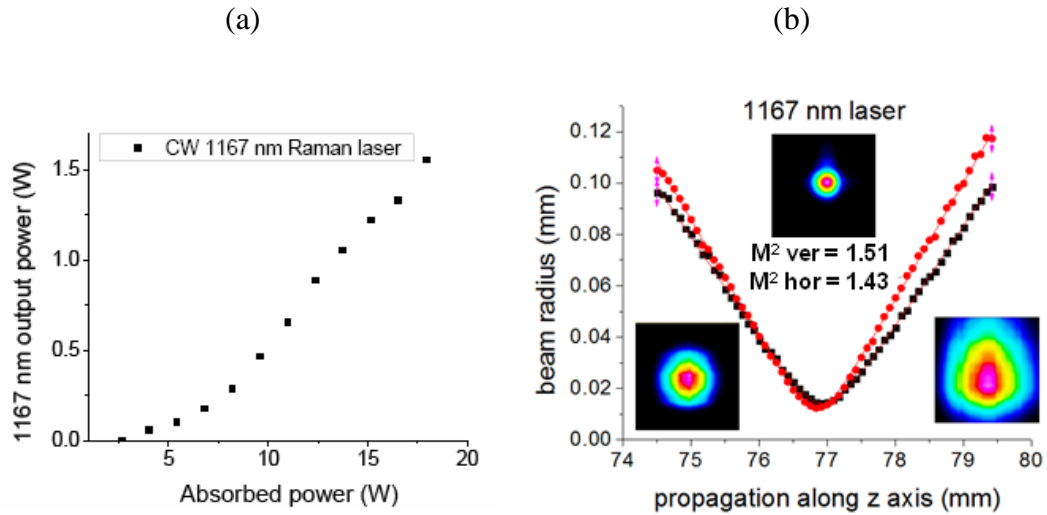


Figure 59. (a) CW 1167 nm output power as function of absorbed pump power and (b) M^2 measurement of the 1st Stokes laser beam with the beam profiles images in the near field, focus and far field.

The cavity used to produce 1.5 W at 1167 nm is considered a long cavity for Raman lasers, since the most efficient ones were based on self-Raman configurations [69, 87, 90], and in those cases, a strong thermal lens exists, demanding the use of very short cavities. The advantage of a long cavity is in fact its capacity to provide more longitudinal modes, which is a feature that plays an important role for low amplitude noise lasers. Furthermore, Nd:YLF has a gain bandwidth of 358 GHz at 1053 nm compared to 344 GHz for Nd:GdVO₄, 254 GHz for Nd:YVO₄ and 119 GHz for Nd:YAG [115, 116], providing naturally more longitudinal modes than the others. Another advantage brought by the possibility of building long cavities is the design freedom, making it possible to build folded, ring and other types of resonators, or simply to design a resonator with near optimal mode sizes in the laser, Raman and, if present, the frequency mixing crystal.

With the introduction of the LBO crystal, laser emission at 583 nm was obtained. The SHG resulted in 0.61 W, and the corresponding laser behavior is shown in Figure 60. A competition between oscillation at 1053 nm and at 1047 nm was observed, which was not observed when operating at 1167 nm without the SHG crystal. This happened probably because of the LBO coatings introduced extra losses to the 1053 nm emission.

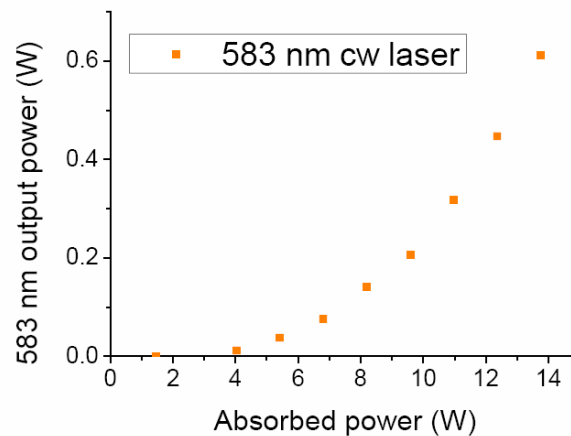


Figure 60. 583 nm CW laser performance.

Pure 1053 nm oscillation was possible only up to 14 W of pump power. Above 14 W, the 1047 nm line starts to oscillate, reducing the 583 nm output power. One way to overcome this problem is to introduce more losses to the 1047 nm line by using a Brewster window or any low loss polarizing optics, since 1053 nm and 1047 nm have orthogonal polarizations.

Knowing that, we tried a Brewster-cut Nd:YLF crystal in the cavity. Single oscillation was then obtained at 1053 nm up to the pump power limits. However, it was not possible to reach the same output powers and efficiencies as with the flat-flat crystal. The maximum Stokes power achieved was 0.50 W for a pump power of 17 W. We believe this low performance is due to some kind of axis misalignment between the Nd:YLF, BaWO₄ and LBO crystals. Since the Nd:YLF Brewster face impose the direction of the polarization, we may need to rotate the BaWO₄ crystal to match with more accuracy its strongest Raman cross section with the imposed polarization, but no rotation mount was used in the Raman crystal in this experiment.

4.2. Nd:YLF/KGW Raman laser

The second Raman laser built is a Nd:YLF/KGW laser, which uses the KGd(WO₄)₂ crystal as the Raman active medium. The crystal presents two different Raman shifts with strong gain. In this case the quasi-CW operation of the lasers was also investigated, and for this purpose, a chopper was placed after the diode's fiber. This chopper was operated with 50% duty cycle and frequency of 850 Hz so the thermal energy deposited in the crystal would be approximately 50% as much as during CW operation. In this mode of operation it is possible to reach higher peak powers and also predict the CW output power that could be achieved by pumping the crystal harder, without taking the risk of a thermal fracture.

We used a Nd:YLF Brewster plane cut crystal with 1 at% Nd³⁺ doping concentration and dimensions of 4×4×15 mm³. The crystal's flat face was coated with the same coating of the Nd:YLF used for the BaWO₄ experiments. The Brewster-cut on the other face introduced losses for the 1047 nm, thereby enabling the 1053 nm fundamental wavelength to oscillate without competition. We chose 1053 nm as the fundamental wavelength because it generally has a weaker thermal lens than 1047 nm [25] and was therefore more likely to deliver good beam qualities and freedom to design long cavities. There are resonator designs that allow the laser to operate under strong thermal lensing, such as telescopic resonators [117], however, they typically operate only for a short range of pump powers, and generally introduce extra optics to the resonator, increasing the intracavity losses.

The KGW crystal used has dimensions of $5 \times 5 \times 24 \text{ mm}^3$. It was AR-coated at the fundamental and Stokes wavelengths ($R < 0.1\%$ at 1053-1170 nm), and cut for propagation along the N_p axis. The Raman spectrum for KGW is complex [118] and for this reason a measurement of the Raman spectra was performed for the two orientations we used in this work, using a Renishaw InVia Reflex microRaman spectrometer with resolution of 1 cm^{-1} .

A special copper mount was designed for the KGW crystal, Figure 61, so it could be rotated in order to access either the 901 cm^{-1} shift (fundamental and Stokes polarization parallel to the N_m refractive index axis) or the 768 cm^{-1} shift (fundamental and Stokes polarization parallel to the N_g refractive index axis). Table 11 shows the combinations of fundamental, Stokes, yellow and lime-green emission generated using the two Raman shifts.

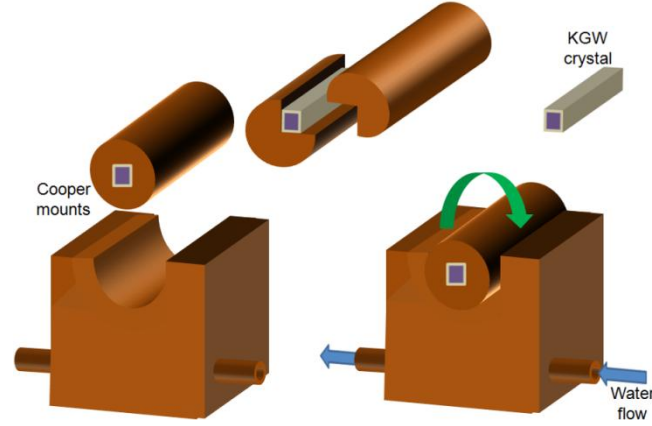


Figure 61. KGW rotating stage with water cooling.

Table 11. 1st Stokes, SHG and SFG wavelengths generated by Nd:YLF/KGW system.

Shift	Fundamental	1 st Stokes	SHG	SFG
768 cm^{-1}	1053 nm	1147 nm	573 nm	549 nm
901 cm^{-1}		1163 nm	581 nm	552 nm

The cavity used to obtain 1st Stokes laser emission is shown in Figure 62. The input mirror had high reflectivity ($>99.99\%$) at 1053 nm, 1147 nm and 1163 nm, and high transmission ($T > 90\%$) at 880 nm, with 400 mm of ROC. The output coupler for the 1st Stokes had a $R > 99.99\%$ at 1053 nm, 0.2% transmission at 1163 nm and 0.1% transmission

at 1147 nm, with 250 mm of ROC. The distance from the last end face of the KGW to the O.C. was 115 mm and the overall cavity length was 160 mm. The TEM₀₀ resonator mode had 420 μm diameter in the laser crystal and 400 μm diameter in the Raman crystal, calculated using the ABCD resonator model (LASCAD).

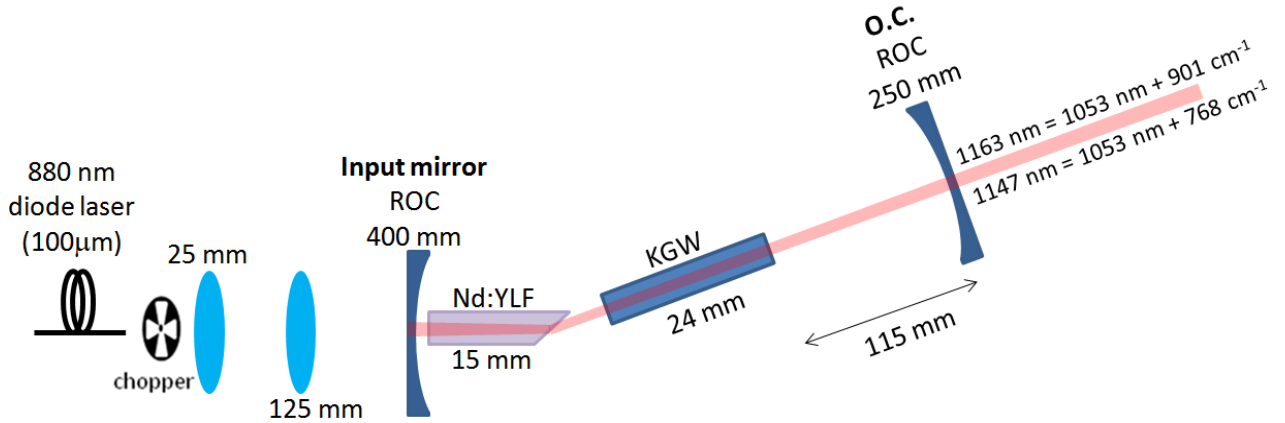


Figure 62. Nd:YLF/KGW 1st Stokes laser setup.

A lithium triborate (LBO) crystal ($4 \times 4 \times 10 \text{ mm}^3$) was used for intracavity SHG/SFG. It was cut for type-I non-critical phase-matching, and AR-coated at the fundamental, Stokes and SHG/SFG wavelengths ($R < 0.1\%$ at 1053-1170 nm and $T > 95\%$ at 570-590 nm). This was the same coating used in the Nd:YLF/BaWO₄ laser. The LBO crystal was positioned next to the KGW, as shown in Figure 63, and temperature tuned to 63°C for 573 nm or 50°C for 581 nm. The TEM₀₀ resonator mode diameters were calculated to be 380 μm, 366 μm and 368 μm respectively in the laser, Raman and doubling crystals. The curved (200 mm ROC) output coupler had high reflectivity, $R > 99.99\%$ at the fundamental and Stokes wavelengths and high transmission, ranging from 80-95%, at the yellow and lime-green wavelengths. An intracavity mirror was also introduced between the KGW and LBO crystals in order to redirect the backwards propagating yellow beam toward the O.C. This intracavity mirror had an AR-coating at 1053 nm ($R < 0.1\%$), 1147 nm and 1163 nm ($R < 0.1\%$), and a HR-coating at 573 nm and 581 nm ($R > 98\%$).

For the SFG operation at 549 nm and at 552 nm, the same configuration was used. The temperatures of the LBO crystal required for phase matching were 109°C for 549 nm and 101°C for 552 nm.

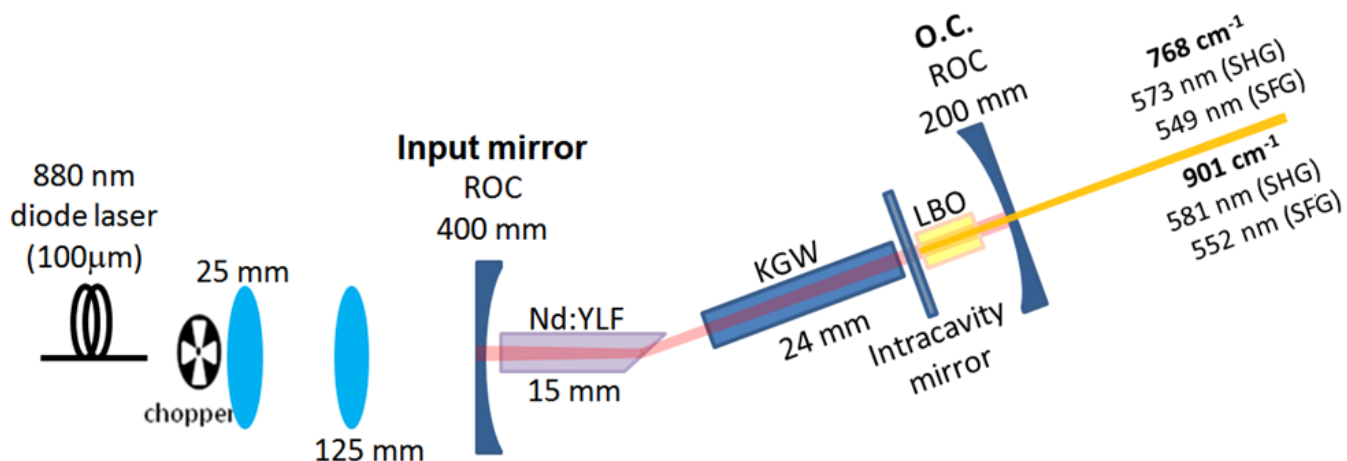


Figure 63. Nd:YLF/KGW/LBO yellow and lime-green laser setup.

Results

The Raman spectra, at the two orientations of the KGW used in this work, were measured in a Raman spectrometer as described above. The result is shown in Figure 64.

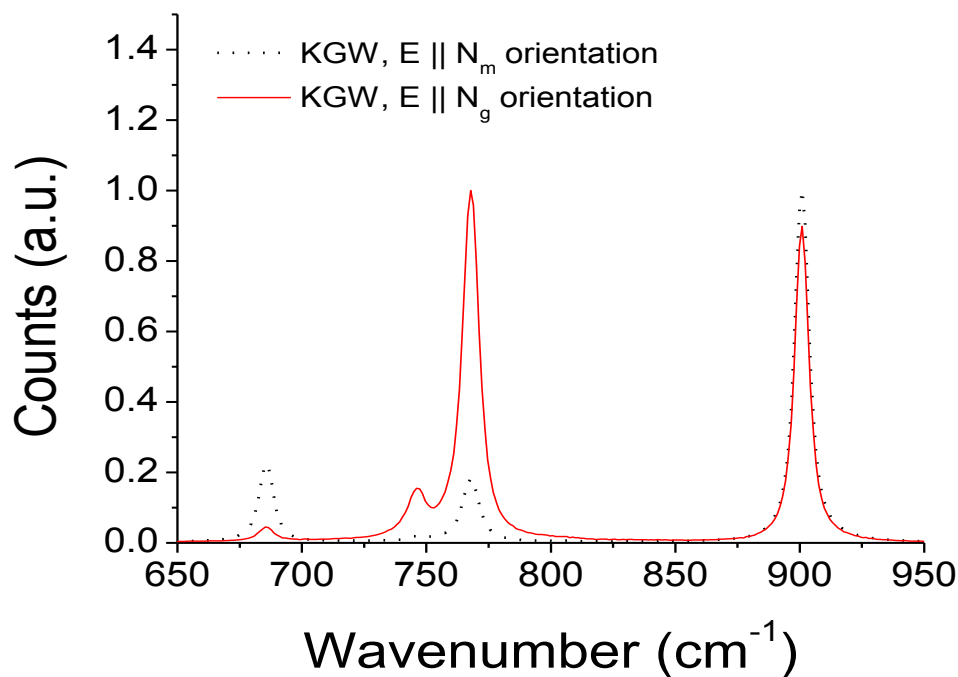


Figure 64. Raman spectra at the two orientations used in the Nd:YLF/KGW laser.

These spectra are normalized and it is possible to observe that when the electric field is aligned to the N_m axis, the 901 cm^{-1} shift is the strongest, and when it is aligned to

the N_g axis, the 768 cm^{-1} is stronger than the 901 cm^{-1} . So, orientating the KGW in one of those conditions, it is possible to select the shift between 901 cm^{-1} and 768 cm^{-1} .

Laser operating at the 901 cm^{-1} shift

When the KGW was oriented to access the 901 cm^{-1} shift, the 1st Stokes laser delivered a maximum CW power of 0.95 W at 1163 nm for an absorbed pump power of 12.3 W. The beam quality was measured to have an M^2 of 1.49. For quasi-CW operation 1.56 W of peak power was obtained for 21 W peak absorbed pump power. Figure 65(a) shows the input-output power performance of this laser. The Stokes beam profile was elliptical, due to the Brewster angle in the cavity, and the M^2 and beam sizes mentioned are average values for the two planes. We did not measure the beam quality of the fundamental beam (1053 nm) because the mirrors have a very high reflectivity at this wavelength ($>99.9\%$), thus, the residual power leaking from the cavity was not enough to make a reliable M^2 measurement.

When the 10 mm LBO crystal temperature was tuned to $50\text{ }^\circ\text{C}$ for the SHG of 1163 nm, a CW output power of 1.10 W at 581 nm was obtained, with M^2 of 1.93. In quasi-CW mode, 1.65 W of peak power was obtained, Figure 65(b). It is interesting to note that the powers in the visible are higher than in the infrared and this is attributed to the fact we were not using the optimum output coupling for the 1st Stokes.

When the LBO crystal was tuned to 101°C for SFG of 1053 nm and 1163 nm, we obtained 1.90 W CW at 552 nm for 13 W of absorbed pump power. The corresponding beam quality was $M^2 \sim 2.01$. In quasi-CW operation, 3.12 W of peak power was achieved for 20 W of peak pump power. Figure 65(c) shows the output power performance for this laser.

The spectral linewidths (full width at half-maximum) of the fundamental, first Stokes and visible lines were measured using an ocean optics HR4000 spectrometer to be 0.3 nm.

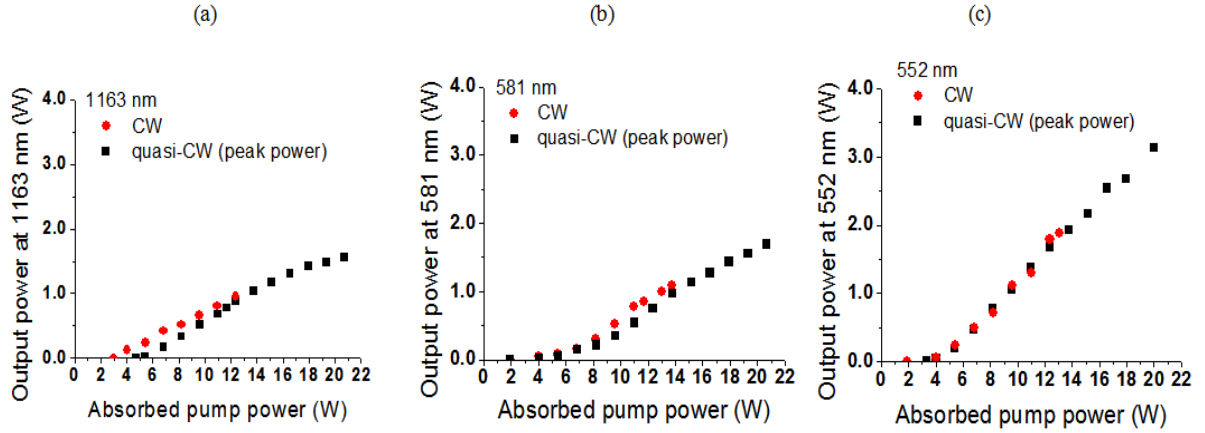


Figure 65. Output power as a function of absorbed pump power for (a) 1163 nm, (b) 581 nm and (c) 552 nm.

Laser operating with the 768 cm⁻¹ shift

When the KGW crystal was rotated to access the best gain for the 768 cm⁻¹ shift, the first Stokes laser delivered 0.70 W CW power at 1147 nm for 13 W of absorbed pump power and for quasi-CW operation, 1.20 W of peak power for 20 W peak absorbed pump power, as shown in Figure 66(a). The beam quality was measured to be $M^2 \sim 1.44$.

When optimized for frequency doubling the 1st Stokes at 1147 nm, we obtained 0.60 W CW power at 573 nm for an absorbed pump power of 13 W (see Figure 66(b)) and the corresponding beam quality was measured to be $M^2 \sim 1.76$. In quasi-CW operation the maximum peak yellow power was 1.25 W for 18 W of peak pump power. At higher (18-20 W) pump powers the 901 cm⁻¹ Raman transition began to compete. Looking at the Raman spectra in Figure 64, we can see that for this orientation the 901 cm⁻¹ and 768 cm⁻¹ lines have similar intensities, with the 768 cm⁻¹ only slightly stronger. The competition arises because there are losses for the 768 cm⁻¹ shift through the SHG process, but no such losses for the 901 cm⁻¹ shift.

When optimized for sum frequency to generate 549 nm, a maximum power of 0.65 W was achieved in CW regime and 1.20 W peak power when chopped, as seen in Figure 66(c). Unfortunately coating damage occurred on the KGW crystal and the low thresholds obtained previously could not be realized. It is very likely that considerably higher output powers could be achieved at 549 nm using a KGW crystal with un-damaged coatings.

The spectral linewidths (full width at half-maximum) of the fundamental, first Stokes and visible lines were measured to be 0.3 nm.

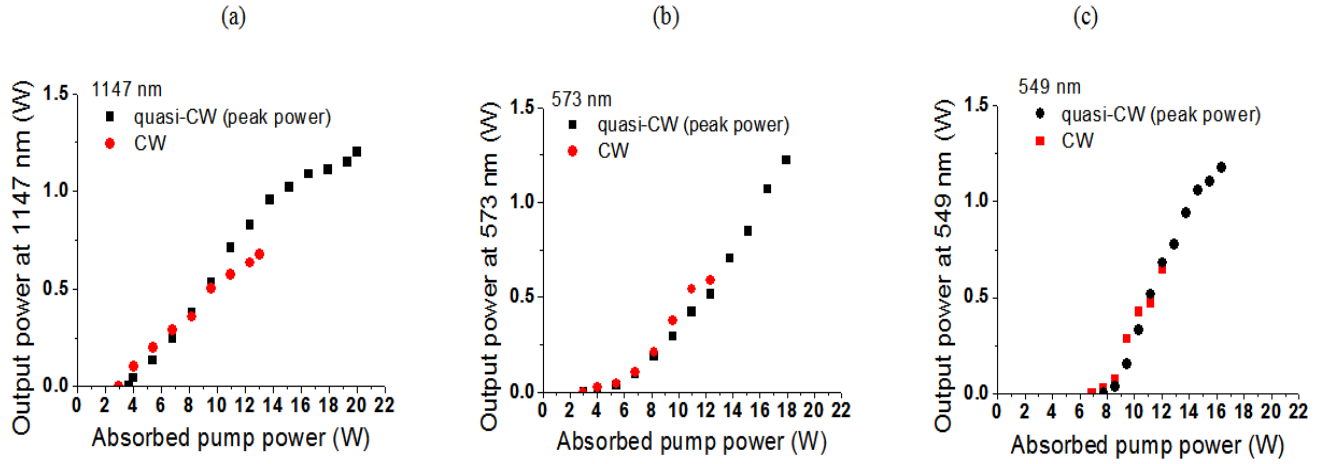


Figure 66. Output power as a function of absorbed pump power for (a) 1147 nm, (b) 573 nm and (c) 549 nm.

An analysis of the laser results, showed in the sections 4.1 and 4.2, is made in the next section.

4.3. Discussion

Using Nd:YLF as the laser crystal in a CW intracavity Raman laser offers several advantages as discussed in the introduction chapter and they include a naturally polarized emission and weak thermal lensing. Having π and σ -polarized emissions at two wavelengths, 1047 nm and 1053 nm respectively, combined with the two Raman shifts in KGW, enables an interesting selection of near-infrared and visible wavelengths to be accessed. Figure 67 shows all the wavelengths that can be achieved by such combination, highlighting the ones obtained in this work.

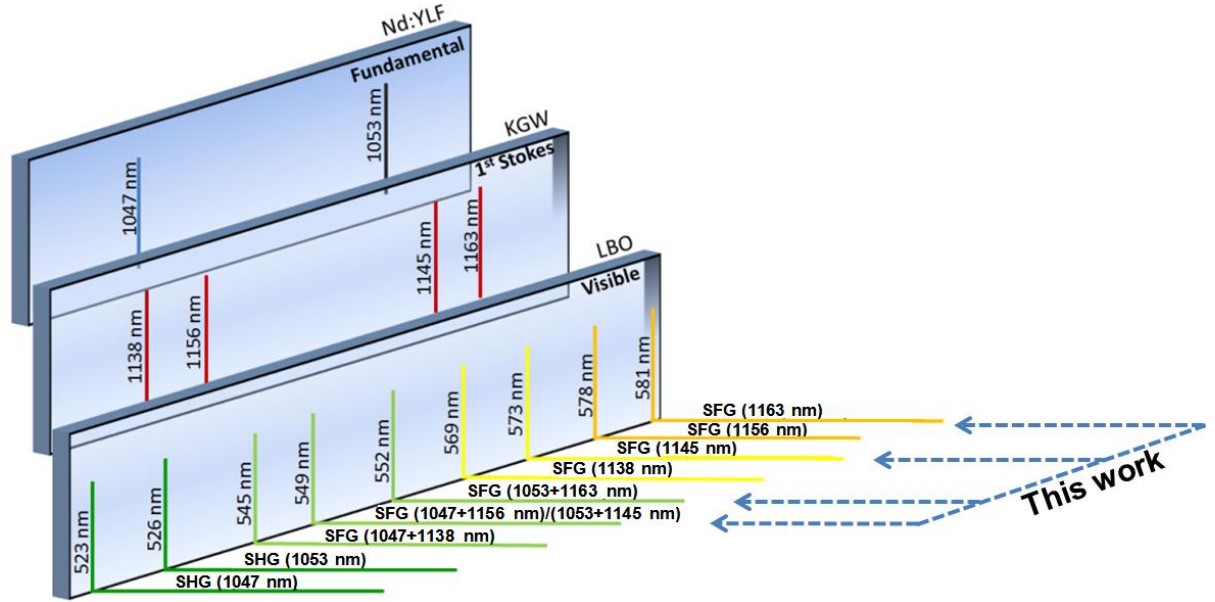


Figure 67. Wavelengths generated by the combination of Nd:YLF and KGW.

The laser performances shown in Figure 59, Figure 65 and Figure 66 are very good in terms of output power and efficiency, particularly if we consider that the coatings on the crystals and mirrors were specifically designed for a system having the 1064 nm as the fundamental wavelength (ie. not 1053 nm). The lasers reported here operate over a useful range of wavelengths and output powers, with good efficiencies. The highest conversion efficiency (with respect to absorbed pump power) reported here is 14% in the case of SFG to 552 nm, and this can be compared against 20% obtained in a self-Raman Nd:GdVO₄ laser with SFG to 559 nm [69], which is the highest efficiency reported in the literature. The higher efficiency in [69] can be attributed to lower resonator losses, enabled by very low loss AR-coatings on the crystals and the fact there is one less crystal present. For the yellow, we achieved a conversion efficiency of 7.8% for generation of 581 nm, somewhat lower than the highest-reported conversion efficiency (17%) for a self-Raman [89] operating at 586 nm, but again the difference is due to extremely low resonator losses in [89]. In the case of the 1st Stokes, our conversion efficiency of 9% when generating first Stokes output at 1167 nm can be compared against 13.8% for the best CW self-Raman performance, from a composite Nd:KGW/KGW laser operating at 1181 nm [119]. Furthermore, the Nd:YLF Raman lasers we have demonstrated had good beam quality, with $M^2 \sim 1.5$ for the 1st Stokes laser at 1163 nm and 1167 nm and with $M^2 \leq 2$ for CW

operation at 1147 nm and in the visible at 581 nm and at 552 nm. This beam quality is considerably better than for the Nd:GdVO₄ self-Raman lasers in which the beam quality during the sum frequency mixing was $M^2 \sim 10$ [69], and for the second harmonic it was $M^2 \sim 6$ [88], both at maximum pump power. The good beam quality reported here for Nd:YLF Raman lasers is a consequence of the much weaker thermal lensing, since the beam quality is strongly linked to thermal lensing, which in the case of self-Raman laser is typically very strong and aberrated. A summary of the results obtained in this work is shown in Table 12.

Table 12. Summary of the Nd:YLF Raman lasers demonstrated in this work.

	Nd:YLF/BaWO ₄	Nd:YLF/KGW
1st Stokes wavelength (nm)	1167	1147 (768 cm ⁻¹) 1163 (901 cm ⁻¹)
1st Stokes output power (W)	1.5	0.70(CW) / 1.20(qCW) 0.95(CW) / 1.56(qCW)
Diode-Stokes efficiency (%)	9	5.4 7.7
Beam quality M²	1.5	1.5
Visible sources		
SHG/SFG wavelength (nm)	583/-	573 / 549 581 / 552
SHG/SFG power (W)	0.6	0.60(CW), 1.25(qCW) / 0.65(CW), 1.20(qCW) 1.10(CW), 1.65(qCW) / 1.90(CW), 3.12(qCW)
SHG/SFG diode-visible efficiency (%)	4	4.6 / 5.0 7.8 / 14.6
SHG/SFG beam quality M²	-	1.76 / - 1.90 / 2.01

We can also compare our results to other Raman lasers reported using Nd:YLF. Savitski *et al.* reported the highest output power of 6.1 W [82] for any CW Raman laser, by combining the 1047 nm fundamental from Nd:YLF and the 768 cm⁻¹ shift in KGW. However, the overall diode to first Stokes efficiency of ~4% was substantially lower than the 9% reported here, and also the beam quality, $M_x^2 \sim 5$ and $M_y^2 \sim 6$, is not good as the $M^2 \sim 1.5$ reported here. Interestingly, the beam quality they found using diamond (instead of KGW) was an excellent $M_x^2 \sim 1.1$ and $M_y^2 \sim 1.2$, which given the very high thermal conductivity of the diamond, suggests that some of the beam degradation occurs in the Raman crystal. In the work of Bu. *et al.* [96], the (absorbed) diode to yellow conversion efficiency is estimated to be 7.4%, quite similar to the conversion efficiency we have obtained (7.8%). An attractive feature used in [96] is the coupled cavity setup. This reduces

considerably the intracavity losses for the Stokes field, yielding lower thresholds for SRS: 1.35 W compared to our lowest threshold of 2 W for yellow (581 nm).

We anticipate that substantial improvements in efficiency will be possible in the future by improving the characteristics of the mirror and crystal coatings, particularly the AR-coatings on the Raman crystals and the visible transmission of the output coupler. For all the cases investigated here, the 1st Stokes laser performance was superior when using the BaWO₄ crystal, compared to the KGW results in CW regime. While the 1167 nm laser provided a maximum CW power near 1.5 W, the 1163 nm reached 1 W and the 1147 nm only achieved about 700 mW. In the visible, the 581 nm laser delivered more than 1 W with a threshold of 2 W of absorbed power, while the 573 nm laser provided a maximum of 600 mW, similar to that obtained at 583 nm, with a threshold of 3 W of absorbed power. These distinct performances could be due to differences either in Raman gain or resonator losses at the various wavelengths. In the KGW case, according to the literature [120], as well as our measured spectrum in Figure 64, the 768 cm⁻¹ shift has higher Raman gain than 901 cm⁻¹, but we believe such a difference is not enough to explain the different performances we have observed. Considering all the mirror and crystal coatings, we found the round trip losses for both Stokes wavelengths to be similar, with the 1147 nm losing 0.1% more power per round trip than the 1163 nm, which may contribute to the small difference between their thresholds. Moreover the output coupler has a transmission of about 0.1% at 1147 nm and 0.2% at 1163 nm. This higher output coupling contributes to the higher power at 1163 nm. The maximum powers at 1147 nm were slightly limited by the onset of competition between the 901 cm⁻¹ and 768 cm⁻¹ shifts for absorbed pump powers above 18 W. With regard to the different output powers that were obtained in the yellow, we note that the O.C. mirror has about 20% of reflectivity at 573 nm and <5% at 581 nm, and this is likely to be the main cause for the reduced performance of 573 nm when compared to 581 nm. The powers at the two sum frequency wavelengths cannot be compared due to the crystal damage that occurred when optimising performance at 549 nm.

The output powers demonstrated here for Nd:YLF Raman lasers are substantial, particularly in the visible: CW operation yielded up to 1.5 W in the near-ir (1167 nm) and 1.9 W in the visible (552 nm). Quasi-CW operation at 50% duty cycle resulted in peak output powers up to 1.65 W in the near-ir (1163 nm) and over 3 W in the visible (552 nm).

Higher peak powers would be achieved at lower duty cycles, and there are many applications for which modulated laser output is suitable. Our capacity to scale to higher powers has been constrained by the need to avoid fracture of the Nd:YLF. However, there are recent developments in power-scaling CW Nd:YLF in which up to 60 W of output power at 1053 nm was demonstrated [28] by using large mode sizes in the Nd:YLF, and accordingly, we believe there is considerable potential for efficiently scaling Nd:YLF-based Raman lasers to much higher powers.

Yet another exciting possibility for the future exists to build a low-noise, multi-Watt yellow laser, this possibility stemming from the broad (~ 360 GHz) emission band of Nd:YLF. Here the concept is to build a sufficiently-long Raman resonator that operates simultaneously on a large number (100s) of longitudinal modes, an approach previously used to solve the “green problem” [121, 122].

Chapter 5

Study of a blue luminescence in solid state Raman lasers

- 5.1. Introduction to the problem**
- 5.2. Spectral characterization**
- 5.3. Multi-variate analysis of the blue luminescence (collaboration)**
- 5.4. Lifetime of the emission**
- 5.5. External cavity probing: Q-switch laser probe test**
- 5.6. Trace element concentrations – ICP-MS**
- 5.7. Proposed excitation mechanism for blue fluorescence**
- 5.8. Measurement of the blue power**
- 5.9. Implications of blue emission for Raman laser efficiency**
- 5.10. Implications of blue emission for thermal loading of Raman crystals**
- 5.11. Chapter summary**

5. Study of a blue luminescence in solid state Raman lasers

In this section the characterization and analyses of a blue luminescence, characteristic in some Raman crystals when operating above SRS threshold, is described. First it will be contextualized in the introductory section, and then the methods used for characterization will be discussed in the other sections. Finally, a discussion over all the characterization is made and some conclusions about the phenomenon are provided.

5.1. Introduction to the problem

With the rise of the solid state Raman lasers, one special side effect has been observed, a blue luminescence. Such luminescence is strong, clearly visible and bright in a well-lit room. This blue emission around 475 nm comes out of the Raman active crystal when reached the threshold for the Stokes oscillation. Several groups have reported the effect in their Raman lasers, showing the presence of the phenomenon in many different crystals, KGW [123, 124], BaWO₄ [79, 81], SrWO₄ [125, 126], YVO₄ [86], GdVO₄ [127] and SrMoO₄ [128]. Some of them tried to explain the origin of the emission, either by an upconversion in Nd³⁺ ions or by an upconversion in Tm³⁺ ions present in the crystals as impurities. However, the scope of those works were the laser performance, thus they presented a very brief discussion on the blue emission topic.

Nowadays, Raman lasers have reached a level of development that makes the reduction of resonator losses and thermal effects very relevant to their performance. Given that, there is the need of a better understanding of the blue luminescence phenomenon in order to comprehend not only the origin of the emission, but also its influence on Raman laser performance, either as an extra loss, or as an extra heating source, which may be originated from non-radiative decays derived from the upconversion process.

Recently, two works were published discussing specifically the blue emission [129, 130]. Zhu *et al.* [129], characterized the emission in three crystals, YVO₄, GdVO₄ and SrWO₄, with fundamental oscillations at 1063 nm, 1064 nm, 1079 nm and 1342 nm. The strongest emissions were found for the SrWO₄ crystals, when the fundamental was in the 1 μ m range, but no luminescence was observed for the 1342 nm fundamental. The conclusion found by them is that the luminescence is produced with only fundamental

oscillation around 1 μm , and no Stokes is needed for the process. However, they could not explain the origin of the emission. In [130], Kodasevich *et al.* made a deeper analyses of the phenomenon, comparing the experimental emission from a KGW crystal with the expected shape obtained by calculation for a Nd:KGW crystal and a Tm:YLF crystal. As a result, they found more similarities with the Neodymium emission band around 475 nm than with the Thulium one, although it was not enough to state that Nd^{3+} is the responsible for such emission. Both works discarded the Nd and Tm impurities hypothesis and they suggested at the end that usual theories do not apply to this phenomenon and a new one might be needed.

In all the cases reported, the groups were looking for the origin of the phenomenon, but no considerations was given to possible consequences for laser operation in terms of laser efficiency or thermal loading of the crystals. We present here the characterization methods we have used to analyze the origin of the blue emission for the Raman lasers: spectral analyses of different Raman crystals; lifetime; extra-cavity probing; quantification of impurity ion concentration; and power measurement. Finally we consider the implication of the blue luminescence for laser operation, particularly with regard to laser efficiency and thermal loading of the Raman crystal.

5.2. Spectral characterization

We selected four crystals in which the blue emission had been previously reported: KGW, BaWO_4 , Nd:GdVO₄ (from two suppliers) and Nd:YVO₄. The setup used to measure the fluorescence was very simple. The Raman lasers were built with the Raman medium of interest, then from one of the crystal faces the blue emission was collected using two spherical lenses in order to capture as much light as possible and couple it in a fiber with a 200 μm core diameter. This fiber injected the light collected into the HR4000 spectrometer module (Ocean Optics). Figure 68(a) shows the blue light emitted in a long line path, which overlaps the resonator modes. Figure 68(b) shows the setup used to measure the spectra of a self-Raman laser, while Figure 68(c) shows the setup for a laser with the laser and Raman crystals separated. Another approach used to collect the blue emission was to insert the fiber in a hole on the side of the heat sink mount of the Raman crystal, as per Figure 68, although it was less efficient than the previous method.

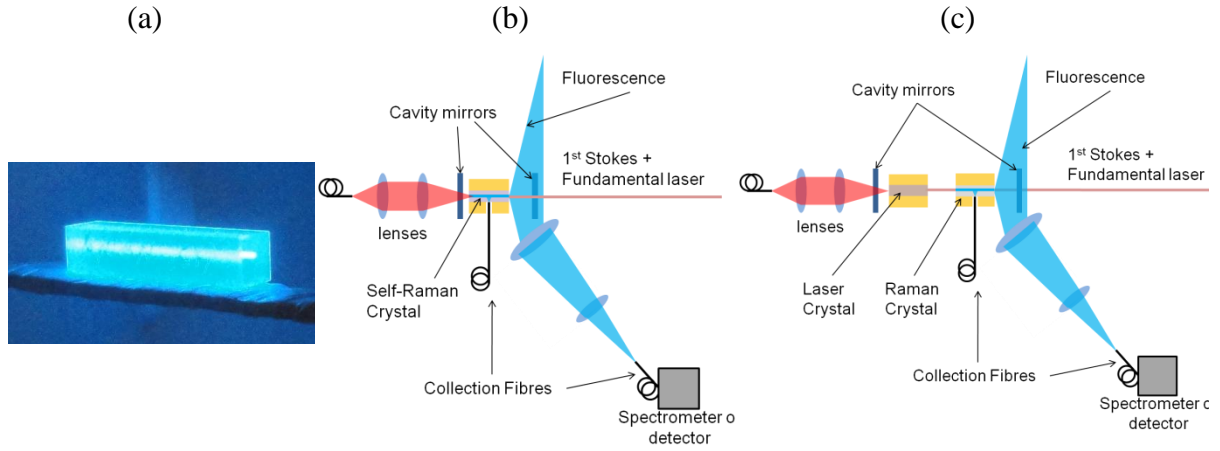


Figure 68. (a) Picture of the blue emission in a KGW crystal and the setup used in the spectral measurements (b) for self-Raman configuration and (c) separated laser and Raman crystals.

The spectra in Figure 69 correspond to the crystals KGW, BaWO_4 , Nd:GdVO_4 and Nd:YVO_4 , and they were obtained using a high resolution spectrometer (Ocean Optics HR4000 , having ~ 0.1 nm of resolution). Note that two of the crystals were intentionally doped with 0.3% Neodymium (ie self-Raman materials). The spectra were recorded above threshold for SRS, for a diode pump power of 15 W.

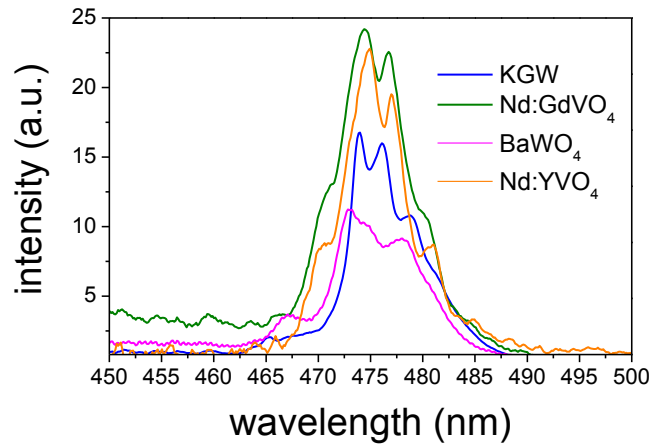


Figure 69. Blue emission spectra of KGW, Nd:GdVO_4 , Nd:YVO_4 and BaWO_4 crystals.

It is possible to see similarities between all the four crystals, despite the fact that two are vanadates and two are tungstates, and that two are intentionally doped with Nd and two are undoped. There are even stronger similarities between tungstate based hosts and between vanadate based hosts. In addition, the good spectral resolution that reveals the multiple peaks of the emission has made allowed us to compare the spectra obtained here with high resolution spectra found in the literature.

The blue is the strongest emission coming out of the Raman crystals, but not the only one. There is also a red emission which was not mentioned in the previous reports. The spectrum in Figure 70 shows this emission band around 650 nm. It can only be seen above SRS threshold. However, such emission is not easy to resolve since it is much weaker than the blue one.

It becomes clear looking at the spectra in Figure 70 that the emissions around 525 nm, 550 nm and 600 nm are present with or without the SRS, but the blue emission (475 nm) and the red emission around 650 nm only happen above the SRS threshold. Below such threshold there are no strong traces of both blue and red emissions, showing that they do not come from the standard Nd^{3+} fluorescence. In the case of KGW, very weak blue luminescence (by at least an order of magnitude) was sometimes observed below SRS threshold.

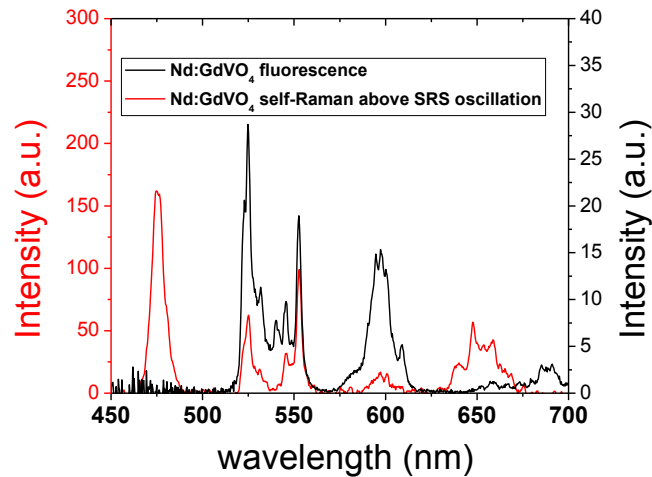


Figure 70. Blue and red emission at 650 nm from a Nd:GdVO₄.

Taking the Nd:YVO₄ spectrum and comparing it with a Tm:YVO₄ spectrum found in [131], with similar resolution, it is possible to see a very good match between them, as

shown in Figure 71(a). The same was done for the KGW, as shown in Figure 71(b). We were not able to get analogous information for the other crystals, mostly because the spectra we found in the literature did not have sufficient resolution.

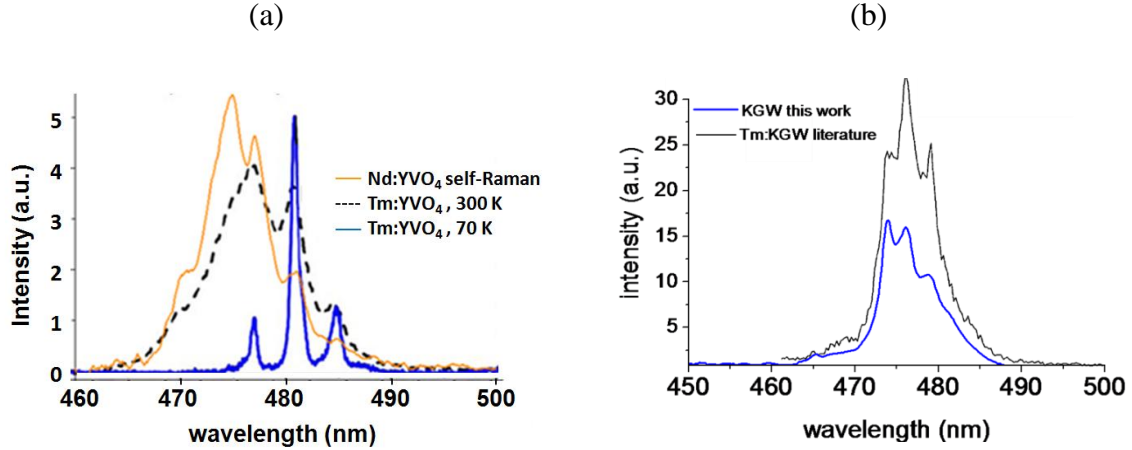


Figure 71. Comparison between blue emission in a Nd:YVO₄ self-Raman and (a) Tm:YVO₄ blue emission and (b) between KGW Raman laser and Tm:KGW [132].

We also observed that the blue emission intensity increases with the 1st Stokes power. Plotting such function in a log-log scale, we could observe a slope of 1.5, which shows that at least two Stokes photons are likely to be involved in the process. This kind of analysis is well described in [133], but has some restrictions for the experiments here, such as phonon assistance, other complex interactions and that it is hard to interpret the plots due to the fact it is not possible to vary the fundamental and Stokes powers independently. An alternative is to use multi-variate analysis. This analysis was a contribution of a PhD student, Christopher Artlett, also working in the Raman laser group and its description is found in the next subsection.

Observations were also made about the intensity of the blue emission in different crystals under the same conditions of operation. We noticed stronger emission in the KGW crystal than in the BaWO₄ crystal and in the Nd:GdVO₄ crystals. In addition, we have tested two different Nd:GdVO₄ crystals, with different origins. In this case, we observed that one of them (from the Northrop Grumman -NG) had stronger emission than the other (from Castech). This emission was even stronger than the one observed in the KGW crystal. The blue emission from BaWO₄ was the weakest.

Using different laser crystals to generate the fundamental, specifically Nd:YLF and Nd:YAG, we also noticed some blue emission inside the laser active medium, which has not been reported before. The spectra are shown in Figure 72(a) for the Nd:YLF and Figure 72(b) for the Nd:YAG.

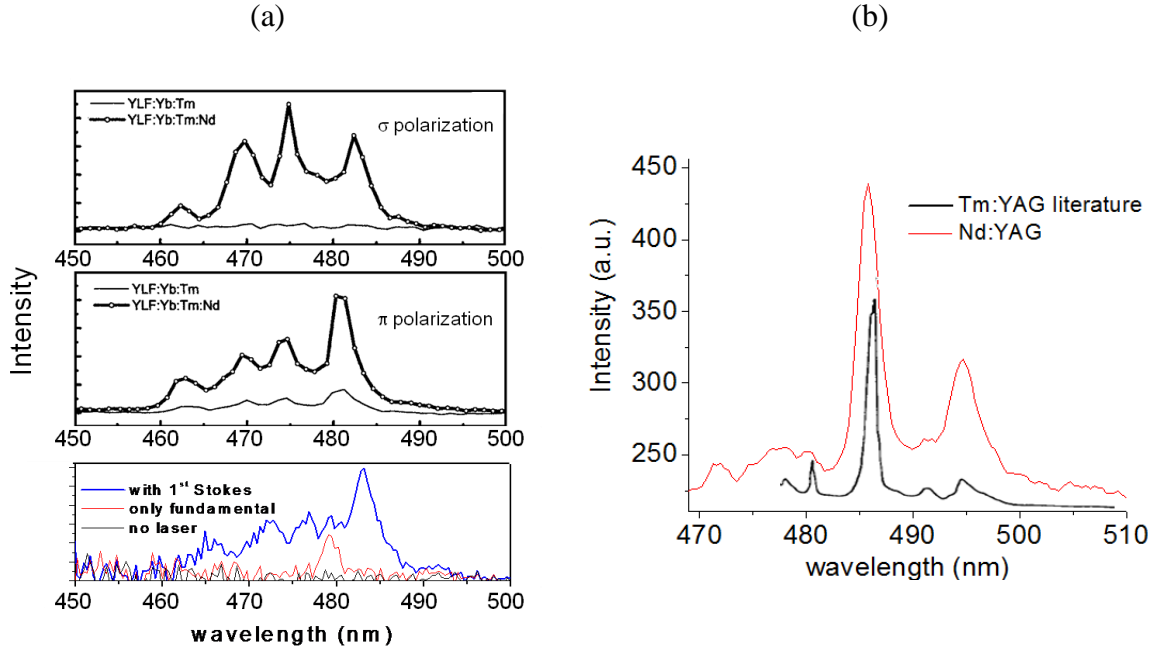


Figure 72. Blue fluorescence found in Nd:YLF and Nd:YAG under Raman lasers operation compared to (a) Tm:Yb:Nd:YLF [134] and (b) Tm:YAG [135] found in the literature.

Comparing the spectra obtained from the literature for the equivalent hosts doped with Tm^{3+} , it is again possible to see similarities. However, the blue emission from these crystals is not nearly as strong as for the blue emission coming from a Raman shifting medium.

Looking at the emission in separate crystals and self-Raman configurations, we observed that the Nd:GdVO_4 crystal presents the emission when used in a self-Raman configurations, although no emission is seen if the same crystal is not operating as the Raman active medium. It shows the phonons in the Raman process do play an important role for generating the blue emission, which could be due to some kind of phonon assistance supported by the huge amount of phonons generated in the stimulated shift.

Finally, an odd effect was observed in a very specific case. One of the Nd:GdVO₄ crystals showed a strong increase of its characteristic green emission at a very specific pump power. The emission became much stronger than the blue, which was weaker than that obtained for lower pump power. It was not observed in any other case. It suggests that in this case, an energy transfer took place and aided to populate the green emitting level ($^4G_{7/2} \rightarrow ^4I_{9/2}$) in the Nd ions, Figure 73. This emphasizes the complexity of this system.

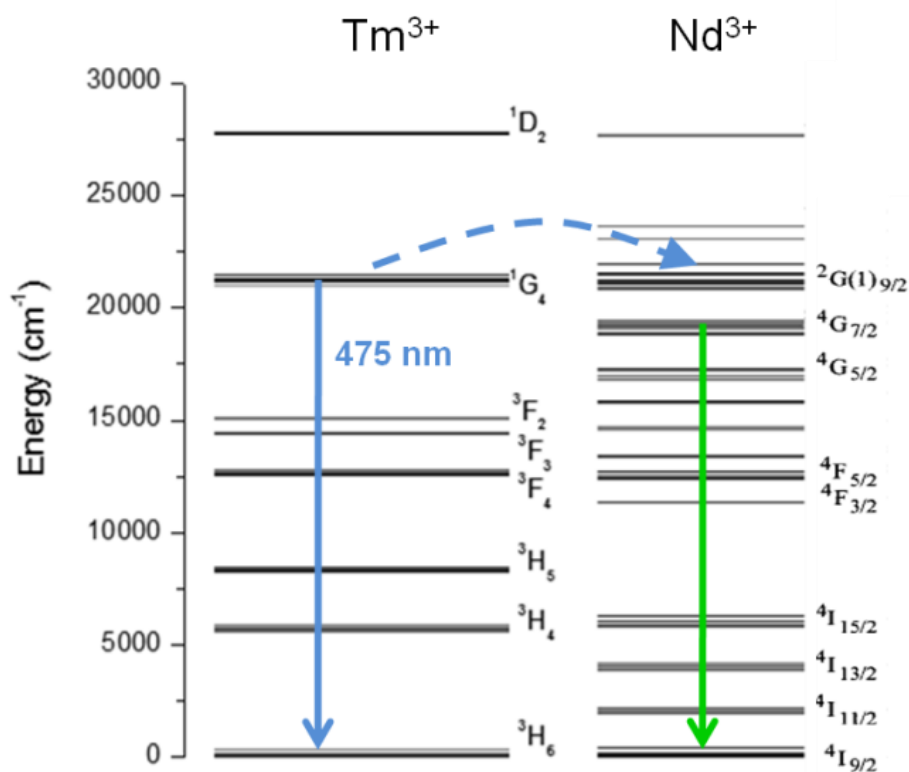


Figure 73. Possible path for energy transfer between Tm and Nd ions.

5.3. Multi-variate analysis of the blue luminescence (collaboration)

A detailed investigation was made of the emission spectra as a function of incident diode pump power. We have observed the changes of the emission intensities as a function of pump power, using a Nd:GdVO₄ self-Raman laser, as seen in Figure 74. The fundamental and Stokes powers measured through the output were recorded.

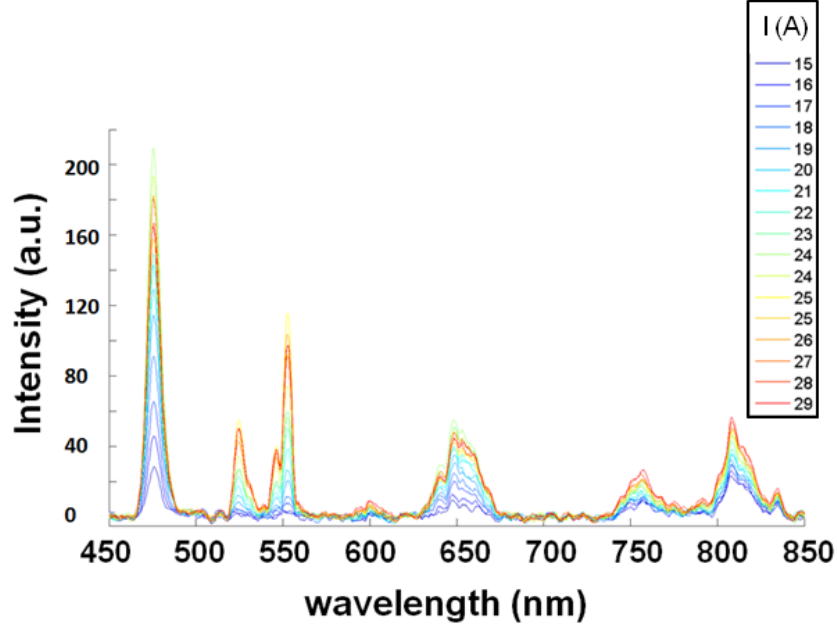


Figure 74. Emission spectra of the Nd:GdVO₄ Raman laser for different diode pump currents.

We used absorbed pump powers from 5 W to 19 W, corresponding to a diode current range from 15 A to 29 A, as shown in Figure 74. The spectra were processed (smoothed, Savitsky-Golay, 3rd order, 17 pts) and then, statistically analyzed by means Principal Component Analysis (PCA). I collected the experimental data, and the analysis was made by Christopher Artlett, a PhD student in our group who has the expertise with such statistical methods.

Multivariate data consists of many different attributes or variables recorded for each observation. In this particular case at each pump power the emission spectrum was collected (one observation) containing the intensity of each wavelength (variables). Multi-dimensional hyperspace is often difficult to visualize, and thus the main objectives of such method are to reduce dimensionality and score the observations based on a composite index and clustering similar observations together based on multi-attributes. It becomes possible to display graphically in case these attributes are reduced to two or three (dimensions), and kept a minimal loss of information.

PCA summarizes the variation in a correlated multi-attribute to a set of uncorrelated components, each of which is a particular linear combination of the original variables. The

extracted uncorrelated components are called principal components (PC) and are estimated from the eigenvectors of the covariance or correlation matrix of the original variables. These PCs are extracted in decreasing order of importance so that the first PC accounts for as much of the variation as possible and each successive component accounts for a little less.

The plots extracted from the PCA analysis are PC loadings and PC scores. PC loadings measure the importance of each variable in accounting for the variability in the PC. It is possible to interpret the first few PCs in terms of 'overall' effect or a 'contrast' between groups of variables based on the structures of PC loadings. PC scores are the derived composite scores computed for each observation based on the eigenvectors for each PC.

Intensities for relevant fluorescence peaks were collated for each pump current level. Peak intensity data were then imported into The Unscrambler (Camo Software), a statistical analysis program primarily designed for spectroscopic analysis and chemometrics. The data were then analysed.

PCA Model – All Data

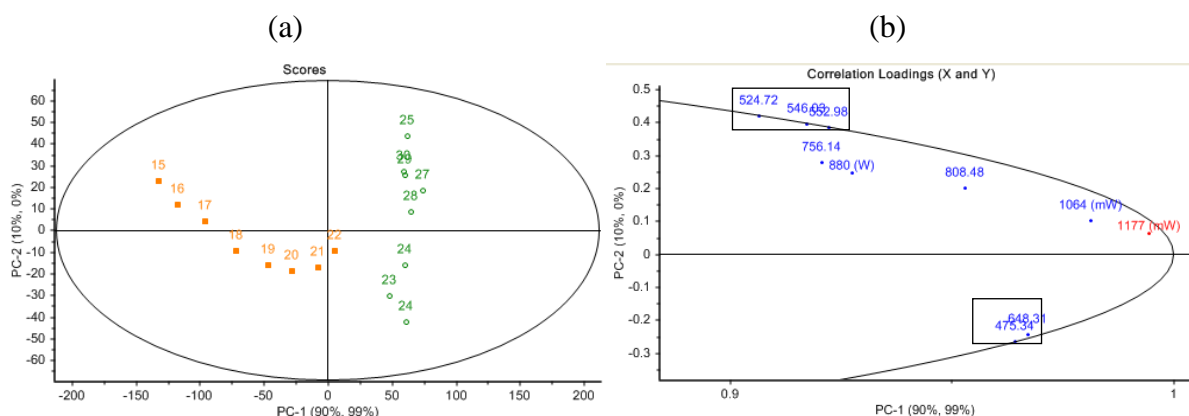


Figure 75. PCR plots for all spectral data. (a) Scores, (b) Loadings.

The points in Figure 75(a) represent the combination of spectra for each diode current level in terms of new axes PC1 and PC2 (Principal Components). Orange points are the lower current measurements, while the green points are the higher current measurements. Figure 75(b) represents the strength of the relationship between the various fluorescence bands and PC1 and PC2. Some clustering of these data is evident, with the

475 and 648 nm emissions strongly correlated, with the same occurring for the 524-552 nm bands. Significantly, they cluster away from each other, which is suggestive of different mechanisms.

The two current segments which are shown in the scores plot (Figure 75) were next investigated independently.

PCA Model – Low Current Regime

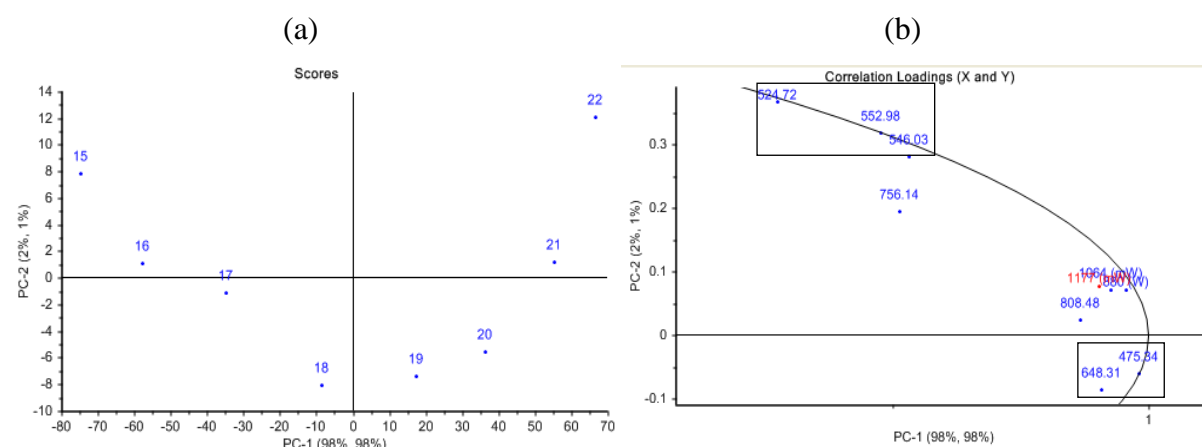


Figure 76. PCR plots of low current data. (a) Scores, (b) Loadings.

The low diode current data in Figure 76 show somewhat similar behaviour to the complete data seen in Figure 75.

PCA Model – High Current Regime

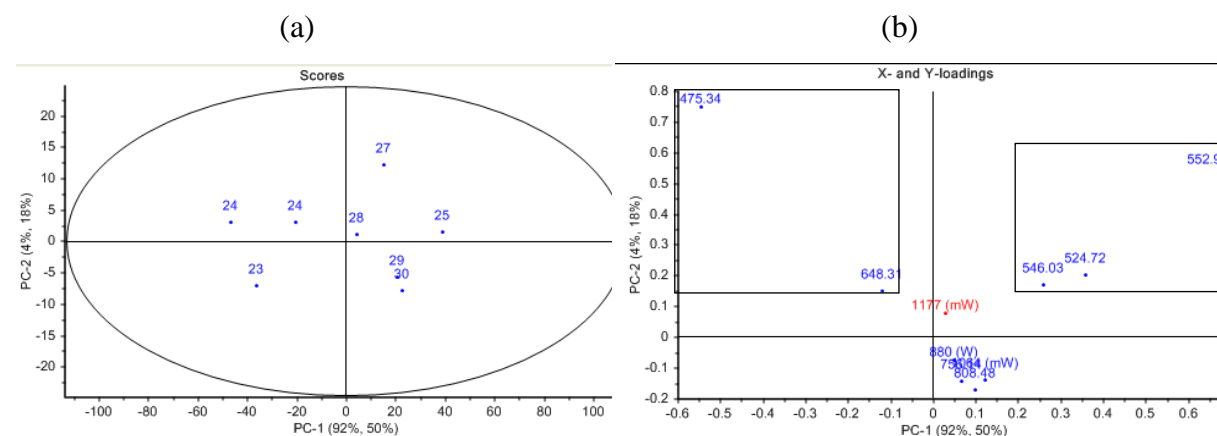


Figure 77. PCR plots of high current data. (a) Scores, (b) Loadings.

High current regime data (Figure 77) appear to show separation between Raman and “Raman-linked” emissions in terms of PC2, and the 475/648 nm and 524-552 nm emission bands in PC1.

In summary, Principal Component Analysis provided more information about the relationships the emissions have with each other. As a result, the 475 nm and 648 nm emissions seem to cluster near each other in all the cases, which indicate they are originated from correlated mechanisms, such as decays from the same level. In the case of Tm^{3+} , the blue and red emissions decay from the $^1\text{G}_4$ level to different lower energy levels, 475 nm ($^1\text{G}_4 \rightarrow ^3\text{H}_6$) and 648 nm ($^1\text{G}_4 \rightarrow ^3\text{H}_4$) which is strongly supported by the PCA analysis.

5.4. Lifetime characterization

In order to measure the decay time of the blue emission, four Q-switched Raman lasers were built using each one of the Raman active crystals studied here. A Nd:YAG crystal was used as the laser active medium in the case of YVO_4 , KGW and BaWO_4 . For the Nd:GdVO_4 a self-Raman laser was built since there was no undoped GdVO_4 crystal available. Using a 50 mm lens to collect the blue emission from the Raman crystal and a 75 mm lens to image it into a Photomultiplier tube (Hamamatsu R456), it was possible to measure the lifetimes. Two visible band pass filters (FGS900 Thorlabs) together with a short pass filter, which reflects the green and yellow emission (nonlinearly generated in the Q-switch crystal), were used in order to allow only the specific blue emission at 475 nm to get in the PMT. Figure 78 shows the decay curves collected.

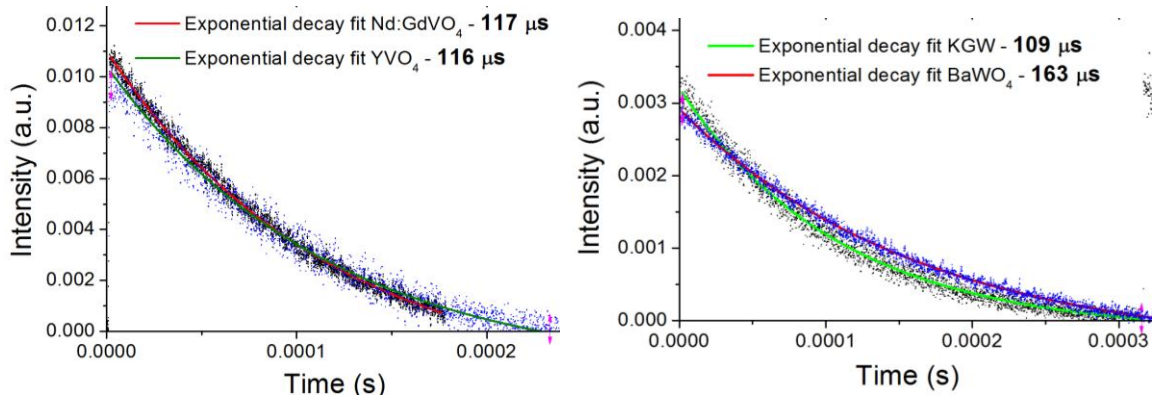


Figure 78. Fluorescence lifetime decays for Nd:GdVO₄, YVO₄, KGW and BaWO₄ crystals.

Table 13 below summarizes the lifetimes measured for each crystal. Also, it shows the lifetime values found in the literature for the Tm³⁺ ¹G₄ transition (475 nm) in the respective hosts.

Table 13. Lifetimes obtained in this work and the ones for the corresponding Tm³⁺ doped hosts.

	Fluorescence lifetime – this work (μs)	475 nm Tm ³⁺ lifetime – literature (μs)	Ref
KGW	109	127 (0.1 at%) fluorescence lifetime	[136]
BaWO₄	163	-	-
Nd:GdVO₄	117	140 radiative lifetime	[137]
YVO₄	116	131 radiative lifetime	[138]

We found similar lifetime values for three of the crystals we measured, Nd:GdVO₄, YVO₄ and KGW. There is no such information for the BaWO₄ crystal in the literature, it started to be used for laser purposes recently. For the KGW the fluorescence lifetime described in [136] is from a 0.1 at% Tm doped crystal, which is a small concentration, good to compare to our measurements, where the Tm concentration is supposed to be very low. For the vanadates we found the radiative lifetimes, which do not consider any parallel process that may quench the emitting level, which could shorten the lifetimes. Therefore, considering an impurity as a very low concentration of Tm, in this case, one should observe

fluorescence lifetimes close or slightly shorter to their radiative lifetimes. Based on that, it is feasible to compare the lifetimes measured here to the reported ones. All the lifetimes found in the literature were just a little bit longer than the ones measured in the Raman crystals, but they are in the same order of magnitude, differing only 20 μs to 30 μs . Given that, it is very possible that the decay in the Raman crystals is coming from the $^1\text{G}_4$ level of Tm^{3+} impurities, reinforcing this hypothesis.

5.5. External cavity probing: Q-switch laser probe test

Two reasons were found to support an external probing of the Raman crystals. The first one is the fact that the thulium $^1\text{G}_4$ blue emitting level could have been populated using only 1st Stokes photons with some support of non-radiative transitions. Also, it could need the support of some fundamental photons added to the Stokes field, but may have no need of phonons originated from the Raman scattering. Using a Q-switched laser it is possible to obtain intensities as high as the ones found intracavity in a CW laser, and then analyze the influence of the fundamental and Stokes fields independently. Figure 79 shows the Tm^{3+} energy level scheme and the possible paths to populate the $^1\text{G}_4$ level.

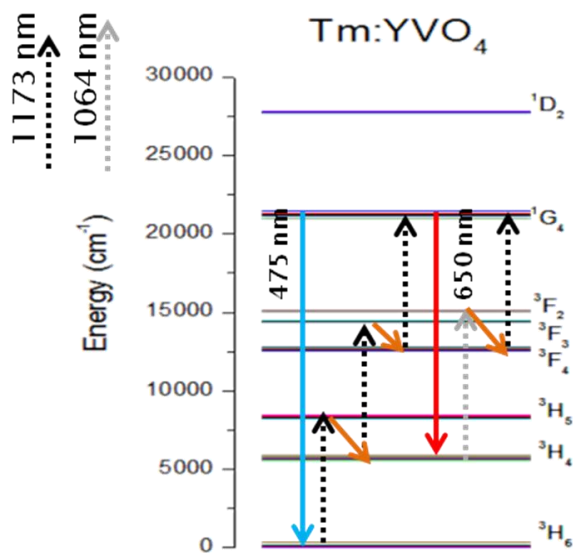


Figure 79. Tm:YVO_4 energy level scheme and the possible paths to populate the blue emitting level.

The other reason is related to the fact that this kind of measurement is useful even if there is no Tm^{3+} involved. It gives a general understanding on how the blue emission behaves in the presence of each field separately.

For such experiment a Nd:YAG/YVO₄ active Q-switch Raman laser was built. A 10 mm long Nd:YAG with 1.0 at% of Nd^{3+} was used as the active medium. The frequency was then shifted by a 20 mm YVO₄ crystal. Placed between the crystals there was an acousto-optic Q-switch unit to modulate the laser. The cavity consisted in a 200 mm of ROC (radius of curvature) mirror as the pump mirror and a flat mirror with 5% transmission at the 1st Stokes wavelength as the output coupler. From this laser it was obtained 20 ns pulses with 3 kHz of repetition rate and an average power of 0.5 W at the 1st Stokes. Using either a 50 mm or a 30 mm focal length lenses, the beam intensity was increased to values higher than the intracavity ones observed in CW Raman lasers. Figure 80 shows the setup used in the experiment.

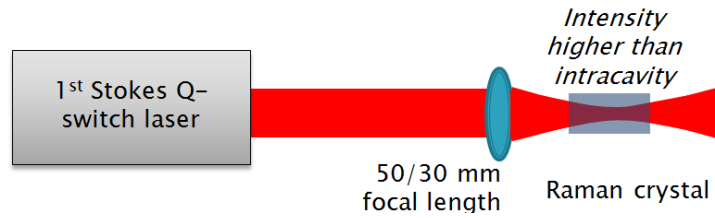


Figure 80. Setup used for the Q-switch Raman laser probe tests.

The CW intracavity intensity obtained in previously built lasers was calculated to be about 200 kW/cm². With the configuration above, it was obtained intensities at least 100 times higher. Operating at this condition the blue emission should be visible even by naked eyes, once the 0.02% of duty cycle reduces in 50 times the blue intensity we can see (since the eyes can only distinguish the average power at this repetition rate), but on the other hand there was an increase of at least 100 times in the intensity we are using to pump the crystal which should be enough to make it visible again.

The crystals used for the probe were two Nd:YVO₄ crystals and a KGW crystal. Using a filter to block the residual fundamental laser leaking from the output coupler, the crystals were probed with a very intense and pure 1st Stokes field in different positions and orientations, either the c-axis parallel or perpendicular to the polarization of the beam and changing the focusing lens either to 50 mm or to 30 mm lens. Also, the filter that blocked

the fundamental field was removed leaving some amount of fundamental photons to get in the probe crystal, providing a probe with both fields simultaneously.

As a result the blue emission was not observed in all cases. Analyzing such result we can figure out that either the phonons generated by the scattering process must play a role to populate the 1G_4 level or there is a specific proportion for the number of 1064 nm photons and the 1st Stokes photons that make it turn on. To further support it, other researchers in our group have built Raman lasers with a Nd:GdVO₄ as the laser crystal and a BaWO₄ as the Raman medium, and it was found out that when SRS takes place in the BaWO₄ crystal, the blue is strong only in the BaWO₄ and not in the Nd:GdVO₄. On the other hand, if the SRS takes place in the Nd:GdVO₄, the opposite happens, with a strong blue emission at the Nd:GdVO₄ but not at the BaWO₄.

5.6. Trace element concentrations – ICP-MS (Inductively coupled plasma mass spectrometry)

We have measured the elements concentration using an ICP-MS to verify the presence of Tm³⁺ in two different Nd:GdVO₄ crystals from Northrop Grumman (NG) and Castech, in a KGW and in a BaWO₄ crystal. For each of the crystals, measurements were made in three different spots measured (S1, S2 and S3). The concentration and other relevant parameters obtained in the measurements are summarized in the Table 14.

Table 14. ICP-MS Tm³⁺ concentration measurements (full data in Appendix C).

BaWO₄	Trace element concentration (ppm)	Error	Minimum detection limits	Counts
S1	0.00032	0.0001	0.00025	84
S2	<0.00024	0.0001	0.00024	26
S3	<0.00027	0.0001	0.00027	69
Nd:GdVO₄ (Castech)	Trace element concentration (ppm)	Error	Minimum detection limits	Counts
S1	0.00129	0.00011	0.00015	213
S2	0.0012	0.0001	0.00015	196
S3	0.00103	0.0001	0.00015	164
KGW	Trace element concentration (ppm)	Error	Minimum detection limits	Counts
S1	0.00168	0.00012	0.00025	466
S2	0.00182	0.00013	0.00024	491

S3	0.00133	0.00013	0.00028	352
----	----------------	---------	---------	-----

Nd:GdVO₄ (NG)	Trace element concentration (ppm)	Error	Minimum detection limits	Counts
S1	0.00385	0.00021	0.00016	636
S2	0.00365	0.0002	0.00015	620
S3	0.00384	0.0002	0.00016	641

As noted in section 5.2, the blue emission in the Nd:GdVO₄ crystal from NG was stronger than for the crystal from Castech. This corresponds well with the measured Tm concentration being more than two times higher for the NG crystal. Similarly, blue emission from KGW was much stronger than for BaWO₄, and this corresponds to a much higher Tm concentration in the KGW. So, it is in very good agreement with the Tm³⁺ concentration found in the ICP-MS measurements. In the case of BaWO₄, only one sample (S1) presented traces of Tm³⁺ above the detectable limit. Other researchers from Macquarie have since found significant differences in the blue emission intensity from different BaWO₄ crystals.

5.7. Proposed excitation mechanism for blue fluorescence

Based on the observations in previous sections, we believe that the blue fluorescence originates from the ¹G₄ to ³H₆ transition in Tm³⁺, which is present as an impurity in the crystals we have studied. The proposed mechanism is strongly supported by the spectral similarities observed between the blue emitted by the Raman crystals measured in this work and by their Tm-doped version. The multi-variate analysis shows a strong correlation between the blue and red emissions, supporting the same emission mechanism (same upper energy level), which is characteristic in Tm-doped materials. Also, the lifetimes measured for different Raman crystals are consistent with the ones found in the literature for Tm-doped crystals with the respective hosts. Finally, the ICP-MS showed out the presence of Tm³⁺ impurities in all the hosts studied here, with higher Tm concentration in crystals with more fluorescence.

Given this strong evidence to support the Tm impurity hypothesis, it is possible to propose the sequential absorption mechanism that raises the ions to the ¹G₄ emitting level, in the case, two or three Stokes photons should be involved, as shown in Figure 81. The

first transition is ${}^3\text{H}_6 \rightarrow {}^3\text{H}_5$ by means of the absorption of a 1st Stokes photon (S1); then follows a non-radiative decay ${}^3\text{H}_5 \rightarrow {}^3\text{H}_4$ (H1); the second step is the absorption of another 1st Stokes photon ${}^3\text{H}_4 \rightarrow {}^3\text{F}_3$ (S2) or a fundamental photon ${}^3\text{H}_4 \rightarrow {}^3\text{F}_2$ (F1); then another non-radiative decay ${}^3\text{F}_3 \rightarrow {}^3\text{F}_4$ (H2); and finally another Stokes photon is absorbed ${}^3\text{F}_4 \rightarrow {}^1\text{G}_4$ (S3), populating the ${}^1\text{G}_4$ level.

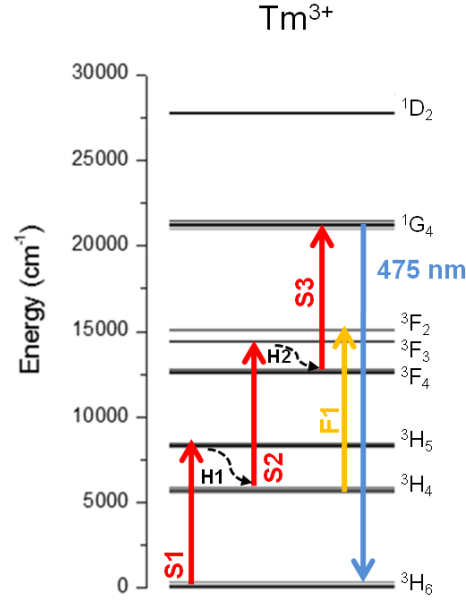


Figure 81. Blue upconversion steps.

The energy level scheme shown in Figure 81 is built using the data found in [139]. The reference contains the Tm^{3+} energy distribution for different hosts. The one shown in the figure corresponds to $\text{Tm}:\text{YVO}_4$ at 300K.

5.8. Measurement of the blue power

To quantify the power of the blue emission accurately, we used an integrating sphere (Labsphere) and the setup displayed in Figure 83. For that, we built a Raman resonator using a $\text{Nd}:\text{YLF}$ crystal as the active medium and a KGW as the Raman active medium. The Stokes wavelength was at 1163 nm. This combination of crystals was chosen because the KGW (901 cm^{-1} shift) was the crystal presenting the strongest blue emission amongst all we observed (not considering the self-Raman crystals), and the $\text{Nd}:\text{YLF}$ was used because its weak thermal lens enabled a long cavity to be made which would accommodate the

integrating sphere (diameter of 9.5 cm). Another precaution taken was not use a self-Raman configuration, such as Nd:GdVO₄ or even a Nd:KGW, in order to avoid pump light by Nd³⁺ which could complicate the measurement. Finally, a photopic filter [140] was placed in front of the detector, in order to avoid any infrared photons to be measured.

The laser performance was not as good as the ones obtained in chapter 4, mainly due to poor mode matching, but efficiency was not considered important in this case. Using an output coupler with transmission of 0.2% at 1163 nm, the laser performance was recorded, and the results are shown in Figure 82.

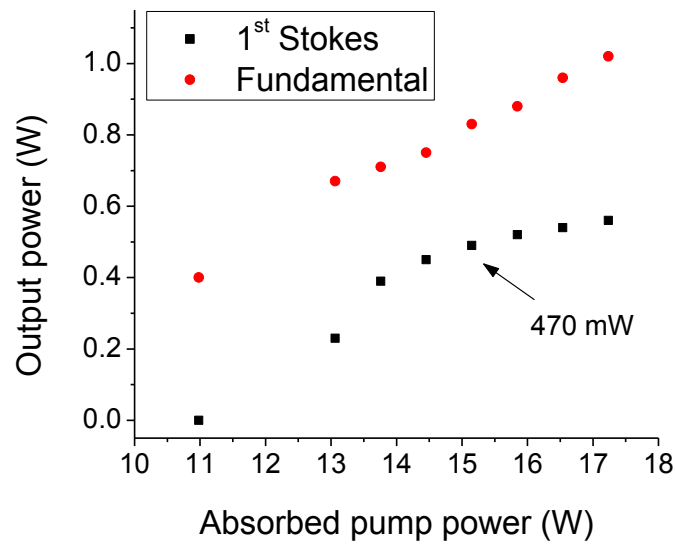


Figure 82. Nd:YLF/KGW laser performance.

Higher threshold and output powers lower than the ones obtained before are explained by the fact the cavity was modified to introduce the integrating sphere, thus the overlap of the pump and laser mode was not as good as before. Also, the KGW crystal was not actively cooled as before, which may influence in the laser performance as well. Figure 83 shows the setup used to measure the blue power.

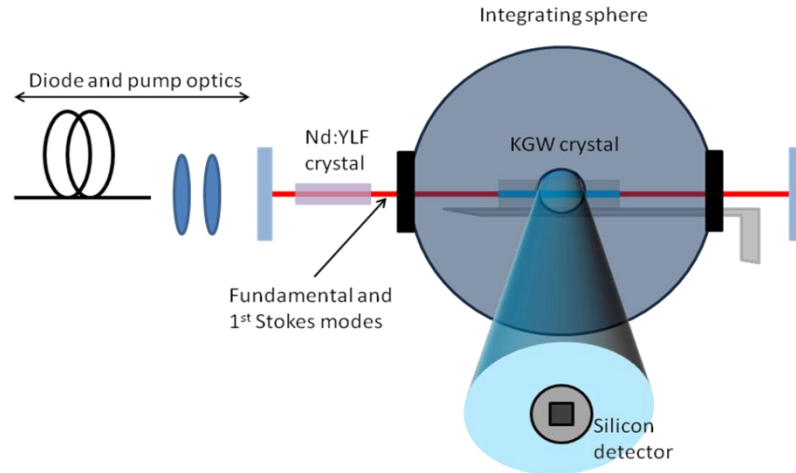


Figure 83. Laser cavity with the integrating sphere used to measure the blue emission power.

Looking from another angle it is possible to see the solid angle that effectively reaches the detector, Figure 84.

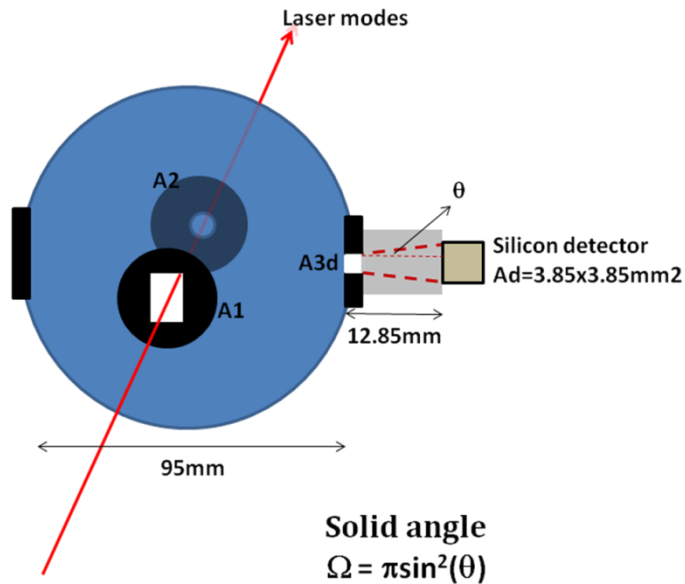


Figure 84. Another perspective of the sphere showing the detector field of view.

Using a known laser source, a green laser (532 nm; 3.5 mW), we performed the calibration of the sphere. We determined the areas of all the ports where the light escapes from the sphere and used the specified reflectivity of the internal surface of the sphere (spectrafect- 97% reflectivity at 475 nm). Then the flux of light into the detector was

calculated and compared to the value measured. If the numbers are different, it means that the real system has extra losses that the calculation did not consider, like the crystal holder we introduced to place the KGW crystal in the center of the sphere. This was wrapped the holder with white Teflon tape to maximize its reflectivity. Finally, we included an extra loss factor (calibration factor) in the calculation which could be varied until the calculated power agreed with the measured power. Having calibrated the system in this way, it was then used to determine the blue power. Yet another approach to estimate the blue power was used, with the measured powers in the detector (corrected for the filter transmission and detector sensitivity at the respective wavelengths) and the total green laser power, the blue total power can be estimated by proportionality. The detailed calculations can be found in the Appendix A (Estimation of the Blue fluorescence power using an Integrating sphere), which brings the MathCad worksheet used for these calculations.

As a result, it was measured a total blue power of 17.4 mW using the first measure and 19.2 mW using the linear relation, both for 15 W of absorbed pump power in the Nd:YLF crystal. The source of such difference in the two approaches used can be due to the fact the sphere used was not in the best condition. Probably the main source of the error is the internal coating degradation, which would reduce its reflectivity, and consequently increasing the blue power measured to values closer to the one found using the linear approach. The estimated error is calculated to be of $\pm 15\%$, as shown in Appendix A. The following sections use 19 mW for the power of the blue emission.

5.9. Implications of blue emission for Raman laser efficiency

In order to estimate the maximum power extracted from the 1st Stokes field, by the stepwise upconversion process, one should consider the worst case scenario, which is the use of three Stokes photons to reach the 1G_4 level. However, not every Tm in the 1G_4 level will decay by emitting a blue photon and so, the branching ratio (β) of the 1G_4 level and the quantum efficiency (η_{qe}), have to be taken in account. The branching ratio is found in the literature [138], and it is 0.4, while the quantum efficiency is calculated from the ratio of the measured fluorescence lifetime (τ_f) to the radiative lifetime (τ_r).

$$\eta_{qe} = \frac{\tau_f}{\tau_r} \quad (42)$$

Based on the lifetime values described in the previous section, the quantum efficiency is calculated to be 0.86. The power (P_{total}) loss from 1G_4 in order to generate 19 mW of blue (P_{blue}) is calculated by (43),

$$P_{total} = \frac{P_{blue}}{\eta_{qe} \cdot \beta} \quad (43)$$

The power is calculated to be 55.3 mW. Now we assume that three Stokes photons were consumed for each 1G_4 level that decays (radiatively and nonradiatively) and the power extracted from the Stokes field is given by

$$P_{Stokes} = \frac{3 \cdot h\nu_S}{h\nu_{blue}} \cdot P_{total} \quad (44)$$

where h is the Planck constant, ν_s is the Stokes frequency and ν_{blue} is the blue frequency. 68 mW of Stokes power is expected to be extracted from the intracavity field per round-trip.

We compare this 68 mW of Stokes power lost from the system to the power lost by the passive losses and by the output coupler. For the cavity used in these experiments, the intracavity field is of the order of 230 W for the 1st Stokes. Therefore, the 68 mW represents a loss of around 0.029% for the Stokes field (see calculations in the Appendix A - Blue fluorescence loss and thermal contribution in Raman Lasers). For the case of only two photons involved in the process, this loss is going to be lower. The coatings in the crystals have a reflectivity of about 0.05% at the Stokes wavelength, although it is partially minimized by aligning the crystals, which traps the reflected photons on the resonator axis, contributing minimally for the resonator loss. Comparing the 68 mW lost to the Stokes output power of 470 mW, it represents a small percentage of 14.5%. Based on that, the influence of the blue fluorescence in terms of loss is fairly low for the specific cavity used here.

Finally, the blue fluorescence may have some thermal influence that deserves further investigation. It can add to the thermal lensing of the crystal, which would also degrade the laser performance.

5.10. Implications of blue emission for thermal loading of Raman crystals

The importance of considering the involvement of the blue to the thermal loading in Raman lasers was pointed out by Dekker *et al.* [78] in 2007 and more recently by Omatsu *et al.* [91] in 2012. Both works treated deeply the thermal lens issue in Raman lasers, and both raised the possibility that the blue fluorescence might contribute to the “higher than expected” heat found in their measurements. However, there is no research in the literature characterizing this thermal load created by the blue fluorescence. Given that, we decided to estimate such extra heat.

We can begin by making a very approximate calculation about the thermal loading associated with 19 mW blue fluorescence. To a first approximation, we can simply take the difference between the 68 mW Stokes power consumed to generate the 19 mW blue emission. This provides an upper limit on the power deposited as heat of 49 mW. We can then compare this to the phonon heating which accompanies the first Stokes output power of 470 mW. This phonon heating is found to be 44.5 mW, from the difference in fundamental and first Stokes photon energies.

Given the similarity between these powers, it appears that the blue fluorescence phenomena could be contributing a significant thermal load to the KGW, relative to Raman heating. We therefore consider the issue in more depth. The calculations described below were made using the MathCad worksheet in Appendix A, and we maintain our assumption that 3 Stokes photons are required to excite a Tm ion to the 1G_4 level.

First consider the excitation of the 1G_4 level. As shown in Figure 81, the energy of 3 Stokes photons exceeds the energy level of Tm (1G_4) and the difference is accounted for the nonradiative decays indicated by the black arrows. This gives a first contribution to the thermal load associated with the blue fluorescence.

$$P_{heat\ blue\ 1} = \frac{3 \cdot h\nu_S - h\nu_{blue}}{h\nu_{blue}} \cdot P_{Stokes} = 12.47\ mW \quad (45)$$

Next we consider the Tm - 1G_4 ions that decay by emitting a blue photon. Since these decay to the ground state there is no thermal load associated with these.

$$P_{heat\ blue\ 2} = 0 \quad (46)$$

Then we consider the thermal load associated with the 14% of Tm- 1G_4 ions that decay nonradiatively. We assume that all the corresponding energy associated with this ends up as thermal load.

$$P_{heat\ blue\ 3} = P_{total} \cdot (1 - \eta_{qe}) = 7.84\ mW \quad (47)$$

Finally we consider the other 60% of Tm- 1G_4 ions that decay radiatively eg at 650 nm or 800 nm to levels other than the ground state. For these, we estimate that ~1/3 of the energy is deposited as heat.

$$P_{heat\ blue\ 4} = \frac{P_{475nm} \cdot \frac{0.6}{0.4}}{3} = 9.5\ mW \quad (48)$$

Adding up the relative contributions we find that the amount of heat deposited in the KGW Raman crystal that is associated with the blue emission is ~30 mW. The main uncertainties in this estimate is that all the blue photons emitted from Tm- 1G_4 are detected, ie that there is no reabsorption of the blue emission. Given the low Tm concentration, this seems to be a reasonable assumption.

Next we consider the Raman heating in more depth, so that the two heat loads can be compared. The thermal lens depends directly on the Stokes photons generated per second. We assumed in our rough calculation that this corresponded to the Stokes output power (ie transmitted through the output coupler). However, it must include Stokes power lost by reflection/transmission losses at the AR coatings and mirrors, as well as scattering losses in the crystals. These are difficult to quantify but have been estimated recently for a self Raman laser using similar components (but shorter crystals) in Li *et al.* [141]. It was noted here that scattering losses dominated coating losses from the crystals when the

crystals are aligned to have their end faces normal to the resonator beam. For our Nd:YLF/KGW Raman laser we estimate the following losses shown in Table 15.

Table 15. Passive losses for the Nd:YLF/KGW resonator.

Component	Round-trip losses
Input mirror	0.004%
Nd:YLF coatings + scattering losses	0.2%
KGW coatings + scattering losses	0.3%

The output coupled Stokes power (P_{Sout}) is related to the total Stokes power generated ($P_{Stokes}^{generated}$) by

$$P_{Sout} = P_{Stokes}^{generated} \cdot \frac{T_{oc}}{T_{oc} + L} \quad (49)$$

where T_{oc} is the output coupler transmission and L the other resonator round-trip loss.

So accordingly we estimate that the generated Stokes power is 3.5 times higher than the Stokes output power of 470 mW, then the generated power is 1.65 W. The thermal load associated with Raman heating is ~154 mW.

Comparing the blue fluorescence heat of 30 mW with the estimated Raman heat of ~154 mW (calculated including the passive losses), it appears that the contribution associated with the blue fluorescence contributes to an additional 16% compared to the usual Raman heating. Given the uncertainties in the estimates of passive resonator loss, this factor is quite approximate, and further study is required to fully characterise these losses and estimate more precisely the influence of the blue fluorescence on thermal loads.

For the self-Raman cases, the heat load associated with 19 mW of blue emission would be even less significant, contributing with only 1% of the total heat. In this case, the quantum defect between the pump and fundamental is the most relevant, contributing with ~80% of the total heat load. However, the self-Raman case needs more considerations in order to reach a more reliable conclusion. I did not measure the blue emission power for a self-Raman laser and there is a possible energy transfer path between Tm and Nd ions, as per Figure 73, which would reduce the blue yield.

5.11. Chapter summary

The characterization of the blue fluorescence and analysis strongly indicate that the blue 475 nm emission comes from Tm^{3+} , present in all the crystals studied as an impurity. We shown that the emission obtained in the Raman crystals are very similar to the respective host doped with Tm^{3+} , supported by the lifetimes measured from the $^1\text{G}_4$ level for each one of the crystals, also similar to the values found in the literature. ICP-MS measurements added the information that small quantities of the Tm^{3+} ion were present in the crystals, and that there was a correlation between Tm^{3+} concentration and the intensity of blue light emitted by the crystals. The extra cavity probing of those crystals showed in some way the dependence on both fields, fundamental and Stokes, as well as the need of the phonon field, in order to obtain such luminescence. With this information we described the apparent path through the energy levels to populate the blue emitting level, as well as the photons involved. Finally, a statistical analysis (PCA) exposed the behavior of each peak on the emission spectra for different pump powers, showing that the blue and red emission clustered in all the cases, indicating they probably come from the same level ($^1\text{G}_4$) and that they originate from a different process compared to the other emission lines.

Based on what was found in the characterization, we then proposed the possible path to populate the $^1\text{G}_4$ level of the Tm ion, and based on that path we studied the influence of the blue upconversion on laser performance (efficiency and thermal load).

First the blue power generated was estimated using an integrating sphere, giving values of around 19 mW $\pm 15\%$ of total blue power for an absorbed pump power of 15 W. With this result it was possible to observe the implications it have in terms of efficiency for the laser, adding an extra loss for the Stokes field. Such loss was calculated to be 68 mW, which corresponds to a loss of 0.029% for the 230 W intracavity Stokes field. Also, it was compared with the output Stokes power of 470 mW, and in this case the 68 mW represents a percentage of 14.5%. As a result, the blue fluorescence does not seem to be a relevant influence in terms of loss for the Raman laser studied here, but it may make the difference in high Q cavities, where the transmission of the output coupler is much lower.

In terms of heat we estimate the blue fluorescence was contributing 30 mW heat load (for 15 W of absorbed pump power). This extra heat was then compared with the other heating

mechanism in the KGW crystal, which comes from the inelastic nature of SRS (Raman heating). Two values were found, one not considering the resonator passive losses (L), only the transmission of the output mirror (T_{oc}), giving 44.5 mW of heat. The other value was found considering the passive losses, which was an estimated value, resulting in ~154 mW of heat. Using the value found considering ($L+T_{oc}$), the extra heat given by the blue is around 16%, which seems to be a modest but significant contribution. For self-Raman lasers, if one supposes the same intracavity conditions, such as fundamental and Stokes intensities similar to the ones found in the case described here, the heat load originated from the blue should be the same. However, the total heat generated in the self-Raman case involves the quantum defect from the pump-fundamental conversion, which is responsible for ~80% of the total heat, while the blue contribution becomes only ~1%. Given that, the relevance of the blue in terms of thermal loading in self-Raman lasers becomes lower than in the case with separated laser and Raman crystals.

Chapter 6

Conclusion and future works

6. Conclusion and Future works

6.1. Conclusions

This research had the objective of exploring the use of Nd:YLF crystal in low gain lasers. This crystal has interesting characteristics for lasers in general, such as weak thermal lensing, polarised emission, longer upper level laser lifetime ($\sim 500 \mu\text{s}$) and shorter laser wavelengths when compared to other Nd^{3+} -doped crystals commonly used for the same purpose. In fact, for the low gain laser systems studied in this thesis, the most interesting features are the shorter emission wavelengths and the weak thermal lensing effect. In terms of wavelength, the Nd:YLF quasi-three level laser allowed deep blue lasers to be built (454 nm) and for the Raman lasers it unleashed the demonstration of new wavelengths in the lime-green region. Regarding the weak thermal lensing, it becomes a very interesting feature for the Raman lasers, which are frequently power-limited due to very strong thermal lensing, especially for the self-Raman configurations in which heat loading arises from both pump heating associated with the generating the fundamental and also Raman heating associated with the inelastic nature of the Raman process. The use of the Nd:YLF unleashes a way to obtain more stable Raman lasers with very good beam qualities due to the resultant weak thermal lens.

The quasi-three level transition of the Nd:YLF was studied and demonstrations of efficient and power scalable 908 nm lasers were described on the text. Peak output power of 5.5 W at 908 nm was achieved, with a slope efficiency of 33.6%. The best result reported for this laser has reached an output power of 4.7 W with a slope efficiency of 43%. However, the authors of this work pumped the laser directly to the upper laser level (880 nm), which generally raises the efficiency and decreases the heat load.

Also, deep blue laser emission at 454 nm was achieved through the SHG of the 908 nm. A peak output power of 3.5 W was demonstrated, with a corresponding diode to visible conversion efficiency of 13.7%. This efficiency is nearly the same as the one obtained in the best result reported so far, although they have direct pumping and operated in the CW regime and we used traditional pumping at 806 nm and operated in the quasi-CW regime (3% of duty cycle). The pump power threshold obtained here is ~ 1 W lower

than the one found in their work, probably due to fact the CW regime adds more heat than the quasi-CW, thus increasing the reabsorption loss. Continuous wave operation has also been demonstrated in this thesis, but the performance of the lasers were not as good as in their quasi-CW versions. Given that, blue lasers which are very much desired in the applications market, either to improve existing functions or to enable new ones, were developed in this thesis demonstrating a good potential of the Nd:YLF for the blue laser market.

Original infrared and visible laser lines were demonstrated by the Nd:YLF Raman lasers developed in the thesis. The 1.1 μm and yellow-orange ranges are hard to reach regions on the electromagnetic spectrum which has few laser light sources available in the market. The combination of different laser crystals and Raman crystals has recently been supplying a comb of new wavelengths in the region, with very good performances. Here in this thesis two combinations were demonstrated, Nd:YLF/BaWO₄ and Nd:YLF/KGW, which can give rise to six different 1st Stokes wavelengths and more than ten different visible wavelengths. The thesis did not explored all of them, it was demonstrated here three different 1st Stokes lasers, 1147 nm, 1163 nm and 1167 nm and five visible lasers, 549 nm, 552 nm, 573 nm, 581 nm and 583 nm.

With the Nd:YLF/BaWO₄ laser it was achieved a CW output power of 1.5 W at 1167 nm, which was the best 1st Stokes result obtained in the thesis. For the visible, the Nd:YLF/KGW was the one which showed the best performance, with CW output powers above 1W at 552 nm and 581 nm. For quasi-CW operation, the maximum peak power reached was of 3.12 W at 552 nm. All the Raman lasers demonstrated here using Nd:YLF, presented good beam quality, $M^2 \leq 2$, which is considered better than for the most multi-Watt CW Raman lasers . The results showed to be competitive and in some cases better (better efficiencies and beam quality) than the ones found in the literature for Nd:YLF operating in Raman lasers.

In addition, associating Nd:YLF with BaWO₄ and KGW Raman crystals, it was possible to prototype CW Raman lasers with long resonators, due to the weak Nd:YLF thermal lens, still providing output powers of a few Watts. It is an interesting observation, since the self-Raman lasers are usually limited to very short cavities, due to the strong thermal lensing, which prevents the investigation of different resonator geometries. Also

the capability to make a long cavity offers an approach to reduce the amplitude noise of SHG lasers. Using Nd:YLF these two directions are able to be explored. Finally, from the five visible wavelengths demonstrated, two of them were obtained for the first time in crystalline Raman lasers, 549 nm and 552 nm.

The third stage of my research addressed a well-known phenomena in many Raman lasers that utilise vanadates, tungstates and molybdate crystals. It is a blue fluorescence that emerges from the Raman crystals when the SRS threshold is reached. I performed a complete investigation of this blue emission to investigate its origin, and any consequences it may have for laser operation, in particular its influences on the losses and as a heat source. Analysing the spectral data collected from different crystals (Nd:GdVO₄, KGW, Nd:YVO₄ and BaWO₄), strong similarities were found with the spectra in the literature for Tm doped crystals with the corresponding hosts. Lifetime measurements supported the hypothesis of Tm emission, as the decay times were also similar to the Tm doped version of the crystals from the literature. Also, it was observed in the ICP-MS measurements the presence of Tm impurities in all the crystals studied, with the concentration correlating to the emission intensity observed in each of the crystals. In addition to it, PCA analyses indicated a strong coupling between the blue and red (much weaker than the blue, not noticed in other works) emissions present in the Raman crystals during the operation. With these indications, we proposed the possible upconversion mechanism in Tm³⁺, finding out that two to three Stokes photons must be consumed in the process.

Based on the upconversion mechanism proposed, it was found out that ~68 mW of Stokes power was consumed to generate an amount of ~19 mW of blue. This represents only 0.029% of the intracavity Stokes field (~230 W), and 14.5% of the output Stokes output power (470 mW). In both cases the loss added does not seem to be relevant, however, this was measured for a low-Q cavity with output transmission of 0.2%, but the high-Q cavities, used for visible generation, generally have much lower passive losses, and then it might influence more.

In terms of thermal load, a moderate influence was found for the total heat load, considering the case of separated laser and Raman crystal as studied here. An amount of ~30 mW of heat is added to the Raman crystal due to the blue fluorescence. Comparing it to the Raman heating (from the Raman shifting process) of ~154 mW, it corresponds to

20% of the Raman heat and 16% of the total heat loaded into the Raman crystal. In the case of the self-Raman lasers, where three heating mechanisms are together in the same crystal (quantum defect, Raman heating and blue), we believe it is much less relevant as the quantum defect of the pump-fundamental conversion is responsible for a much higher amount of heat, ~80%, with the blue contributing for only ~1% to the heat.

6.2. Future works

For the future, the Nd:YLF laser has a great potential in both low gain laser systems demonstrated in this work. There is still scope to explore even further its proved abilities such as the high energy pulses at the deep blue wavelength using Q-switch techniques as well as cavity design flexibility for Raman lasers due to the overall weak thermal lens, enabling higher conversion efficiencies and low amplitude noise operation. The quasi-three level laser can be further explored in terms of wavelength, as only one work has reported the operation of such laser at the 903 nm line, with very poor performance. With that, an even deeper blue line can be reached at 451 nm. Also, the investigation of the 1047 nm emission for Raman shifting would raise new wavelengths and maybe higher output powers can be achieved, as it has stronger stimulated emission cross section.

More than that, the Nd quasi-three level technology could be combined with the Raman technology in order to create a new set of versatile blue lasers. It was not done before for the best of my knowledge, and must be a hard task in a first glance, since it is a combination of two low gain amplification processes. However, as a good support for such combination, comes the fact that the Raman gain increases for shorter wavelengths, which could help to improve the efficiency of this kind of association.

Appendix A

MathCad worksheets

Estimation of the Blue fluorescence power using an Integrating sphere

Units

$$\text{mW} := 10^{-3}\text{W} \quad \mu\text{V} := 10^{-6}\text{V}$$

$$\mu\text{W} := 10^{-6}\text{W} \quad \text{nm} := 10^{-9}\text{m}$$

Sphere parameters

$$\phi_i := 3.5\text{mW} \quad \text{laser pointer power}$$

$$\rho := 0.97 \quad \text{sphere reflectance (spectralect)}$$

$$R := 4.75\text{cm} \quad \text{sphere radius}$$

$$A_s := 4\pi R^2 \quad \text{sphere total surface area}$$

$$A_1 := 1.425\text{cm} \cdot 0.925\text{cm} \quad \text{port 1 area}$$

$$A_2 := \pi (2.5\text{mm})^2 \quad \text{port 2 area}$$

$$A_d := 3.85^2\text{mm}^2 \quad \text{detector area}$$

$$A_{3d} := \pi \cdot (1.22\text{mm})^2 \quad \text{detector port area}$$

$$\text{Loss} := 0.032 \quad \text{calibration loss!!!}$$

$$f := \frac{A_1 + A_2 + A_{3d}}{A_s} + \text{Loss} \quad \text{Ports area/loss factor + calibration loss}$$

$$L_s := \frac{\phi_i}{\pi A_s} \cdot \frac{\rho}{1 - \rho \cdot (1 - f)} \quad L_s = 0.574 \frac{\text{W}}{\text{m}^2} \quad \text{sphere surface radiance}$$

$$M := \frac{\rho}{1 - \rho \cdot (1 - f)} \quad M = 14.613 \quad \text{sphere multiplier}$$

$$\Omega := \pi \cdot \sin(6.3\text{deg})^2$$

$$\Omega = 0.038$$

Solid angle: detector field of view

Flux on the photodetector

$$\phi_d := L_s \cdot A_d \cdot \Omega \cdot 1.25$$

Includes 80%T at 532 nm photopic filter *1.25 factor

$$\phi_d = 0.402 \mu\text{W}$$

$$\text{Res}_{\text{green}} := 0.28 \frac{\text{A}}{\text{W}}$$

detector responsivity at 532 nm

$$V := 10^6 \text{ ohm} \cdot \phi_d \cdot \text{Res}_{\text{green}}$$

$$V = 112.686 \text{ mV}$$

voltage expected to be measured for the green pointer

Measured voltage for the green pointer = 113 mV

Now calibrate the system!
(eg. insert extra loss)

Blue fluorescence measurement

$$\text{Res}_{\text{blue}} := 0.15 \frac{\text{A}}{\text{W}}$$

detector responsivity at 475 nm

$$\text{zero} := 1 \text{ mV}$$

background noise

measured voltage for the blue emission = 24 mV

$$V_{\text{blue}} := 24 \text{ mV} - \text{zero}$$

$$\phi_{\text{dblue}} := \frac{V_{\text{blue}}}{10^6 \text{ ohm} \cdot \text{Res}_{\text{blue}} \cdot 0.1}$$

$$\phi_{\text{dblue}} = 1.533 \mu\text{W}$$

power measured by the detector at 475 nm

$$L_s := \frac{\phi_{d\text{blue}}}{A_d \cdot \Omega}$$

$$L_s = 2.735 \frac{\text{W}}{\text{m}^2} \quad \text{sphere surface radiance}$$

$$\phi_{\text{blue}} := \frac{L_s \cdot \pi \cdot A_s \cdot [1 - \rho \cdot (1 - f)]}{\rho}$$

$$\phi_{\text{blue}} = 16.669 \text{ mW}$$

Another approach to estimate the blue power: linear relation

Using another experimental data:

Green pointer voltage = 218 mV ; Blue voltage = 80 mV

* This experimental data was collected using collection optics in front of the detector port!

$$\text{Green} := \frac{218 \text{ mV}}{10^6 \text{ ohm} \cdot \text{Res}_{\text{green}}} \quad \frac{\text{Green}}{0.8} = 0.973 \mu\text{W}$$

$$\text{Blue} := \frac{80 \text{ mV}}{10^6 \text{ ohm} \cdot \text{Res}_{\text{blue}}} \quad \frac{\text{Blue}}{0.1} = 5.333 \mu\text{W}$$

$$\text{BF}_{\text{huo}} := \frac{\frac{\text{Blue}}{0.1}}{\frac{\text{Green}}{0.8} \cdot \phi_i}$$

Blue generated

$$\text{BF}_{\text{huo}} = 19.18 \text{ mW}$$

Estimated error of the experiments

Different experiments to estimate the error

$$M1 := 19.2\text{mW}$$

$$M2 := 12.8\text{mW}$$

$$M3 := 18.7\text{mW}$$

$$M4 := 16.7\text{mW}$$

$$AVG := \frac{M1 + M2 + M3 + M4}{4} \qquad AVG = 16.85\text{mW}$$

$$SD := \sqrt{\frac{(M1 - AVG)^2 + (M2 - AVG)^2 + (M3 - AVG)^2 + (M4 - AVG)^2}{4}}$$

$$SD = 2.518\text{mW} \qquad \text{standard deviation}$$

$$\frac{SD}{AVG} = 14.946\% \qquad \text{Estimated Error}$$

Blue fluorescence loss and thermal contribution in Raman Lasers

Units and constants

$$\begin{array}{llll} \mu\text{s} := 10^{-6}\text{s} & \text{nm} := 10^{-9}\text{m} & \text{mW} := 10^{-3}\text{W} & \text{mJ} := 10^{-3}\text{J} \\ h := 6.626 \cdot 10^{-34}\text{J}\cdot\text{s} & c := 2.997 \cdot 10^8 \frac{\text{m}}{\text{s}} & & \text{nJ} := 10^{-9}\text{J} \end{array}$$

Quantum efficiency

$$\tau_f := 109\mu\text{s} \quad \text{fluorescence lifetime}$$

$$\tau_r := 127\mu\text{s} \quad \text{radiative lifetime}$$

$$\eta_{qe} := \frac{\tau_f}{\tau_r}$$

$$\eta_{qe} = 0.858 \quad \text{quantum efficiency = probability of a radiative decay occur}$$

$$a := 1 - \eta_{qe}$$

$$a = 0.142 \quad \text{probability of a radiationless decay}$$

Powers measured

$$P_{475\text{nm}} := 19\text{mW} \quad \text{blue power measured for 15 W of absorbed 880 nm pump}$$

$$P_p := 15\text{W} \quad \text{Absorbed power at 880 nm}$$

$$P_{\text{int}} := 230\text{W} \quad \text{intracavity Stokes power}$$

Wavelengths involved

$$\lambda_p := 880\text{nm}$$

$$\lambda_f := 1053\text{nm}$$

$$\lambda_s := 1163\text{nm}$$

$$\lambda_R := \frac{1}{901\text{cm}^{-1}}$$

Power needed to generate the blue fluorescence, considering the branching ratio of the 1G4

$$\beta := 0.4 \quad \text{Branching ratio for the 475 nm transition (Lit)}$$

$$P_t := \frac{P_{475\text{nm}}}{\eta_{qe} \cdot \beta} \quad \text{Total power needed to populate 1G4}$$

$$P_t = 55.344 \text{ mW}$$

Stokes power used to generate the blue fluorescence

$$P_{\text{Stokes}} := \frac{3 \cdot h \cdot \frac{c}{\lambda_s}}{h \cdot \frac{c}{475\text{nm}}} \cdot P_t \quad P_{\text{Stokes}} = (3 \cdot \text{Energy_stokes} / \text{Energy_blue}) \cdot P_t$$

* considering 3 Stokes photons participating in the upconversion

$$P_{\text{Stokes}} = 67.812 \text{ mW}$$

Blue fluorescence Loss

$$\text{Loss} := \frac{\frac{3 \cdot h \cdot \frac{c}{\lambda_s}}{h \cdot \frac{c}{475\text{nm}}} \cdot P_t}{P_{\text{int}}}$$

$$\text{Loss} = 0.029\%$$

Blue fluorescence contribution to the thermal load

$$P_{\text{Sout}} := 0.470 \text{ W}$$

Stokes output power measured at 15 W of absorbed pump power

$$P_{\text{phononStokes}} := P_{\text{Sout}} \cdot \left(1 - \frac{h \cdot \frac{c}{\lambda_s}}{h \cdot \frac{c}{\lambda_f}} \right)$$

$$P_{\text{phononStokes}} = 44.454 \text{ mW}$$

Power converted into heat from the fundamental-Stokes conversion

Now considering the cavity passive losses

$$L := 0.003 + 0.002 + 0.00004 \quad \text{Cavity passive losses}$$

$$\frac{P_{\text{Sout}}}{\frac{0.002}{0.002+L}} = 1.654 \text{ W} \quad \text{Generated Stokes power}$$

$$P_{\text{LT}} := P_{\text{Sout}} \cdot \left(1 - \frac{h \cdot \frac{c}{\lambda_s}}{h \cdot \frac{c}{\lambda_f}} \right) + P_{\text{int}} \cdot L \cdot \left(1 - \frac{h \cdot \frac{c}{\lambda_s}}{h \cdot \frac{c}{\lambda_f}} \right)$$

$$P_{\text{LT}} = 154.095 \text{ mW}$$

Power converted into heat from the fundamental-Stokes conversion

Heat load contribution from the blue fluorescence

$$\frac{\left(3 \cdot h \cdot \frac{c}{\lambda_s} \right) - h \cdot \frac{c}{475 \text{ nm}}}{h \cdot \frac{c}{475 \cdot \text{nm}}} \cdot P_t = 12.468 \text{ mW}$$

Power consumed by the **bridging** phonons in the upconversion process

$$\frac{P_{475 \text{ nm}} \cdot \frac{0.6}{0.4}}{3} = 9.5 \text{ mW}$$

Power from 1G4 phonon decays

* considering that all the the decays but the blue, occur by multiphonon all the way down! 60% of the decays become heat! ~1/3 of them becomes heat.

$$P_t \cdot a = 7.844 \text{ mW}$$

14% of the 1G4 that do not decay radiatively (quantum efficiency).

$$P_{\text{Total}} := \frac{P_{475 \text{ nm}} \cdot \frac{0.6}{0.4}}{3} + \left[\frac{\left(3 \cdot h \cdot \frac{c}{\lambda_s} \right) - h \cdot \frac{c}{475 \cdot \text{nm}}}{h \cdot \frac{c}{475 \cdot \text{nm}}} \cdot P_t \right] + P_t \cdot a$$

$$P_{\text{Total}} = 29.812 \text{ mW}$$

Total power converted into heat

Blue heat compared to the Raman heat

$$\frac{P_{\text{Total}}}{P_{\text{LT}} + P_{\text{Total}}} = 16.21 \%$$

Percentage of the heat originated by the blue

Self-Raman case

$$P_{\text{quantumdefect}} := P_p \cdot \left(1 - \frac{h \cdot \frac{c}{\lambda_f}}{h \cdot \frac{c}{\lambda_p}} \right)$$

Power converted into heat from the pump-fundamental conversion

$$P_{\text{quantumdefect}} = 2.464 \text{ W}$$

$$\frac{P_{\text{Total}}}{P_{\text{LT}} + P_{\text{Total}} + P_{\text{quantumdefect}}} = 1.126 \%$$

Percentage of the heat originated by the blue

$$\frac{\left(\frac{P_{\text{Sout}}}{0.002} \right)}{\left(\frac{P_{\text{Sout}}}{0.002 + L} \right)} = 3.52$$

The intracavity generated Stokes is 3.52 times higher than the coupled out by the O.C.

Appendix B

Spectral data of the coatings (mirrors)

Raman mirrors

Spectra for

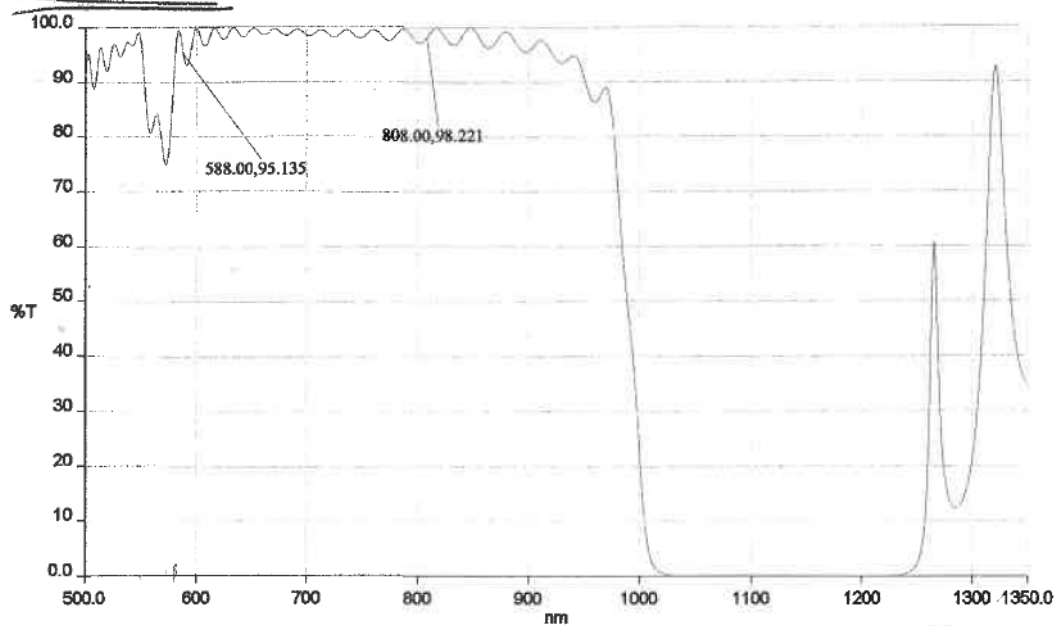
#60

Advanced Thin Films
PE900 Spectrophotometer Data

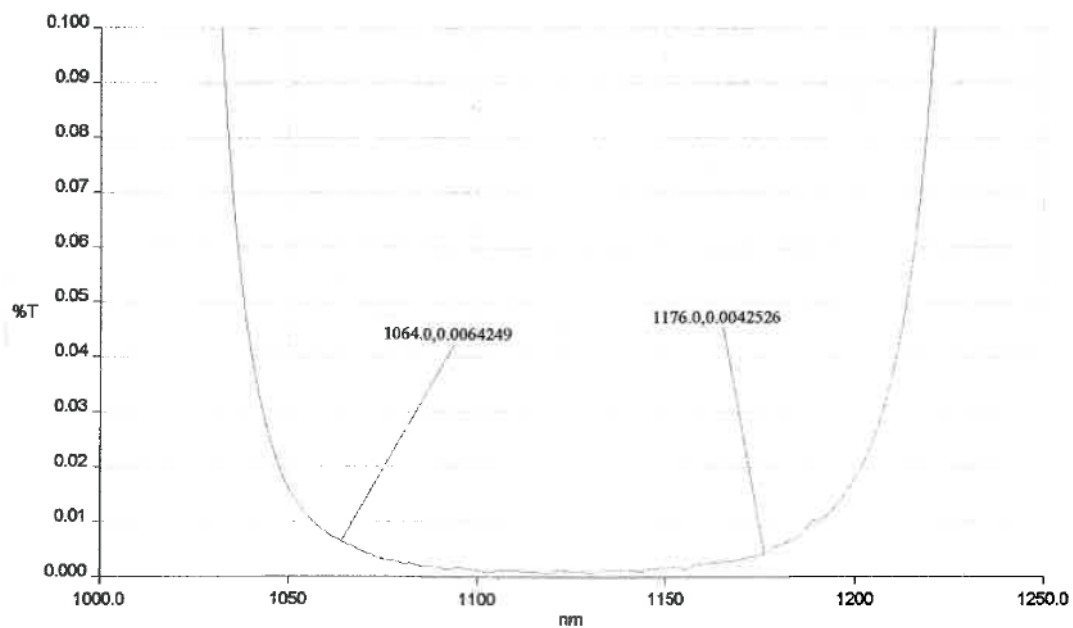
#60

copy

Time: 3:51:08 PM Date: 8/16/2006



SCAN5845.SP - 8/16/2006 - V2-850 FS Wit, AB300, 0°, F=1.0357



SCAN5846.SP - 8/16/2006 - V2-850 FS Wit, AB300, 0°, F=.01

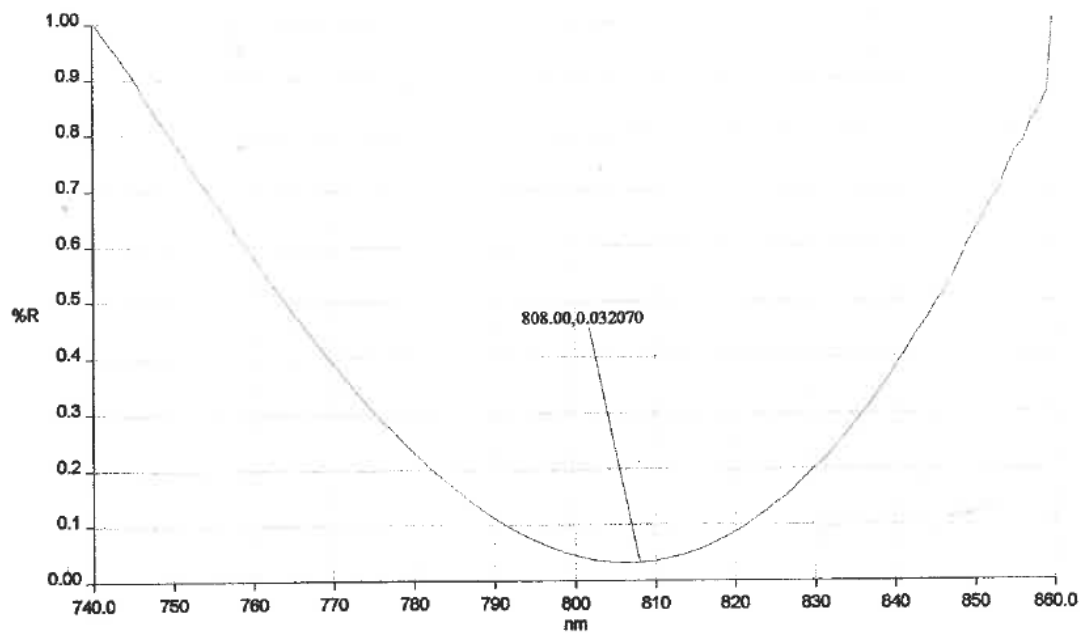
#60.

COPY

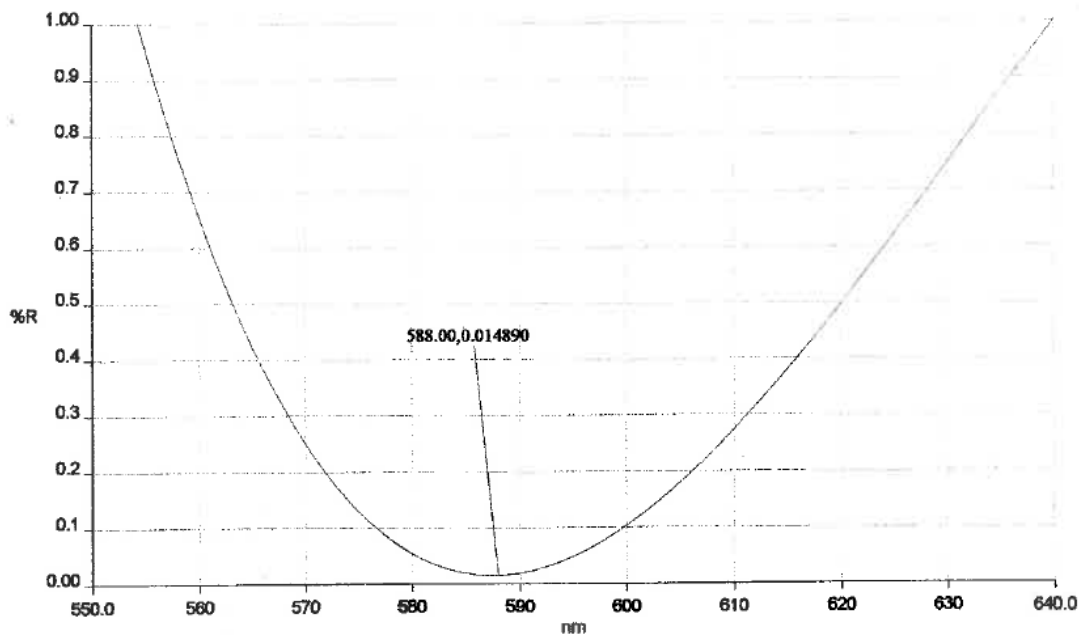
#60

Advanced Thin Films
PE900 Spectrophotometer Data

Time: 3:06:46 PM Date: 8/15/2006

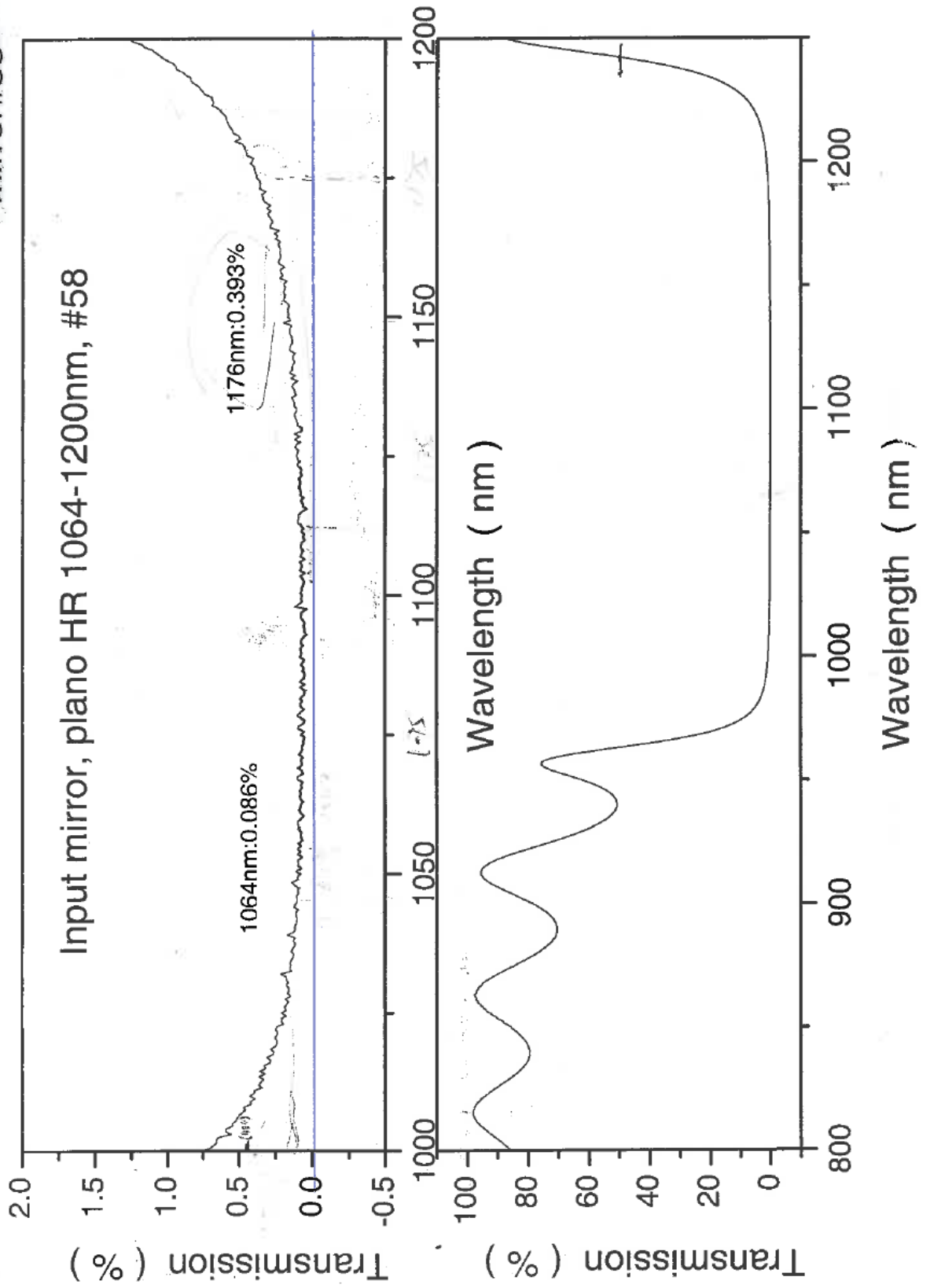


SCAN5826.SP - 8/15/2006 - V2-851, FS WITNESS, 5° AOI, F=.0417



SCAN5826.SP - 8/15/2006 - V2-851, FS WITNESS, 5° AOI, F=.0417

mirror#58

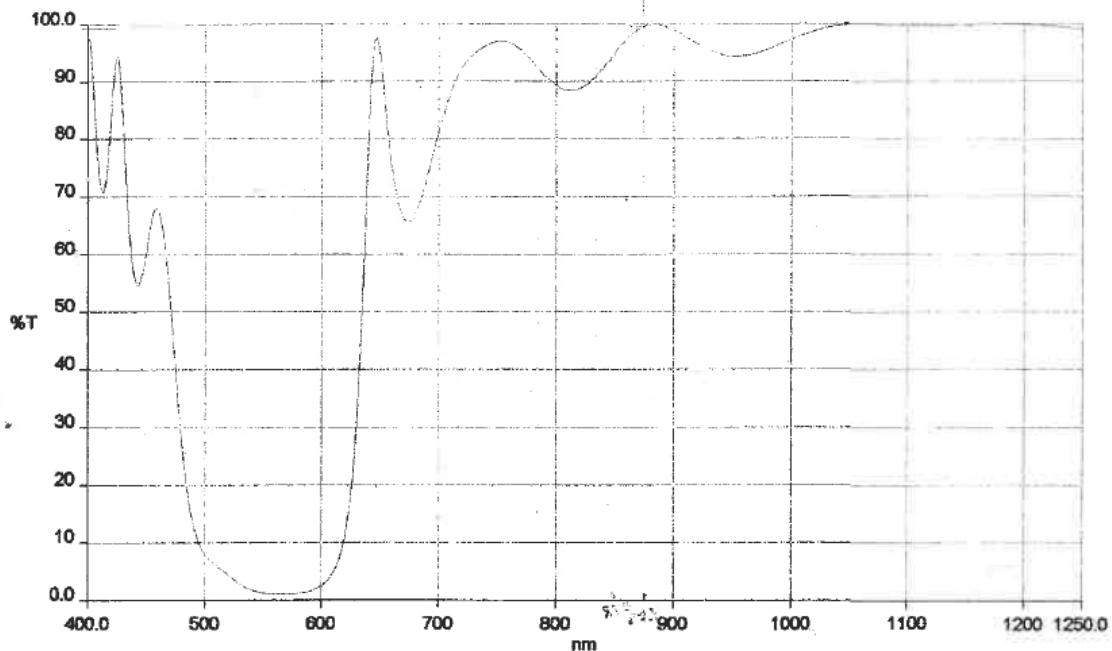


Surface 1 #80

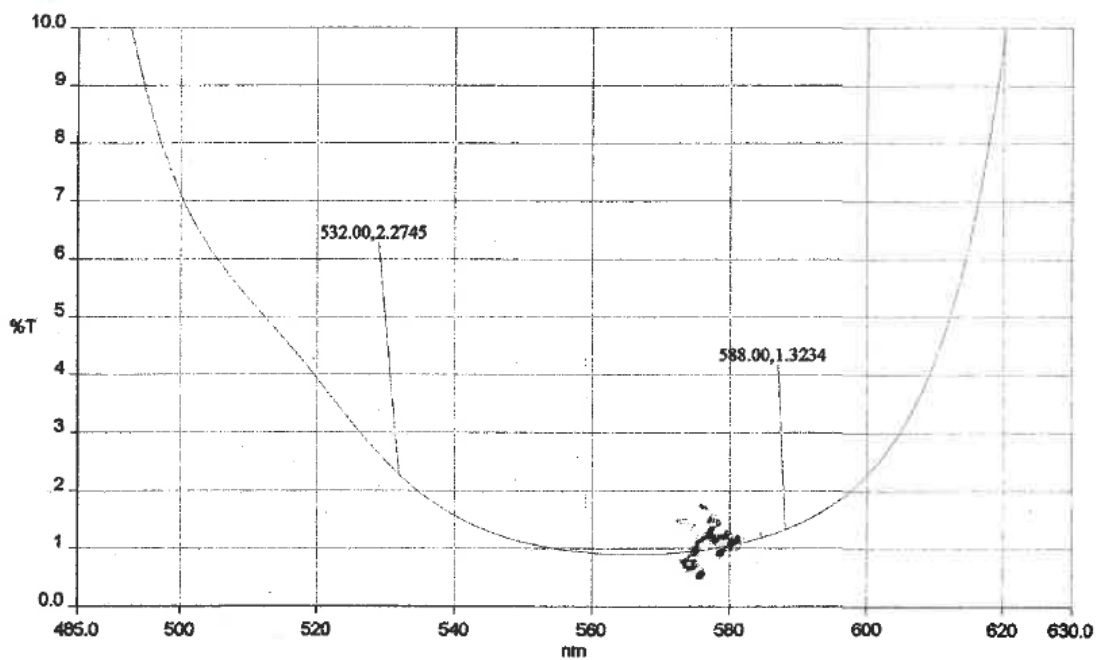
copy

Advanced Thin Films
PE900 Spectrophotometer Data

Time: 8:43:25 AM Date: 5/16/2007



SAM1014.SP - 5/16/2007 - V2-1088 FS Wit, AB450, 0°, F=1.0348



SAM1015.SP - 5/16/2007 - V2-1088 FS Wit, AB450, 0°, F=.01

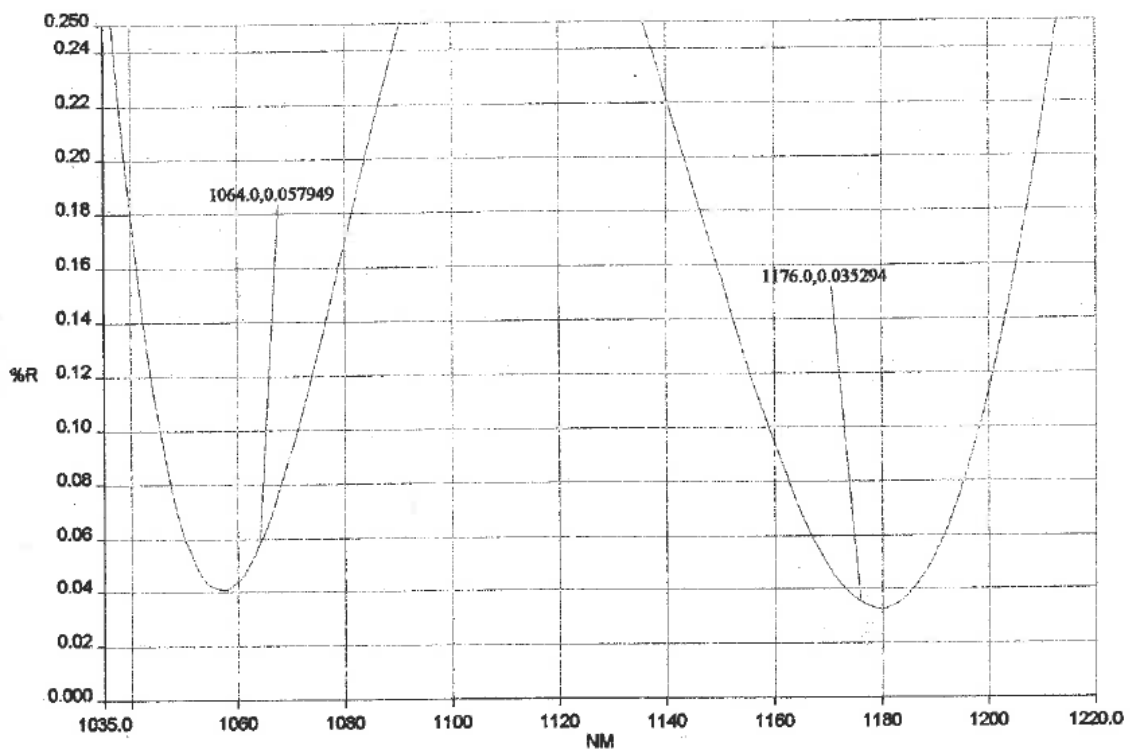
Surface 1. #80

copy

80

Advanced Thin Films
PE 900 Spectrophotometer Data

Time: 8:31:54 AM Date: 5/16/2007



SAM1012.SP - 5/16/2007 - V2-1088 FS Wit, AB450, 5°, F=.0408

Surface 2.

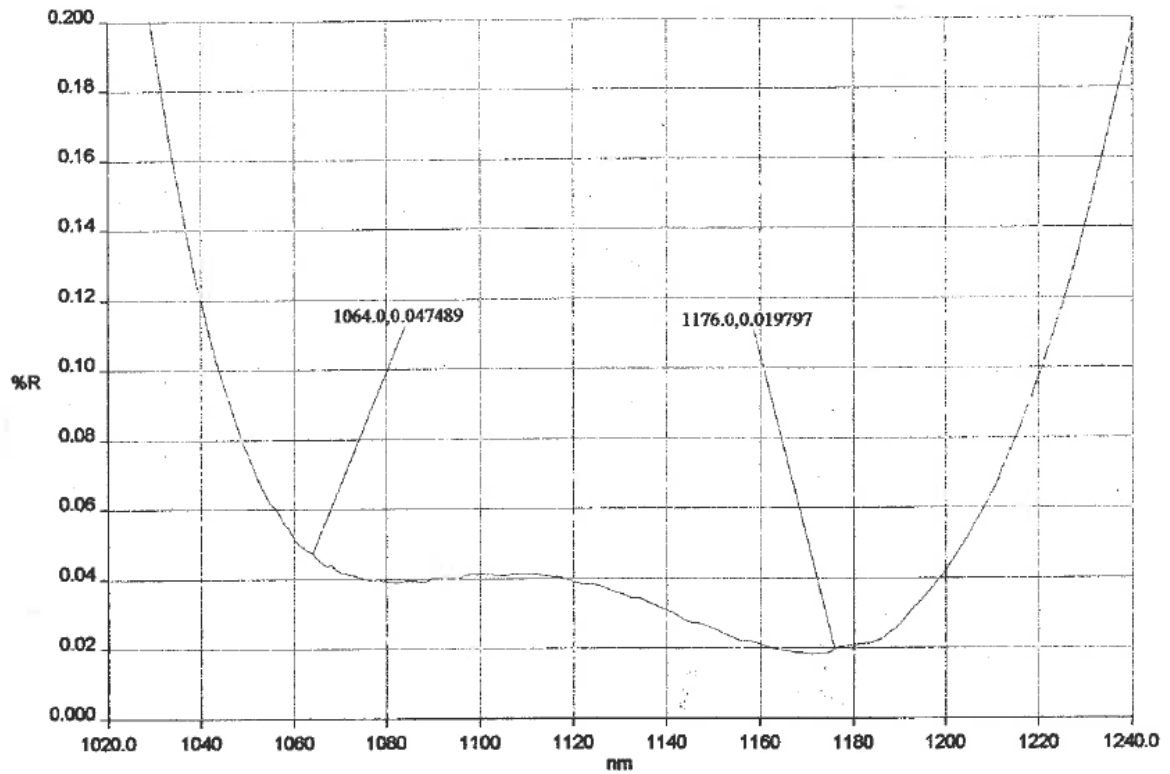
#80

#

Advanced Thin Films

PE 900 Spectrophotometer Data

Time: 6:40:45 AM Date: 5/14/2007

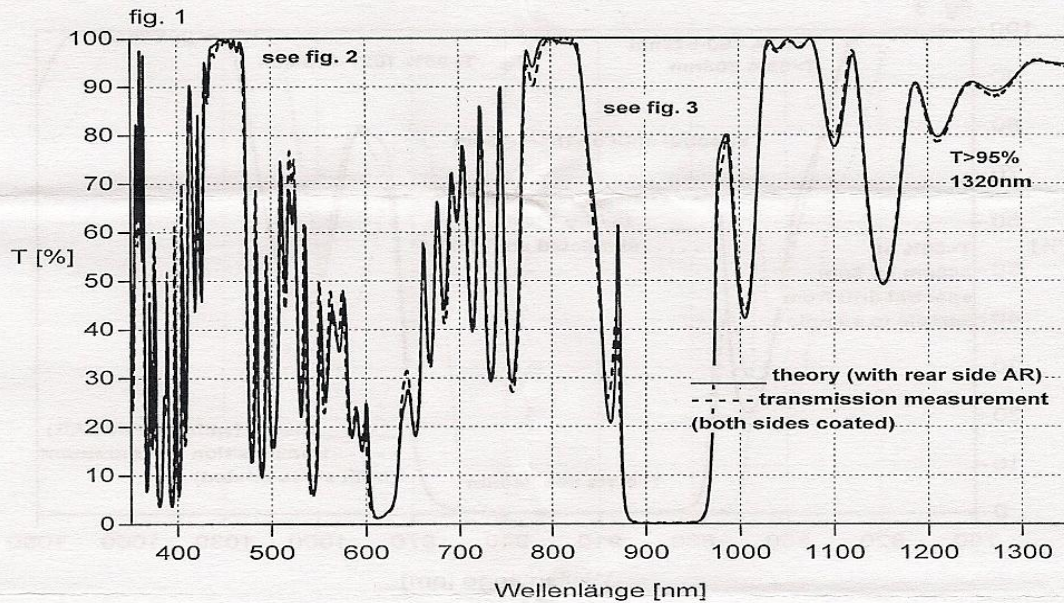


SAM992.SP - 5/14/2007 - V2-1089, FS Witness, BB, 5° AOI, F=.0408

Quasi-three level laser mirrors

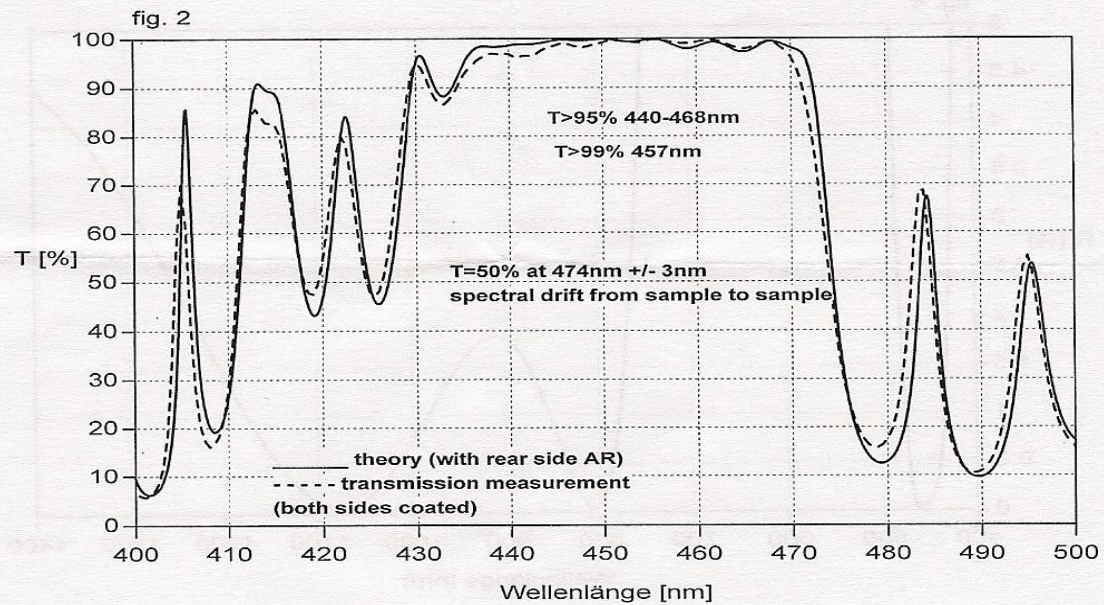
Donnerstag 11.12.2008

batch Z1208010 - transmission measurement + refined theory

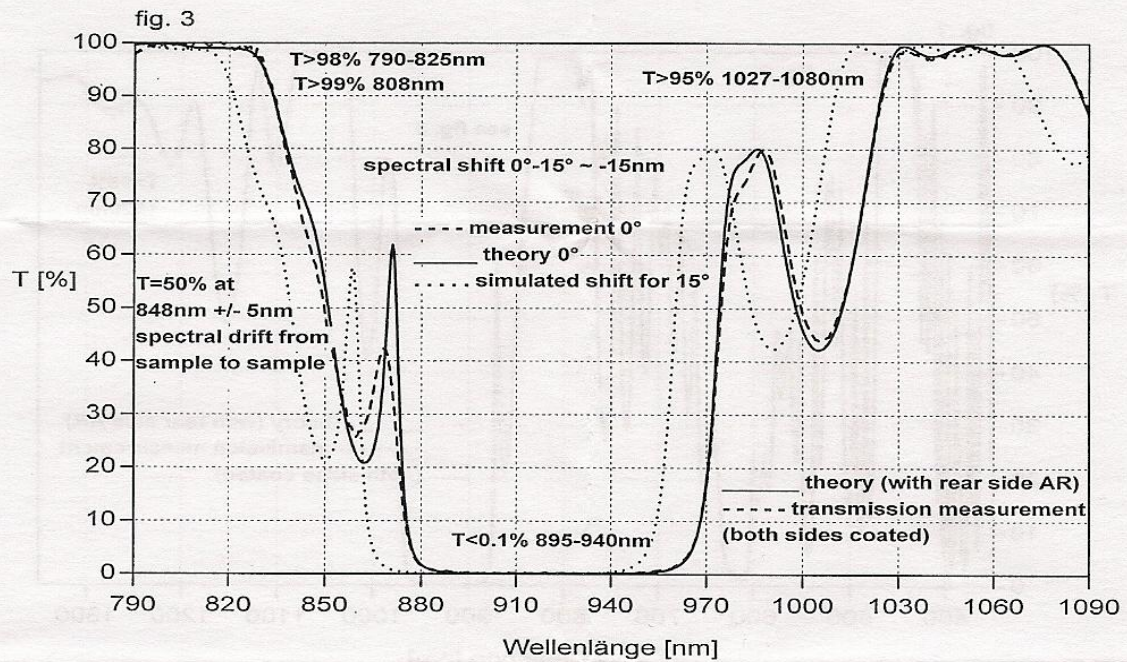


Donnerstag 11.12.2008

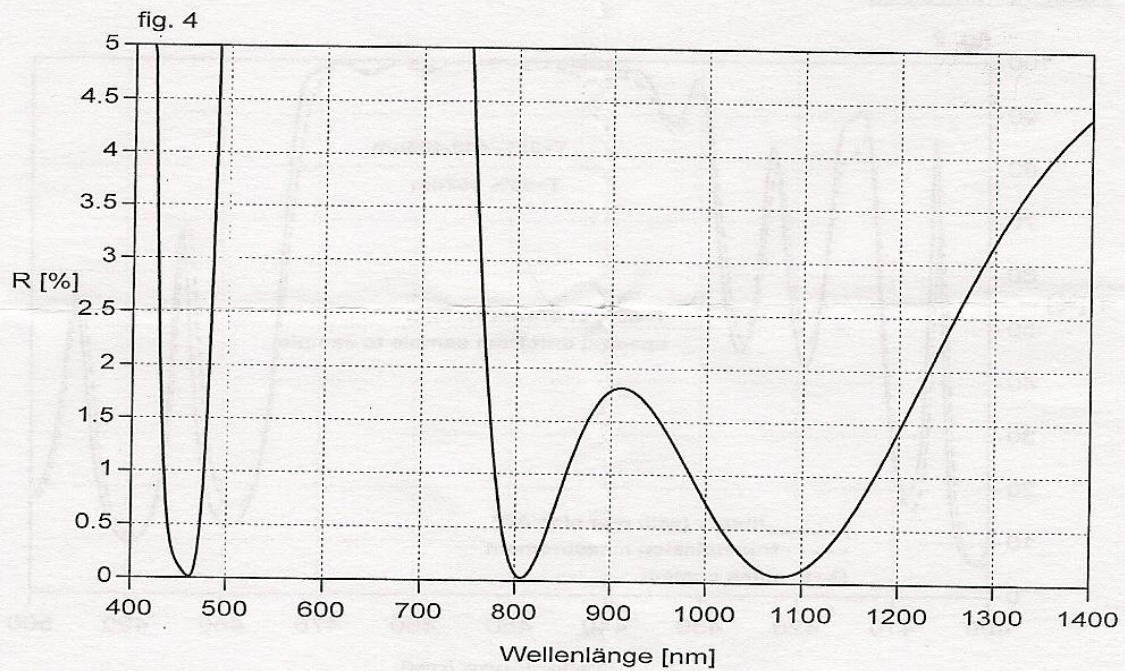
detail 457nm region



detail 808-910-1064nm region



theory rear side reflection at 0°



Appendix C

ICP-MS full data

GLITTER! 4.4[svn]: Laser Ablation Analysis Results

Y:\jakutis_jonas\2011_04_05\run1.B
Created: Tue Apr 05 11:11:50 2011

All values are reported in ppm

GLITTER!: Trace Element Concentrations MDL filtered.

Element	STD610-01	STD610-02	BCR2-01	KGW-1	KGW-2	KGW-3	BW-1	BW-2	BW-3
Li7	485.82	483.5	10.11	<0.00050	<0.00053	<0.00056	293.41	277.06	<243.84
Be9	471.21	460.01	2.12	<0.0036	<0.0037	<0.0038	<1909.98	<1744.12	<1748.18
B11	337.25	381.9	9.39	0.0106	0.0107	0.0087	5249.53	5500.73	5686.25
Na23	94990.52	95468.6	23747.66	0.0667	0.0687	0.072	4901.43	4757.29	4042.28
Mg25	470.64	459.53	21086.79	<0.0065	<0.0073	<0.0075	<3549.52	10802.08	<3260.37
Al27	10070.63	9939.5	73920.1	<0.0051	<0.0070	<0.008	<3320.45	16920.85	<3344.74
Si29	328298.56	328632.44	274556.22	<1.29	<1.33	<1.31	<632886.06	2841062.75	1256093.88
P31	335.44	349.26	1453.66	<0.043	<0.045	<0.044	77407.88	<19622.40	<18742.75
K39	482.92	490.7	17069.16	570.56	586.27	583.14	<3805.18	14343.57	4933.29
Ca42	81518.88	82252.34	51059.91	0.54	<0.46	<0.46	<225810.92	<204160.02	<198072.52
Ca43	81833.27	81833.27	51029.65	<1.86	<1.93	<2.01	<970390.69	1983253.25	1743440.13
Sc45	441.56	440.69	39.07	<0.00167	<0.00175	<0.00177	<835.13	<764.37	<756.82
Ti49	435.23	432.81	13260.25	<0.0092	<0.0105	<0.0106	<5058.43	<4768.89	<4526.81
V51	440.86	443.22	435.22	<0.00088	<0.00096	<0.00098	977.31	536.19	<447.89
Cr53	391.68	421.72	13.09	<0.0119	<0.0135	<0.0135	<6417.33	<5893.89	<5884.90
Mn55	437.05	429.51	1505.08	<0.00198	<0.00210	<0.00220	<1061.68	1717.97	<955.78
Fe57	464.15	450.2	80401.8	<0.087	<0.096	<0.102	50997.72	<47900.82	<48351.09
Co59	405.82	404.2	38.62	<0.00085	<0.00088	<0.00088	<436.26	<411.50	<414.31
Ni60	442.04	446.17	12.48	<0.0032	<0.0033	<0.0037	<1766.49	<1653.27	<1624.72
Ni62	448.47	438.88	20.8	<0.0222	<0.0226	<0.0240	<11645.31	<10692.50	<10636.05
Cu63	439.13	421.48	17.01	<0.00138	<0.00141	<0.00153	<745.23	<680.65	<695.87
Cu65	438.45	422.02	17.9	<0.0034	<0.0036	<0.0038	526171.13	517989	463059.78
Zn66	452.61	461.07	158.63	<0.0060	<0.0064	<0.0068	1077598.75	1028561.5	913434.69
Ga69	440.03	436.05	71.87	<0.00168	<0.00182	<0.00195	*****	*****	*****
Ga71	441.47	434.75	23.68	<0.0026	<0.0030	<0.0032	1719.74	<1490.06	<1495.71

Ge72	426.69	426.14	3.93	<0.0032	<0.0034	<0.0035	<1706.96	<1605.18	<1568.25
As75	274.43	389.22	<2.13	<0.0073	<0.0072	<0.0072	<3327.55	<2940.41	<2919.07
Rb85	429.94	432.69	52.1	0.00591	0.00667	0.00706	<520.20	<495.72	<499.07
Sr86	496.32	499.32	330.46	<0.0067	<0.0070	<0.0072	239825.38	234279.98	206609.88
Sr88	496.47	498.69	331.22	<0.00039	<0.00039	<0.00042	246400.36	238422.91	211219.72
Y89	451.39	448.62	30.42	0.00622	0.0063	0.00654	34349.71	33934.06	29762.05
Zr90	443.38	436.48	168.29	0.0364	0.0017	0.00816	<402.47	<388.89	<393.06
Nb93	420.6	418.56	11.08	0.0346	0.0337	0.0361	25365.13	25066.53	22055.22
Mo95	366.04	390.28	254.27	<0.0041	<0.0046	<0.0047	43714.57	41106.73	36106.78
Cs133	360.83	361.06	1.282	<0.00034	<0.00037	<0.00041	<193.03	<174.66	<169.94
Ba137	423.32	425.28	672.25	0.0072	0.0053	0.004	*****	*****	*****
La139	455.56	459.94	25.94	<0.00032	<0.00037	<0.00034	4935.28	4757.65	3823.49
Ce140	449.5	446.24	53.55	0.00034	<0.00030	<0.00032	<160.78	152.07	<143.21
Pr141	427.44	432.86	6.57	<0.00024	<0.00025	<0.00025	<126.14	<117.03	<112.94
Nd146	429.9	432.04	28.22	0.00372	0.00225	0.00263	742.97	<660.97	<664.17
Sm147	447.39	454.67	6.6	<0.00186	<0.00191	<0.00203	1310.18	1604.27	1420
Eu153	461.17	461.53	2.137	0.00095	0.00079	0.00108	41478.33	40065.5	34235.31
Gd157	419.28	421.19	6.01	2273.12	2273.12	2273.12	3453.57	3453.57	3453.57
Tb159	443.81	442.24	0.948	0.00477	0.00432	0.0043	<171.40	200.78	<162.55
Dy161	428.99	424.18	6.17	0.0129	0.01096	0.01049	<822.67	<747.34	<758.86
Ho165	451.52	447.66	1.237	0.00196	0.00195	0.00201	<146.23	<120.81	<121.33
Er167	428.78	423.35	3.16	<0.00110	0.00128	0.00151	<589.00	<532.58	<529.17
Tm169	422.98	417.44	0.425	0.00168	0.00182	0.00133	163.45	<120.19	<116.93
Yb173	465.27	458.03	3.63	2.235	2.222	2.141	<870.34	<802.89	<807.04
Lu175	438.52	431.07	0.498	0.0593	0.0539	0.0485	<139.96	<130.47	<128.34
Hf178	419.27	416.46	4.36	0.0028	0.00381	0.002	1628.56	1910.91	1649.05
Ta181	377.42	376.09	0.616	0.00213	0.00229	0.00208	5202.2	4678.34	4248.19
W182	440.21	451.64	0.68	5333.43	5514.59	5471.64	*****	*****	*****
Pb208	410.1	417.49	11.42	0.00106	0.00128	0.00189	5039.15	3508.66	2736.4
Th232	452.48	449.04	5.82	0.0003	<0.00030	<0.00030	<141.40	<133.89	<128.81
U238	457.47	457.26	1.813	<0.00025	<0.00026	0.00027	<132.25	<125.34	<123.41

LITTER!; 1 sigma error.

Element STD610-01 STD610-02 BCR2-01 KGW-1 KGW-2 KGW-3 BW-1 BW-2 BW-3

Li7	15.69	15.62	0.35	0.00019	0.0002	0.00021	110.73	104.1	94.72
Be9	39.14	38.25	0.43	0.0014	0.0014	0.0014	742	688.78	656.84
B11	29.06	32.68	0.89	0.0016	0.0016	0.0015	1032.06	1030.7	1004.52
Na23	3128.68	3145.91	789.36	0.0027	0.0028	0.003	892.18	839.31	733.86
Mg25	16.92	16.56	760.28	0.0025	0.0027	0.0028	1371.39	1900.03	1228.33
Al27	362.28	357.8	2681.85	0.002	0.0085	0.014	8688.35	2154.24	9063.33
Si29	15356.99	15388.93	12926.04	0.49	0.7	0.65	413218	413212.34	251288.69
P31	62.01	63.97	263.44	0.02	0.042	0.023	23862.05	15445.29	21214.29
K39	19.08	19.46	686.45	20.51	21.18	21.21	2250.42	2083.57	1346.77
Ca42	2691.69	2718.8	1705.75	0.17	0.17	0.17	96908.96	83684.2	75535.26
Ca43	2615.59	2615.91	1656.64	0.71	0.73	0.75	393897.25	418564.72	376485.13
Sc45	14.26	14.24	1.3	0.00064	0.00066	0.00066	333.76	311.23	284.26
Ti49	14.44	14.38	436.4	0.0036	0.0039	0.004	1954.1	1891.15	1734.84
V51	15.61	15.73	15.63	0.00033	0.00036	0.00036	217.5	186.98	170.48
Cr53	20.08	21.73	1.48	0.0045	0.0053	0.0052	2508.02	2408.41	2245.12
Mn55	14.75	14.52	51.41	0.00076	0.00079	0.00083	411.66	428.74	371.07
Fe57	20.93	20.57	3417.01	0.034	0.036	0.038	20562.45	19074.1	18170.59
Co59	13.62	13.58	1.33	0.00032	0.00033	0.00034	172.13	165.34	155.32
Ni60	15.86	16.03	0.62	0.0012	0.0013	0.0014	683.66	653.09	608.91
Ni62	17.15	16.85	2.56	0.0084	0.0085	0.0091	4515.31	4271.97	3990.39
Cu63	18.28	17.7	0.77	0.00052	0.00053	0.00059	291.9	280.24	275.07
Cu65	17.81	17.29	0.87	0.0013	0.0013	0.0014	64145.8	61008.89	50797.13
Zn66	21.24	21.68	7.61	0.0023	0.0024	0.0026	134923.84	123902.5	101965.61
Ga69	14.06	13.94	2.34	0.00065	0.00069	0.00073	*****	*****	*****
Ga71	14.84	14.64	0.88	0.001	0.0011	0.0012	642.5	585.86	564.99
Ge72	14.44	14.43	0.39	0.0012	0.0013	0.0013	672.25	631.56	588.16
As75	64.76	89.75	0.82	0.0032	0.0028	0.0027	1297.18	1258.11	1113.74
Rb85	13.83	13.93	1.71	0.00043	0.00047	0.0005	208.06	195.14	187.33
Sr86	17.23	17.37	11.69	0.0026	0.0027	0.0027	27615.94	25722.36	20624.55
Sr88	15.7	15.78	10.58	0.00015	0.00015	0.00016	28445.75	26280.07	21215.98
Y89	14.8	14.73	1.02	0.00029	0.00029	0.00031	3972.49	3746.42	2993.92
Zr90	15.1	14.89	5.82	0.0014	0.00035	0.0005	159.42	152.32	147.08
Nb93	14.47	14.42	0.4	0.0013	0.0012	0.0013	2938.77	2771.48	2221.24
Mo95	17.04	18.23	12.11	0.0016	0.0017	0.0018	5487.36	5006.72	4132.91

Cs133	11.26	11.26	0.061	0.00013	0.00014	0.00015	75.56	69.91	65.88
Ba137	13.57	13.64	21.73	0.001	0.0011	0.0011	*****	*****	*****
La139	15.16	15.32	0.88	0.00012	0.00013	0.00013	578.24	532.12	392.09
Ce140	14.45	14.35	1.75	0.00011	0.00012	0.00012	61.98	60.33	53.59
Pr141	13.97	14.16	0.23	0.00009	0.0001	0.0001	48.63	45.85	42.22
Nd146	13.53	13.6	0.95	0.00058	0.00059	0.00062	293.32	268.64	257.14
Sm147	15.64	15.92	0.34	0.00072	0.00073	0.00078	417.69	407.76	379.63
Eu153	15.28	15.31	0.098	0.00019	0.0002	0.00021	4765.38	4388.6	3408.31
Gd157	14.46	14.55	0.31	71.88	71.88	71.88	548.81	522.01	471.87
Tb159	15.13	15.1	0.052	0.00022	0.00021	0.00021	70.64	66.82	60.94
Dy161	14.38	14.23	0.29	0.00081	0.00079	0.00079	318.85	293.08	284.03
Ho165	15.65	15.54	0.058	0.00013	0.00014	0.00014	57.31	48.93	45.57
Er167	14.33	14.17	0.18	0.00043	0.00046	0.00047	227.25	208.55	199.11
Tm169	14.46	14.29	0.033	0.00012	0.00013	0.00013	54.8	48.18	46.51
Yb173	16.7	16.47	0.23	0.076	0.076	0.074	335.89	314.54	302.48
Lu175	15.29	15.05	0.036	0.0021	0.0019	0.0017	54.26	52.85	48.11
Hf178	14.27	14.19	0.2	0.00037	0.00038	0.00039	269.23	280.5	232.42
Ta181	12.54	12.51	0.036	0.00013	0.00013	0.00013	603.45	518.57	428.57
W182	15.51	15.93	0.13	188.83	196.9	197.46	*****	*****	*****
Pb208	14.34	14.6	0.42	0.00022	0.00023	0.00024	600.75	410.11	297.76
Th232	15.52	15.41	0.21	0.00011	0.00011	0.00011	54.98	52.57	49.98
U238	15.67	15.67	0.076	0.0001	0.0001	0.0001	51.01	49.36	46.1

GLITTER!: Minimum detection limits (99% confidence).

Element	STD610-01	STD610-02	BCR2-01	KGW-1	KGW-2	KGW-3	BW-1	BW-2	BW-3
Li7	0.113	0.118	0.141	0.0005	0.00053	0.00056	264.72	245.95	243.84
Be9	0.856	0.797	0.995	0.00363	0.00371	0.00382	1909.98	1744.12	1748.18
B11	0.784	0.711	0.837	0.00296	0.00298	0.00311	1507.04	1352.62	1261.35
Na23	0.798	0.787	0.911	0.00333	0.00347	0.00362	1756.59	1642.9	1609.32
Mg25	1.54	1.56	1.8	0.00649	0.00727	0.00746	3549.52	3420.54	3260.37
Al27	1.21	1.19	1.37	0.00515	0.007	0.00826	3320.45	2395.95	3344.74
Si29	350.58	335.82	382.65	1.29	1.33	1.31	632886.06	573284.06	551167.13
P31	11.6	11.25	13.01	0.0433	0.0452	0.0437	20758.39	19622.4	18742.75
K39	1.95	1.88	2.19	0.00725	0.00784	0.00788	3805.18	3391.8	3319.62

Ca42	115.4	111.13	130.72	0.432	0.46	0.462	225810.92	204160.02	198072.52
Ca43	452.77	445.82	521.63	1.86	1.93	2.01	970390.69	893233.25	874879.5
Sc45	0.443	0.426	0.481	0.00167	0.00175	0.00177	835.13	764.37	756.82
Ti49	2.2	2.26	2.63	0.00919	0.0105	0.0106	5058.43	4768.89	4526.81
V51	0.21	0.202	0.238	0.00088	0.00096	0.00098	462.62	441.7	447.89
Cr53	2.86	2.81	3.31	0.0119	0.0135	0.0135	6417.33	5893.89	5884.9
Mn55	0.488	0.478	0.564	0.00198	0.0021	0.0022	1061.68	963.64	955.78
Fe57	20.04	19.87	24.18	0.0872	0.0962	0.102	50409.59	47900.82	48351.09
Co59	0.195	0.197	0.23	0.00085	0.00088	0.00088	436.26	411.5	414.31
Ni60	0.781	0.767	0.858	0.00325	0.00333	0.00367	1766.49	1653.27	1624.72
Ni62	5.17	5.25	5.95	0.0222	0.0226	0.024	11645.31	10692.5	10636.05
Cu63	0.311	0.308	0.362	0.00138	0.00141	0.00153	745.23	680.65	695.87
Cu65	0.775	0.78	0.9	0.00337	0.00359	0.0038	1869.64	1690.78	1720.48
Zn66	1.41	1.4	1.66	0.00601	0.00641	0.00678	3111.61	2953.85	2967.81
Ga69	0.403	0.393	0.462	0.00168	0.00182	0.00195	941.26	889.38	874.46
Ga71	0.607	0.602	0.726	0.00262	0.00296	0.00316	1560.18	1490.06	1495.71
Ge72	0.808	0.772	0.892	0.00319	0.00338	0.00351	1706.96	1605.18	1568.25
As75	2	1.93	2.13	0.0073	0.0072	0.00722	3327.55	2940.41	2919.07
Rb85	0.2	0.204	0.239	0.00092	0.001	0.00106	520.2	495.72	499.07
Sr86	1.66	1.67	1.89	0.00674	0.00698	0.00717	3539.23	3323.68	3207.64
Sr88	0.0937	0.0889	0.104	0.00039	0.00039	0.00042	206.74	190.05	183.86
Y89	0.0857	0.0875	0.0999	0.00038	0.00039	0.00041	199.23	188.21	186.43
Zr90	0.189	0.186	0.208	0.00078	0.00086	0.00089	402.47	388.89	393.06
Nb93	0.122	0.123	0.143	0.00051	0.00056	0.00059	286.94	262.01	258.47
Mo95	0.96	0.958	1.12	0.00413	0.00458	0.0047	2338.95	2180.23	2147.49
Cs133	0.0809	0.0824	0.0953	0.00034	0.00037	0.00041	193.03	174.66	169.94
Ba137	0.6	0.604	0.722	0.00248	0.00268	0.00292	1362.88	1260.64	1250.8
La139	0.0726	0.0779	0.0894	0.00032	0.00037	0.00034	172.91	155.29	161.07
Ce140	0.0724	0.0666	0.0774	0.00028	0.0003	0.00032	160.78	142.69	143.21
Pr141	0.0566	0.0548	0.062	0.00024	0.00025	0.00025	126.14	117.03	112.94
Nd146	0.335	0.321	0.373	0.00137	0.0015	0.00155	700.74	660.97	664.17
Sm147	0.435	0.417	0.477	0.00186	0.00191	0.00203	968.7	889.76	902.18
Eu153	0.11	0.113	0.124	0.00046	0.0005	0.00051	251.88	229.97	234.38
Gd157	0.386	0.382	0.443	0.00164	0.00172	0.00184	882.97	819.41	771.71

Tb159	0.0695	0.0731	0.0866	0.00032	0.00034	0.00035	171.4	155.62	162.55
Dy161	0.342	0.331	0.394	0.00149	0.0016	0.00162	822.67	747.34	758.86
Ho165	0.0621	0.0624	0.0702	0.00026	0.00028	0.00029	146.23	120.81	121.33
Er167	0.251	0.259	0.3	0.0011	0.00117	0.0012	589	532.58	529.17
Tm169	0.0564	0.0556	0.0672	0.00025	0.00024	0.00028	127.74	120.19	116.93
Yb173	0.356	0.368	0.395	0.00162	0.0016	0.00169	870.34	802.89	807.04
Lu175	0.0601	0.0631	0.0696	0.00027	0.00028	0.00029	139.96	130.47	128.34
Hf178	0.197	0.209	0.239	0.00086	0.00083	0.00098	450.71	418.05	391.24
Ta181	0.054	0.0522	0.0615	0.00022	0.00024	0.00025	117.79	113.87	108.16
W182	0.285	0.281	0.309	0.00116	0.00125	0.00127	603.74	546.86	558
Pb208	0.132	0.128	0.142	0.00054	0.00057	0.00057	265.26	261.39	240.59
Th232	0.0663	0.0645	0.0794	0.00027	0.0003	0.0003	141.4	133.89	128.81
U238	0.0601	0.0569	0.0706	0.00025	0.00026	0.00026	132.25	125.34	123.41

GLITTER!: Trace element concentrations normalised to chondrite.

Element	STD610-01	STD610-02	BCR2-01	KGW-1	KGW-2	KGW-3	BW-1	BW-2	BW-3
Li7	202.43	201.46	4.21	0	0	0	122.25	115.44	0
Be9	11780.17	11500.2	53	0	0	0	0	0	0
B11	177.5	201	4.94	0.00558	0.00563	0.00456	2762.91	2895.12	2992.77
Na23	13.11	13.18	3.28	0.00001	0.00001	0.00001	0.68	0.66	0.56
Mg25	0.00329	0.00321	0.1475	0	0	0	0	0.076	0
Al27	0.781	0.771	5.73	0	0	0	0	1.31	0
Si29	2.052	2.054	1.716	0	0	0	0	17.76	7.85
P31	0.146	0.152	0.63	0	0	0	33.66	0	0
K39	0.565	0.575	19.99	0.668	0.687	0.683	0	16.8	5.78
Ca42	6.04	6.09	3.78	0.00004	0	0	0	0	0
Ca43	6.06	6.06	3.78	0	0	0	0	146.91	129.14
Sc45	51.11	51.01	4.52	0	0	0	0	0	0
Ti49	0.665	0.662	20.28	0	0	0	0	0	0
V51	5.19	5.21	5.12	0	0	0	11.5	6.31	0
Cr53	0.0985	0.1061	0.00329	0	0	0	0	0	0
Mn55	0.1487	0.1461	0.512	0	0	0	0	0.58	0
Fe57	0.00167	0.00162	0.289	0	0	0	0.183	0	0
Co59	0.531	0.529	0.0506	0	0	0	0	0	0

Ni60	0.02679	0.02704	0.00076	0	0	0	0	0	0	0	0	0	0
Ni62	0.0272	0.0266	0.00126	0	0	0	0	0	0	0	0	0	0
Cu63	2.61	2.51	0.1013	0	0	0	0	0	0	0	0	0	0
Cu65	2.61	2.51	0.1065	0	0	0	0	0	0	3131.97	3083.27	2756.31	2756.31
Zn66	0.98	0.998	0.343	0	0	0	0	0	0	2332.46	2226.32	1977.13	1977.13
Ga69	28.95	28.69	4.73	0	0	0	0	0	0	7874039	7619016.5	6718654	6718654
Ga71	29.04	28.6	1.558	0	0	0	0	0	0	113.14	0	0	0
Ge72	8.83	8.82	0.0813	0	0	0	0	0	0	0	0	0	0
As75	95.62	135.62	0	0	0	0	0	0	0	0	0	0	0
Rb85	124.62	125.42	15.1	0.00171	0.00193	0.00205	0	0	0	0	0	0	0
Sr86	41.71	41.96	27.77	0	0	0	0	0	0	20153.39	19687.39	17362.18	17362.18
Sr88	41.72	41.91	27.83	0	0	0	0	0	0	20705.91	20035.54	17749.56	17749.56
Y89	200.62	199.39	13.52	0.00277	0.0028	0.00291	0.00291	0.00291	0.00291	15266.54	15081.81	13227.58	13227.58
Zr90	80.03	78.79	30.38	0.00656	0.00031	0.00147	0.00147	0.00147	0.00147	0	0	0	0
Nb93	1121.61	1116.15	29.55	0.0924	0.0898	0.0963	0.0963	0.0963	0.0963	67640.34	66844.08	58813.92	58813.92
Mo95	265.25	282.81	184.25	0	0	0	0	0	0	31677.22	29787.49	26164.33	26164.33
Cs133	1293.29	1294.13	4.6	0	0	0	0	0	0	0	0	0	0
Ba137	124.14	124.71	197.14	0.00211	0.00155	0.00117	0.00117	0.00117	0.00117	*****	*****	*****	*****
La139	1241.3	1253.24	70.69	0	0	0	0	0	0	13447.64	12963.63	10418.22	10418.22
Ce140	469.7	466.29	55.95	0.00036	0	0	0	0	0	0	158.91	0	0
Pr141	3120.01	3159.58	47.98	0	0	0	0	0	0	0	0	0	0
Nd146	604.64	607.65	39.69	0.00523	0.00317	0.00369	0.00369	0.00369	0.00369	1044.96	0	0	0
Sm147	1936.77	1968.27	28.59	0	0	0	0	0	0	5671.78	6944.88	6147.19	6147.19
Eu153	5300.78	5304.97	24.56	0.011	0.0091	0.0124	0.0124	0.0124	0.0124	476762.41	460523.03	393509.31	393509.31
Gd157	1370.18	1376.42	19.64	7428.5	7428.5	7428.5	7428.5	7428.5	7428.5	11286.16	11286.16	11286.16	11286.16
Tb159	7651.9	7624.9	16.34	0.0822	0.0746	0.0742	0.0742	0.0742	0.0742	0	3461.7	0	0
Dy161	1125.96	1113.32	16.2	0.0339	0.0288	0.0275	0.0275	0.0275	0.0275	0	0	0	0
Ho165	5305.78	5260.45	14.54	0.023	0.0229	0.0236	0.0236	0.0236	0.0236	0	0	0	0
Er167	1722	1700.2	12.7	0	0.0052	0.006	0.006	0.006	0.006	0	0	0	0
Tm169	11881.47	11725.83	11.93	0.0471	0.0512	0.0373	0.0373	0.0373	0.0373	4591.42	0	0	0
Yb173	1876.08	1846.91	14.64	9.01	8.96	8.63	8.63	8.63	8.63	0	0	0	0
Lu175	11509.59	11314.07	13.07	1.556	1.415	1.274	1.274	1.274	1.274	0	0	0	0
Hf178	2342.3	2326.62	24.35	0.0156	0.0213	0.0112	0.0112	0.0112	0.0112	9098.12	10675.45	9212.57	9212.57
Ta181	14516.29	14465.13	23.69	0.0818	0.088	0.0801	0.0801	0.0801	0.0801	200084.72	179936.23	163391.86	163391.86

W182	4946.21	5074.62	7.64	59926.17	61961.68	61479.11	*****	*****	*****
Pb208	112.36	114.38	3.13	0.00029	0.00035	0.00052	1380.59	961.28	749.7
Th232	10646.7	10565.64	137.01	0.007	0	0	0	0	0
U238	37497.7	37480.43	148.61	0	0	0.0219	0	0	0

GLITTER!: Mean Raw CPS background subtracted.

Element	STD610-01	STD610-02	BCR2-01	KGW-1	KGW-2	KGW-3	BW-1	BW-2	BW-3
Li7	349786	348633	6391	5	0	0	91	92	64
Be9	46692	45669	184	0	28	0	7	8	0
B11	44822	51659	1131	349	345	278	332	376	444
Na23	64194520	64700880	14125038	10731	10665	10986	1450	1500	1437
Mg25	25458	24897	1001479	34	0	0	0	270	9
Al27	4279506	4233485	27617182	0	0	0	0	3342	0
Si29	3323461	3331075	2438621	45	0	0	0	13278	6608
P31	14061	14820	54643	0	0	0	1499	0	0
K39	296934	301921	9197432	82957664	82169552	80167896	0	4056	1569
Ca42	405257	409308	222586	633	0	0	0	462	303
Ca43	88586	88806	48584	96	27	0	453	999	990
Sc45	297294	296813	23036	0	0	0	182	197	0
Ti49	16429	16358	439120	55	0	0	0	19	43
V51	264668	265883	228311	0	0	0	251	146	59
Cr53	21241	22936	624	2	0	0	0	114	0
Mn55	325312	319362	978317	129	0	0	0	580	319
Fe57	7796	7499	1162273	262	0	22	350	163	0
Co59	213872	212715	17763	0	0	50	43	50	0
Ni60	47697	48122	1177	11	11	0	0	0	0
Ni62	6879	6734	279	0	0	33	2	27	0
Cu63	131780	125094	4370	0	0	84	26	68	87
Cu65	61482	58554	2150	0	0	0	29749	30769	30555
Zn66	28997	29576	8916	0	0	49	29939	30416	30406
Ga69	219850	218086	31488	98	19	0	25892796	26659706	26457026
Ga71	143912	141850	6768	157	0	36	242	0	72
Ge72	65264	65310	527	8	0	8	49	0	0
As75	14622	21438	27	0	0	0	10	45	0

Rb85	279586	281872	29757	912	992	1032	105	6	0
Sr86	48036	48422	28101	0	115	17	10110	10520	10452
Sr88	408790	411732	239981	0	21	33	88746	91534	91417
Y89	390803	388944	23115	1276	1247	1270	12908	13575	13404
Zr90	181751	179210	60566	3534	159	751	32	0	0
Nb93	306992	306080	7106	5998	5630	5927	8061	8485	8410
Mo95	46011	49351	28306	0	0	46	2449	2463	2447
Cs133	364031	366543	1146	53	30	0	24	35	63
Ba137	53235	53702	74597	216	153	114	102253520	104923256	104767672
La139	416843	422778	20966	4	0	37	1997	2056	1866
Ce140	449159	447257	47110	81	61	29	0	71	0
Pr141	546233	555780	7420	4	9	21	0	0	0
Nd146	90283	91151	5235	186	109	125	69	39	46
Sm147	75586	77179	985	30	44	57	98	128	128
Eu153	283876	285455	1162	140	113	151	11306	11665	11260
Gd157	74225	74945	940	96400880	93330912	91946776	271	289	327
Tb159	511007	512147	966	1317	1157	1135	86	110	0
Dy161	90599	90046	1152	652	536	506	1	0	0
Ho165	497625	495706	1204	516	497	505	0	34	0
Er167	114549	113673	747	40	79	91	0	0	3
Tm169	492356	488099	436	466	491	352	84	26	69
Yb173	84520	83523	581	96899	93133	88313	0	0	0
Lu175	480526	475066	483	15592	13731	12190	1	38	0
Hf178	135558	135594	1250	217	288	149	236	296	289
Ta181	453486	454919	656	614	641	575	2799	2694	2768
W182	103012	106376	141	300181792	300886880	294500320	270498720	277225312	275733632
Pb208	203967	209912	5078	128	151	220	1149	860	762
Th232	426421	427171	4893	68	5	0	5	0	42
U238	468676	472727	1655	48	5	63	0	1	0

GLITTER! 4.4[svn]: Laser Ablation Analysis Results

Y:\jakutis_jonas\2011_04_05\run2.B
Created: Tue Apr 05 13:59:02 2011

All values are reported in ppm

GLITTER!: Trace Element Concentrations MDL filtered.

Element	STD610-05	STD610-06	BCR2-02	YVO-2	YVO-3	GDVO-1	GDVO-2	GDVO-3	NGGDVO-1	NGGDVO-2	NGGDVO-3
Li7	463.47	514.06	10.47	0.00512	0.00429	0.00109	<0.00083	<0.00085	0.0127	0.0135	0.0116
Be9	449.6	485.65	2.09	<0.0096	<0.0103	<0.0049	<0.0048	<0.0053	<0.0052	<0.0048	<0.0047
B11	341.64	375.7	8.3	0.0281	0.0322	0.0199	0.0225	0.0172	0.0274	0.0389	0.0246
Na23	94852.91	95623.96	22995.74	<0.030	<0.030	<0.0148	<0.0151	<0.0151	<0.0145	<0.0144	<0.0151
Mg25	466	464.65	21204.11	<0.0199	<0.0215	0.0175	0.0145	<0.0103	0.0173	0.0134	0.0223
Al27	9965.51	10048.88	72126.57	<0.0131	<0.0133	0.0149	<0.0062	<0.0063	<0.0062	<0.0060	<0.0062
Si29	327205.53	329732.06	270028.69	8.39	6.73	2.39	1.26	1.95	2.71	2.88	2.02
P31	344.68	339.62	1318.17	<0.16	<0.137	0.641	0.64	0.605	3.52	3.47	3.54
K39	491.88	480.42	16411.88	0.259	<0.030	<0.0150	<0.0152	<0.0152	<0.0146	<0.0142	<0.0148
Ca42	82243.98	81380.7	50637.18	4.8	<1.71	<0.84	<0.84	<0.85	<0.82	<0.79	<0.82
Ca43	81833.27	81833.27	51029.65	<1.50	<1.60	<0.67	<0.64	<0.69	<0.63	<0.64	<0.63
Sc45	444.9	436.73	32.58	<0.00203	<0.00218	<0.00106	<0.00107	<0.00097	<0.00104	<0.00097	<0.00092
Ti49	436.97	430.88	12903.27	<0.0229	<0.0224	<0.0113	<0.0117	<0.0111	<0.0101	<0.0110	<0.0122
V51	449.11	433.89	430.02	3765.07	3765.07	1871.56	1871.56	1871.56	1871.56	1871.56	1871.56
Cr53	408.86	401.09	15.7	0.026	0.027	<0.0121	<0.0125	<0.0125	<0.0122	<0.0118	<0.0125
Mn55	437.26	429.01	1509.93	<0.0056	<0.0057	<0.0027	<0.0027	<0.0027	<0.00262	<0.00254	<0.00269
Fe57	471.8	444.86	82918.14	<0.254	<0.27	<0.132	<0.130	<0.133	<0.131	<0.123	<0.129
Co59	411.23	398.15	37.61	<0.00220	<0.00223	<0.00117	<0.00098	<0.00110	<0.00100	<0.00109	<0.00111
Ni60	451.37	435.75	12.35	<0.0068	<0.0076	<0.0034	<0.0036	<0.0036	<0.0035	<0.0033	<0.0035
Ni62	452.87	433.79	15.11	<0.048	<0.049	<0.0227	<0.0265	<0.028	<0.0255	<0.0224	<0.0242
Cu63	436.2	423.65	18.29	0.008	0.0163	0.00416	0.00447	0.01063	<0.00180	0.00211	<0.00183
Cu65	430.69	429.64	17.76	0.0101	0.0815	0.0059	0.0051	0.0107	0.0055	0.003	<0.0032
Zn66	461.3	451.38	150.1	0.0123	0.0129	<0.0053	<0.0054	0.009	<0.0052	<0.0047	<0.0054
Ga69	444.59	431.08	52.57	<0.00135	<0.00145	<0.00065	<0.00063	<0.00070	<0.00068	<0.00066	<0.00065
Ga71	444.18	431.51	22.9	<0.00169	<0.00181	0.1041	0.1016	0.1033	0.0852	0.0812	0.0823

Ge72	432.81	419.24	6.24	<0.0099	<0.0099	0.1899	0.1936	0.1998	0.1543	0.1584	0.155
As75	324.65	309.75	<1.16	<0.0163	<0.0150	0.1151	0.1095	0.1119	0.0882	0.0917	0.0842
Rb85	439.96	421.86	49.82	<0.00105	<0.00103	<0.00048	<0.00041	<0.00051	<0.00045	<0.00038	<0.00045
Sr86	507.94	486.17	318.36	<0.0238	<0.0251	<0.0120	<0.0124	<0.0123	<0.0121	<0.0115	<0.0120
Sr88	508.83	485.45	320.37	0.00193	0.00181	<0.00032	<0.00034	0.00037	<0.00031	<0.00031	<0.00032
Y89	462.64	436.6	29.73	7203.38	7227.75	0.1223	0.1226	0.1213	1.865	1.854	1.829
Zr90	452.56	426.73	162.49	0.0799	0.0782	0.00408	0.0034	0.00377	0.00979	0.00929	0.00871
Nb93	430.61	407.83	10.9	<0.00069	0.00073	<0.00033	<0.00036	<0.00037	<0.00034	<0.00037	0.00034
Mo95	384.23	368.96	238.26	<0.0040	<0.0043	<0.00186	<0.00234	<0.00203	0.0194	0.017	0.0181
Cs133	372.2	349.69	1.176	<0.00046	<0.00049	<0.00020	<0.00020	<0.00028	<0.00022	<0.00021	<0.00022
Ba137	438.68	409.21	633.79	<0.0034	<0.0033	<0.00181	0.00465	0.00414	<0.00170	<0.00166	<0.00169
La139	475.13	439.81	25.03	<0.00045	<0.00043	0.00727	0.00813	0.00761	0.0027	0.00252	0.00287
Ce140	463.11	432.43	51.9	0.00052	<0.00043	0.00306	0.00287	0.00288	0.00212	0.002	0.00217
Pr141	445.98	413.72	6.2	<0.00031	<0.00029	0.00653	0.00626	0.00614	0.00206	0.00218	0.00222
Nd146	449.76	411.8	27.13	<0.00213	<0.00196	21.68	21.75	21.36	17.71	17.23	17.4
Sm147	466.69	433.94	6.29	<0.00180	<0.00219	0.00256	0.00187	0.0025	0.00444	0.00508	0.00377
Eu153	476.44	445.48	1.98	0.00207	0.00171	0.00546	0.00461	0.00517	0.0363	0.0371	0.0372
Gd157	434.37	404.95	6.01	<0.00236	<0.00199	6183.1	6171.55	6147.62	6298.95	6253.5	6360.05
Tb159	460.53	425.16	0.916	0.00558	0.00681	0.00864	0.00852	0.00856	0.00969	0.01013	0.00993
Dy161	442.66	409.92	5.53	<0.00178	<0.00138	0.028	0.0277	0.0261	0.0257	0.0258	0.0262
Ho165	469.43	429.78	1.152	0.00083	0.00094	0.00046	0.00057	0.00041	0.00151	0.00149	0.0014
Er167	445.23	406.82	3.05	<0.00146	0.00215	0.0476	0.0479	0.0467	0.00346	0.00449	0.00343
Tm169	439.17	401.48	0.431	<0.00030	<0.00027	0.00129	0.0012	0.00103	0.00388	0.00368	0.00388
Yb173	481.63	441.3	3.22	<0.00203	<0.00205	3.69	3.7	3.61	3.82	3.75	3.8
Lu175	455.68	414.4	0.44	<0.00031	<0.00033	0.1305	0.1277	0.1265	0.1384	0.1379	0.1391
Hf178	439.51	396.64	4.2	<0.00085	<0.00083	0.00454	0.00444	0.00449	0.00578	0.00521	0.00509
Ta181	397.68	356.85	0.586	0.0035	0.00029	<0.00011	<0.00015	<0.00014	0.2	0.0493	0.0848
W182	467.37	423.98	0.484	<0.00135	<0.00161	<0.00070	<0.00072	<0.00074	0.00181	0.002	0.00216
Pb208	444.59	385.88	10.44	0.00149	0.01075	0.00241	0.00778	0.00459	0.00161	<0.00033	0.00197
Th232	497.21	412.89	5.37	<0.00030	0.00036	<0.00016	<0.00018	<0.00013	<0.00014	<0.00015	<0.00018
U238	507.19	417.77	1.63	<0.00030	0.00031	<0.00	<0.00016	0.00019	0.0023	0.00221	0.00254
Element	GLITTER!: 1 sigma error.										
	STD610-05	STD610-06	BCR2-02	YVO-2	YVO-3	GDVO-1	GDVO-2	GDVO-3	NGGDVO-1	NGGDVO-2	NGGDVO-3

Li7	29.33	32.56	0.69	0.00081	0.0008	0.00033	0.00032	0.00034	0.0013	0.0014	0.0013	0.0013
Be9	45.36	48.93	0.36	0.0036	0.0038	0.0018	0.0018	0.0019	0.002	0.0018	0.002	0.0017
B11	25.85	28.57	0.73	0.0047	0.0049	0.0027	0.003	0.0028	0.0036	0.0047	0.0036	0.0035
Na23	3212.67	3242.13	783.45	0.011	0.011	0.0056	0.0058	0.0057	0.0055	0.0055	0.0055	0.0056
Mg25	16.52	16.5	741.63	0.0075	0.0081	0.0039	0.0036	0.004	0.0042	0.0039	0.0042	0.0041
Al27	368.9	372.27	2681.57	0.005	0.005	0.0025	0.0023	0.0024	0.0023	0.0023	0.0023	0.0023
Si29	16610.82	16760	13763.33	0.83	0.8	0.38	0.37	0.38	0.38	0.37	0.38	0.37
P31	62.19	61.2	236.51	0.14	0.052	0.096	0.096	0.091	0.51	0.5	0.51	0.51
K39	20.32	19.91	685.33	0.014	0.011	0.0057	0.0059	0.0057	0.0056	0.0054	0.0056	0.0056
Ca42	2650.32	2624.36	1641.61	0.62	0.65	0.32	0.32	0.32	0.31	0.3	0.31	0.31
Ca43	2615.34	2617.2	1644.22	0.58	0.59	0.25	0.25	0.26	0.24	0.24	0.24	0.24
Sc45	15.17	14.91	1.14	0.00079	0.00082	0.0004	0.0004	0.00038	0.00038	0.00037	0.00038	0.00035
Ti49	15.17	15	440.09	0.0088	0.0085	0.0043	0.0044	0.0042	0.0041	0.0042	0.0041	0.0045
V51	17.01	16.47	16.44	119.06	119.06	59.18	59.18	59.18	59.18	59.18	59.18	59.18
Cr53	14.28	14.05	0.98	0.01	0.01	0.0046	0.0047	0.0047	0.0045	0.0045	0.0045	0.0046
Mn55	14.65	14.39	50.85	0.0021	0.0022	0.001	0.001	0.001	0.00099	0.00096	0.00099	0.001
Fe57	36.77	34.88	6421.78	0.097	0.1	0.05	0.049	0.051	0.053	0.047	0.051	0.049
Co59	15.4	14.94	1.44	0.00083	0.00085	0.00043	0.00038	0.0004	0.00039	0.0004	0.00039	0.00041
Ni60	17.88	17.31	0.62	0.0025	0.0028	0.0013	0.0013	0.0014	0.0013	0.0013	0.0013	0.0013
Ni62	19.76	19.05	1.71	0.019	0.019	0.0087	0.0098	0.01	0.0094	0.0086	0.0094	0.0089
Cu63	17.08	16.6	0.77	0.0015	0.0016	0.00075	0.00074	0.00092	0.00071	0.00063	0.00071	0.0007
Cu65	15.47	15.44	0.75	0.0027	0.005	0.0013	0.0012	0.0014	0.0012	0.0012	0.0012	0.0013
Zn66	22.49	22.07	7.49	0.0046	0.0044	0.0021	0.0021	0.0022	0.002	0.0018	0.002	0.002
Ga69	15.61	15.17	1.89	0.00051	0.00055	0.00026	0.00025	0.00027	0.00026	0.00025	0.00026	0.00026
Ga71	15.41	15	0.84	0.00067	0.00069	0.0036	0.0035	0.0036	0.003	0.0029	0.003	0.0029
Ge72	15.77	15.3	0.4	0.0038	0.0037	0.0069	0.007	0.0072	0.0059	0.0059	0.0059	0.0058
As75	30.88	29.52	0.45	0.0061	0.0058	0.0096	0.0092	0.0094	0.0076	0.0078	0.0076	0.0073
Rb85	16.87	16.23	1.95	0.00039	0.00038	0.00018	0.00016	0.00019	0.00017	0.00015	0.00017	0.00017
Sr86	19.68	18.9	12.54	0.0091	0.0094	0.0045	0.0046	0.0046	0.0045	0.0044	0.0045	0.0045
Sr88	19.97	19.11	12.73	0.00029	0.00031	0.00012	0.00013	0.00011	0.00012	0.00012	0.00012	0.00013
Y89	20.18	19.11	1.32	257.6	261	0.0046	0.0046	0.0047	0.072	0.073	0.072	0.073
Zr90	19.73	18.67	7.2	0.0032	0.0031	0.00037	0.00035	0.00037	0.00056	0.00054	0.00056	0.00054
Nb93	18.15	17.25	0.48	0.00027	0.00029	0.00013	0.00013	0.00014	0.00013	0.00014	0.00013	0.00013
Mo95	14.81	14.27	9.33	0.0016	0.0016	0.00073	0.00085	0.00078	0.0013	0.0013	0.0013	0.0012

Cs133	17.23	16.27	0.063	0.00017	0.00018	0.00008	0.00008	0.00001	0.00008	0.00008	0.00009
Ba137	21.02	19.69	30.85	0.0013	0.0013	0.0007	0.00077	0.00076	0.00064	0.00063	0.00064
La139	23.96	22.28	1.29	0.00017	0.00017	0.00036	0.0004	0.00038	0.00018	0.00018	0.00019
Ce140	21.68	20.34	2.48	0.00017	0.00017	0.00018	0.00018	0.00018	0.00015	0.00015	0.00016
Pr141	22.03	20.53	0.32	0.00012	0.00011	0.0003	0.0003	0.0003	0.00014	0.00014	0.00015
Nd146	24.91	22.93	1.56	0.0008	0.00076	1	1.03	1.05	0.9	0.9	0.95
Sm147	22.65	21.16	0.35	0.00072	0.00082	0.00053	0.00052	0.00048	0.0006	0.00057	0.00063
Eu153	22.1	20.77	0.1	0.00031	0.0003	0.00031	0.00029	0.0003	0.0015	0.0016	0.0016
Gd157	20.71	19.41	0.33	0.00088	0.00078	240.22	244.48	248.96	261.36	266.37	278.54
Tb159	23.99	22.26	0.054	0.00034	0.00038	0.00042	0.00042	0.00044	0.0005	0.00054	0.00054
Dy161	22.67	21.11	0.32	0.00068	0.00057	0.0015	0.0015	0.0015	0.0014	0.0015	0.0015
Ho165	26.18	24.11	0.071	0.00016	0.00014	0.00008	0.00009	0.00008	0.00012	0.00013	0.00012
Er167	25.37	23.31	0.2	0.00059	0.00056	0.0025	0.0026	0.0026	0.00038	0.00044	0.00041
Tm169	24.75	22.76	0.03	0.00012	0.00011	0.00011	0.0001	0.0001	0.00024	0.00024	0.00026
Yb173	26.56	24.49	0.21	0.00079	0.00078	0.17	0.18	0.18	0.19	0.2	0.21
Lu175	26.86	24.58	0.031	0.00012	0.00012	0.0067	0.0067	0.0069	0.0078	0.0081	0.0085
Hf178	27.15	24.67	0.28	0.00035	0.00034	0.00039	0.0004	0.0004	0.00046	0.00045	0.00045
Ta181	25.54	23.09	0.042	0.00026	0.00011	0.00005	0.00006	0.00005	0.012	0.0032	0.0057
W182	27.58	25.23	0.055	0.00055	0.00062	0.00028	0.00029	0.00029	0.00033	0.00034	0.00033
Pb208	35.33	31.01	0.86	0.0003	0.00088	0.00025	0.00064	0.00043	0.00021	0.00013	0.00026
Th232	50.85	42.65	0.57	0.00012	0.00012	0.00006	0.00007	0.00005	0.00006	0.00006	0.00007
U238	53.18	44.31	0.18	0.00012	0.00012	<0.00	0.00006	0.00006	0.00029	0.00029	0.00035

GLITTER!: Minimum detection limits (99% confidence).

Element	STD610-05	STD610-06	BCR2-02	VVO-2	VVO-3	GDVO-1	GDVO-2	GDVO-3	NGGDVO-1	NGGDVO-2	NGGDVO-3
Li7	0.107	0.115	0.111	0.00158	0.00167	0.00078	0.00083	0.00085	0.00082	0.00072	0.00088
Be9	0.631	0.574	0.641	0.00963	0.0103	0.00488	0.00478	0.00529	0.00523	0.00485	0.00465
B11	0.643	0.634	0.644	0.00943	0.00924	0.00466	0.00477	0.00517	0.00488	0.00462	0.00477
Na23	1.72	1.76	1.74	0.0296	0.0301	0.0148	0.0151	0.0151	0.0145	0.0144	0.0151
Mg25	1.08	1.23	1.26	0.0199	0.0215	0.00914	0.00853	0.0103	0.00993	0.00929	0.00957
Al27	0.884	0.923	0.838	0.0131	0.0133	0.00635	0.00617	0.00635	0.00624	0.00604	0.00624
Si29	129.56	129.94	131.66	1.85	1.9	0.938	0.95	0.956	0.911	0.879	0.928
P31	10.93	11.03	11.24	0.16	0.137	0.065	0.065	0.0643	0.0608	0.0593	0.0619
K39	1.92	1.92	1.96	0.027	0.0303	0.015	0.0152	0.0152	0.0146	0.0142	0.0148

Ca42	111.08	110.9	112.55	1.56	1.71	0.843	0.845	0.846	0.816	0.79	0.819
Ca43	98.82	98.7	86.3	1.5	1.6	0.669	0.637	0.69	0.631	0.638	0.626
Sc45	0.134	0.128	0.135	0.00203	0.00218	0.00106	0.00107	0.00097	0.00104	0.00097	0.00092
Ti49	1.42	1.22	1.27	0.0229	0.0224	0.0113	0.0117	0.0111	0.0101	0.011	0.0122
V51	0.0935	0.0847	0.0819	0.00145	0.00136	0.00069	0.00065	0.00067	0.00067	0.00061	0.00061
Cr53	1.59	1.65	1.58	0.0253	0.0254	0.0121	0.0125	0.0125	0.0122	0.0118	0.0125
Mn55	0.39	0.381	0.381	0.00557	0.00574	0.00268	0.00274	0.00268	0.00262	0.00254	0.00269
Fe57	19.1	17.03	17.02	0.254	0.274	0.132	0.13	0.133	0.131	0.123	0.129
Co59	0.164	0.139	0.136	0.0022	0.00223	0.00117	0.00098	0.0011	0.001	0.00109	0.00111
Ni60	0.383	0.482	0.447	0.00677	0.00761	0.00337	0.00357	0.00364	0.00355	0.00334	0.0035
Ni62	3.21	3.33	3.23	0.0481	0.0486	0.0227	0.0265	0.0283	0.0255	0.0224	0.0242
Cu63	0.217	0.208	0.226	0.00342	0.00313	0.00173	0.0017	0.0017	0.0018	0.00154	0.00183
Cu65	0.39	0.362	0.367	0.00634	0.00617	0.00317	0.00291	0.00298	0.00278	0.00301	0.00321
Zn66	0.673	0.565	0.658	0.0114	0.0106	0.00529	0.00537	0.00514	0.00517	0.00469	0.0054
Ga69	0.0914	0.0837	0.0864	0.00135	0.00145	0.00065	0.00063	0.0007	0.00068	0.00066	0.00065
Ga71	0.111	0.104	0.123	0.00169	0.00181	0.00089	0.00102	0.00105	0.00097	0.00084	0.00101
Ge72	0.763	0.7	0.695	0.00989	0.00992	0.00477	0.00466	0.00489	0.00507	0.00443	0.00456
As75	1.28	1.12	1.16	0.0163	0.015	0.00752	0.00718	0.00758	0.00688	0.00622	0.00686
Rb85	0.0551	0.0518	0.0584	0.00105	0.00103	0.00048	0.00041	0.00051	0.00045	0.00038	0.00045
Sr86	1.58	1.6	1.64	0.0238	0.0251	0.012	0.0124	0.0123	0.0121	0.0115	0.012
Sr88	0.0417	0.0377	0.0398	0.00063	0.00068	0.00032	0.00034	0.00027	0.00031	0.00031	0.00032
Y89	0.0377	0.0382	0.0344	0.0006	0.0007	0.0003	0.00031	0.0003	0.00031	0.00029	0.00034
Zr90	0.0843	0.0767	0.0749	0.00133	0.00145	0.00065	0.00066	0.00068	0.00062	0.00054	0.00068
Nb93	0.0474	0.0465	0.0524	0.00069	0.00072	0.00033	0.00036	0.00037	0.00034	0.00037	0.00033
Mo95	0.228	0.265	0.22	0.00399	0.00429	0.00186	0.00234	0.00203	0.00204	0.00206	0.00182
Cs133	0.0272	0.0247	0.0271	0.00046	0.00049	0.0002	0.0002	0.00028	0.00022	0.00021	0.00022
Ba137	0.203	0.22	0.197	0.00345	0.00326	0.00181	0.00165	0.00168	0.0017	0.00166	0.00169
La139	0.0274	0.0261	0.0276	0.00045	0.00043	0.00021	0.0002	0.00021	0.0002	0.00022	0.00021
Ce140	0.0304	0.0248	0.0251	0.0004	0.00043	0.0002	0.00022	0.0002	0.00021	0.0002	0.00021
Pr141	0.0185	0.0187	0.018	0.00031	0.00029	0.00015	0.00016	0.00017	0.00017	0.00016	0.00016
Nd146	0.117	0.0999	0.116	0.00213	0.00196	0.00082	0.00071	0.0009	0.00093	0.00085	0.00097
Sm147	0.136	0.158	0.137	0.0018	0.00219	0.0012	0.00124	0.00106	0.00121	0.00102	0.0014
Eu153	0.0374	0.0398	0.0335	0.00065	0.00067	0.0003	0.00038	0.00028	0.00033	0.00027	0.00028
Gd157	0.127	0.126	0.123	0.00236	0.00199	0.00089	0.00103	0.00357	0.001	0.00112	0.00099

Tb159	0.02	0.0175	0.0193	0.00036	0.00027	0.00016	0.00014	0.00014	0.00017	0.00013	0.00017
Dy161	0.112	0.119	0.102	0.00178	0.00138	0.00081	0.00078	0.00096	0.00084	0.00077	0.00083
Ho165	0.0182	0.0185	0.0204	0.00034	0.00027	0.00017	0.00018	0.00018	0.00014	0.00016	0.00014
Er167	0.0791	0.0922	0.0877	0.00146	0.00128	0.00064	0.00065	0.00062	0.00062	0.00065	0.00072
Tm169	0.0183	0.0176	0.0193	0.0003	0.00027	0.00015	0.00015	0.00015	0.00016	0.00015	0.00016
Yb173	0.125	0.115	0.101	0.00203	0.00205	0.001	0.00086	0.00097	0.0009	0.00093	0.00091
Lu175	0.0177	0.0194	0.02	0.00031	0.00033	0.00017	0.00014	0.00015	0.00016	0.00015	0.00013
Hf178	0.0731	0.0658	0.0608	0.00085	0.00083	0.00051	0.00056	0.00052	0.0004	0.0005	0.00048
Ta181	0.0176	0.0163	0.0162	0.00029	0.00028	0.00011	0.00015	0.00014	0.00014	0.00014	0.00014
W182	0.0843	0.0942	0.0803	0.00135	0.00161	0.0007	0.00072	0.00074	0.00069	0.00069	0.00062
Pb208	0.0425	0.0387	0.0402	0.00064	0.0007	0.00033	0.00029	0.00036	0.0003	0.00033	0.00037
Th232	0.0183	0.0173	0.0223	0.0003	0.00027	0.00016	0.00018	0.00013	0.00014	0.00015	0.00018
U238	0.0265	0.0157	0.0195	0.0003	0.00027	0.00013	0.00016	0.00013	0.00013	0.00014	0.00012

GLITTER!: Trace element concentrations normalised to chondrite.

Element	STD610-05	STD610-06	BCR2-02	YVO-2	YVO-3	GDVO-1	GDVO-2	GDVO-3	NGGDVO-1	NGGDVO-2	NGGDVO-3
Li7	193.11	214.19	4.36	0.00213	0.00179	0.00045	0	0	0.00529	0.00561	0.00484
Be9	11239.9	12141.35	52.34	0	0	0	0	0	0	0	0
B11	179.81	197.74	4.37	0.0148	0.017	0.0105	0.0119	0.009	0.0144	0.0205	0.013
Na23	13.09	13.2	3.17	0	0	0	0	0	0	0	0
Mg25	0.00326	0.00325	0.1483	0	0	0	0	0	0	0	0
Al27	0.773	0.779	5.59	0	0	0	0	0	0	0	0
Si29	2.05	2.06	1.688	0.00005	0.00004	0.00001	0.00001	0.00001	0.00002	0.00002	0.00001
P31	0.15	0.148	0.57	0	0	0.00028	0.00028	0.00026	0.00153	0.00151	0.00154
K39	0.576	0.563	19.22	0.0003	0	0	0	0	0	0	0
Ca42	6.09	6.03	3.75	0.00036	0	0	0	0	0	0	0
Ca43	6.06	6.06	3.78	0	0	0	0	0	0	0	0
Sc45	51.49	50.55	3.77	0	0	0	0	0	0	0	0
Ti49	0.668	0.659	19.73	0	0	0	0	0	0	0	0
V51	5.28	5.1	5.06	44.29	44.29	22.02	22.02	22.02	22.02	22.02	22.02
Cr53	0.1029	0.1009	0.00395	0.00001	0.00001	0	0	0	0	0	0
Mn55	0.1487	0.1459	0.514	0	0	0	0	0	0	0	0
Fe57	0.0017	0.0016	0.298	0	0	0	0	0	0	0	0
Co59	0.538	0.521	0.0492	0	0	0	0	0	0	0	0

Ni60	0.0274	0.0264	0.00075	0	0	0	0	0	0	0	0	0	0	0
Ni62	0.0274	0.0263	0.00092	0	0	0	0	0	0	0	0	0	0	0
Cu63	2.6	2.522	0.1089	0.00005	0.0001	0.00002	0.00003	0.00006	0	0.00001	0	0	0	0
Cu65	2.564	2.557	0.1057	0.00006	0.00049	0.00004	0.00003	0.00006	0.00003	0.00002	0	0	0	0
Zn66	0.998	0.977	0.325	0.00003	0.00003	0	0	0.00002	0	0	0	0	0	0
Ga69	29.25	28.36	3.46	0	0	0	0	0	0	0	0	0	0	0
Ga71	29.22	28.39	1.507	0	0	0.00685	0.00669	0.0068	0.0056	0.00534	0.00541	0.00541	0.00541	0.00541
Ge72	8.96	8.68	0.1291	0	0	0.00393	0.00401	0.00414	0.0032	0.00328	0.00321	0.00321	0.00321	0.00321
As75	113.12	107.93	0	0	0	0.0401	0.0382	0.039	0.0307	0.0319	0.0293	0.0293	0.0293	0.0293
Rb85	127.53	122.28	14.44	0	0	0	0	0	0	0	0	0	0	0
Sr86	42.68	40.85	26.75	0	0	0	0	0	0	0	0	0	0	0
Sr88	42.76	40.79	26.92	0.00016	0.00015	0	0	0.00003	0	0	0	0	0	0
Y89	205.62	194.05	13.21	3201.5	3212.33	0.0543	0.0545	0.0539	0.829	0.824	0.813	0.813	0.813	0.813
Zr90	81.69	77.03	29.33	0.01443	0.01411	0.00074	0.00061	0.00068	0.00177	0.00168	0.00157	0.00157	0.00157	0.00157
Nb93	1148.3	1087.54	29.06	0	0.00196	0	0	0	0	0	0.0009	0.0009	0.0009	0.0009
Mo95	278.43	267.36	172.65	0	0	0	0	0	0.01407	0.01229	0.01312	0.01312	0.01312	0.01312
Cs133	1334.04	1253.35	4.21	0	0	0	0	0	0	0	0	0	0	0
Ba137	128.65	120	185.86	0	0	0	0.00136	0.00121	0.0207	0.00737	0.00686	0.00782	0.00782	0.00782
La139	1294.63	1198.38	68.21	0	0	0.01981	0.0222	0.0207	0.00737	0.00686	0.00782	0.00782	0.00782	0.00782
Ce140	483.92	451.85	54.23	0.00054	0	0.0032	0.003	0.00301	0.00222	0.00209	0.00227	0.00227	0.00227	0.00227
Pr141	3255.36	3019.84	45.24	0	0	0.0477	0.0457	0.0448	0.0151	0.0159	0.0162	0.0162	0.0162	0.0162
Nd146	632.58	579.18	38.16	0	0	30.5	30.59	30.05	24.91	24.23	24.48	24.48	24.48	24.48
Sm147	2020.32	1878.52	27.22	0	0	0.0111	0.0081	0.0108	0.0192	0.022	0.0163	0.0163	0.0163	0.0163
Eu153	5476.35	5120.48	22.7	0.0238	0.0196	0.0627	0.053	0.0595	0.418	0.427	0.427	0.427	0.427	0.427
Gd157	1419.5	1323.38	19.64	0	0	0.149	0.1469	0.1475	0.1671	0.1746	0.1712	0.1712	0.1712	0.1712
Tb159	7940.1	7330.29	15.79	0.0961	0.1173	0.0735	0.0728	0.0686	0.0675	0.0678	0.0688	0.0688	0.0688	0.0688
Dy161	1161.83	1075.91	14.53	0	0	0.00544	0.0067	0.00483	0.0178	0.0175	0.0164	0.0164	0.0164	0.0164
Ho165	5516.23	5050.29	13.54	0.0098	0.011	0.0086	0.0086	0.0086	0.0086	0.0086	0.0086	0.0086	0.0086	0.0086
Er167	1788.06	1633.8	12.27	0	0.0086	0.191	0.192	0.187	0.0139	0.018	0.0138	0.0138	0.0138	0.0138
Tm169	12336.15	11277.6	12.11	0	0	0.0363	0.0338	0.0289	0.109	0.1035	0.1089	0.1089	0.1089	0.1089
Yb173	1942.07	1779.44	12.99	0	0	14.86	14.9	14.57	15.4	15.13	15.34	15.34	15.34	15.34
Lu175	11959.98	10876.55	11.56	0	0	3.42	3.35	3.32	3.63	3.62	3.65	3.65	3.65	3.65
Hf178	2455.35	2215.86	23.44	0	0	0.0254	0.0248	0.0251	0.0323	0.0291	0.0284	0.0284	0.0284	0.0284
Ta181	15295.31	13724.81	22.53	0.135	0.0112	0	0	0	7.71	1.9	3.26	3.26	3.26	3.26

W182	5251.38	4763.77	5.44	0	0	0	0.00294	0.00066	0.00213	0	0.0204	0.0224	0.0243
Pb208	121.81	105.72	2.86	0.00041						0.00126	0.00044	0	0.00054
Th232	11699.12	9715.03	126.41	0	0.0085	0	0.0085	0	0	0	0	0	0
U238	41573.06	34243.7	133.97	0	0.0254	0	0.0254	0	0	0.0155	0.189	0.181	0.209
GLITTER!: Mean Raw CPS background subtracted.													
Element	STD610-05	STD610-06	BCR2-02	YVO-2	YVO-3	GDVO-1	GDVO-2	GDVO-3	NGGDVO-1	NGGDVO-2	NGGDVO-3		
Li7	167798	181358	3643	116	96	50	17	37	601	659	563		
Be9	24690	25939	110	0	0	0	0	0	0	0	0		
B11	27073	28785	622	137	153	195	218	163	267	389	241		
Na23	36222144	35368860	8338409	0	0	0	0	559	0	0	0		
Mg25	13756	13303	595991	0	0	64	53	19	64	51	84		
Al27	2345379	2292194	16139892	0	0	440	0	0	0	0	0		
Si29	1821947	1778324	1427727	2895	2265	1659	868	1320	1881	2055	1415		
P31	9375	8977	34273	0	7	2214	2201	2048	12257	12504	12565		
K39	190817	180577	6049790	6242	276	0	0	0	0	0	0		
Ca42	261974	251304	153435	951	80	0	0	0	0	0	0		
Ca43	56739	55043	33703	36	0	2	42	0	0	6	38		
Sc45	189543	180363	13202	38	1	0	0	44	0	9	38		
Ti49	10416	9956	292533	3	4	11	1	0	25	0	0		
V51	169971	159060	154554	88493544	86222680	88545952	87795704	86166520	88430424	91035112	89422456		
Cr53	14447	13736	527	57	58	0	0	0	0	12	0		
Mn55	210255	199951	690404	0	0	0	0	0	0	28	0		
Fe57	5070	4626	844776	83	0	0	0	0	0	0	0		
Co59	141564	132736	12290	0	9	0	14	0	19	0	0		
Ni60	32370	30264	840	0	0	15	0	5	0	6	0		
Ni62	4724	4387	149	15	15	5	0	0	0	8	0		
Cu63	78786	74332	3155	90	180	95	101	238	32	50	17		
Cu65	36987	35827	1455	54	427	64	54	113	59	34	26		
Zn66	22133	21001	6854	36	37	22	17	53	7	9	4		
Ga69	160919	151032	18044	0	0	14	23	9	4	6	23		
Ga71	108478	102041	5308	16	1	3173	3069	3060	2588	2540	2526		
Ge72	49818	46811	683	11	0	2752	2786	2826	2244	2375	2286		
As75	17952	16592	9	0	20	796	751	753	609	652	588		

Rb85	230712	214160	24780	0	0	0	0	22	0	0	7	19	7
Sr86	41050	38076	24455	55	0	0	0	0	0	0	0	14	0
Sr88	355243	328458	212632	83	76	0	0	11	31	16	22	21	
Y89	334296	305994	20454	324750336	317889440	11123	11075	11075	10765	170124	174254	169113	
Zr90	153819	140610	52538	1692	1614	174	144	144	156	418	409	377	
Nb93	258245	237007	6210	13	26	10	0	0	0	6	0	25	
Mo95	42572	39584	25053	10	0	13	0	0	6	267	240	252	
Cs133	369328	335417	1103	0	0	2	12	12	0	0	0	15	
Ba137	55625	50278	76371	0	16	12	73	73	63	0	2	2	
La139	438780	393604	21975	3	10	842	934	934	858	313	300	336	
Ce140	466884	421871	49596	32	19	383	357	357	351	265	257	273	
Pr141	590513	530637	7794	0	5	1082	1028	1028	990	341	371	370	
Nd146	99262	88036	5686	0	8	598977	595679	595679	574154	488344	489070	485179	
Sm147	83893	75582	1074	10	0	57	41	41	54	99	117	85	
Eu153	318987	288621	1253	86	68	454	380	380	418	3013	3167	3111	
Gd157	84348	76129	1107	0	10	149781232	148140784	148140784	144736176	152098976	155350464	155099856	
Tb159	588762	526338	1111	442	526	1380	1348	1348	1328	1543	1659	1598	
Dy161	104866	93990	1243	2	15	826	810	810	749	756	781	777	
Ho165	582542	516030	1354	63	70	71	86	86	61	232	235	216	
Er167	134873	119279	877	23	39	1797	1789	1789	1712	130	173	130	
Tm169	581291	514207	540	16	14	213	196	196	164	636	620	641	
Yb173	100063	88663	633	6	3	95020	94311	94311	90325	97801	98760	98149	
Lu175	581942	511907	532	11	0	20705	20069	20069	19472	21834	22360	22108	
Hf178	170885	149136	1543	16	16	219	211	211	210	277	256	245	
Ta181	575385	498966	801	312	25	10	0	0	0	35554	8979	15136	
W182	131251	114890	128	16	8	19	23	23	12	61	69	73	
Pb208	282824	236267	6228	57	404	186	591	591	340	121	12	148	
Th232	619260	496083	6302	12	26	8	0	0	10	14	18	0	
U238	697002	552817	2107	16	25	0	0	0	30	377	369	415	

Appendix D

Publications

Published works related to the thesis

1) Jonas Jakutis Neto, Fabíola de Almeida Camargo, and Niklaus Ursus Wetter, “**Deep Blue Nd:LiYF₄ Laser in Quasi-Continuous and Continuous Operation**,” Conference Paper Advanced Solid-State Photonics (ASSP) San Diego, California, ATuA12 (2010).

Deep blue Nd:LiYF₄ laser in quasi-continuous and continuous operation

Jonas Jakutis Neto, Fabíola de Almeida Camargo and Niklaus Ursus Wetter

Centro de Lasers e Aplicações, Instituto de Pesquisas Energéticas e Nucleares, 055508-000 São Paulo/SP, Brazil

Author e-mail address: nuwetter@gmail.com

Abstract: In this work we present continuous and quasi-continuous operation of Nd:YLF operating at 908 nm and frequency conversion to 454 nm using LBO and BiBO nonlinear crystals with different sizes.

@2010 Optical Society of America

OCIS codes: (140.3580) Lasers, solid state; (140.3530) Lasers, neodymium; (140.3480) Laser, diode-pumped; (140.3515) Lasers, frequency doubled; (140.7300) Visible Lasers.

1. Introduction

Lasers operating in the blue spectral range have been studied for many years around the world especially due to applications in data storage and display technology. RGB displays demand deep blue wavelengths to expand the color gamut which is the area inside a polygon formed by the linkage of three or more points (wavelengths), in the CIE 1976 diagram to obtain more combinations of colors. Data storage applications benefit from the lower wavelength to increase the storage capacity on compact disks.

One of the many possibilities to achieve blue wavelength is the intracavity frequency doubling of neodymium doped crystals operating on quasi-three level transition lines. Neodymium solid state lasers operating on the three level transition ${}^4F_{3/2} \rightarrow {}^4I_{9/2}$ generally use the highest fundamental stark level as lower laser level to generate photons between 900 nm and 950 nm, which can be efficiently converted to the blue spectral range between 450 nm and 475 nm by intracavity frequency doubling. A maximum blue output power of 14.8 W at 456 nm was reported using Nd:GdVO₄ [1]. Different wavelength with less output power in the blue have been demonstrated using other crystals such as Nd:YAG and Nd:YVO₄ [2,3]. In most cavity designs a folded mirror cavity was employed that produces two waists, one in the laser crystal and other smaller one in the doubling crystal, which improves the conversion efficiency for the SHG. In almost all cases the output power of these lasers is limited by the onset of resonator instability due to the strong thermal lens inside the active media.

A deeper blue emission at 451.5 nm and 454 nm may be achieved with neodymium doped yttrium-lithium-fluoride (Nd:YLF), which is a well known birefringent laser media (and therefore naturally polarized) that shows strong emission lines at 1053nm and 1047nm. Additionally it has another advantage for this specific application, which is its very weak thermal lensing due to the combination of a negative index lens and positive end face bulging. In Nd:YLF, the transition ${}^4F_{3/2} \rightarrow {}^4I_{9/2}$ generates photons of lower wavelength when compared to other neodymium doped crystals working also on the highest fundamental Stark level. The wavelength of the fundamental σ -polarization is 908 nm and of the π -polarization is 903 nm. The transition cross-section of both fundamental wavelengths is approximately $1 \times 10^{-20} \text{ cm}^2$, which is roughly 15 and 20 times smaller than the respective cross-section at the four-level transition of 1053 nm and 1047 nm [4]. Laser action in continuous wave operation (cw) has been reported on both transitions with 1 W and 0.6 W at 908 nm and 903 nm, respectively [5]. Blue laser with 270mW in cw operation at 454 nm was obtained using an L cavity and a 5mm long LBO crystal [6].

In this work we present continuous and quasi-continuous operation of Nd:YLF operating at 908 nm and frequency conversion to 454 nm using LBO and BiBO nonlinear crystals with different sizes.

2. Laser setup

A linear cavity set-up with a curved pump mirror (ROC=100 mm) and another flat mirror, both highly reflective ($R > 99.8\%$) at 908 nm and anti-reflection coated at 1047/1053 nm, 805 nm and 454 nm was employed (Fig.1). For the pump source, a fiber coupled diode laser of 50 W maximum output power was used whose fiber had 100 μm diameter and NA of 0.22 (Apollo Instruments). Two doublets with focal

length of 50 mm and 200 mm were used to focus the fiber output into the crystal providing a focus of 450 μm spot size inside the crystal. For quasi-continuous operation (qcw) the diode laser was temperature tuned (31°C) to 805.7 nm using re-circulating chiller. The Nd:YLF crystal, used during the qcw experiments, had dimensions of $3\times 3\times 10\text{ mm}^3$ and a Nd^{3+} concentration of 0.7 at% in order to reduce the pump absorption and up-conversion losses inside the crystal. All crystals were AR coated at 454nm, 908nm, 1047/1053 nm and the pump wavelength of 806 nm. A total of 90% of the pump radiation was absorbed inside the crystal. A total of 90% of the pump radiation was absorbed inside the crystal.. Pulses of 2 ms duration and duty cycle of 3% were used. For continuous wave (cw) operation the diode laser was temperature tuned to 802 nm (20°C) and a 15 mm long crystal was used in order to decrease the total absorption to 83% and distribute the heat load more uniformly throughout the crystal. All crystals were AR coated at 454 nm, 908 nm, 1047/1053 nm and the pump wavelength of 806 nm.

The SHG was studied using two different type I nonlinear crystals, BiBO and LBO, as well as different lengths, 10, 15 and 20mm. The nonlinear crystal was placed near the flat mirror where the beam waist was smaller, around $125\mu\text{m}$ for the 4 cm long cavity, in order to obtain a better conversion. Detection was achieved using a blue band-gap filter (BG40) and a thermopile detector (COHERENT Corp., model PS-19).

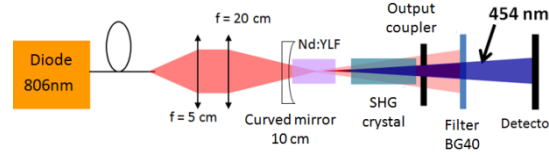


Fig. 1: Laser cavity set-up. A blue band gap filter (BG40) was used to block the infrared radiation from the detector.

3. Results

Laser operation at 908 nm was characterized using an intracavity Brewster plate on a rotation stage. Using the extra-cavity measured reflectivity of the Brewster plate as a function of rotation angle we determined the maximum output power as a function of effective reflectivity.

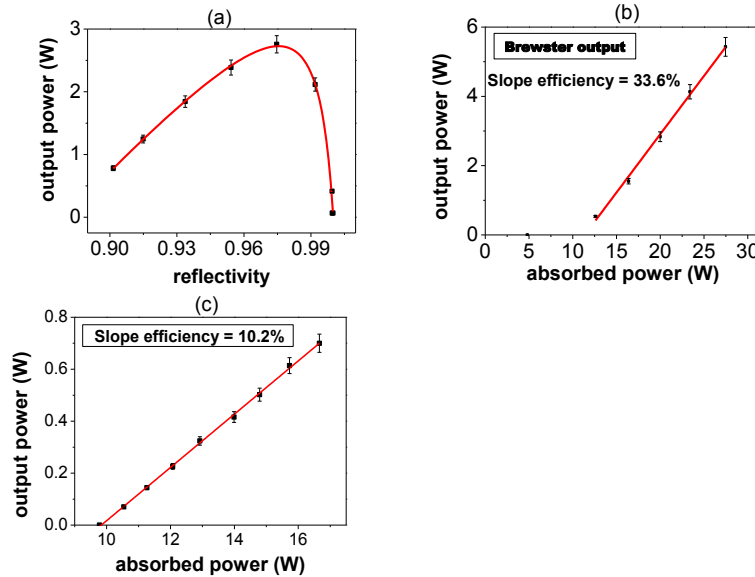


Fig. 2. (a)) output power as function of effective mirror reflectivity, (b) slope efficiency in qcw operation. (c):slope efficiency in cw operation.

In qcw operation a maximum peak output power of 5.5 W were achieved for a total Brewster plate reflectivity of 2.5%. The respective slope efficiency is 33.6%. In cw operation, using the longer crystal

and pump wavelength of 802 nm, a slope efficiency of 10.2% and output power of 700 mW were achieved at 16.5 W of absorbed pump power (Fig. 2c).

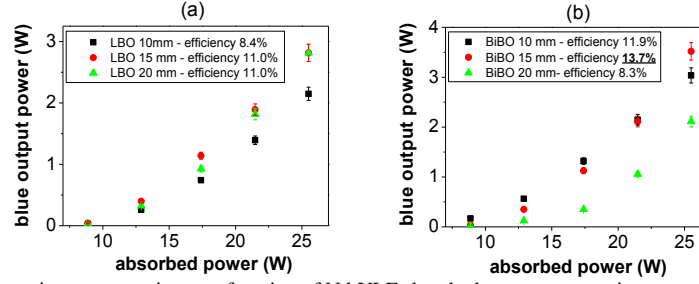


Fig. 3. Blue output power in qcw operation as a function of Nd:YLF absorbed pump power using crystals of different size, (a) LBO and (b) BiBO.

Using LBO we achieved the best results with crystal length of 15 mm and 20 mm. In this case the conversion efficiency was 11% (Fig. 3a). Using BiBO the best result was with a 15 mm long crystal and the efficiency was 13.7% (Fig. 3b).

In the cw regime, using the 15 mm-long BiBO crystal, 200 mW at 454 nm were obtained (Fig. 4a). The theory for the second harmonic generation for a gaussian beam using type I crystals results in a conversion efficiency Γ of [7,8].

$$\Gamma = \frac{P_{2\omega}}{P_{\omega}^2} = \frac{2\omega^2 d_{\text{eff}}^2}{\pi \epsilon_0 c^3 n_{\omega}^2 n_{2\omega}} L k_{\omega} h(\sigma)$$

$$h(\sigma) = \frac{1}{2l} \cdot \int_{-l/2}^{l/2} \int_{-l/2}^{l/2} d\tau d\tau' \frac{\exp[-\beta^2(\tau - \tau')^2 - i\sigma(\tau - \tau')]}{(1 + i\tau)(1 - i\tau')}$$

$$\beta = \frac{\rho z_R}{w_0}, \quad l = \frac{L}{z_R}, \quad z_R = \frac{1}{2} k_{\omega} w_0^2, \quad k_{\omega} = \frac{2\pi n_{\omega}}{\lambda_{\omega}}$$

Where d_{eff} is the effective nonlinear coefficient, n is the refraction index, L is the nonlinear crystal length and w_0 is the beam waist inside the nonlinear crystal. The parameter σ is the normalized wave vector mismatch given by $\Delta k z_R$. The mismatch and walk off effects appear in the h function (where ρ is the walk off angle). Using this theory it is possible to simulate the conversion efficiency of a 15 mm long BiBO in function of different beam waists, Fig. 4.

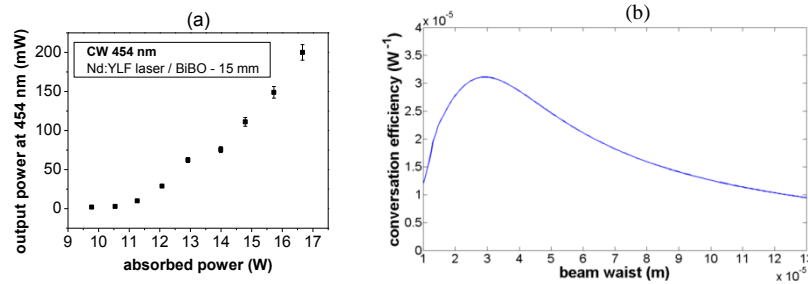


Fig. 4. (a) Output power in the blue during cw operation and (b) simulation of the conversion efficiency.

4. Discussion and conclusion

As in our experimental setup a linear cavity was used, the beam waist inside the nonlinear crystal was relatively large, around 125 μm , giving low conversion efficiency. In the literature a maximum of 270 mW was obtained in the deep blue using a Nd:YLF pumped at 792 nm and a 5 mm-long LBO as nonlinear crystal with a beam waist of 41 μm [4]. In order to obtain a higher power in the blue emission we intend to make a L cavity to achieve smaller waists. This should result in a 3 times higher efficiency. The qcw blue output power of 3.5 W was obtained in this research and it is the highest reported so far.

5. References

- [1] Z. Quan, Y. Yi, L. Bin, Z. Kai, L. Yang, and Z. Ling, "Experimental study of the generation of a blue laser by intracavity frequency doubling of a cw Nd:GdVO₄ laser with lithium borate," *Applied Optics* **48**(16), 2979-2982 (2009).
- [2] Y. Chen, H. Peng, W. Hou, Q. Peng, A. Geng, L. Guo, D. Cui, and Z. Xu, "3.8 W of cw blue light generated by intracavity frequency doubling of a 946-nm Nd:YAG laser with LBO," *Applied Physics B* **83**, 241-243 (2006).
- [3] Q. H. Xue, Q. Zheng, Y. K. Bu, F. Q. Jia, and L. S. Qian, "High-power efficient diode-pumped Nd:YVO₄/LiB₃O₅ 457 nm blue laser with 4.6 W of output power," *Optics Letters* **31**, 1070-1072 (2006).
- [4] S. Spiekermann, "Compact diode-pumped solid-state lasers," Doctoral Thesis (Laser Physics and Quantum Optics, Department of Physics, The Royal Institute of Technology, Stockholm, Sweden 2004)
- [5] S. Spiekermann and F. Laurell, "Continuous wave and Q-switched operation of diode pumped quasi-three level Nd:YLF lasers", *Advanced Solid State Lasers* **34**, 60-62 (2000).
- [6] M. Pierrou and F. Laurell, "Efficient blue-light generation through intracavity frequency doubling of cw Nd:YAG and Nd:YLF lasers", *Conference on Lasers and Electro-Optics, CLEO*, 387 (1998).
- [7] J. J. Zondy, D. Touahri, and O. Acef, "Absolute value of the d_{36} nonlinear coefficient of AgGaS₂: prospect for a low-threshold doubly resonant oscillator-based 3:1 frequency divider," *Journal of Optical Society of America B* **14**, 2481-2497 (1997).
- [8] R. Sarrouf, T. Badr, and J. J. Zondy, "Intracavity second-harmonic generation of diode -pumped continuous-wave, single-frequency 1.3 μ m Nd:YLiF₄ lasers," *Journal of Optics A: Pure and Applied Optics* **10**, 104011-104021 (2008).

2) Andrew Lee, Jonas Jakutis Neto and Helen Margaret Pask, “**Generation of combs of wavelengths in the infrared and visible using cascaded stimulated Raman scattering in potassium titanyl phosphate,**” Conference proceedings of the Quantum Electronics Conference & Lasers and Electro-Optics (CLEO/IQEC/PACIFIC RIM), Sydney, NSW, 1247-1249 (2011).

Generation of combs of wavelengths in the infrared and visible using cascaded stimulated Raman scattering in potassium titanyl phosphate

Andrew. J. Lee¹, Jonas Jakutis-Neto^{1,2} and Helen. M. Pask¹

¹*MQ Photonics Research Centre, Department of Physics and Astronomy, Macquarie University, Australia*

²*Instituto de Pesquisas Energéticas e Nucleares, CNEN/SP, Universidade de São Paulo, CEP 05508-000, São Paulo/SP, Brazil*
Presenting author e-mail address: andrew.lee@mq.edu.au

Abstract: We report the generation of a comb of emission wavelengths in the near-infrared, and wavelength-tunable emission at up to five discrete wavelengths in the visible between 534 nm and 572 nm by making use of cascaded stimulated Raman scattering in potassium titanyl phosphate in combination with Nd:GdVO₄ and Nd:YLF laser crystals.

1. Introduction

Stimulated Raman scattering (SRS) in crystalline materials is an established method of wavelength converting laser systems and it has been demonstrated with great efficiency in vanadates, tungstates and molybdates in both pulsed and continuous-wave modalities [1,2,3]. Potassium Titanyl Phosphate (KTP) is a well known crystal which features high second and third-order nonlinearities and it is often used for frequency-doubling, parametric generation and electro-optic modulation [4]. The application of KTP as a Raman-shifting medium has however, received relatively little attention, with the only published work (to the best of our knowledge) being that of Chen [5], where he demonstrated operation of a Q-switched laser using Nd:YAG as the laser medium and an x-cut KTP crystal as the Raman medium. In contrast with other Raman-active crystals such as vanadates, tungstates and molybdates, KTP has a strong Raman-shift at a low wavenumber, 270 cm⁻¹ with secondary shifts at 214 cm⁻¹ and 694 cm⁻¹. By cascading this strong Raman shift it is therefore possible to generate a comb of closely spaced wavelengths in the infrared. Then, by using intracavity sum-frequency and second-harmonic generation (SFG and SHG), it is also possible to generate a comb of wavelengths in the visible.

In this work, we examine the performance of KTP as an intracavity SRS medium in a continuous-wave (CW) laser. We examine its use with two different laser crystals, Nd:GdVO₄ and Nd:YLF. Nd:GdVO₄ was chosen for its polarised emission and its high emission cross-section. Nd:YLF was investigated as an alternative to Nd:GdVO₄ due to its weak thermal lens, and because it is not Raman-active.

2. Experimental Setup

For both combinations of crystals, Nd:GdVO₄/KTP and Nd:YLF/KTP, we investigated power scaling performance using two resonators, one to generate cascaded Stokes emission, and the other to generate visible emission. The general resonator layout is shown in Figure 1, and the resonator elements are summarised in Table 1.

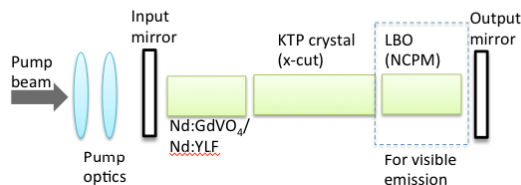


Fig 1: General resonator layout used in this work.

Table 1: Summary of resonator elements

Pump Source (fibre-coupled)	Nd:GdVO ₄ systems: 879 nm, 25 W, 200 µm core diameter. Pump spot diameter~ 460 µm. Nd:YLF systems: 881 nm, 50 W, 100 µm core diameter. Pump spot diameter ~ 500 µm.
Nd:GdVO ₄	0.3 at. % Nd-doped, 4×4×10 mm, AR/AR coated, R<0.1 % @ 1063-1190 nm.
Nd:YLF	1 at. % Nd-doped, 4×4×15 mm, AR/AR coated, R<0.45 % @ 1054-1190 nm.
KTP	x-cut, 4×4×20 mm, AR/AR coated, R<0.48 % @ 1054-1190 nm.
Lithium Triborate (LBO)	Non-critically phase-matched (NCPM), $\Theta=90^\circ$, $\Phi=0^\circ$, 4×4×10 mm, AR/AR coated, R<0.09 % @ 1054-1180 nm. Note: This was inserted into the resonator to generating visible emission.
Input Mirror	Nd:GdVO ₄ system: flat, R>99.97 % @ 1063 nm/ R >99.993 % @ 1173-1308 nm. Nd:YLF system: 400 mm radius of curvature (ROC), R>99.992 % @ 1054 nm-1173 nm.
Output Mirror	Nd:GdVO ₄ and Nd:YLF, Stokes systems: 250 mm ROC, R=99.91 % @ 1054 nm/1064 nm, R=99.4 % @ 1173 nm. Nd:GdVO ₄ visible systems: 100 cm ROC, R>99.997 % @ 1063 nm/ R >99.993 % @ 1173-1308 nm. Nd:YLF visible system: 200 mm ROC, R>99.992 % @ 1054 nm-1173 nm.

The resonators used with the Nd:GdVO₄/KTP combination were plano-convex, and were kept as short as possible to help offset the strong positive thermal lens generated in the Nd:GdVO₄ laser crystal. In contrast, due to the weaker thermal lens generated in the Nd:YLF crystal, the resonators formed using the Nd:YLF/KTP combination were concave-concave and featured spacing of 4 mm between the input mirror and the Nd:YLF crystal, and 10 mm between the Nd:YLF and KTP crystals in order to maintain good pump overlap and mode-match within the KTP crystal. Visible emission was obtained by temperature-tuning the LBO crystal (NCPM).

The Stokes output was separated from the residual fundamental emission using a long-pass filter and similarly, a short-pass filter was used to isolate the visible emission from the infrared. A fibre-coupled spectrometer (Ocean Optics HR 4000/USB2000) was used to monitor the emission from each resonator as the incident pump power was increased, this was also used to help determine the thresholds for emission at each wavelength.

3. Results/Discussion

Nd:GdVO₄/KTP System

Results obtained from the Stokes and visible resonators are summarised in Table 2.

Table 2: Summary of output powers achieved from the Stokes and visible resonators using Nd:GdVO₄/KTP

Wavelength (nm)	Threshold Pump Power (W)- Absorbed	Max Output Power (mW)
1063.0 nm (Fundamental)	0.397	676
1065.0 nm (Fundamental-orthogonal pol)	8.72	694
1094.3 nm (1st-Stokes 270 cm ⁻¹)	2.09	468
1127.4 nm (2nd-Stokes 270 cm ⁻¹)	3.08	587
1147.8 nm (1st-Stokes 690 cm ⁻¹)	4.49	115
1165.6 nm (3rd-Stokes 270 cm ⁻¹)	9.57	< 20 mW
1173 nm (self-Raman 1063 nm line)	5.34	< 20 mW
1175.8 nm (self-Raman 1065 nm line)	9.71	< 20 mW
539.3 nm (SFM fund+1st-Stokes)	1.95	183
547 nm (SHG 1st Stokes)	2.37	542
555.4 nm (SFM 1st+2nd-Stokes)	4.07	78
563.7 nm (SHG 2nd-Stokes)	3.78	62
572.35 nm (SFM 2nd+3rd Stokes)	4.34	35

The Stokes resonator exhibited a low fundamental (1063 nm) emission threshold of 0.397 W and progressively higher thresholds of 2.1 W, 3.1 W and 9.6 W for first, second and third-Stokes respectively. Maximum emission of 468 mW at the first-Stokes (1094 nm) and 587 mW at the second-Stokes (1127.4 nm) was achieved. In addition to the fundamental and cascaded-Stokes emission lines, other lines at 1065 nm (fundamental emission wavelength for the orthogonal polarisation of Nd:GdVO₄), 1147.8 nm (first-Stokes generated by the 694 cm⁻¹ line), 1173 nm (self-Raman of the 1063 nm fundamental) and 1175.8 nm (self-Raman of the 1065 nm fundamental) were observed. These additional lines occurred at pump powers above the threshold for first-Stokes and were found to oscillate in competition with the cascaded Stokes orders. This competition is a subject of our ongoing research.

The maximum power emitted in the visible was 542 mW, achieved at 547 nm (the SHG of the first-Stokes). As the number of Stokes orders increased with the incident pump power (due to cascaded SRS), it became increasingly difficult to achieve emission at a single visible wavelength, and the resonator became increasingly unstable, as evidenced by a rapid decrease in output power. The resonator also operated highly multi-mode. We were unable to generate emission at the second-harmonic of the third-Stokes order because the temperature which the LBO had to be tuned to was very close to that required for second-harmonic generation of the Nd:GdVO₄ self-Raman line (first-Stokes).

Nd:YLF/KTP System

In light of the significant competition effects we observed when using Nd:GdVO₄ with the KTP crystal, we investigated the application of Nd:YLF as the active laser medium because it is not Raman-active. Results obtained from the Stokes and visible resonators are summarised in Table 3.

Table 3: Summary of output powers achieved from the Stokes and visible resonators using Nd:YLF/KTP

Wavelength (nm)	Threshold Pump Power (W)- Absorbed	Max Output Power (mW)
1053 nm (Fundamental)	0.55	831
1084 nm (1 st -Stokes 270 cm ⁻¹)	5.91	173
1117 nm (2 nd -Stokes 270 cm ⁻¹)	10.98	16
534.5 nm (SFG Fund and 1 st -Stokes)	1.945	200
542 nm (SHG 1 st -Stokes)	2.64	130
558 nm (SHG 2 nd -Stokes)	12.37	5

The lasing thresholds using Nd:YLF were higher, and the overall emitted powers lower, in comparison to the Nd:GdVO₄/KTP system. This was due to the fact that the round-trip resonator losses at the fundamental (1053 nm), first (1084 nm) and second (1117 nm) Stokes wavelengths were approximately 2.5 times higher than that in the Nd:GdVO₄-based system. The maximum incident pump power used was also lower in comparison to that used in the Nd:GdVO₄/KTP system, due to potential damage to the crystal. Despite the lower overall output power from both the Stokes and visible resonators, the emission spectra were significantly cleaner than that obtained from the Nd:GdVO₄/KTP system, with the absence of orthogonally polarised fundamental emission and self-Raman lines. Our ongoing work is focussed on reducing the round-trip losses within the Nd:YLF/KTP based resonator, and increasing the overall output power at each visible wavelength.

3. Conclusion

We have demonstrated the generation of a span of emission wavelengths in the near-IR and the visible by making use of cascaded SRS in KTP. When used with Nd:GdVO₄ as the laser medium, it was possible to generate emission at the third Stokes-order, and wavelength selectable visible emission at five discrete wavelengths in the visible between 539 and 573 nm. Maximum output power was limited by the onset of additional fundamental emission lines and self-Raman generation in the Nd:GdVO₄ crystal. When KTP was combined with Nd:YLF as the laser medium, we were able to generate cascaded Stokes emission to the second Stokes-order, and visible emission at three discrete lines between 534 and 558 nm. While the maximum output power at each wavelength was limited, the spectral purity was excellent with no undesired lines being observed. We anticipate that improved performance will be obtained when the system is optimised for lower loss.

4. References

- [1] A. J. Lee, D. J. Spence, J. A. Piper and H. M. Pask, "A wavelength-versatile, continuous-wave, self-Raman solid-state laser operating in the visible," *Opt. Expr.* **18**, 20013-20018 (2010).
- [2] Z. H. Cong, X. Y. Zhang, Q. P. Wang, Z. J. Liu, S. T. Li, X. H. Chen, X. L. Zhang, S. Z. Fan, H. J. Zhang, and X. T. Tao, "Efficient diode-end-pumped actively Q-switched Nd:YAG/SrWO₄/KTP yellow laser," *Opt. Lett.* **34**, 2610-2612 (2009).
- [3] A. J. Lee, H. M. Pask, J. A. Piper, H. J. Zhang, and J. Y. Wang, "An intracavity, frequency-doubled BaWO₄ Raman laser generating multi-watt continuous-wave, yellow emission," *Opt. Express* **18**, 5984-5992 (2010).
- [4] J. D. Bierlein and H. Vanherzele, "Potassium titanyl phosphate: properties and new applications," *J. Opt. Soc. Am. B*, **6**, 622-633, (1989).
- [5] Y. F. Chen, "Stimulated Raman scattering in a potassium titanyl phosphate crystal: simultaneous self-sum frequency mixing and self-frequency doubling," *Opt. Lett.* **30**, 400-402, (2005).

3) Jonas Jakutis Neto, Jipeng Lin, Andrew Lee, Huaijin Zhang, Jiyang Wang, Niklaus Ursus Wetter and Helen Pask, “**High beam quality cw 1.5 W BaWO₄ Raman laser using Nd: YLF as laser active medium,**” Conference proceedings of the Quantum Electronics Conference & Lasers and Electro-Optics (CLEO/IQEC/PACIFIC RIM), Sydney, NSW, 306-308 (2011).

High beam quality cw 1.5 W BaWO₄ Raman laser using Nd:YLF as laser active medium

Jonas Jakutis Neto^{1,2}, Jipeng Lin¹, Andrew J. Lee¹, Huaijin Zhang³, Jiyang Wang³, Niklaus Ursus Wetter² and Helen Pask¹

1. MQ Photonics Research Centre, Department of Physics, Macquarie University, Sydney, NSW 2109, Australia
2. Instituto de Pesquisas Energéticas e Nucleares, CNEN/SP, Universidade de São Paulo, CEP 05508-000, São Paulo/SP, Brazil
3. State Key Laboratory of Crystal Materials and Institute of Crystal Materials, Shandong University, Jinan, 250100, PR China
jonas.jakutis-neto@mq.edu.au

Abstract: 1.5 W of 1st Stokes, 1167 nm, cw output power was produced using a Nd:YLF laser crystal associated to a BaWO₄ Raman crystal. The laser built provided a M² of 1.51 and 1.43, vertical and horizontal, respectively. This high beam quality and Watt level power laser was built in a long cavity, demonstrating the advantages of Nd:YLF, which will ultimately enable low amplitude noise Raman lasers and allowing long length cavity geometries, such as “V” shape, for better conversion efficiencies. A preliminary result for a cw 583 nm laser has delivered 0.61 W of output power.

1. Introduction

CW solid state Raman lasers have been explored during the past 6 years due to their capacity to reach new wavelengths in the near infrared as well as in the yellow-orange visible spectrum range [1-3]. Also, such lasers have demonstrated a great versatility in terms of multiple wavelength generation when further cascaded into higher Stokes orders [4]. Given that, and the fact that these lasers, in general, use similar design to the most common and efficient Nd lasers, we decided to explore different approaches in order to improve their engineering.

The main problem reported for these lasers is the strong thermal lens found in crystals like Nd:GdVO₄, Nd:YVO₄ extensively used in self-Raman configurations [1,3,5,6]. This stronger thermal lens is mostly built up from the combination of pump thermal loading and the inelastic Raman shifting process, which generates phonons during the wavelength conversion. As an alternative, Nd:YAG presents a higher thermal conductivity than Nd:YVO₄ and Nd:GdVO₄, weaker thermal lens, but it does not have polarized emission, also required for an efficient Stokes shifting.

In this paper, we explore the performance of Raman lasers using Nd:LiYF₄ (Nd:YLF). Nd:YLF provides a naturally polarized emission and a weak thermal lens. Nd:YLF has a negative dn/dT which partially compensates the positive lens generated in the crystal's face bulging. In addition, π and σ emissions have different wavelengths 1047 nm and 1053 nm, respectively, both shorter than the more conventional 1063 nm and 1064 nm, thereby providing a new range of Stokes wavelengths. A disadvantage of this crystal is the low thermal fracture limit, which limits the maximum absorbed pump power. This can be partly mitigated by using a direct pumping system, by means of a diode emitting at 881 nm instead of the usual 806 nm and 797 nm, which are the other main absorption peaks of Nd:YLF. In this case one non-radiative decay is eliminated in the lasing process, reducing the thermal loading.

In this paper we reported a high beam quality cw Nd:YLF/BaWO₄ Raman laser system, emitting at 1167 nm with a maximum output power of 1.5 W for 17 W of absorbed power. In addition, we have demonstrated second harmonic generation (SHG) of the laser, obtaining 0.61 W cw at 583 nm.

2. Experimental setup

We used a Nd:YLF crystal, 1.0 at% Nd³⁺-doped, a-cut with dimensions of 4x4x15 mm³. The length and relatively high doping concentration were chosen in order to absorb more at the direct pumping wavelength, 881 nm. Furthermore, this crystal oscillated at 1053 nm, favored by the mirrors and crystal coatings. Such line presents the weakest thermal lens compared to the 1047 nm transition, providing better stability and good beam quality for the laser even under high pump powers.

As Raman active crystal BaWO₄ was chosen because of its high Raman gain of ~8.5 cm/GW compared to KGW (~4.4 cm/GW), GdVO₄ (>4.5 cm/GW) and YVO₄ (>4.5 cm/GW) [7]. This crystal was a-cut and 25 mm long since in the steady-state regime, the Stokes field increases exponentially with the interaction path along the crystal. The Raman shift provided by BaWO₄ is 926 cm⁻¹, so then, the shift of 1053 nm is to 1167 nm.

The best cavity configuration was found to be the one using a high reflectivity (HR) flat mirror as the pump mirror and a 250 mm of radius of curvature (ROC) as the output coupler. Both mirrors have a reflectivity at 1053

nm higher than 99.9%, while the pump mirror has similar high reflectivity at 1167 nm and the output coupler has 0.4% of transmission at 1167 nm. The cavity was 240 mm long, as shown in the Figure 1.

In order to estimate the focal length of the thermal lens, the Nd:YLF was set in a high Q cavity with the same mirrors, apart the output coupler, which in this case had a 300 mm of ROC and HR($R > 99.9\%$) at 1053 nm and 1167 nm. Given this cavity, the output coupler was translated so as to vary the cavity length from 18 mm to 265 mm and the 1053 nm output power measured.

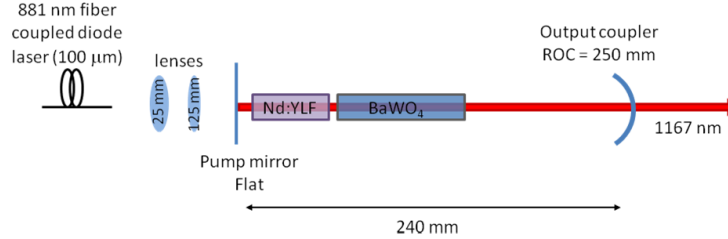


Fig. 1. Nd:YLF/BaWO₄ Raman laser setup.

This pump focusing optics delivered a pump beam waist (radius) of 250 μm and the fundamental resonator mode was slightly smaller than the pump. The mode in the Raman crystal was about 400 μm of diameter.

Finally, we tried to obtain some yellow conversion by SHG in a $4 \times 4 \times 10 \text{ mm}^3$, type I, LBO crystal cut for non-critical phase matching. As a first test, we modified the cavity to one with HR mirrors, $R > 99.99\%$ at 1053 nm and 1167 nm and high transmission at 583 nm ($T > 95\%$). Also, we changed the curvature of the mirrors, to achieve a small mode size in the doubling crystal. The pump mirror used had a ROC of 400 mm and the output coupler a ROC of 200 mm, and the cavity was 80 mm long. An intracavity mirror, antireflection coated (AR) at 1053 nm and 1167 nm and with $T > 95\%$ of reflectivity at 583 nm, was used to reflect the backward propagating yellow beam to the output of the laser.

3. Results and discussions

Figure 2(a) shows the output power at the fundamental for different, high Q, cavity lengths. The results show that the thermal lens of Nd:YLF under high Q condition is longer than 250 mm, since no rollover was noticed for a cavity of 265 mm. Hardman et. al. found a thermal lens for 1053 nm of more than 1 m when lasing for 12 W of incident pump power [8]. In our case, we could expect a slightly shorter focal length than 1 m because we pumped the crystal up to 17 W, but using a direct pumping wavelength, 881 nm, which reduces the thermal loading.

Figure 2(b) shows the output power at 1167 nm as a function of absorbed power. The Raman laser provided a maximum output power of 1.5 W operating in CW regime. The beam quality was measured using a beam scope (Beamscope P8, GENTEC) when the laser was pumped with 15 W. The result is a M^2 of 1.43 in the horizontal and 1.51 in the vertical, Figure 2(c).

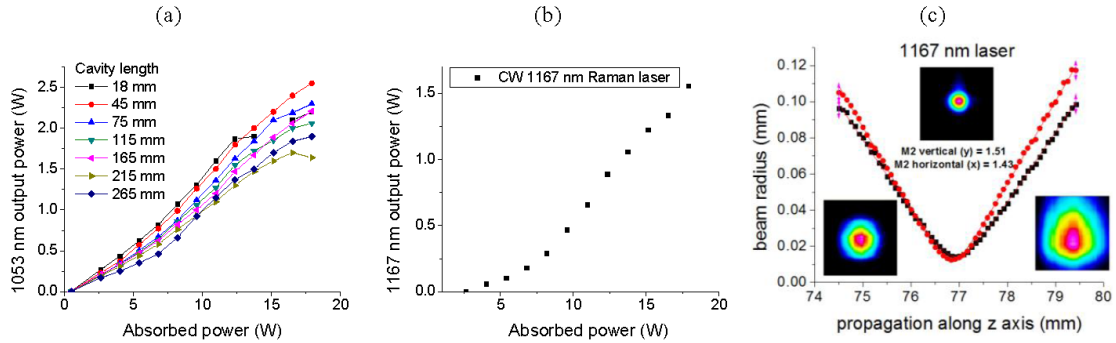


Fig. 2. (a) high Q cavity 1053 nm output powers for different cavity lengths, (b) CW 1167 nm output power as function of absorbed pump power and (c) M^2 measurement of the Raman laser with beam profiles in the near field, focus and far field.

The cavity used to produce 1.5 W at 1167 nm is considered a long cavity for Raman lasers, since the most efficient ones were based on self-Raman configurations [3,6,9], and in those cases, a strong thermal lens takes place, demanding the use of very short cavities. The advantage of a long cavity is in fact its capacity to provide more longitudinal modes, which is a feature that plays an important role for low amplitude noise lasers. Furthermore, Nd:YLF has a gain bandwidth of 358 GHz at 1053 nm compared to 344 GHz for Nd:GdVO₄, 254 GHz for Nd:YVO₄ and 119 GHz for Nd:YAG [10,11], providing naturally more longitudinal modes than the others.

The preliminary SHG test resulted in 0.61 W at 583 nm, and the corresponding laser characteristics is shown in Figure 3. A competitive oscillation between 1053 nm and 1047 nm, which was not observed when operated at 1167 nm. It happened due to the fact that now, an extra loss is introduced by the SHG to the 1053 nm line.

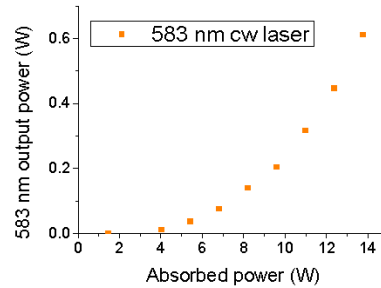


Fig. 3. 583 nm cw laser performance.

The pure oscillation of 1053 nm was possible only up to 14 W of pump power. Above 14 W, the 1047 nm line starts to oscillate, reducing the 583 nm output power. One way to overcome this problem is to introduce more losses to the 1047 nm line, as an example, a Brewster window or any low loss polarizing optics, since 1053 nm and 1047 nm have orthogonal polarizations. By solving this issue, we expect to be able to power scale the yellow emission in order to achieve multi-Watt yellow powers.

4. Conclusion

We have proved the capacity of Nd:YLF crystal to operate in long Raman laser cavities without lose stability, high power and good beam quality. Our ongoing work is aimed at obtaining very low amplitude noise Raman lasers and higher conversion efficiencies for Raman shift, second harmonic generation and sum frequency by means of “V” shaped cavities. We have also showed some preliminary cw yellow laser generation, reaching 600 mW, but limited by competition between fundamental transitions.

Acknowledgements

We are grateful to CAPES for supporting Jonas, CAPES scholar: Proc n° 5381/09-6.

4. References

- [1] Y. Lü, W. Cheng, Z. Xiong, J. Lu, L. Xu, G. Sun, and Z. Zhao, "Efficient CW laser at 559 nm by intracavity sum-frequency mixing in a self-Raman Nd:YVO₄ laser under direct 880 nm diode laser pumping," *Laser Physics Letters* **7** (11), 787-789 (2010).
- [2] Walter Lubeigt, Vasili G. Savitski, Gerald M. Bonner, Sarah L. Geoghegan, Ian Friel, Jennifer E. Hastie, Martin D. Dawson, David Burns, and Alan J. Kemp, "1.6 W continuous-wave Raman laser using low-loss synthetic diamond," *Optics Express* **19** (7), 6938-6944 (2011).
- [3] A. J. Lee, H. M. Pask, D. J. Spence, and J. A. Piper, "Efficient 5.3 W cw laser at 559 nm by intracavity frequency summation of fundamental and first-Stokes wavelengths in a self-Raman Nd:GdVO₄ laser," *Optics Letters* **35** (5), 682-684 (2010).
- [4] Andrew J. Lee, David J. Spence, James A. Piper, and Helen M. Pask, "A wavelength-versatile, continuous-wave, self-Raman solid-state laser operating in the visible," *Optics Express* **18** (19), 20013-20018 (2010).
- [5] C. Du, L. Zhang, Y. Yu, S. Ruan, and Y. Guo, "3.1 W laser-diode-end-pumped composite Nd:YVO₄ self-Raman laser at 1176 nm," *Applied Physics B: Lasers and Optics*, 1-4 (2010).
- [6] H. Y. Zhu, Y. M. Duan, G. Zhang, C. H. Huang, Y. Wei, H. Y. Shen, Y. Q. Zheng, L. X. Huang, and Z. Q. Chen, "Efficient second harmonic generation of double-end diffusion-bonded Nd:YVO₄ self-Raman laser producing 7.9 W yellow light," *Optics Express* **17** (24), 21544-21550 (2009).
- [7] J. A. Piper and H. M. Pask, "Crystalline Raman lasers," *IEEE Journal of Selected Topics in Quantum Electronics* **13** (3), 692-704 (2007).
- [8] P. J. Hardman, W. A. Clarkson, G. J. Friel, M. Pollnau, and D. C. Hanna, "Energy-transfer upconversion and thermal lensing in high-power end-pumped Nd:YLF laser crystals," *IEEE Journal of Quantum Electronics* **35** (4), 647-655 (1999).
- [9] Andrew J. Lee, Jipeng Lin, and Helen M. Pask, "Near-infrared and orange-red emission from a continuous-wave, second-Stokes self-Raman Nd:GdVO₄ laser," *Optics Letters* **35** (18), 3000-3002 (2010).
- [10] P. Bado, M. Bouvier, and J. Scott Coe, "Nd:YLF mode-locked oscillator and regenerative amplifier," *Opt. Lett.* **12** (5), 319-321 (1987).
- [11] M. Li, S. Zhao, K. Yang, G. Li, D. Li, and J. An, "Diode-pumped actively Q-switching and mode-locking Nd:GdVO₄ laser," *Laser Physics Letters* **5** (10), 722-725 (2008).

4) Jonas Jakutis Neto, Jipeng Lin, Niklaus Ursus Wetter and Helen Margaret Pask, **“Continuous-wave Watt-level Nd: YLF/KGW Raman laser operating at near-IR, yellow and lime-green wavelengths,”** Optics Express 20 (9), 9841-9850 (2012).

Continuous-wave watt-level Nd:YLF/KGW Raman laser operating at near-IR, yellow and lime-green wavelengths

Jonas Jakutis-Neto,^{1,2,*} Jipeng Lin,¹ Niklaus Ursus Wetter,² and Helen Pask¹

¹*MQ Photonics Research Centre, Department of Physics, Macquarie University, Sydney, NSW 2109, Australia*

²*Instituto de Pesquisas Energéticas e Nucleares, CNEN/SP, Universidade de São Paulo, CEP 05508-000, São Paulo/SP, Brazil*

*jonas.jakutis-neto@mq.edu.au

Abstract: A Nd:YLF/KGW Raman laser has been investigated in this work. We have demonstrated CW output powers at six different wavelengths, 1147 nm (0.70 W), 1163 nm (0.95 W), 549 nm (0.65 W), 552 nm (1.90 W), 573 nm (0.60 W) and 581 nm (1.10 W), with higher peak powers achieved under quasi-CW operation. Raman conversion of the 1053 nm fundamental emission is reported for the first time, enabling two new wavelengths in crystalline Raman lasers, 549 nm and 552 nm. The weak thermal lensing associated with Nd:YLF has enabled to achieve good beam quality, $M^2 \leq 2.0$, and stable operation in relatively long cavities.

©2012 Optical Society of America

OCIS codes: (140.3550) Lasers, Raman; (140.3580) Lasers, solid-state; (140.7300) Visible lasers; (140.3530) Lasers, neodymium.

References and links

1. A. S. Grachtchikov, V. A. Lisinetskii, V. A. Orlovich, M. Schmitt, R. Maksimenka, and W. Kiefer, "Multimode pumped continuous-wave solid-state Raman laser," *Opt. Lett.* **29**(21), 2524–2526 (2004).
2. A. A. Demidovich, A. S. Grachtchikov, V. A. Lisinetskii, V. N. Burakevich, V. A. Orlovich, and W. Kiefer, "Continuous-wave Raman generation in a diode-pumped Nd³⁺:KGd(WO₄)₂ laser," *Opt. Lett.* **30**(13), 1701–1703 (2005).
3. H. M. Pask, "Continuous-wave, all-solid-state, intracavity Raman laser," *Opt. Lett.* **30**(18), 2454–2456 (2005).
4. A. J. Lee, H. M. Pask, D. J. Spence, and J. A. Piper, "Efficient 5.3 W cw laser at 559 nm by intracavity frequency summation of fundamental and first-Stokes wavelengths in a self-Raman Nd:GdVO₄ laser," *Opt. Lett.* **35**(5), 682–684 (2010).
5. L. Fan, Y.-X. Fan, Y.-Q. Li, H. Zhang, Q. Wang, J. Wang, and H.-T. Wang, "High-efficiency continuous-wave Raman conversion with a BaWO₄ Raman crystal," *Opt. Lett.* **34**(11), 1687–1689 (2009).
6. V. G. Savitski, I. Friel, J. E. Hastie, M. D. Dawson, D. Burns, and A. J. Kemp, "Characterization of single-crystal synthetic diamond for multi-watt continuous-wave Raman lasers," *IEEE J. Quantum Electron.* **48**(3), 328–337 (2012).
7. Y. Lü, W. Cheng, Z. Xiong, J. Lu, L. Xu, G. Sun, and Z. Zhao, "Efficient CW laser at 559 nm by intracavity sum-frequency mixing in a self-Raman Nd:YVO₄ laser under direct 880 nm diode laser pumping," *Laser Phys. Lett.* **7**(11), 787–789 (2010).
8. A. J. Lee, D. J. Spence, J. A. Piper, and H. M. Pask, "A wavelength-versatile, continuous-wave, self-Raman solid-state laser operating in the visible," *Opt. Express* **18**(19), 20013–20018 (2010).
9. H. Y. Zhu, Y. M. Duan, G. Zhang, C. H. Huang, Y. Wei, H. Y. Shen, Y. Q. Zheng, L. X. Huang, and Z. Q. Chen, "Efficient second harmonic generation of double-end diffusion-bonded Nd:YVO₄ self-Raman laser producing 7.9 W yellow light," *Opt. Express* **17**(24), 21544–21550 (2009).
10. V. A. Lisinetskii, A. S. Grachtchikov, A. A. Demidovich, V. N. Burakevich, V. A. Orlovich, and A. N. Titov, "Nd:KGW/KGW crystal: efficient medium for continuous-wave intracavity Raman generation," *Appl. Phys. B: Lasers Opt.* **88**(4), 499–501 (2007).
11. P. Dekker, H. M. Pask, D. J. Spence, and J. A. Piper, "Continuous-wave, intracavity doubled, self-Raman laser operation in Nd:GdVO₄ at 586.5 nm," *Opt. Express* **15**(11), 7038–7046 (2007).
12. A. J. Lee, H. M. Pask, P. Dekker, and J. A. Piper, "High efficiency, multi-Watt CW yellow emission from an intracavity-doubled self-Raman laser using Nd:GdVO₄," *Opt. Express* **16**(26), 21958–21963 (2008).
13. Y. M. Duan, H. Y. Zhu, G. Zhang, C. H. Huang, Y. Wei, C. Y. Tu, Z. J. Zhu, F. G. Yang, and Z. Y. You, "Efficient 559.6 nm light produced by sum-frequency generation of diode-end-pumped Nd:YAG/SrWO₄ Raman laser," *Laser Phys. Lett.* **7**(7), 491–494 (2010).
14. M. Pollnau, P. J. Hardman, M. A. Kern, W. A. Clarkson, and D. C. Hanna, "Upconversion-induced heat generation and thermal lensing in Nd:YLF and Nd:YAG," *Phys. Rev. B* **58**(24), 16076–16092 (1998).

15. Y. F. Lü, X. H. Zhang, A. F. Zhang, X. D. Yin, and J. Xia, "Efficient 1047 nm CW laser emission of Nd:YLF under direct pumping into the emitting level," *Opt. Commun.* **283**(9), 1877–1879 (2010).
16. W. A. Clarkson, P. J. Hardman, and D. C. Hanna, "High-power diode-bar end-pumped Nd:YLF laser at 1.053 microm," *Opt. Lett.* **23**(17), 1363–1365 (1998).
17. C. Bollig, C. Jacobs, M. J. D. Esser, E. H. Bernhardt, and H. M. von Bergmann, "Power and energy scaling of a diode-end-pumped Nd:YLF laser through gain optimization," *Opt. Express* **18**(13), 13993–14003 (2010).
18. Y. K. Bu, C. Q. Tan, and N. Chen, "Continuous-wave yellow light source at 579 nm based on intracavity frequency-doubled Nd:YLF/SrWO₄/LBO Raman laser," *Laser Phys. Lett.* **8**(6), 439–442 (2011).
19. A. A. Kaminskii, K. Ueda, H. J. Eichler, Y. Kuwano, H. Kouta, S. N. Bagaev, T. H. Chyba, J. C. Barnes, G. M. A. Gad, T. Murai, and J. Lu, "M. A. Gad, T. Murai, and J. Lu, "Tetragonal vanadates YVO₄ and GdVO₄ - new efficient χ^3 -materials for Raman lasers," *Opt. Commun.* **194**(1-3), 201–206 (2001).
20. P. J. Hardman, W. A. Clarkson, G. J. Friel, M. Pollnau, and D. C. Hanna, "Energy-transfer upconversion and thermal lensing in high-power end-pumped Nd:YLF laser crystals," *IEEE J. Quantum Electron.* **35**(4), 647–655 (1999).
21. D. C. Hanna, C. G. Sawyers, and M. A. Yuratich, "Telescopic resonators for large-volume TEM₀₀-mode operation," *Opt. Quantum Electron.* **13**(6), 493–507 (1981).
22. I. V. Mochalov, "Laser and nonlinear properties of the potassium gadolinium tungstate laser crystal KGd(WO₄)₂:Nd³⁺-(KGW:Nd)," *Opt. Eng.* **36**(6), 1660–1669 (1997).
23. M. E. Innocenzi, H. T. Yura, C. L. Fincher, and R. A. Fields, "Thermal modeling of continuous-wave end-pumped solid-state lasers," *Appl. Phys. Lett.* **56**(19), 1831–1833 (1990).
24. A. A. Kaminskii, C. L. McCray, H. R. Lee, S. W. Lee, D. A. Temple, T. H. Chyba, W. D. Marsh, J. C. Barnes, A. N. Annanenko, V. D. Legun, H. J. Eichler, G. M. A. Gad, and K. Ueda, "High efficiency nanosecond Raman lasers based on tetragonal PbWO₄ crystals," *Opt. Commun.* **183**(1-4), 277–287 (2000).
25. G. E. James, E. M. Harrell II, C. Brackowski, K. Wiesenfeld, and R. Roy, "Elimination of chaos in an intracavity-doubled Nd:YAG laser," *Opt. Lett.* **15**(20), 1141–1143 (1990).
26. V. Magni, G. Cerullo, S. De Silvestri, O. Svelto, L. J. Qian, and M. Danailov, "Intracavity frequency doubling of a cw high-power TEM₀₀ Nd:YLF laser," *Opt. Lett.* **18**(24), 2111–2113 (1993).

1. Introduction

The ability to generate continuous wave (CW) laser output in the near-infrared region between 1.1 μm and 1.2 μm , and in the yellow-orange range, has seen CW Raman lasers undergo rapid development in the past 7 years. In 2004 the first CW external-resonator crystalline Raman laser was reported by Grabitchikov *et al.* [1], then in 2005, CW intracavity crystalline Raman lasers were reported by Demidovich *et al.* [2] and Pask [3]. Following these important milestones, multi-Watt CW Raman laser operation in the infrared has been demonstrated using a variety of different Raman crystals such as Nd:GdVO₄ [4], BaWO₄ [5] and diamond [6]. CW intracavity Raman lasers are built using the same components as conventional diode-pumped solid state lasers (DPSSL), and they have the capacity to generate hard to reach wavelengths. By incorporating intracavity frequency mixing, new wavelengths in the visible can be generated [7]. Further, by generating higher order Stokes intracavity fields via cascading the Stimulated Raman Scattering (SRS) process, wavelength selectable lasers have been demonstrated [8]. The diode to visible efficiency with which these lasers operate is high, typically 10-20% [8], and as such, many groups are pursuing different approaches to improve the performance of CW Raman lasers.

As with conventional DPSSLs, thermal lensing is an important issue in Raman lasers that frequently limits the output powers to which they can be scaled. For Raman lasers there is an additional thermal load due to the inelastic nature of the Raman shifting process, which generates phonons during the wavelength conversion. With the exception of [5], the most efficient CW Raman lasers reported to date tend to be self-Raman lasers, in which the laser crystal itself is Raman active; examples include Nd:GdVO₄, Nd:KGW and Nd:YVO₄ lasers [4, 9, 10]. In comparing these self-Raman lasers to Raman lasers with a separate Raman crystal, we can see that the resonator losses are lower, because there are fewer crystal interfaces, and they are as compact as the equivalent fundamental wavelength laser. Yet thermal loading is highest for self-Raman lasers, and the suitable materials (vanadates and tungstates) are not the crystals with best thermal properties. In many cases, it is thermal lensing that limits the maximum output powers that can be achieved from self-Raman lasers [11, 12], and further, such strong thermal lensing can impact on beam quality and restrict cavity design. Distributing the thermal load by using separate laser and Raman crystals, is one approach to manage thermal lensing. In fact the most efficient, multi-Watt, first Stokes laser,

generating 3.36 W at 1180 nm with a diode to first Stokes efficiency of 13.2% was obtained from a Nd:YVO₄/BaWO₄ Raman laser [5]. Nd:YAG offers better thermal properties compared to Nd:YVO₄ and Nd:GdVO₄, and has been used with some success [13], however Nd:YAG has no naturally-polarized emission, and birefringence loss is detrimental to Raman laser performance. In this work, we have chosen to explore another well-known crystal, Nd:YLF.

The benefits of using Nd:LiYF₄ (Nd:YLF) as the fundamental laser crystal in a CW intracavity Raman laser are that it provides a naturally polarized emission and a weak thermal lens [14]. The weak thermal lens is not due to superior thermal conductivity e.g. as in YAG, but rather it arises because the crystal has a negative dn/dT value which partially compensates the positive lens generated from end face bulging. It has π and σ polarized emissions at different wavelengths, 1047 nm and 1053 nm, respectively, shorter than the traditional 1064 nm, thus providing an unusual range of Stokes wavelengths and corresponding visible wavelengths. As a disadvantage it has a low thermal fracture limit, which restricts the maximum absorbed pump power. This can be partly alleviated by using direct excitation of the upper laser level, by means of a diode emitting at 881 nm instead of the usual 806 nm and 797 nm wavelengths typically used to pump Nd:YLF. Pumping directly into the upper laser level eliminates multiphonon decay to the upper laser level, so the total energy required to excite a Nd ion to the upper laser level is reduced by ~4%. There is a corresponding decrease of 33% in the total heat generated from quantum defect. Pumping at 881 nm also increases the optical to optical efficiency of the Nd:YLF laser [15]. In addition, the relatively weak absorption at 881 nm is such that the absorption is distributed uniformly over the length of the crystal, so that the local temperature rise in the crystal is minimized. Regarding the relatively-low fracture limit for Nd:YLF, many works have now overcome this problem achieving high output power CW lasers using Nd:YLF [16, 17].

There have been two main reports to date of CW Raman lasers based on Nd:YLF. First, Savitski *et al.* [6] used a Nd:YLF laser module (side pumped with 153 W of diode power) operating at 1047 nm to intracavity pump a diamond crystal, obtaining 5.1 W of CW output at 1217 nm ($M^2 \sim 1.1$). In this same system, they also pumped a KGW crystal, obtaining 6.1 W at 1139 nm ($M^2 \sim 5.5$). This is the highest reported output power for a CW Raman laser reported to date, and the corresponding diode to Stokes conversion efficiency was a modest 4%. The second Nd:YLF-based laser was reported by Bu *et al.* [18]; it combined the 1047 nm Nd:YLF fundamental, the 921 cm⁻¹ Raman shift in a 30 mm long SrWO₄ crystal and frequency doubled in LBO to create a CW yellow laser source at 579 nm for ophthalmology. 889 mW was generated at a diode to yellow conversion efficiency of 5.8%.

In this work, our emphasis is on investigating how the thermal and optical properties of Nd:YLF can enhance the operation of CW Raman lasers. We report a Nd:YLF/KGW CW intracavity Raman laser where the Nd:YLF operates at 1053 nm fundamental. We chose KGW as the Raman-active crystal because it has similar Raman gain to the vanadates, ~4.5 cm/GW [19], used in self-Raman lasers to deliver the best intracavity frequency-doubled CW Raman laser results to date. We find that thermal lensing in our Nd:YLF/KGW CW Raman lasers is weak (as expected), thereby permitting lasers to be designed with cavity lengths of 25 cm and potentially much longer, and resulting in relatively high beam quality parameters (compared to self Raman lasers) of between 1.2 and 2.5. An advantage of KGW is the fact that it has two strong Raman lines at 768 cm⁻¹ and at 901 cm⁻¹, with similar Raman gain, that can be accessed separately, just by orientation of the KGW. Given that, and the capacity of Nd:YLF to emit in two different wavelengths, it is therefore possible to obtain four different Stokes wavelengths with this system, 1139 nm, 1147 nm, 1156 nm and 1163 nm. Consequently many visible lines from the green to the yellow-orange range of the visible may be achieved by second harmonic generation (SHG) or sum frequency generation (SFG) as shown in Fig. 1. Here we demonstrate two of those combinations by using the 1053 nm fundamental wavelength and then, shifting to 1147 nm (0.70 W-CW) and 1163 nm (0.95 W-CW). In addition, we have demonstrated the SHG and SFG of those new wavelengths, obtaining emission at 549 nm (0.65 W-CW), 552 nm (1.90 W-CW), 573 nm (0.60 W-CW)

and 581 nm (1.10 W-CW). As this is the first time a Raman laser has been investigated using the 1053 nm fundamental transition of Nd:YLF, we were able to demonstrate two wavelengths not reported before in crystalline Raman lasers, 549 nm and 552 nm.

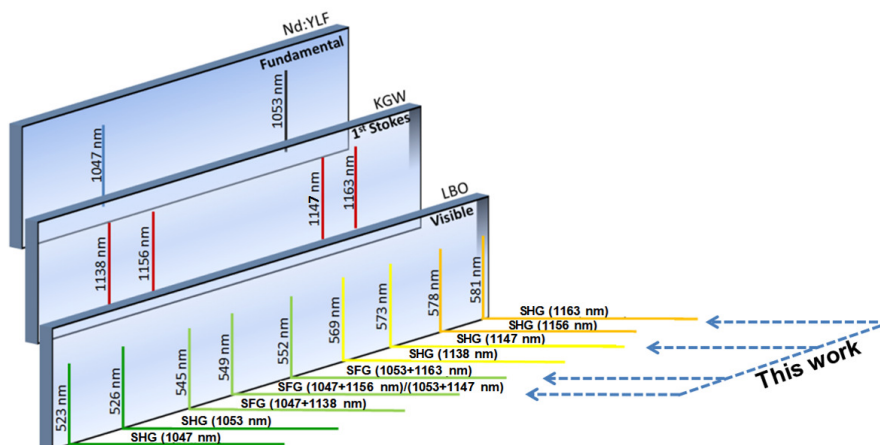


Fig. 1. Wavelengths that can be generate using the combination of Nd:YLF/KGW/LBO.

2. Lasers experimental setup

The lasers described in this section were all pumped with the same pump source, a 60 W fiber coupled diode laser (LIMO) emitting at 880 nm, with a fiber diameter of 100 μm and a numerical aperture (N.A.) of 0.22. A 25 mm focal length lens was used for collimation and a 125 mm lens was used for focusing, delivering a pump spot of 500 μm of diameter in the Nd:YLF laser crystal. The diode output wavelength was temperature-tuned to 881 nm, in order to match an absorption peak of the Nd:YLF crystal [15]. The fraction of pump power absorbed in the 15 mm crystal was 43%, and this is something that could be optimized in the future, for example by double-passing the pump. Direct pumping has two main benefits: first, a 33% reduction in heat by eliminating the multiphonon decay from the pump level to the upper laser level, and second, as the absorption coefficient at this wavelength is smaller than the ones at conventional pump wavelengths, distributing the absorption over the whole length of the crystal so that the local temperature rise in the crystal is minimized. A chopper was placed after the diode fiber in order to investigate quasi-CW operation; in this case, the chopper was operated with 50% duty cycle and frequency of 850 Hz, so the thermal lens was approximately 50% of the CW case. In this mode of operation we can predict the CW output power that could be achieved by pumping the crystal harder, without taking the risk of a thermal fracture.

We used a Nd:YLF plane-Brewster cut crystal with 1 at% Nd^{3+} doping concentration and dimensions of $4 \times 4 \times 15 \text{ mm}^3$. The 1 at% doping concentration was chosen in order to have a reasonable absorption at 881 nm and also to minimize energy transfer upconversion (ETU) [20]. The crystal's flat face was coated for high transmission ($T > 95\%$) at 881 nm, with low reflectivity for fundamental 1047/1053 nm ($R < 0.2\%$) and first Stokes wavelength range 1135-1170 nm ($R < 0.1\%$). The Brewster-cut on the other face introduced losses for 1047 nm, thereby enabling the 1053 nm fundamental wavelength to oscillate without competition. We chose 1053 nm as the fundamental wavelength because it generally has a weaker thermal lens than 1047 nm [14] and was therefore more likely to deliver good beam qualities and freedom to design long cavities. There are resonator designs that allow the laser to operate under strong thermal lensing, such as telescopic resonators [21], however, they typically operate only for a short range of pump powers, and generally introduce extra optics to the resonator, increasing the intracavity losses. Accordingly, we did not investigate their use here.

We used a 5×5×24 mm KGW crystal as the Raman-active medium. It was AR-coated at the fundamental and Stokes wavelengths ($R < 0.1\%$ at 1053–1170 nm), and cut for propagation along the N_p axis. The Raman spectrum for KGW is complex [22] and Fig. 2 shows the Raman spectra measured (using a Renishaw InVia Reflex microRaman spectrometer with resolution 2 cm^{-1}) for the two orientations we used in this work. The KGW crystal was placed in a copper mount that could be rotated in order to access either the 901 cm^{-1} shift (fundamental and Stokes polarization parallel to the N_m refractive index axis) or the 768 cm^{-1} shift (fundamental and Stokes polarization parallel to the N_g refractive index axis). Table 1 shows the combinations of fundamental, Stokes, yellow and lime-green emission generated using the two Raman shifts.

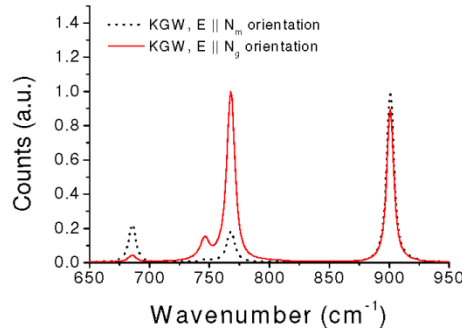


Fig. 2. Raman spectra at the two orientations used for the laser.

Table 1. 1st Stokes, SHG and SFG Wavelengths Generated by Nd:YLF/KGW System

Shift	Fundamental	1st Stokes	SHG	SFG
768 cm^{-1}	1053 nm	1147 nm	573 nm	549 nm
901 cm^{-1}		1163 nm	581 nm	552 nm

The cavity used to obtain 1st Stokes laser emission is shown in Fig. 3. The input mirror had high reflectivity ($>99.99\%$) at 1053 nm, 1147 nm and 1163 nm, and high transmission ($T > 90\%$) at 880 nm, with 400 mm radius of curvature (ROC). The output coupler (O.C.) for the 1st Stokes had a $R > 99.99\%$ at 1053 nm, 0.2% transmission at 1163 nm and 0.1% transmission at 1147 nm, with 250 mm of ROC. The distance from the last end face of the KGW to the O.C. was 115 mm and the overall cavity length was 160 mm. The TEM_{00} resonator mode had 420 μm diameter in the laser crystal and 400 μm diameter in the Raman crystal, calculated using an ABCD resonator model (LASCAD GmbH).

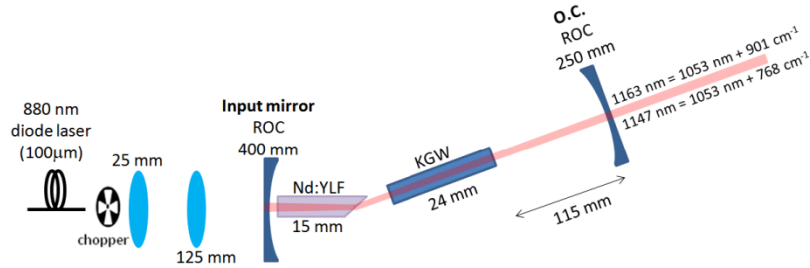


Fig. 3. Nd:YLF/KGW 1st Stokes laser setup.

A lithium triborate (LBO) crystal ($4 \times 4 \times 10 \text{ mm}^3$) was used for intracavity SHG/SFG. It was cut for Type I non-critical phase-matching, and AR-coated at the fundamental, Stokes and SHG/SFG wavelengths ($R < 0.1\%$ at 1053–1170 nm and $T > 95\%$ at 570–590 nm). The LBO crystal was positioned next to the KGW, as shown in Fig. 4, and temperature tuned to 63°C for 573 nm or 50°C for 581 nm. The TEM_{00} resonator mode diameters were 380 μm , 366 μm and 368 μm respectively in the laser, Raman and doubling crystals. The curved (200 mm ROC) output coupler had high reflectivity, $R > 99.99\%$ at the fundamental and Stokes wavelengths and high transmission, ranging from 80 to 95%, at the yellow and lime-green wavelengths. An intracavity mirror was also introduced between the KGW and LBO crystals in order to redirect the backwards propagating yellow beam toward the O.C. This intracavity mirror had an antireflective (AR) coating at 1053 nm ($R < 0.1\%$), 1147 nm and 1163 nm ($R < 0.1\%$), and a HR at 573 nm and 581 nm ($R > 98\%$).

For the SFG cases, 549 nm and 552 nm, the same configuration was used. The temperatures of the LBO crystal required for phase matching were 109°C for 549 nm and 101°C for 552 nm.

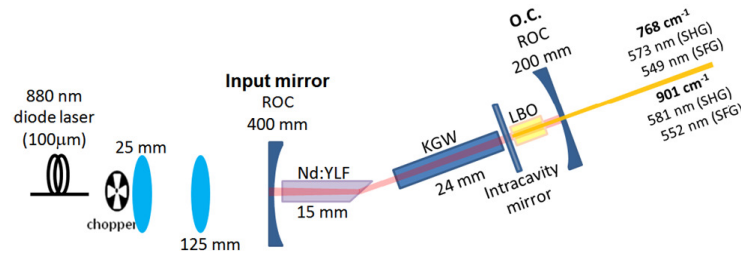


Fig. 4. Nd:YLF/KGW/LBO yellow and lime-green laser setup.

3. Results

The results are presented in three different sections, the first one concerns the thermal lens characterization, and the following two sections concern laser operation using the two different Stokes shifts for KGW (768 cm^{-1} and 901 cm^{-1}).

3.1. Estimating the thermal lens

In order to estimate the thermal lens of the Nd:YLF crystal, we built a high-Q, plane-parallel cavity (using a Nd:YLF crystal without Brewster cut) for the 1053 nm field with length 120 mm, and made observations about resonator stability. Strong laser emission from the flat-flat resonator indicated that the thermal lens was positive. Next, we focused the 881 nm beam to a 300 μm diameter spot into the crystal, and found that the laser operated stably for absorbed pump powers up to 14 W, above which the laser output decreased and could not be sustained. Accordingly, we concluded that the focal length of the thermal lens in the Nd:YLF was 120 mm under these conditions, in the plane which corresponds to the strongest thermal lensing.

From [23], the thermal lens focal length depends on the square of the pump radius, ω_p , and we can thereby infer that the focal length for the 500 μm diameter used in our Raman lasers is around 330 mm. This is consistent with our observations using a 500 μm pump diameter and the resonator shown in Fig. 3, in which stable output power at the fundamental was obtained for pump powers up to 17.5 W and for resonator lengths as long as 265 mm. Inserting the Raman crystal, we observed stable Stokes oscillation for cavity lengths from 45 mm to 250 mm. Accordingly, for the lasers described in the following sections, the resonators operated well away from the regions of resonator instability. Moreover there is clearly scope in the future for designing longer resonators to optimize laser performance.

3.2. Laser operating at the 901 cm^{-1} shift

When the KGW was oriented to access the 901 cm^{-1} shift, the 1st Stokes laser delivered a maximum CW power of 0.95 W at 1163 nm for an absorbed pump power of 12.3 W. The beam quality was measured to have M^2 of 1.49. For quasi-CW operation 1.56 W of peak power was obtained for 21 W absorbed pump power. Figure 5(a) shows the output power performance of this laser. The Stokes beam profile was elliptical, due to the Brewster angle in the cavity, and the M^2 and beam sizes mentioned are average values for the two planes. We did not measure the beam quality of the fundamental beam (1053 nm) because the mirrors have a very high reflectivity at this wavelength (>99.9%), thus, the residual power leaking from the cavity was not enough to make a good M^2 measurement.

When the 10 mm LBO crystal temperature was tuned to 50 °C for the SHG of 1163 nm, a CW output power of 1.10 W at 581 nm was obtained, with M^2 of 1.93. In quasi-CW mode, 1.65 W of peak power was obtained, Fig. 5(b). It is interesting to note that the powers in the visible are higher than in the infrared and this is attributed to the fact we were not using the optimum output coupling for the 1st Stokes.

When the LBO crystal was tuned to 101°C for SFG of 1053 nm and 1163 nm, we obtained 1.90 W CW at 552 nm for 13 W of absorbed pump power. The corresponding beam quality was $M^2 \sim 2.01$. In quasi-CW operation, 3.12 W of peak power was achieved for 20 W of pump. Figure 5(c) shows the output power performance for this laser.

The spectral linewidths (full width at half-maximum) of the fundamental, first Stokes and visible lines were measured to be 0.3 nm.

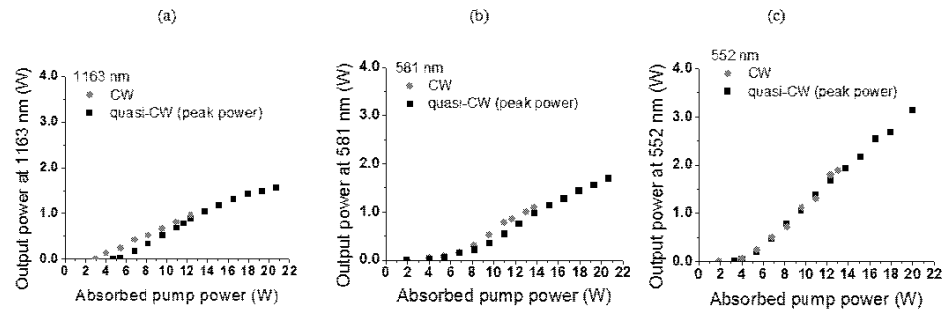


Fig. 5. Output power as a function of absorbed pump power for (a) 1163 nm, (b) 581 nm and (c) 552 nm.

3.3. Laser operating with the 768 cm^{-1} shift

When the KGW crystal was rotated to access the best gain for the 768 cm^{-1} shift, the first Stokes laser delivered 0.70 W CW power at 1147 nm for 13 W of absorbed pump power and for quasi-CW operation, 1.20 W of peak power for 20 W absorbed pump power, as shown in Fig. 6(a). The beam quality was measured to be $M^2 \sim 1.44$.

When optimized for frequency doubling the 1st Stokes, we obtained 0.60 W CW power at 573 nm for an absorbed pump power of 13 W (see Fig. 6(b)) and the corresponding beam quality was measured to be $M^2 \sim 1.76$. In quasi-CW operation the maximum peak yellow power was 1.25 W for 18 W of pump power. At higher (18-20 W) pump powers the 901 cm^{-1} Raman transition began to compete. Looking at the Raman spectra in Fig. 2, we can see that for this orientation the 901 cm^{-1} and 768 cm^{-1} lines have similar intensities, with the 768 cm^{-1} only slightly stronger. The competition arises because there are losses for the 768 cm^{-1} shift through the SHG process, but no such losses for the 901 cm^{-1} shift.

When optimized for sum frequency to generate 549 nm, a maximum power of 0.65 W was achieved in CW regime and 1.20 W peak power when chopped, as seen in Fig. 6(c).

Unfortunately coating damage occurred on the KGW crystal and the low thresholds obtained previously could not be realized. It is very likely that considerably higher output powers could be achieved at 549 nm using a KGW crystal with un-damaged coatings.

The spectral linewidths (full width at half-maximum) of the fundamental, first Stokes and visible lines were measured to be 0.3 nm.

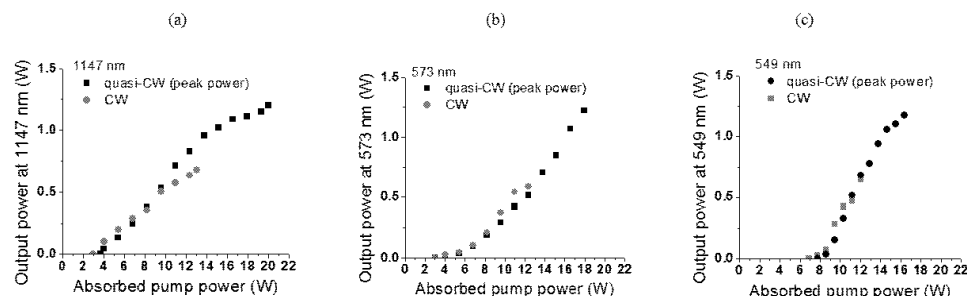


Fig. 6. Output power as a function of absorbed pump power for (a) 1147 nm, (b) 573 nm and (c) 549 nm.

4. Discussion

The laser performance shown in Fig. 5 and 6 is very good in terms of output power and efficiency, particularly when we consider that the coatings on the crystals and mirrors were specifically designed for a system having a 1064 nm fundamental wavelength (ie. not 1053 nm). The lasers reported here operate over a useful range of wavelengths and output powers, with good efficiencies. The highest conversion efficiency (with respect to absorbed pump power) reported here is 14% in the case of SFG to 552 nm, and this can be compared against 20% obtained in a self-Raman Nd:GdVO₄ laser with SFG to 559 nm [4], which is the highest efficiency reported in the literature. The higher efficiency in [4] can be attributed to lower resonator losses, enabled by very low loss AR-coatings on the crystals. For the yellow, we achieved a conversion efficiency of 7.8% for generation of 581 nm, somewhat lower than the highest-reported conversion efficiency (17%) for a self-Raman [8] operating at 586 nm, but again the difference is due to extremely low resonator losses in [8]. In the case of the 1st Stokes, our conversion efficiency of 7.3% when generating first Stokes output at 1163 nm can be compared against 13.8% for the best CW self-Raman performance, from a composite Nd:KGW/KGW laser operating at 1181 nm [10]. Furthermore, the Nd:YLF Raman lasers we have demonstrated had good beam quality, with $M^2 \sim 1.49$ for the 1st Stokes laser at 1163 nm, and with $M^2 \leq 2$ for CW operation at 1147 nm and in the visible at 581 nm and at 552 nm. This beam quality is considerably better than for the Nd:GdVO₄ self-Raman lasers in which the beam quality for the sum frequency was $M^2 \sim 10$ [4], and for the second harmonic was $M^2 \sim 6$ [12], both at maximum pump power. The good beam quality reported here for Nd:YLF Raman lasers is a consequence of the much weaker thermal lensing, since the beam quality is strongly linked to thermal lensing, which in the case of self-Raman laser is typically very strong and aberrated.

We can also compare our results to other Raman lasers reported using Nd:YLF. Savitski *et al.* reported the highest output power of 6.1 W [6] for any CW Raman laser, by combining the 1047 nm fundamental from Nd:YLF and the 768 cm⁻¹ shift in KGW. However, the overall diode to first Stokes efficiency of ~4% was substantially lower than the 7.3% reported here, and also the beam quality, $M_x^2 \sim 5$ and $M_y^2 \sim 6$, is not so good as the $M^2 \sim 1.5$ reported here. Interestingly, the beam quality they found using diamond (instead of KGW) was an excellent $M_x^2 \sim 1.1$ and $M_y^2 \sim 1.2$, which given the very high thermal conductivity of diamond, suggests that some of the beam degradation occurs in the Raman crystal. In the work of Bu. *et al.* [18], the (absorbed) diode to yellow conversion efficiency is estimated to be 7.4%, quite similar to

the conversion efficiency we have obtained (7.8%). An attractive feature used in [18] is the coupled cavity setup. This reduces considerably the intracavity losses for the Stokes field, yielding lower thresholds for SRS: 1.35 W compared to our lowest threshold of 2 W for yellow (581 nm).

We anticipate substantial improvements in efficiency will be possible in the future by improving the characteristics of the mirror and crystal coatings, particularly the AR-coatings on the Raman crystals and the visible transmission of the output coupler. For all the cases investigated here, the laser performance was superior when using the 901 cm^{-1} shift, compared to the 768 cm^{-1} shift. While the 1163 nm laser provided a maximum CW power near 1 W, the 1147 nm only achieved about 700 mW. For the visible, the 581 nm laser delivered more than 1 W with a threshold of 2 W of absorbed power, while the 573 nm laser provided a maximum of 600 mW with a threshold of 3 W of absorbed power. These differing performances could be due to differences, either in Raman gain or resonator losses, for the various wavelengths. According to the literature [24] as well as our measured spectrum in Fig. 2, the 768 cm^{-1} shift has higher Raman gain than 901 cm^{-1} , but we believe such a difference is not enough to explain the different performances we have observed. Considering all the mirror and crystal coatings, we found the round trip losses for both Stokes wavelengths to be similar, with the 1147 nm losing 0.1% more power per round trip than the 1163 nm, which may contribute to the small difference between their thresholds. Moreover the output coupler has a transmission of about 0.1% at 1147 nm and 0.2% at 1163 nm, this higher output coupling contributes to the higher power at 1163 nm. The maximum powers at 1147 nm were slightly limited by the onset of competition between the 901 cm^{-1} and 768 cm^{-1} shifts for absorbed pump powers above 18 W. With regard to the different output powers that were obtained in the yellow, we note that the O.C. mirror has about 20% of reflectivity at 573 nm and <5% at 581 nm, and this is likely to be the main cause for the reduced performance of 573 nm when compared to 581 nm. The powers at the two sum frequency wavelengths cannot be compared due to the crystal damage that occurred when optimising performance at 549 nm.

Our observations of resonator stability, for fundamental oscillation only, in resonators up to 265 mm long (17.5 W of absorbed power/500 μm pump diameter) show that thermal lensing is quite weak in our Nd:YLF crystal, with a focal length of ~ 330 mm at maximum pump power. This is much weaker than what is typically found in CW Nd:GdVO₄ self Raman lasers, such as in [11] where it is 60 mm long (18 W of absorbed power, 808 nm/400 μm pump diameter) and in [12] where it is 70 mm long (20 W of absorbed power, 880 nm/400 μm pump diameter). The relative-weakness of the thermal lens in Nd:YLF is also apparent in the laser performance under CW and quasi-CW (50% duty cycle) operation of our Nd:YLF Raman lasers. The performances were very similar for up to ~ 14 W pump power, the maximum CW pump power that was used, indicating that an approximately 50% decrease in thermal lens, made little difference to the mode sizes in the laser and Raman crystals, and ultimately the output power. This is quite different to the scenario of self Raman lasers such as in Nd:GdVO₄ [11] where strong thermal lensing, even in very short (few cm) resonators made the resonator become unstable (and the output power declines steeply) under CW pumping, while for quasi-CW (50% duty cycle) pumping, the output power continued to increase over the power range tested. In the future, the relatively long thermal lens in Nd:YLF will enable us to explore folded cavity designs that enable the mode sizes in the laser, Raman and doubling crystals to be optimized for higher conversion efficiencies and multi-Watt CW output powers across the range of wavelengths demonstrated here, as well as the set of wavelengths that can be accessed using the 1047 nm fundamental transition in Nd:YLF.

The output powers we have reported here for Nd:YLF Raman lasers are substantial, particularly in the visible: CW operation yielded up to 0.95 W in the near-ir (1163 nm) and 1.9 W in the visible (552 nm) quasi-CW operation at 50% duty cycle resulted in peak output powers up to 1.65 W in the near-ir (1163 nm) and over 3 W in the visible (552 nm). Higher peak powers would be achieved at lower duty cycles, and there are many applications for which modulated laser output is suitable. Our capacity to scale to higher powers has been constrained by the need to avoid fracture of the Nd:YLF. Here we note recent developments

in power-scaling CW Nd:YLF in which up to 60 W of output power at 1053 nm was demonstrated [17] by using large mode sizes in the Nd:YLF, and accordingly, we believe there is considerable potential for efficiently scaling Nd:YLF-based Raman lasers to much higher powers.

Yet another exciting possibility exists to build a low-noise, multi-Watt yellow laser, this possibility stemming from the broad (~ 360 GHz) emission band of Nd:YLF. Here the concept is to build a sufficiently-long Raman resonator that operates simultaneously on a large number (100s) of longitudinal modes, an approach previously used to solve the “green problem” [25, 26].

5. Conclusions

Nd:YLF is a suitable laser crystal for Raman lasers and CW output powers of 0.6 W to 1.9 W have been achieved in the near-infrared at 1147 nm and 1163 nm and visible at 549 nm, 552 nm, 573 nm and 581 nm. To the best of our knowledge, this is the first time a Raman laser has been investigated using the 1053 nm fundamental of Nd:YLF and as a consequence, it is the first time a crystalline Raman laser has been operated at this sequence of visible wavelengths. We have demonstrated that thermal lensing is quite weak, much less than for the self-Raman lasers, and this provides a strong platform for constructing efficient, multi-Watt Raman lasers with high beam quality.

Acknowledgements

Jonas is a CAPES scholar: Proc n° 5381/09-6.

List of main publications during the PhD period (2008-2012)

- 1 J. Jakutis-Neto, J. Lin, N.U. Wetter, and H. Pask, "CW and quasi-CW operation of a Nd:YLF/KGW Raman Laser at 1163 nm, 552 nm and 581 nm," presented at the 5th EPS-QEOD Europhoton Conference, Stockholm-Sweeden, 2012.
- 2 J. Jakutis-Neto, J. Lin, N.U. Wetter, and H. Pask, "Continuous-wave Watt-level Nd:YLF/KGW Raman laser operating at near-IR, yellow and lime-green wavelengths," *Optics Express* **20** (9), 9841-9850 (2012).
- 3 J. Jakutis-Neto, J. Lin, A.J. Lee, H. Zhang, J. Wang, N.U. Wetter, and H. Pask, "High beam quality cw 1.5 W BaWO₄ Raman laser using Nd: YLF as laser active medium," presented at the Quantum Electronics Conference & Lasers and Electro-Optics (CLEO/IQEC/PACIFIC RIM), Sydney- Australia, 2011.
- 4 A.J. Lee, J. Jakutis-Neto, and H.M. Pask, "Generation of combs of wavelengths in the infrared and visible using cascaded stimulated Raman scattering in potassium titanyl phosphate," presented at the Quantum Electronics Conference & Lasers and Electro-Optics (CLEO/IQEC/PACIFIC RIM), Sydney - Australia, 2011.
- 5 S.L. Baldochi, F.R. Silva, J.R. De Moraes, J. Jakutis-Neto, N.U. Wetter, and A.M.E. Santo, "Synthesis and growth of materials for solid state lasers: Nd:YLF and Nd:LLW single crystal fibers," *Journal of Crystal Growth* **317** (1), 4-7 (2011).
- 6 J. Jakutis-Neto, T.S. Moura, F.R. Da Silva, S.L. Baldochi, and N.U. Wetter, "Lasing of a single crystal Nd³⁺ fluoride fiber," *Optics Communications* **283** (18), 3487-3491 (2010).
- 7 J. Jakutis-Neto, F.A. Camargo, and N.U. Wetter, "Deep Blue Nd:LiYF₄ Laser in Quasi-Continuous and Continuous Operation," presented at the Advanced Solid-State Photonics, San Diego, California, 2010.
- 8 J. Jakutis-Neto, L. Gomes, C.T. Amancio, L.R.P. Kassab, J.R. Martinelli, and N.U. Wetter, "Increased Er³⁺ upconversion in tellurite fibers and glasses by co-doping with Yb³⁺," *Optical Materials* **33** (1), 107-111 (2010).

- 9 L.R.P. Kassab, FA Bomfim, J.R. Martinelli, N.U. Wetter, J. Jakutis-Neto, and C.B. de Araújo, "Energy transfer and frequency upconversion in Yb³⁺/Er³⁺ doped PbO-GeO₂ glass containing silver nanoparticles," *Applied Physics B: Lasers and Optics* **94** (2), 239-242 (2009).
- 10 J. Jakutis-Neto, CT Amancio, LRP Kassab, NU Wetter, N.U. Wetter, and J. Frejlich, "Increasing Er³⁺ Up-Conversion Intensities By Co-Doping Telluride Glasses With Yb³⁺," *AIP Conference Proceedings* **992** (1), 1201 (2008).
- 11 F.A. Bomfim, J.R. Martinelli, L.R.P. Kassab, N.U. Wetter, and J. Jakutis-Neto, "Effect of the ytterbium concentration on the upconversion luminescence of Yb³⁺/Er³⁺ co-doped PbO-GeO₂-Ga₂O₃ glasses," *Journal of Non-Crystalline Solids* **354** (42-44), 4755-4759 (2008).

References

- [1] T. H. Maiman, "Stimulated Optical Radiation in Ruby," *Nature* **187** (4736), 493-494 (1960).
- [2] R. W. Hellwarth, "Theory of the Pulsation of Fluorescent Light From Ruby," *Physical Review Letters* **6** (1), 9-12 (1961).
- [3] P. P. Sorokin and M. J. Stevenson, "Stimulated Infrared Emission from Trivalent Uranium," *Physical Review Letters* **5** (12), 557-559 (1960).
- [4] L. F. Johnson, G. D. Boyd, K. Nassau, and R. R. Soden, "Continuous Operation of a Solid-State Optical Maser," *Physical Review* **126** (4), 1406-1409 (1962).
- [5] J. E. Geusic, H. M. Marcos, and L. G. Van Uitert, "Laser Oscillations in Nd-doped Yttrium aluminum, Yttrium Gallium and Gadolinium Garnets," *Appl. Phys. Lett.* **4** (10), 182-184 (1964).
- [6] W. Koechner and M. Bass (eds), *Solid State Lasers Engineering - A Graduate Text*. (Springer, New York, 2003), 1st ed.
- [7] "http://www.lle.rochester.edu/omega_facility/omega/", (accessed on 15/10/2012).
- [8] C.J. Koester and E. Snitzer, "Fiber laser as a light amplifier," *Journal of the Optical Society of America* **53** (4), 515 (1963).
- [9] D. J. Richardson, J. Nilsson, and W. A. Clarkson, "High power fiber lasers: current status and future perspectives [Invited]," *J. Opt. Soc. Am. B* **27** (11), B63-B92 (2010).
- [10] Jr Nick Holonyak and S. F. Bevacqua, "Coherent (visible) Light Emission from Ga(As_{1-x}P_x) Junctions," *Appl. Phys. Lett.* **1** (4), 82-83 (1962).
- [11] J. L. A. Chilla, S. D. Butterworth, A. Zeitschel, J. P. Charles, A. L. Caprara, M. K. Reed, and L. Spinelli, "High-power optically pumped semiconductor lasers," presented at the Solid State Lasers XIII: Technology and Devices, San Jose, Ca, USA, 2004.
- [12] G. Overton and S. G. Anderson, "LASER MARKETPLACE 2009: Photonics enters a period of high anxiety", in *Laser Focus World* (2009), Vol. 45.
- [13] A. Minassian, B. Thompson, and M. J. Damzen, "Ultrahigh-efficiency TEM₀₀ diode-side-pumped Nd:YVO₄ laser," *Applied Physics B: Lasers and Optics* **76** (4), 341-343 (2003).
- [14] A. Deana, I. Ranieri, S. Baldochi, and N. Wetter, "Compact, diode-side-pumped and Q-switched Nd:YLiF₄ laser cavity operating at 1053 nm with diffraction limited beam quality," *Applied Physics B: Lasers and Optics* **106** (4), 877-880 (2012).

- [15] X. Ding, R. Wang, H. Zhang, X.-Yi Yu, W.-Qi Wen, P. Wang, and J. Quan Yao, "High-efficiency Nd:YVO₄ laser emission under direct pumping at 880 nm," *Optics Communications* **282** (5), 981-984 (2009).
- [16] Y. F. Lu, X. H. Zhang, A. F. Zhang, X. D. Yin, and J. Xia, "Efficient 1047 nm CW laser emission of Nd:YLF under direct pumping into the emitting level," *Optics Communications* **283** (9), 1877-1879 (2010).
- [17] W. Liang, X. Zhang, Z. Liang, and Y. Liu, "Efficient continuous-wave 908 nm Nd:YLF laser emission under direct 880 nm pumping," *Laser Physics* **21** (2), 320-322 (2011).
- [18] R. K. Watts, "Branching Ratios for YA1G:Nd³⁺," *J. Opt. Soc. Am.* **61** (1), 123_121-124 (1971).
- [19] C. Czeranowsky, *Resonatorinterne Frequenzverdopplung von diodengepumpten Neodym-Lasern mit hohen Ausgangsleistungen im blauen Spektralbereich*. (Shaker, 2002).
- [20] Y. Sato and T. Taira, "Comparative study on the spectroscopic properties of Nd:GdVO₄ and Nd:YVO₄ with hybrid process," *Selected Topics in Quantum Electronics, IEEE Journal of* **11** (3), 613-620 (2005).
- [21] Y. Sato and T. Taira, "Thermo-optical and -mechanical parameters of Nd:GdVO₄ and Nd:YVO₄," presented at the Lasers and Electro-Optics, 2007. CLEO 2007. Conference on, 2007.
- [22] Z. Ma, J. C. Gao, D. J. Li, J. L. Li, N. L. Wu, and K. M. Du, "Thermal stress effects of the diode-end-pumped Nd : YLF slab," *Optics Communications* **281** (13), 3522-3526 (2008).
- [23] M. Pollnau, P. J. Hardman, M. A. Kern, W. A. Clarkson, and D. C. Hanna, "Upconversion-induced heat generation and thermal lensing in Nd:YLF and Nd:YAG," *Physical Review B* **58** (24), 16076 (1998).
- [24] A. Grzechnik, K. Syassen, I. Loa, M. Hanfland, and J. Y. Gesland, "Scheelite to fergusonite phase transition in YLiF₄ at high pressures," *Physical Review B* **65** (10), 104102 (2002).
- [25] M. Pollnau, P. J. Hardman, W. A. Clarkson, and D. C. Hanna, "Upconversion, lifetime quenching, and ground-state bleaching in Nd³⁺: LiYF₄," *Optics Communications* **147** (1-3), 203-211 (1998).
- [26] P. J. Hardman, W. A. Clarkson, G. J. Friel, M. Pollnau, and D. C. Hanna, "Energy-transfer upconversion and thermal lensing in high-power end-pumped Nd : YLF laser crystals," *Ieee Journal of Quantum Electronics* **35** (4), 647-655 (1999).
- [27] A. M. Deana and N. U. Wetter, "High-efficiency Q-switched and diffraction-limited Nd:YLF side-pumped laser," presented at the SPIE, Brussels, Belgium, 2012.

- [28] C. Bollig, C. Jacobs, M. J. D. Esser, E. H. Bernhardt, and H. M. von Bergmann, "Power and energy scaling of a diode-end-pumped Nd:YLF laser through gain optimization," *Optics Express* **18** (13), 13993-14003 (2010).
- [29] X. Y. Peng, L. Xu, and A. Asundi, "High-power efficient continuous-wave TEM00 intracavity frequency-doubled diode-pumped Nd : YLF laser," *Applied Optics* **44** (5), 800-807 (2005).
- [30] Y. F. Lu, X. H. Zhang, W. B. Cheng, and J. Xia, "All-solid-state cw frequency-doubling Nd:YLiF4/LBO blue laser with 4.33 W output power at 454 nm under in-band diode pumping at 880 nm," *Applied Optics* **49** (21), 4096-4099 (2010).
- [31] J. Jakutis Neto, F. A. Camargo, and N. U. Wetter, "Deep Blue Nd: LiYF4 Laser in Quasi-Continuous and Continuous Operation," presented at Advanced Solid-state Photonics, San Diego-California, 2010.
- [32] Y. Louyer, F. Balembois, M. D. Plimmer, T. Badr, P. Georges, P. Juncar, and M. E. Himbert, "Efficient cw operation of diode-pumped Nd:YLF lasers at 1312.0 and 1322.6 nm for a silver atom optical clock," *Optics Communications* **217** (1–6), 357-362 (2003).
- [33] F. Balembois, D. Boutard, E. Barnasson, M. Baudrier, R. Pariès, C. Schwach, and S. Forget, "Efficient diode-pumped intracavity frequency-doubled CW Nd:YLF laser emitting in the red," *Optics & Laser Technology* **38** (8), 626-630 (2006).
- [34] R. Sarrouf, V. Sousa, T. Badr, G. Xu, and J. J. Zondy, "Watt-level single-frequency tunable Nd:YLF/periodically poled KTiOPO4 red laser," *Opt. Lett.* **32** (18), 2732-2734 (2007).
- [35] E. Jequier and F. Constant, "Water as an essential nutrient: the physiological basis of hydration," *Eur J Clin Nutr* **64** (2), 115-123 (2009).
- [36] J. J. Zondy, F. A. Camargo, T. Zanon, V. Petrov, and N. U. Wetter, "Observation of strong cascaded Kerr-lens dynamics in an optimally-coupled cw intracavity frequency-doubled Nd:YLF ring laser," *Opt. Express* **18** (5), 4796-4815 (2010).
- [37] R. Boyd, *Nonlinear Optics*. (Elsevier/Academic Press, Rochester, 2008), 3rd ed.
- [38] W. P. Risk, "Modeling of longitudinally pumped solid-state lasers exhibiting reabsorption losses: errata," *J. Opt. Soc. Am. B* **14** (12), 3457-3457 (1997).
- [39] T. Taira, W. M. Tulloch, and R. L. Byer, "Modeling of quasi-three-level lasers and operation of cw Yb:YAG lasers," *Appl. Opt.* **36** (9), 1867-1874 (1997).
- [40] F. Auge, F. Druon, F. Balembois, P. Georges, A. Brun, F. Mougél, G. Aka, and D. Vivien, "Theoretical and experimental investigations of a diode-pumped quasi-three-level laser: the Yb³⁺ doped Ca₄GdO(BO₃)₃ (Yb:GdCOB) laser," *Quantum Electronics, IEEE Journal of* **36** (5), 598-606 (2000).

- [41] T. Y. Fan and Robert L. Byer, "Continuous-wave operation of a room-temperature, diode-laser-pumped, 946-nm Nd:YAG laser," *Opt. Lett.* **12** (10), 809-811 (1987).
- [42] P. Zeller and P. Peuser, "Efficient, multiwatt, continuous-wave laser operation on the $4F(3/2)-4I(9/2)$ transitions of Nd:YVO₄ and Nd:YAG," *Opt. Lett.* **25** (1), 34-36 (2000).
- [43] C. Czeranowsky, E. Heumann, and G. Huber, "All-solid-state continuous-wave frequency-doubled Nd:YAG BiBO laser with 2.8-W output power at 473 nm," *Opt. Lett.* **28** (6), 432-434 (2003).
- [44] R. Zhou, E. Li, H. Li, P. Wang, and J. Yao, "Continuous-wave, 15.2 W diode-end-pumped Nd:YAG laser operating at 946 nm," *Opt. Lett.* **31** (12), 1869-1871 (2006).
- [45] Q. Xue, Y. Bu, F. Jia, and Q. Zheng, "Compact efficient 1.5 W continuous wave Nd:YVO₄/LBO blue laser at 457 nm," *Optics Communications* **258** (1), 67-71 (2006).
- [46] C. Czeranowsky, M. Schmidt, E. Heumann, G. Huber, S. Kutovoi, and Y. Zavartsev, "Continuous wave diode pumped intracavity doubled Nd:GdVO₄ laser with 840 mW output power at 456 nm," *Optics Communications* **205** (4-6), 361-365 (2002).
- [47] Y. F. Lü, J. Xia, and X. H. Zhang, "Quasi-three-level Nd:LuVO₄ laser under diode pumping directly into the emitting level," *Laser Physics Letters* **7** (2), 120-123 (2010).
- [48] Y. F. Lü, J. Xia, J. Q. Lin, X. Gao, Y. Dong, L. J. Xu, G. C. Sun, Z. M. Zhao, Y. Tan, J. F. Chen, Z. X. Liu, C. L. Li, H. X. Cai, Z. T. Liu, Z. Y. Ma, and G. B. Ning, "Diode-pumped CW frequency-doubled Nd:CNGG-BiBO blue laser at 468 nm," *Laser Physics Letters* **8** (2), 103-106 (2011).
- [49] Y. F. Lü, X. H. Zhang, J. Xia, A. F. Zhang, X. D. Yin, and L. Bao, "Highly efficient continuous-wave 912 nm Nd:GdVO₄ laser emission under direct 880 nm pumping," *Laser Physics Letters* **6** (11), 796-799 (2009).
- [50] Z. Quan, Y. Yi, L. Bin, Z. Kai, L. Yang, and Z. Ling, "Experimental study of the generation of a blue laser by intracavity frequency doubling of a cw Nd:GdVO₄ laser with lithium borate," *Appl. Opt.* **48** (16), 2979-2982 (2009).
- [51] Z. Quan, Y. Yi, L. Bin, Q. Dapeng, and Z. Ling, "13.2 W laser-diode-pumped Nd:YVO₄/LBO blue laser at 457 nm," *J. Opt. Soc. Am. B* **26** (6), 1238-1242 (2009).
- [52] F. Balembois, M. Castaing, E. Héroult, and P. Georges, "Low-wavelength emission of Nd-doped lasers," *Laser & Photonics Reviews* **5** (5), 659-676 (2011).
- [53] C. V. Raman and K. S. Krishnan, "The negative absorption of radiation," *Nature* **122**, 12-13 (1928).

- [54] D. W. Hahn, "Raman Scattering Theory", (2007), pp. 1-13.
- [55] J. A. Piper and H. M. Pask, "Crystalline Raman lasers," *IEEE Journal of Selected Topics in Quantum Electronics* **13** (3), 692-704 (2007).
- [56] A. J. Lee, J. Jakutis-Neto, and H. M. Pask, "Generation of combs of wavelengths in the infrared and visible using cascaded stimulated Raman scattering in potassium titanyl phosphate," presented at the Quantum Electronics Conference & Lasers and Electro-Optics (CLEO/IQEC/PACIFIC RIM), 2011.
- [57] G.M. Eckhardt E.J. Woodburry, "Apparatus producing stimulated raman emission," USA Patent (1968).
- [58] R. W. Hellwarth, "Theory of Stimulated Raman Scattering," *Physical Review* **130** (5), 1850 (1963).
- [59] G. Eckhardt, D. P. Bortfeld, and M. Geller, "Stimulated emission of stokes and anti-stokes Raman lines from diamond, calcite and alpha -sulfur single crystals," *Appl. Phys. Lett.* **3** (8), 137-138 (1963).
- [60] G. Eckhardt, "Selection of Raman laser materials," *Quantum Electronics, IEEE Journal of* **2** (1), 1-8 (1966).
- [61] N. Bloembergen, "The stimulated Raman effect," *Am. J. Phys.* **35** (11), 989-1023 (1967).
- [62] V. N. Voitsekhovskii, S. N. Karpukhin, and V. E. Yakobson, "Single-Crystal Barium Nitrate and Sodium-Nitrate as Efficient Materials for Laser-Radiation Frequency-Conversion Based on Stimulated Raman-Scattering," *Journal of Optical Technology* **62** (11), 770-776 (1995).
- [63] A. S. Grabtchikov, A. N. Kuzmin, V. A. Lisinetskii, G. I. Ryabtsev, V. A. Orlovich, and A. A. Demidovich, "Stimulated Raman scattering in Nd : KGW laser with diode pumping," *Journal of Alloys and Compounds* **300**, 300-302 (2000).
- [64] Y. F. Chen, T. M. Huang, C. C. Liao, Y. P. Lan, and S. C. Wang, "Efficient high-power diode-end-pumped TEM00 Nd: YVO4 laser," *Photonics Technology Letters, IEEE* **11** (10), 1241-1243 (1999).
- [65] K. R. F. Kleine, L. P. Gonzalez, R. Bhatia, L. R. Marshall, and D. G. Matthews, "High Brightness Nd:YVO4 Laser for Nonlinear Optics", edited by M. Injeyan H. Fejer and U. Keller (Optical Society of America, 1999), Vol. 26, pp. ME16.
- [66] Yung-Fu Chen, S. W. Tsai, and S. C. Wang, "High-power diode-pumped Q-switched and mode-locked Nd:YVO4 laser with a Cr⁴⁺:YAG saturable absorber," *Opt. Lett.* **25** (19), 1442-1444 (2000).

- [67] J. Liu, C. Wang, C. Du, L. Zhu, H. Zhang, X. Meng, J. Wang, Z. Shao, and M. Jiang, "High-power actively Q-switched Nd:GdVO₄ laser end-pumped by a fiber-coupled diode-laser array," *Optics Communications* **188** (1–4), 155-162 (2001).
- [68] A. A. Kaminskii, Ken-ichi Ueda, H. J. Eichler, Y. Kuwano, H. Kouta, S. N. Bagaev, T. s. H. Chyba, J. C. Barnes, G. M. A. Gad, T. Murai, and J. Lu, "Tetragonal vanadates YVO₄ and GdVO₄ - new efficient $\chi^{(3)}$ -materials for Raman lasers," *Optics Communications* **194** (1-3), 201-206 (2001).
- [69] A. J. Lee, H. M. Pask, D. J. Spence, and J. A. Piper, "Efficient 5.3 W cw laser at 559 nm by intracavity frequency summation of fundamental and first-Stokes wavelengths in a self-Raman Nd:GdVO₄ laser," *Optics Letters* **35** (5), 682-684 (2010).
- [70] A. Kaminskii, H. Rhee, H. Eichler, K. Ueda, K. Oka, and H. Shibata, "New $\chi^{(3)}$ -nonlinear-laser manifestations in tetragonal LuVO₄ crystal: more than sesqui-octave Raman-induced Stokes and anti-Stokes comb generation and cascaded self-frequency "tripling"," *Applied Physics B: Lasers and Optics* **93** (4), 865-872 (2008).
- [71] P. G. Zverev, T. T. Basiev, A. A. Sobol, I. V. Ermakov, and W. Gellerman, "BaWO₄ crystal for quasi-cw yellow Raman laser," *Advanced Solid-State Lasers, Proceedings* **50**, 212-217 (2001).
- [72] H. Jelinkova, J. Sulc, M. Nemec, J. K. Jabczynski, and W. Zendzian, "New wavelengths generated by BaWO₄ or KGW intracavity Raman laser," *Solid State Lasers XV: Technology and Devices* **6100**, E1001 (2006).
- [73] W. Lubeigt, G. M. Bonner, J. E. Hastie, M. D. Dawson, D. Burns, and A. J. Kemp, "Continuous-wave diamond Raman laser," *Opt. Lett.* **35** (17), 2994-2996 (2010).
- [74] G. Turri, Y. Chen, M. Bass, D. Orchard, J. E. Butler, S. Magana, T. Feygelson, D. Thiel, K. Fourspring, R. V. Dewees, J. M. Bennett, J. Pentony, S. Hawkins, M. Baronowski, A. Guenther, M. D. Seltzer, D. C. Harris, and C. M. Stickley, "Optical absorption, depolarization, and scatter of epitaxial single-crystal chemical-vapor-deposited diamond at 1.064 μ m," *Optical Engineering* **46** (6), 064002-064010 (2007).
- [75] H. M. Pask, P. Dekker, R. P. Mildren, D. J. Spence, and J. A. Piper, "Wavelength-versatile visible and UV sources based on crystalline Raman lasers," *Progress in Quantum Electronics* **32** (3-4), 121-158 (2008).
- [76] A. S. Grabtchikov, V. A. Lisinetskii, V. A. Orlovich, M. Schmitt, R. Maksimenka, and W. Kiefer, "Multimode pumped continuous-wave solid-state Raman laser," *Optics Letters* **29** (21), 2524-2526 (2004).

- [77] A. A. Demidovich, A. S. Grabtchikov, V. A. Lisinetskii, V. N. Burakevich, V. A. Orlovich, and W. Kiefer, "Continuous-wave Raman generation in a diode-pumped Nd³⁺: KGd(WO₄)(2) laser," *Optics Letters* **30** (13), 1701-1703 (2005).
- [78] P. Dekker, H. M. Pask, D. J. Spence, and J. A. Piper, "Continuous-wave, intracavity doubled, self-Raman laser operation in Nd : GdVO₄ at 586.5 nm," *Optics Express* **15** (11), 7038-7046 (2007).
- [79] L. Fan, Y. X. Fan, Y. Q. Li, H. Zhang, Q. Wang, J. Wang, and H. T. Wang, "High-efficiency continuous-wave Raman conversion with a BaWO₄ Raman crystal," *Opt. Lett.* **34** (11), 1687-1689 (2009).
- [80] J. Jakutis-Neto, J. Lin, N. U. Wetter, and H. Pask, "Continuous-wave Watt-level Nd:YLF/KGW Raman laser operating at near-IR, yellow and lime-green wavelengths," *Opt. Express* **20** (9), 9841-9850 (2012).
- [81] A. J. Lee, H. M. Pask, J. A. Piper, H. J. Zhang, and J. Y. Wang, "An intracavity, frequency-doubled BaWO₄ Raman laser generating multi-watt continuous-wave, yellow emission," *Optics Express* **18** (6), 5984-5992 (2010).
- [82] V. G. Savitski, I. Friel, J. E. Hastie, M. D. Dawson, D. Burns, and A. J. Kemp, "Characterization of Single-Crystal Synthetic Diamond for Multi-Watt Continuous-Wave Raman Lasers," *Ieee Journal of Quantum Electronics* **48** (3), 328-337 (2012).
- [83] E. O. Ammann, "Simultaneous simulated Raman scattering and optical frequency mixing in lithium iodate," *Appl. Phys. Lett.* **34** (12), 838-840 (1979).
- [84] S. Li, X. Zhang, Q. Wang, X. Zhang, Z. Cong, H. Zhang, and J. Wang, "Diode-side-pumped intracavity frequency-doubled Nd:YAG/BaWO₄ Raman laser generating average output power of 3.14 W at 590 nm," *Opt. Lett.* **32** (20), 2951-2953 (2007).
- [85] P. Dekker, H. M. Pask, and J. A. Piper, "All-solid-state 704 mW continuous-wave yellow source based on an intracavity, frequency-doubled crystalline Raman laser," *Optics Letters* **32** (9), 1114-1116 (2007).
- [86] H. Y. Zhu, Y. M. Duan, G. Zhang, C. H. Huang, Y. Wei, W. D. Chen, Y. D. Huang, and N. Ye, "Yellow-light generation of 5.7 W by intracavity doubling self-Raman laser of YVO₄/Nd:YVO₄ composite," *Optics Letters* **34** (18), 2763-2765 (2009).
- [87] H. Y. Zhu, Y. M. Duan, G. Zhang, C. H. Huang, Y. Wei, H. Y. Shen, Y. Q. Zheng, L. X. Huang, and Z. Q. Chen, "Efficient second harmonic generation of double-end diffusion-bonded Nd:YVO₄ self-Raman laser producing 7.9 W yellow light," *Optics Express* **17** (24), 21544-21550 (2009).
- [88] A. J. Lee, H. M. Pask, P. Dekker, and J. A. Piper, "High efficiency, multi-Watt CW yellow emission from an intracavity-doubled self-Raman laser using Nd:GdVO₄," *Optics Express* **16** (26), 21958-21963 (2008).

- [89] A. J. Lee, D. J. Spence, J. A. Piper, and H. M. Pask, "A wavelength-versatile, continuous-wave, self-Raman solid-state laser operating in the visible," *Opt. Express* **18** (19), 20013-20018 (2010).
- [90] A. J. Lee, J. Lin, and H. M. Pask, "Near-infrared and orange-red emission from a continuous-wave, second-Stokes self-Raman Nd:GdVO₄ laser," *Opt. Lett.* **35** (18), 3000-3002 (2010).
- [91] T. Omatsu, M. Okida, A. Lee, and H. Pask, "Thermal lensing in a diode-end-pumped continuous-wave self-Raman Nd-doped GdVO₄ laser," *Applied Physics B: Lasers and Optics* **108** (1), 73-79 (2012).
- [92] G. M. Bonner, H. M. Pask, A. J. Lee, A. J. Kemp, J. Wang, H. Zhang, and T. Omatsu, "Measurement of thermal lensing in a CW BaWO₄ intracavity Raman laser," *Opt. Express* **20** (9), 9810-9818 (2012).
- [93] J. Lin and H. Pask, "Nd:GdVO₄ self-Raman laser using double-end polarised pumping at 880 nm for high power infrared and visible output," *Applied Physics B: Lasers and Optics* **108** (1), 17-24 (2012).
- [94] X. Li, A. J. Lee, Y. Huo, H. Zhang, J. Wang, J. A. Piper, H. M. Pask, and D. J. Spence, "Managing SRS competition in a miniature visible Nd:YVO₄/BaWO₄ Raman laser," *Opt. Express* **20** (17), 19305-19312 (2012).
- [95] D. J. Spence, P. Dekker, and H. M. Pask, "Modeling of continuous wave intracavity Raman lasers," *Ieee Journal of Selected Topics in Quantum Electronics* **13** (3), 756-763 (2007).
- [96] Y. K. Bu, C. Q. Tan, and N. Chen, "Continuous-wave yellow light source at 579 nm based on intracavity frequency-doubled Nd:YLF/SrWO₄/LBO Raman laser," *Laser Physics Letters* **8** (6), 439-442 (2011).
- [97] D. J. Li, Z. Ma, R. Haas, A. Schell, P. Zhu, P. Shi, and K. M. Du, "Diode-end-pumped double Nd : YLF slab laser with high energy, short pulse width, and diffraction-limited quality," *Optics Letters* **33** (15), 1708-1710 (2008).
- [98] W. A. Clarkson, P. J. Hardman, and D. C. Hanna, "High-power diode-bar end-pumped Nd:YLF laser at 1.053 μm ," *Opt. Lett.* **23** (17), 1363-1365 (1998).
- [99] N. U. Wetter, E. C. Sousa, F. D. Camargo, I. M. Ranieri, and S. L. Baldochi, "Efficient and compact diode-side-pumped Nd : YLF laser operating at 1053 nm with high beam quality," *Journal of Optics a-Pure and Applied Optics* **10** (10), - (2008).
- [100] K. W. Su, Y. T. Chang, and Y. F. Chen, "Power scale-up of the diode-pumped actively Q-switched Nd : YVO₄ Raman laser with an undoped YVO₄ crystal as a Raman shifter," *Applied Physics B-Lasers and Optics* **88** (1), 47-50 (2007).

- [101] B. S. Wang, J. Y. Peng, J. G. Miao, Y. M. Li, E. J. Hao, Z. Zhang, L. L. Gao, and H. M. Tan, "Diode end-pumped passively Q-switched Nd³⁺: GdVO₄ self-Raman laser at 1176 nm," Chinese Physics Letters **24** (1), 112-114 (2007).
- [102] V. A. Lisinetskii, H. J. Eichler, H. Rhee, X. Wang, and V. A. Orlovich, "The generation of high pulse and average power radiation in eye-safe spectral region by the third stokes generation in barium nitrate Raman laser," Optics Communications **281** (8), 2227-2232 (2008).
- [103] K. W. Su, Y. T. Chang, and Y. F. Chen, "Efficient high-peak-power diode-pumped actively Q-switched Nd:YAG/YVO₄ intracavity Raman laser," Applied Optics **47** (35), 6675-6679 (2008).
- [104] W. Zheng-Ping, H. Da-Wei, F. Xin, M. Huai-Jin, X. Xin-Guang, W. Ji-Yang, and S. Zong-Shu, "Eye-safe Raman laser at 1.5 μ m based on BaWO₄ crystal," Chinese Physics Letters **25** (1), 122-124 (2008).
- [105] A. Kaminskii, M. Bettinelli, J. Dong, D. Jaque, and K. Ueda, "Nanosecond Nd³⁺:LuVO₄ self-Raman laser," Laser Physics Letters **6** (5), 374-379 (2009).
- [106] "Web site Castech Inc:
http://www.castech.com/newEbiz1/EbizPortalFG/portal/html/ProductInfoExhibit.html?ProductInfoExhibit_ProductID=c373e90570dee4658f7f848a8f232242&ProductInfoExhibit_isRefreshParent=false", Vol. 2010.
- [107] A. V. Smith, SNLO nonlinear optics code (As-Photonics, Albuquerque).
- [108] "<http://teamd.lbl.gov/chem-analysis.html>", (accessed on 10/09/2012).
- [109] "<http://appliedspectra.com/technology/LIBS.html>", (accessed on 10/09/2012).
- [110] "<http://spectra.phy.bris.ac.uk/Media/InVia%20anime.gif>", (accessed on 08/09/2012).
- [111] "<http://pdf1.alldatasheet.com/datasheet-pdf/view/212118/HAMAMATSU/R446.html>", (accessed on 07/09/2012).
- [112] "<http://www.testwall.com/products/product.960.0.0.Tektronix-TDS3054.html>", (accessed on 10/09/2012).
- [113] S. Spiekermann and F. Laurell, "Continuous wave and Q-switched operation of diode pumped quasi-three level Nd:YLF lasers," presented at the Advanced Solid state lasers, 2000.
- [114] R. Polloni and O. Svelto, "Optimum coupling for intracavity second harmonic generation," Quantum Electronics, IEEE Journal of **4** (9), 528-530 (1968).

- [115] P. Bado, M. Bouvier, and J. Scott Coe, "Nd:YLF mode-locked oscillator and regenerative amplifier," *Opt. Lett.* **12** (5), 319-321 (1987).
- [116] M. Li, S. Zhao, K. Yang, G. Li, D. Li, and J. An, "Diode-pumped actively Q-switching and mode-locking Nd:GdVO₄ laser," *Laser Physics Letters* **5** (10), 722-725 (2008).
- [117] D. C. Hanna, C. G. Sawyers, and M. A. Yuratich, "Telescopic resonators for large-volume TEM₀₀-mode operation," *Optical and Quantum Electronics* **13** (6), 493-507 (1981).
- [118] I. V. Mochalov, "Laser and nonlinear properties of the potassium gadolinium tungstate laser crystal KGd(WO₄)₂:Nd³⁺+(KGW:Nd)," *Optical Engineering* **36** (6), 1660-1669 (1997).
- [119] V. A. Lisinetskii, A. S. Grabtchikov, A. A. Demidovich, V. N. Burakevich, V. A. Orlovich, and A. N. Titov, "Nd:KGW/KGW crystal: efficient medium for continuous-wave intracavity Raman generation," *Applied Physics B: Lasers and Optics* **88** (4), 499-501 (2007).
- [120] A. A. Kaminskii, C. L. McCray, H. R. Lee, S. W. Lee, D. A. Temple, T. H. Chyba, W. D. Marsh, J. C. Barnes, A. N. Annanenko, V. D. Legun, H. J. Eichler, G. M. A. Gad, and K. Ueda, "High efficiency nanosecond Raman lasers based on tetragonal PbWO₄ crystals," *Optics Communications* **183** (1-4), 277-287 (2000).
- [121] G. E. James, E. M. Harrell II, C. Bracikowski, K. Wiesenfeld, and R. Roy, "Elimination of chaos in an intracavity-doubled Nd:YAG laser," *Opt. Lett.* **15** (20), 1141-1143 (1990).
- [122] V. Magni, G. Cerullo, S. De Silvestri, O. Svelto, L. J. Qian, and M. Danailov, "Intracavity frequency doubling of a cw high-power TEM₀₀ Nd:YLF laser," *Opt. Lett.* **18** (24), 2111-2113 (1993).
- [123] A. S. Grabtchikov, A. N. Kuzmin, V. A. Lisinetskii, G. I. Ryabtsev, V. A. Orlovich, and A. A. Demidovich, "Stimulated Raman scattering in Nd:KGW laser with diode pumping," *Journal of Alloys and Compounds* **300–301** (0), 300-302 (2000).
- [124] H. M. Pask, "Continuous-wave, all-solid-state, intracavity Raman laser," *Optics Letters* **30** (18), 2454-2456 (2005).
- [125] Y. M. Duan, H. Y. Zhu, G. Zhang, C. H. Huang, Y. Wei, C. Y. Tu, Z. J. Zhu, F. G. Yang, and Z. Y. You, "Efficient 559.6 nm light produced by sum-frequency generation of diode-end-pumped Nd:YAG/SrWO₄ Raman laser," *Laser Physics Letters* **7** (7), 491-494 (2010).
- [126] Y. Duan, F. Yang, H. Zhu, Z. Zhu, C. Huang, Z. You, Y. Wei, G. Zhang, and C. Tu, "Continuous-wave 560 nm light generated by intracavity SrWO₄ Raman and KTP sum-frequency mixing," *Optics Communications* **283** (24), 5135-5138 (2010).

- [127] W. Baoshan, T. Huiming, P. Jiying, M. Jieguang, and G. Lanlan, "Low threshold, diode end-pumped Nd³⁺: GdVO₄ self-Raman laser," *Optical Materials* **29** (12), 1817-1820 (2007).
- [128] H. Yu, Z. Li, A. J. Lee, J. Li, H. Zhang, J. Wang, H. M. Pask, J. A. Piper, and M. Jiang, "A continuous wave SrMoO₄ Raman laser," *Opt. Lett.* **36** (4), 579-581 (2011).
- [129] H. Zhu, Y. Duan, G. Zhang, Y. Zhang, and F. Yang, "Laser Induced Blue Luminescence Phenomenon," *Japanese Journal of Applied Physics* **50** (Copyright (C) 2011 The Japan Society of Applied Physics), 090203 (2011).
- [130] I. Khodasevich, A. Kornienko, E. Dunina, and A. Grabtchikov, "On the influence of dopant ions on blue emission in kgw crystal excited by infrared laser radiation," *Journal of Applied Spectroscopy* **79** (1), 38-45 (2012).
- [131] R. Lisiecki, W. Ryba-Romanowski, and T. Lukasiewicz, "Blue up-conversion with excitation into Tm ions at 808 nm in YVO₄ crystals co-doped with thulium and ytterbium," *Applied Physics B: Lasers and Optics* **81** (1), 43-47 (2005).
- [132] F. Güell, X. Mateos, Jna Gavalda, R. Solé, M. Aguiló, D₁, amp, x, F. az, M. Galan, and J. Massons, "Optical characterization of Tm³⁺-doped KGd(WO₄)₂ single crystals," *Optical Materials* **25** (1), 71-77 (2004).
- [133] M. Pollnau, D. R. Gamelin, S. R. Lüthi, H. U. Güdel, and M. P. Hehlen, "Power dependence of upconversion luminescence in lanthanide and transition-metal-ion systems," *Physical Review B* **61** (5), 3337 (2000).
- [134] L. C. Courrol, I. M. Ranieri, L. V. G. Tarelho, S. L. Baldochi, L. Gomes, and N. D. Vieira Jr, "Study of optical properties of YLF:Nd:Yb:Tm crystals," *Journal of Luminescence* **122–123** (0), 474-477 (2007).
- [135] B. P. Scott, F. Zhao, R. S. F. Chang, and N. Djeu, "Upconversion-pumped blue laser in Tm:YAG," *Opt. Lett.* **18** (2), 113-115 (1993).
- [136] F. Güell, X. Mateos, Jna Gavalda, R. Solé, M. Aguiló, D₁, amp, x, F. az, and J. Massons, "Blue luminescence in Tm³⁺-doped KGd(WO₄)₂ single crystals," *Journal of Luminescence* **106** (2), 109-114 (2004).
- [137] Y. Yang, B. Yao, B. Chen, C. Wang, G. Ren, and X. Wang, "Judd–Ofelt analysis of spectroscopic properties of Tm³⁺, Ho³⁺ doped GdVO₄ crystals," *Optical Materials* **29** (9), 1159-1165 (2007).
- [138] F. S. Ermeneux, C. Goutaudier, R. Moncorgé, M. T. Cohen-Adad, M. Bettinelli, and E. Cavalli, "Growth and fluorescence properties of Tm³⁺ doped YVO₄ and Y₂O₃ single crystals," *Optical Materials* **8** (1–2), 83-90 (1997).

- [139] A. A. Kaminskii, *Laser Crystals: Their Physics and Properties*. (Springer-Verlag, 1981).
- [140] "<http://www.spectra.com/designs/photopic.html>," (accessed on 26/10/12).
- [141] X. Li, H. M. Pask, A. J. Lee, Y. Huo, J. A. Piper, and D. J. Spence, "Miniature wavelength-selectable Raman laser: new insights for optimizing performance," *Opt. Express* **19** (25), 25623-25631 (2011).